Development of a Power to Liquids Process for the Production of Dimethyl Ether by Dehydration of Methanol in a Reactive Distillation Column

Zur Erlangung des akademischen Grades eines
DOKTORS DER INGENIEURWISSENSCHAFTEN (DR.-ING.)

von der KIT-Fakultät für Chemieingenieurwesen und Verfahrenstechnik des
Karlsruher Instituts für Technologie (KIT)
genehmigte

DISSERTATION

von
M.Sc. Malte Gierse (geb. Semmel)
aus Freiburg im Breisgau

Tag der mündlichen Prüfung: 9. Juli 2024

Erstgutachter: Prof. Dr. Jörg Sauer
Zweitgutachter: Prof. Dr. Erik von Harbou

Declaration

I, Malte Gierse, declare that this thesis represents my own work and that I have written it independently by myself, without the use of other documents or sources beyond those stated in the references.

Malte Gierse

Acknowledgements

This thesis was developed during my time as doctoral researcher at Institute of Catalysis Research and Technology (IKFT) at KIT in Karlsruhe in cooperation with Fraunhofer Institute for Solar Energy Systems ISE in Freiburg. What was a challenging but exciting journey to me, was only enabled by the support of many wonderful people, to who I hereby would like to express my appreciation and thankfulness.

Special thanks go to Prof. Dr. Jörg Sauer from KIT, who supervised this work. Thank you for welcoming me to your institute, for giving me the right amount of freedom but also strong scientific support whenever needed, and for your open and sincere nature.

Equally, I would like to thank Dr. Ouda Salem, who supervised this work at Fraunhofer ISE. Thank you for your scientific and personal support during this intense and exciting times, for your energy, and for backing me up, when I was being too hard on myself.

I also want to thank Max Hadrich, Dr. Achim Schaadt and Prof. Dr. Christopher Hebling for giving me the opportunity to perform my thesis in such an exciting and dynamic environment, for their trust, and their organizational support.

I am also extremely thankful for all my wonderful colleagues. Thank you for your great technical support in test stand construction, your experienced help with modelling and scientific brainstorming, thank for silly jokes and memes, and your continuous vitality.

Furthermore, I would like to thank Deutsche Bundesstiftung Umwelt for the financing of this work by a PhD scholarship (20020/662), the trust and the great amount of freedom to focus on my research.

I am very grateful to all the students Leon Steiner, Benedikt Steinbach, Max Bontrup, Malte Kolb, Simon Benninghoff and Maximilian Kerschbaum, who supported this work with their persistence and energy.

Prof. Dr. Erik von Harbou from TU Kaiserslautern is sincerely thanked for his agreement to evaluate this thesis as second reviewer.

Last but not least I want to thank my partner and best friend Sophia. Thank you for always being by my side, for supporting and building me up in my hardest moments, for celebrating every success with me and for making me laugh every day.

Preamble

This is a paper-based thesis, and, therefore, part of the content presented here has been previously published. Hence, parts of the text are identical to published articles, with minor modifications, such as formatting, citation style or modification of the layout.

In order to avoid the repetition of introductory text in each chapter, one detailed introduction of the DME synthesis and the corresponding process technology is provided in chapter 1.

Abstract

The conversion of renewable electricity into chemical energy in so-called "Power-to-X" (PtX) processes is increasingly becoming a central component of the global energy transition. Green hydrogen holds great potential for the sustainable decarbonization of industry and transportation sector, however, hydrogen transport and storage remain challenging. Energy-dense liquid chemical energy carriers in contrast enable an economic large-scale storage and transport of renewable energy over long distances. In this context, dimethyl ether (DME) is a very promising target molecule since it can be used as environmentally benign hydrogen carrier, LPG- and diesel substitute fuel, but also as solvent, refrigerant and propellant.

In this work, the process intensification of the conventional process by applying reactive distillation was studied. This requires shifting the reaction from gas- to liquid phase and significantly lower temperatures. In a catalyst screening using a high throughput batch reactor system, the oversulfonated ion exchange resin Amberlyst 36 and the chlorinated ion exchange resin Treverlyst CAT400 proved to be the most active catalysts under these new reaction conditions. Based on liquid phase kinetic measurements in a fixed-bed profile reactor, a kinetic model valid for the entire operational range reactive distillation was developed. This was achieved by complementing a Langmuir Hinshelwood approach with a dedicated inhibition term to account for the non-linear water inhibition induced by the selective swelling of the resin catalysts. Due to the higher thermal stability, significantly higher reaction rates were reported with the chlorinated resin CAT400.

For the first time in literature, the reactive distillation process with full MeOH conversion was successfully demonstrated with pure and crude MeOH feedstock under industrially relevant conditions using a DN50 pressure distillation column equipped with catalytic packings. Based on 18 experiments, the developed kinetic model could be successfully validated under the process conditions where gas- and liquid phase coexist, and a validated reactive distillation simulation model was developed in Aspen Plus. A system-immanent target conflict between capital and operating expenses was identified when varying the feed mass flow in the experiments. Complementing the process simulation with a factorial economic model allowed to resolve this target conflict and to identify a cost-optimal column sizing. Furthermore, the optimized reactive distillation process concepts with pre-reactor and side-reactor were developed and rigorously optimized. It was found that the developed side-reactor concept presents the most economic and efficient process variant, allowing 39 % cost reduction compared to the conventional gas-phase process. Moreover, it was shown that a plant without external heat demand can be realized when heat integrating MeOH and DME plant.

Kurzzusammenfassung

Die Umwandlung von erneuerbarem Strom in chemische Energie in sogenannten "Power-to-X"-Prozessen (PtX) wird zunehmend zu einem zentralen Bestandteil der globalen Energiewende. Grüner Wasserstoff birgt ein großes Potenzial für die nachhaltige Dekarbonisierung der Industrie und des Verkehrssektors, allerdings bleiben der Transport und die Speicherung von Wasserstoff eine Herausforderung. Energiedichte, flüssige chemische Energieträger ermöglichen dagegen eine wirtschaftliche großtechnische Speicherung und den Transport erneuerbarer Energie über große Entfernungen. In diesem Zusammenhang ist Dimethylether (DME) ein vielversprechendes Zielmolekül, da es als umweltfreundlicher Wasserstoffträger, LPG- und Dieselersatzkraftstoff, aber auch als Lösungsmittel, Kältemittel und Treibstoff eingesetzt werden kann.

In dieser Arbeit wurde die Prozessintensivierung des herkömmlichen Verfahrens durch Anwendung der Reaktivdestillation untersucht. Dies erfordert die Verlagerung der Reaktion von der Gas- in die Flüssigphase und zu deutlich niedrigere Temperaturen. In einem Katalysatorscreening in einem High-Througput Batch-Reaktorsystem erwiesen sich das übersulfonierte Ionenaustauscherharz Amberlyst 36 und das chlorierte Ionenaustauscherharz Treverlyst CAT400 als die aktivsten Katalysatoren unter diesen neuen Reaktionsbedingungen. Basierend auf Flüssigphasen-Kinetikmessungen in einem Festbett-Profilreaktor wurde ein Kinetikmodell entwickelt, das für den gesamten Betriebsbereich der Reaktivdestillation gültig ist. Hierzu wurde ein Langmuir-Hinshelwood-Ansatz mit einen dedizierten Inhibitionsterm ergänzt, um die nichtlineare Wasserinhibierung durch die selektive Quellung der Katalysatoren zu berücksichtigen. Aufgrund der höheren thermischen Stabilität wurden mit dem chlorierten Ionenaustauscherharz CAT400 deutlich höhere Reaktionsgeschwindigkeiten ermittelt.

Bei industriell relevanten Bedingungen unter Verwendung einer DN50-Druckdestillations-kolonne mit katalytischen Packungen wurde zum ersten Mal in der Literatur der Reaktivdestillationsprozess mit vollständigem MeOH-Umsatz mit reinem und Rohmethanol Feedstock erfolgreich demonstriert. Auf der Grundlage von 18 Experimenten konnte das entwickelte Kinetikmodell unter den Prozessbedingungen, bei denen Gas- und Flüssigphase koexistieren, erfolgreich validiert werden, und es wurde ein validiertes Simulationsmodell für die Reaktivdestillation in Aspen Plus entwickelt. Bei der Variation des Feed-Massenstroms in den Experimenten wurde ein systemimmanenter Zielkonflikt zwischen Kapital- und Betriebskosten identifiziert. Durch die Ergänzung der Prozesssimulation mit einem faktoriellen ökonomischen Modell konnte dieser Zielkonflikt aufgelöst und eine kostenoptimale Kolonnenauslegung ermittelt werden. Darüber hinaus wurden optimierte Prozesskonzepte für

die Reaktivdestillation mit Vor- und Seitenreaktor entwickelt und rigoros optimiert. Es zeigte sich, dass das entwickelte Seitenreaktorkonzept die wirtschaftlichste und effizienteste Prozessvariante darstellt, die eine Kostenreduktion von 39 % im Vergleich zum konventionellen Gasphasenprozess ermöglicht. Darüber hinaus wurde gezeigt, dass eine Anlage ohne externen Wärmebedarf realisiert werden kann, wenn MeOH- und DME-Anlage wärmeintegriert werden.

Content

1 Introduction

Declaration of contributions:

Malte Gierse conceptualized the work, did the literature research, organized the data, created the figures, and wrote the manuscript.

Ramy E. Ali supported in creating the figures, contributed to the discussion, and reviewed the manuscript.

Ouda Salem (M. Ouda) conceptualized and supervised the work, contributed to the discussion, and reviewed the manuscript.

Achim Schaadt supervised the work.

Jörg Sauer supervised the work, contributed to the discussion, and reviewed the manuscript.

Christopher Hebling supervised the work.

Chapter redrafted and significantly extended based on the following main publication:

Semmel, M.; Ali, R. E.; Ouda, M.; Schaadt, A.; Sauer, J.; Hebling, C. (2021): Power-to-DME: a cornerstone towards a sustainable energy system. In Giuseppe Spazzafumo (Ed.): Power to Fuel. How to Speed Up a Hydrogen Economy: Elsevier, pp. 123–151.

1.1 Power-to-X as key element for the energy transition

The successive reduction of global CO_2 emissions is one of the greatest challenges of the current generation. The imminent risks for mankind and the environment due to anthropogenic climate change require a rapid and comprehensive defossilization of the global energy and economic system. Renewable, CO_2-neutral replacement technologies must be found for both energy production and material value creation from fossil raw materials. One possibility for sustainable energy production is the use of renewable energy sources such as wind and solar energy. However, weather-related fluctuations in combination with the local agglomeration of renewable energy sources require storage and transport of the generated electrical energy on a large scale. From this perspective, the conversion of electrical energy into chemical energy in the form of hydrogen is increasingly becoming a central component of the energy transition. However, the low volumetric energy density of hydrogen requires high technical, energetic, and economic efforts to convert hydrogen into a transportable and storable form by means of compression or liquefaction [1]. The technology field "Power-to-X" (PtX) offers a promising solution approach. It comprises different routes to produce "green" H_2 from renewable electricity by electrolysis and to convert it together with CO_2 or nitrogen into synthetic energy carriers [2]. In contrast to bio-based energy carriers, the production of PtX fuels does not conflict with food production or biodiversity considerations [1]. In addition to the material use of these energy carriers, for example in the chemical industry, their direct use as sustainable fuel, often referred to as "e fuel", is a particularly promising application. However, the combustion of carbonaceous fuels in vehicles or ships leads to dispersed CO_2-emissions, which complicates the establishment of a closed carbon cycle. For this reason, the utilization of locally emission-free technologies is often enforced by policy makers around the world [2]. Under these circumstances, the application of synthetic energy carriers as hydrogen carriers comes into focus. In this concept, the hydrogen carrier is reformed at a dedicated hub to produce hydrogen for local use, whereas the generated CO_2 arises at a single point where it can be captured for storage or recycled to the hydrogen carrier production site [3].

Due to their high energy density and existing transport infrastructure, synthetic energy carriers offer the perspective of transporting renewable energy on a large scale over long distances. This aspect is particularly relevant when considering the enormous amount of energy imported to industrial countries, currently in the form of fossil-based energy carriers. Since a decreased energy demand is not to be expected in the future and the potential for renewable energy generation in densely populated countries such as Germany is limited, new forms of renewable energy import are needed. Studies estimate that by 2050, the European energy market alone

will need between 550 to 1800 TWh of hydrogen and PtX products annually from which the major part is imported from areas with high renewable energy potential [4].

Beyond that, synthetic energy carriers can allow the use of existing infrastructure for the storage of fossil energy in the form of gas and oil. The existing storage volume for liquid energy sources in Germany, for example, amounts to 90% of the annual gross electricity generation [3].

Synthetic energy carriers offer an opportunity to defossilize energy sectors where the direct use of electrical energy is limited. While overall greenhouse gas emissions in Germany reduced by 27.5% from 1990 to 2017, they slightly increased in the transport sector in the same time frame [4]. This shows the difficulty of defossilization is in this sector. Electrification of road transport can contribute to the reduction of CO_2 emissions in the field of private transport for short distances, but the use of battery-powered vehicles is unsuitable in the field of heavy-duty transport and for long distances [5]. In addition, battery production poses major ecological problems due to the high resource requirements during production, as well as difficult recycling. In the field of air and marine transport, the storage of enormous amounts of energy on board is necessary, which is why liquid fuels are difficult or impossible to replace due to their high energy density [3].

1.2 Dimethyl ether: properties and application

A promising target molecule for PtX processes is dimethyl ether (DME). DME is non-toxic, noncarcinogenic, non-teratogenic and non-mutagenic and has an ozone depletion potential of zero [5]. It is gaseous under standard conditions but can be liquefied under ambient temperature at low pressures of 6 bar [6,7]. Its thermophysical and -chemical properties qualify DME for a wide range of utilization scenarios that will be discussed in the following:

1.2.1 DME as hydrogen carrier

DME is a potential hydrogen carrier for long-range hydrogen transportation. While the hydrogen capacity is typically calculated based on the molecular structure, the “technical hydrogen capacity” should be considered for evaluating the potential of a molecule as hydrogen carrier as proposed by Schühle et al. [3]. Thereby, the mass of hydrogen released in a typical steam-reforming process divided by the mass of hydrogen carrier molecule is considered. Doing so based on the DME reforming equation (1), the technical hydrogen capacity of DME is 26.1 wt.-% instead of 13 wt.-% as calculated based on the molecular structure [3].

$$CH_3OCH_3 + 3H_2O \rightleftharpoons 6H_2 + 2CO_2 \qquad \Delta H^0_{298\,K} = 121.8\ \mathrm{kJ\ mol^{-1}} \qquad (1)$$

This value is 47 % higher than that of ammonia and 39 % higher than that of MeOH, making DME an excellent and environmentally benign hydrogen carrier. Moreover, the similar vapor pressure of DME and CO_2 allow the transport of both molecules in the same ship. This enables back shipping of the CO_2 generated in the steam-reforming process to the place of DME production, for a closed CO_2 cycle [3].

1.2.2 DME as a green fuel

DME is discussed intensively as a green fuel. Besides a great deal of attention in research, many companies such as Volvo [8], Mack Trucks [9] and Ford [10] promote DME as a fuel due to various ecological, technical and economic aspects. A major benefit of DME compared to conventional fuels is the absence of carbon-to-carbon bonds, leading to a practically soot-free combustion [11]. This additionally entails the advantage, that DME engines can be operated with higher exhaust gas recirculation rates in order to reduce NO_x emissions regardless of the NO_x-soot-trade-off present at conventionally fueled engines [12].

DME exhibits a high cetane number (CN) in the range of 55-60 which is slightly higher than that of conventional diesel (CN=51-54), indicating further optimization potential for diesel engines [6,13]. For this reason, DME has been promoted as an alternative diesel fuel since the mid-1990s [7]. Due to its oxygen content, DME has a lower energy density compared to conventional diesel. However, compared to other green fuels such as methane or methanol, the volumetric energy density of DME is superior. Table 1-1 compares the physical properties of DME to that of conventional diesel.

Table 1-1: Physical properties of DME and conventional diesel.

Property	Unit	Diesel	DME	Source
Molecular formula	-	$C_{14}H_{30}$	CH_3OCH_3	Semelsberger et al. [7]
Oxygen content	wt.-%	<1	34.8	Willems et al. [14]
Density	kg l^{-1}	0.856	0.661(*)	Semelsberger et al. [7]
Lower heating value	MJ kg^{-1}	41.66	28.62	Semelsberger et al. [7]
Cetane number	-	51-54	55-60	Willems et al. [14]
Kinematic viscosity (40 °C)	$mm^2\ s^{-1}$	3	0.184	Willems et al. [14]
Normal boiling point	°C	125-400	-24.9	Semelsberger et al. [7]
Vapour pressure	bar	<<0.1	5.3	Park et al. [15]

(*) Density in liquid state at p=1.013 bar and T= - 25 °C

The apparent differences compared to conventional diesel lead to the necessity for technical adaptions of the tank and injection system. Owing to the vapour pressure similar to that of

liquefied petroleum gas (LPG), comparable tank systems can be used to store DME at saturated state between 2 and 7 bar. To account for the lower energy density of DME, an enlargement of the injector nozzle's flow cross-section is necessary. The poor lubrication behaviour of DME requires an oil lubrication of the injection pump [14]. Furthermore, precaution must be taken concerning the chemical stability of the used rubber seals since DME can lead to swelling and dissolution of various rubber materials. Ethylene propylene diene monomer (EPDM) and perfluoro-elastomer (FFKM) have been identified as suitable seal materials [14,16,17].

A major criterion for the potential evaluation of alternative fuels is the required effort to create an infrastructure for the fuel. This comprises not only refuelling stations, but also tank trucks, harbour terminals and tank ships for ocean transport. In this regard, DME benefits from its vapour pressure comparable to that of propane and butane, allowing the use of existing LPG infrastructure [7,18].

Compared to other green fuels such as Fischer-Tropsch (FT) diesel, biodiesel, methanol, ethanol and methane, DME exhibits the lowest well-to-wheel greenhouse gas emissions [7]. Furthermore, considering a hydrogen based production of green fuels, DME shows the highest conversion efficiency and the lowest cost in comparison to the other examined liquid fuels polyoxymethylene dimethyl ethers (OME), FT diesel, iso-octane, ethanol and gasoline from the methanol-to-gasoline process [19].

Another application of DME is the substitution of LPG as residential fuel for heating and cooking. Gas stove systems running on pure DME require modifications of the burner tip, vaporizer and a slightly increased tank volume to account for the reduced energy density compared to LPG [7]. However, using DME for blending with LPG is the major commercial application, representing 90% of Chinas DME demand [20,21]. Recently, the Californian renewable DME producer Oberon Fuels partnered with the world's largest propane distributor SHV Energy, to reduce the carbon footprint of conventional propane gas by blending it with Oberons renewably produced DME [22].

1.2.3 DME in fuel cells

Besides its use in internal combustion engines, DME is also a suitable energy carrier for fuel cell applications. So called direct DME fuel cells use DME at the anode and oxygen at the cathode of Proton Exchange Membrane Fuel Cells [23]. Most research groups used a platinum based electrode on carbon support as anode catalyst [24]. In comparison to other fuels such as methanol, ethanol and formic acid, DME shows low crossover through Nafion® membranes

[23,25]. However, low reaction kinetics is the major drawback of this technology and the reason for ongoing research addressing the development of new catalysts such as platinum based PtRu [26,27] and PtCu [28].

Besides the direct use in fuel cells, DME is also discussed as a hydrogen carrier, allowing easy and efficient energy storage in the liquid phase. By evaporation and catalytic reforming, hydrogen can be formed on-board for further use in a fuel cell. Due to the absence of C-C bonds, catalytic reforming can take place at moderate temperatures of 300-600 °C [29]. In the reforming process CO is formed which is critical to the fuel cell. For this reason, a hydrogen purification step needs to be included such as a Pd-Ag hydrogen permeation membrane [30].

1.2.4 DME as chemical building block

In the chemical industry, DME is of importance as a chemical building block for the production of value-added chemicals. Besides its use for the production of the methylating agent dimethyl sulfate or the solvent methyl acetate, DME is also a potential feedstock for the production of acetic acid and ethanol [31–34].

Particularly in the field of methanol-to-chemicals and methanol-to-fuels, DME plays a key role as an intermediate. It was shown that the methanol-based processes methanol-to-gasoline (MTG), methanol-to-olefins (MTO) and methanol-to-propylene (MTP) are actually based on DME as intermediate, which is synthesized by methanol dehydration as the primary reaction step [35–38]. Thus, it is possible to use DME directly as feedstock. In fact, it was shown that the DME-to-olefins reaction allows higher yields of olefins at lower reaction temperatures compared to the MTO process, while at the same time reducing the degree of exothermicity and the water content of the reaction medium [37]. Same applies for a DME-to-gasoline process, where higher yields are reported compared to the MTG process. Furthermore, it was shown that the lower water concentrations and lower degree of exothermicity are beneficial for the catalyst [36].

Another development is the Mobil olefins-to-gasoline/distillate process, which can be employed subsequent to the MTO process to convert the produced olefins to final fuels, including jet fuel [35,39].

A recently emerging green fuel are OMEs, which – as well as DME – have no C-C bonds, thus enabling a soot free combustion [40]. A product mixture of $OME_{3\text{-}5}$ has similar thermophysical and intrinsic combustion properties as diesel. Contrarily to DME, OMEs are liquid at ambient conditions. Furthermore, OME/diesel blends show advantages regarding tail emissions. For these reasons, OMEs have the potential to use the existing infrastructure and diesel engines

without extensive changes [41]. However, an optimized and efficient production of OMEs still presents a major challenge. The use of DME as an intermediate presents a promising strategy for the production of OMEs, as DME is the source of two methyl groups as well as a formaldehyde-source through oxidation, dehydration, and oxo-dehydrogenation of DME. The combination of integrated formaldehyde synthesis and OME synthesis – referred to as oxidative OME synthesis from DME – presents the opportunity of a one-step OME process, referred to as oxidative OME synthesis from DME. However, this synthesis route is still under early developments [42–47] and the formation of the industrially relevant higher OME chains was not yet successful [48]. In contrast, the non-oxidative OME synthesis from DME requires an external formaldehyde source. While the synthesis based on DME and monomeric formaldehyde has not been realised yet, the reaction with trioxane as formaldehyde source has been patented [49] and published in literature [50,51].

1.2.5 Other uses

DME demonstrated good performance as a green solvent in liquid extraction for a variety of compounds [52]. Due to its high vapour pressure, it can easily be removed from the final product by depressurization. Furthermore, DMEs partial miscibility in water allows the use for the extraction of highly moist products [53].

Additionally, DME was studied as a solvent for enhanced oil recovery and Shell developed a chemical EOR technique called DME-enhanced waterflood. In this process DME is injected into an oil reservoir, leading to swelling and viscosity reduction and consequently an increased yield of crude oil [54].

When released to the atmosphere, DME shows a low global warming potential of 0.3 CO_2-equivalents and an ozone depletion potential of zero. Therefore, DME is discussed as a green refrigerant. To overcome the drawback of DME's flammability, mixtures of DME and other refrigerants can be used [55,56]. On top of that, DME can be used as pesticide, polishing agent and anti-rust agent [18].

1.3 Dimethyl ether production technology

Until 1975 DME was a by-product of the high-pressure methanol synthesis. However, the introduction of the highly selective low pressure methanol synthesis necessitated the development of a dedicated DME synthesis route [31]. This route is referred to as indirect route, in which DME is synthesized from methanol via dehydration and under corresponding water formation. A more recent alternative synthesis route is the so-called direct route which

allows a direct synthesis of DME from synthesis gas. In the following, both production routes are described in detail. In the first instance, the synthesis technology is presented in general. In a second step, the specific conditions, opportunities, and limitations of a CO_2-based production are discussed. Furthermore, alternative production technologies are presented. Finally, the concept of reactive distillation – the focus of this thesis – is presented in detail.

1.3.1 Indirect route

The indirect route represents the conventional process with all existing commercial-scale DME plants being based on that route. The technology is offered by several licensors such as Haldor Topsøe, Toyo Engineering Corporation, Lurgi, Mitsubishi Gas Chemical and ThyssenKrupp Industrial Solutions AG [57]. In this approach, DME is synthesized in two steps. In the first step, methanol is synthesized and subsequently purified via distillation. The second step is the actual DME synthesis by dehydration of methanol according to the exothermic reaction below [48]:

$$2\,CH_3OH \rightleftharpoons CH_3OCH_3 + H_2O \qquad \Delta H^0_{298\,K} = -23.5\ \mathrm{kJ\ mol^{-1}} \qquad (2)$$

The reaction is catalysed by acidic groups, typically using solid weakly acidic catalysts such as γ-Al_2O_3 [6,58]. Due to the exothermic and equimolar reaction, pressure has no significant influence on equilibrium conversion, but low temperatures are favourable for high methanol conversion. All commercial plants are based on a gas phase reaction. In practice, depending on the water content of the feed, reaction temperatures range between 220-360 °C [58,59] at pressures up to 20 bar [58,60–62]. The reaction is equilibrium limited and reaches methanol conversions up to 70-85% [59]. Consequently, the reactor outlet gas consists mainly of the reaction products DME and water but also considerable amounts of unreacted methanol. Although methanol dehydration is highly selective towards DME, the formation of by-products such as hydrocarbons as well as CO and H_2 has been reported [58,63–65].

Process description

The indirect route of DME production starting from crude methanol is depicted in Figure 1-1. For the use in DME synthesis pure methanol is required. The purification of crude methanol is conducted by a series of distillation columns. In a first forerun distillation column, low-boiling by-products such as CO, CO_2, CH_4 and hydrocarbons are removed. The water-methanol mixture is then charged to the methanol column, where water is removed as bottoms product. Purified methanol is discharged from the column head, preheated, and subsequently fed to the DME-synthesis reactor. The DME product mixture is then purified in a first step by removing

water in a mixture column. The methanol and DME containing distillate is charged to the DME column and separated into a methanol stream (bottom) and a DME stream (distillate) representing purified DME product. The methanol stream is recycled to the top of the methanol column. Incondensable gases in the DME stream are fed into a scrubber to recover residual DME.

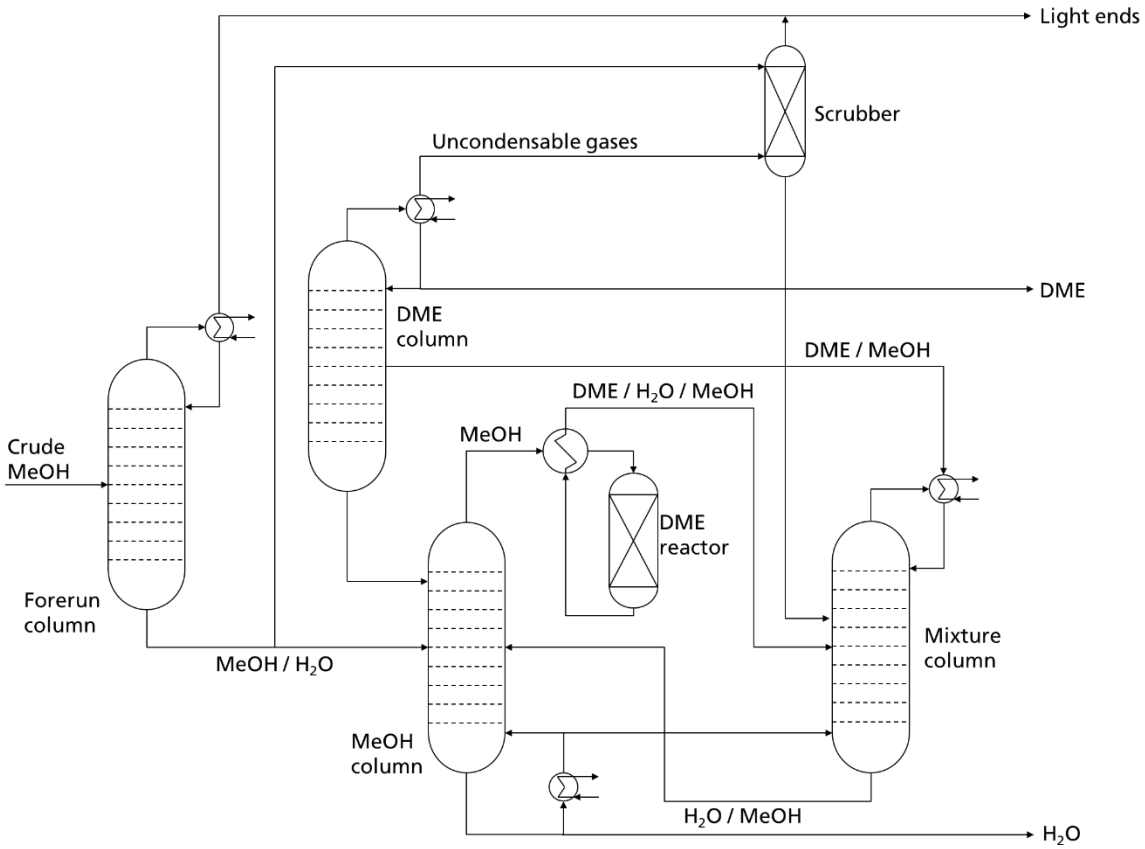

Figure 1-1: Indirect route of DME production based on crude methanol feedstock, according to the Lurgi MegaDME® process [60].

Catalysts

A large amount of research was conducted regarding the catalysis of methanol dehydration reaction. As the reaction is catalysed with an acidic function, a high concentration of acid sites is generally favourable in terms of catalyst activity. However, there is a consensus that the formation of hydrocarbons as an undesired by-product can be attributed to the abundance of acid sites with high acidic strength [64,66–70]. Thus, a high amount of acid sites of low and medium acid strength is desired in order to maintain high activity while concurrently suppressing the formation of by-products.

Researchers agree that the surface reaction is the rate-controlling step. However, two positions exist regarding the mechanism, namely the associative pathway and the dissociative pathway. The associative pathway assumes co-adsorption of two methanol molecules which react on the catalyst surface directly. In contrast, the dissociative pathway involves adsorption of one methanol molecule followed by water elimination and subsequent reaction with another methanol molecule. There is a disagreement considering the appropriate description of the reaction kinetics, with a variety of different kinetic models published. Both Eley-Rideal (ER) [71,72] and Langmuir-Hinshelwood (LH) [73,74] kinetics have been reported.

As already mentioned, γ-Al_2O_3 is the most investigated solid acid catalyst for methanol dehydration. However, a wide range of catalysts including zeolites, heteropoly acids, ion exchange resins, Nafion, and acid activated carbon have been tested and developed specifically for this reaction (see Table 1-2). A detailed overview of catalysis in methanol dehydration is given in the review of Bateni et al. [75].

Table 1-2: Overview of most commonly researched catalysts for methanol dehydration

Catalyst	**Source**
γ-Al_2O_3	[63,67,76–79]
Zeolites	[66,67,69,70,74,77,80–90]
Nafion	[79,91–93]
Heteropoly acids	[94,95]
Ion exchange resins	[71–73]
Acid activated carbon	[96–98]

Advantages of alumina are its low cost, high selectivity up to 400 °C, good performance, catalyst life-time and mechanical and thermal stability [63,76,99]. However, the activity of alumina is strongly affected by the presence of water, which adsorbs on the Lewis acid active sites [75,88]. Zeolites possess both Brønsted and Lewis acid sites. This results in methanol adsorption being preferred over water, thus significantly increasing the stability in the presence of water. A major drawback of zeolites is a reduced selectivity, resulting from the formation of hydrocarbons as a by-product, especially at higher temperatures. Furthermore, deactivation by coking can be critical and needs to be addressed in the selection of the reaction conditions. Lowering the silica/alumina ratio increases the acid strength of the zeolite und leads to a higher activity but also a reduced selectivity [75].

CO_2-based production

As DME synthesis in the indirect route is based on methanol as feedstock, the DME synthesis step itself remains unchanged when using CO_2 instead of CO in methanol production. However, regarding the process steps prior to the DME Reactor in Figure 1-1, a CO_2-based production positively influences the raw methanol purification step. For conventional methanol synthesis based on CO-comprising feedstock such as syngas from steam reforming, impurities with higher vapour pressure are present in the raw methanol. Thus, the purification of the yielded raw methanol is based on the two-step distillation process discussed above. The CO_2-based methanol production in contrast shows a higher selectivity and a strongly reduced amount of impurities [100,101]. Thus, the yielded raw methanol can be purified without a dedicated light ends column. Overall, purification can be simplified to a single heavy ends column including a stripper at the column head to vent dissolved CO_2 [100].

1.3.2 Direct route

The direct route of DME production presents a more recent development and has been studied thoroughly in literature. Although it has not been implemented in commercial scale, several companies offer the technology including Toyo Engineering Corporation, Mitsubishi Gas Chemical Ltd. and Air Liquide S.A. [48]. The direct route is based on the combined synthesis of methanol and the subsequent dehydration to DME in a single reactor. Thus, in this so-called Syngas-to-DME process, DME is synthesized from syngas in a single step. It is important note however, that this single step consists of two separate reactions namely the methanol synthesis and the methanol dehydration. Both reactions occur on their dedicated catalyst sites and the catalyst bed consists of either a physical mixture of methanol catalyst and dehydration catalyst or a bifunctional catalysts, including active centres for both reactions [6].

Methanol synthesis can either be based on CO or CO_2, although recent research suggests that methanol synthesis is mainly due to CO_2 hydrogenation whereas the hydrogenation of CO scarcely occurs [102].

$$CO + 2\,H_2 \rightleftharpoons CH_3OH \qquad \Delta H^0_{298\,K} = -90.4\ kJ\ mol^{-1} \qquad (3)$$

$$CO_2 + 3\,H_2 \rightleftharpoons CH_3OH + H_2O \qquad \Delta H^0_{298\,K} = -49.4\ kJ\ mol^{-1} \qquad (4)$$

The DME synthesis step is represented by the methanol dehydration reaction equation as already depicted in equation (2). The reactions for methanol and DME synthesis are furthermore complemented by the water gas shift (WGS):

$$CO + H_2O \rightleftharpoons H_2 + CO_2 \qquad \Delta H^0_{298\,K} = -41.0\ kJ\ mol^{-1} \qquad (5)$$

Thus, taking into account methanol synthesis, methanol dehydration and WGS, the DME synthesis from syngas can be represented by the overall reaction:

$$3\,CO + 3\,H_2 \rightleftharpoons CH_3OCH_3 + CO_2 \qquad \Delta H^0_{298\,K} = -245.3\ kJ\ mol^{-1} \qquad (6)$$

Besides the integration of two separate reactors in one, this concept has two fundamental advantages due to the synergy of the involved reactions as illustrated in Figure 1-2. Firstly, formed methanol is converted in-situ to DME which enhances the reaction conversion by overcoming the equilibrium limitation of methanol synthesis [103]. Secondly, the water produced in the methanol dehydration step is removed from the reaction equilibrium by the WGS when CO-rich syngas is used [104]. Overall, syngas conversion and volumetric reactor productivity can be increased this way. Furthermore, compared to the indirect route, the required hydrogen supply is reduced which can also be traced back to the WGS, where hydrogen is formed from the reaction of water and CO [105].

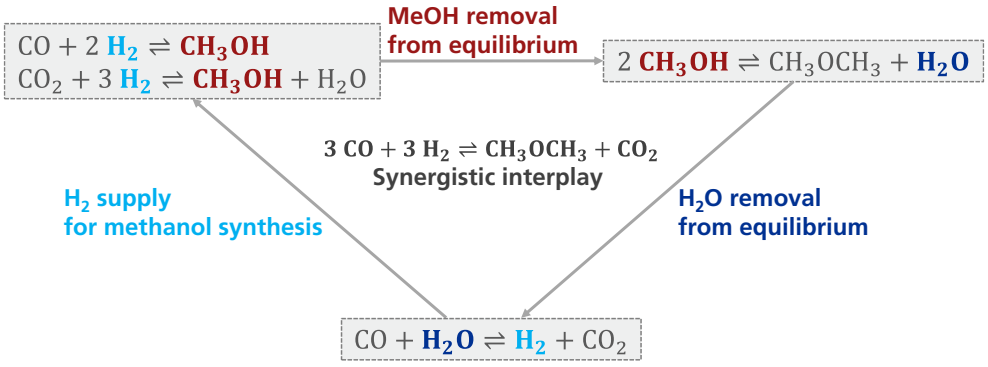

Figure 1-2: Illustration of the synergistic interplay of methanol synthesis, methanol dehydration and WGS.

A drawback of the direct route is the complex purification of the product mixture exiting the reactor. Whereas in the indirect route methanol, water and small amounts of hydrocarbons are the only by-products, the product mixture in the direct route additionally includes unreacted syngas and CO_2. Due to the lower vapour pressure of DME a separation of CO_2 and syngas from DME in a flash column is not possible. Additionally, the presence of methanol hampers the separation of CO_2 and DME. For this reason, in a suggested purification process by Peng et al. [106], methanol and water are condensed in a flash column and subsequently fed in a separate methanol dehydration reactor as depicted in Figure 1-3. The gas phase consisting

mainly of DME, syngas and CO_2 is then fed to an absorber. Here, DME and CO_2 are absorbed while syngas leaves the absorber and is subsequently recycled into the reactor. The absorbed DME and CO_2 are diluted in the absorbent and consequently need to be purified. In a flash column the absorbent is regenerated and recycled to the absorber. DME and CO_2 exit the flash column in the gas stream and are charged to a distillation column, where pure DME is finally obtained as bottom stream.

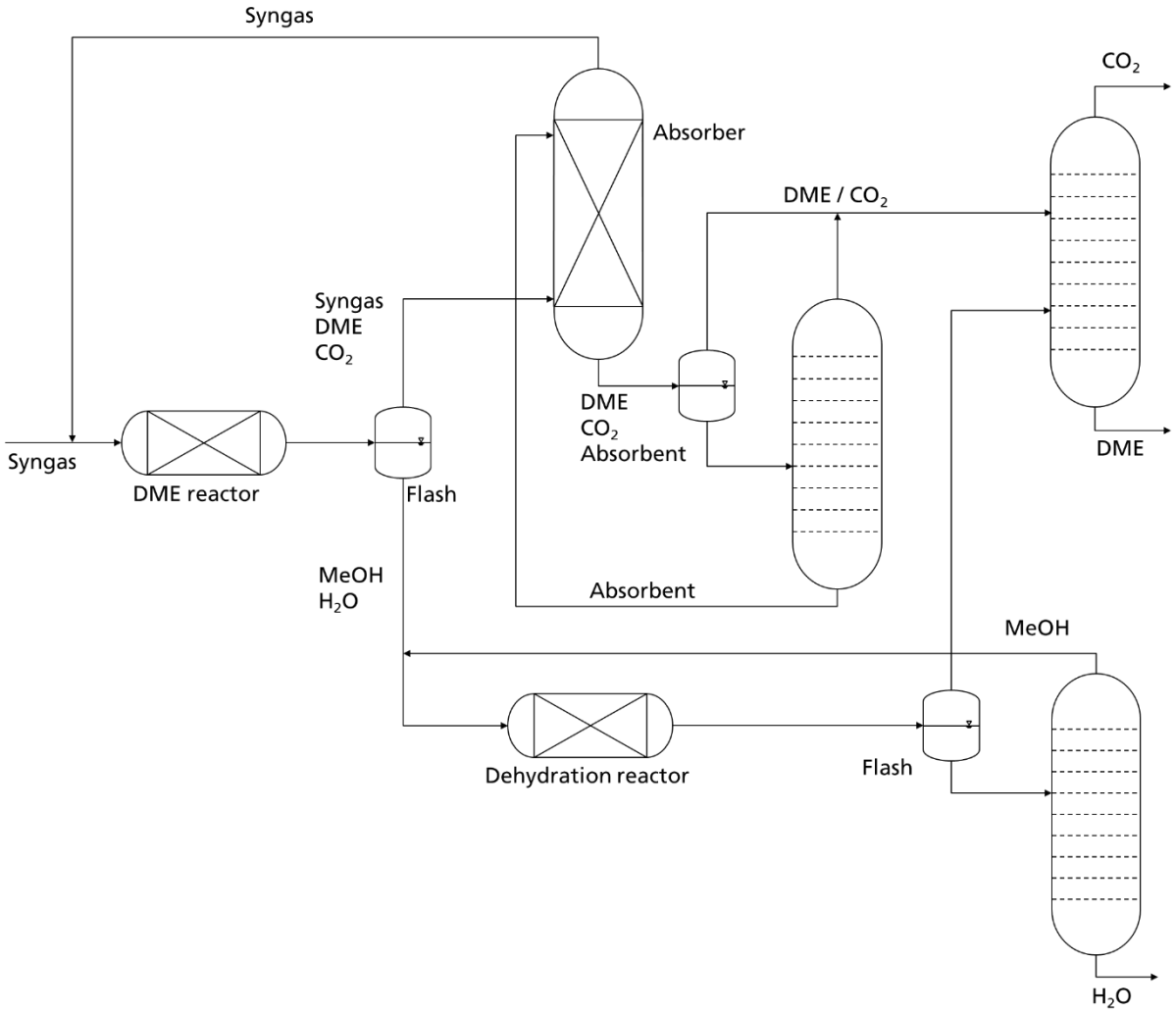

Figure 1-3: Process flowsheet for the direct route including syngas recycle and purification according to Patent US6458856B1 [106].

Due to the exothermic nature of methanol synthesis, methanol dehydration and WGS, the direct DME synthesis from syngas is highly exothermic. This leads to challenges in the reactor design to avoid hot spots, which promote deactivation of the methanol catalyst due to sintering [107]. Another disadvantage of the direct route is the generation of CO_2 when using CO as carbon source. Due to the water generation in the methanol dehydration, the WGS reaction

leads to the oxidation of CO to CO_2 according to equation (5). Thus, the direct route of DME production from syngas is a net CO_2 producing process.

CO_2-based production

As discussed above, the direct DME synthesis route is premised on the synergetic interplay of methanol synthesis, methanol dehydration and WGS. Thus, replacing CO with CO_2 as carbon source has a significant influence on the syngas-to-DME process. Regardless of the carbon source, the thermodynamic inhibition from methanol can be overcome due to the in-situ conversion to DME.

However, when using pure CO_2 and hydrogen as feedstock, the reverse WGS (rWGS) dominates compared to the WGS, thus producing water. The water from the rWGS adds to the water generated in the methanol synthesis and methanol dehydration, leading to a thermodynamic inhibition of all involved reactions, where water is a by-product (compare equation (2) and (4). The absence of CO in the feed gas eliminates the possibility of water removal from the chemical equilibrium through WGS. The synergistic interplay between the reactions as illustrated earlier is thus not present when using CO_2 rather than CO as carbon source. As a result, the equilibrium DME yield strongly decreases when gradually replacing CO with CO_2. Figure 1-4 illustrates the influence of CO_2 on equilibrium yield and water formation in the direct DME synthesis reaction. The carbon oxide ratio (COR) is a measure for the CO_2 content of the feed and is defined as follows [102]:

$$\mathrm{COR} = \frac{y_{\mathrm{CO_2}}}{y_{\mathrm{CO_2}} + y_{\mathrm{CO}}} \tag{7}$$

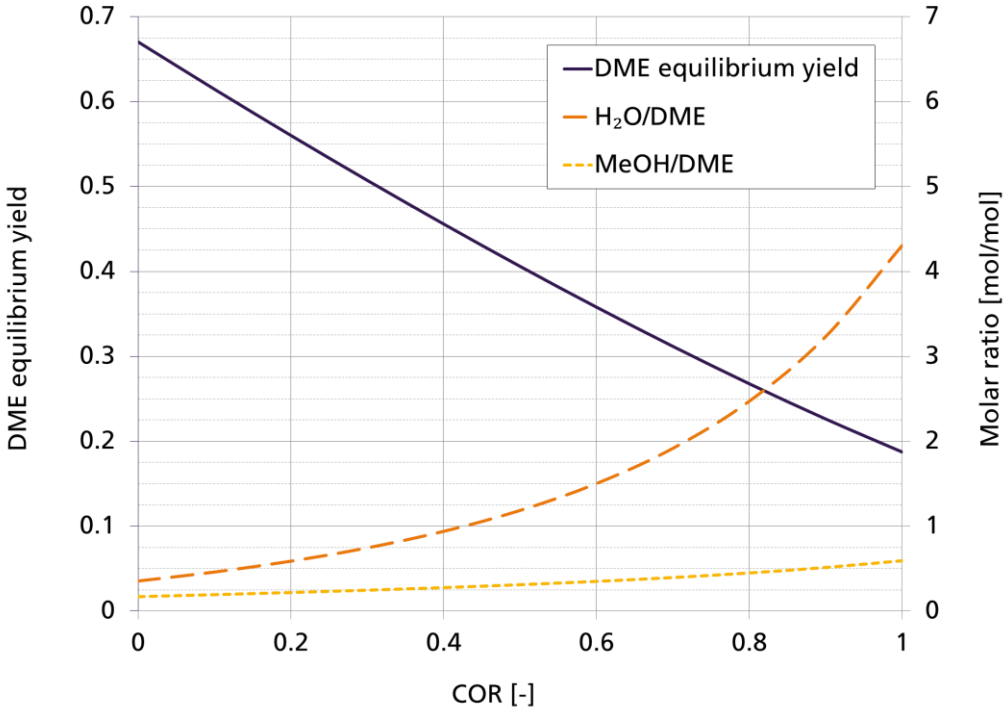

Figure 1-4: Influence of COR on the DME equilibrium yield and moles of water/methanol produced per mole of DME (T=275 °C, *p*=50 bar, H_2/CO_x=3). Equilibrium simulations performed in Aspen Plus.

Due to the exothermic nature of the involved reactions, lower reaction temperatures are beneficial for the equilibrium yield. However, the low reaction rate below 250 °C due to kinetic limitation should be noted [107]. Increasing the reaction pressure is beneficial for the DME yield, however high pressure promote catalyst deactivation by coking [108].

Besides thermodynamic limitations, the CO_2-induced water generation furthermore affects catalysis. Due to competitive adsorption, water molecules block not only the metallic sites of the methanol catalyst, but also the acid sites of the methanol dehydration catalyst [108,109]. Therefore catalysts with high acid strength like zeolite FER are preferred as dehydration catalysts [110]. This phenomenon further reduces the performance of the CO_2-based direct DME synthesis. There is a consensus that process intensification techniques for in-situ water removal are required to overcome the thermodynamic inhibition by water and increase DME yield [105,109,111].

In principle, a preceding rWGS reactor could be used in order to convert CO_2 to CO and thus to allow high yields in the direct route. However, the addition of a separate reversible reaction step in a process that already involves multiple steps and catalysts significantly would have a critical influence on the performance [111].

1.3.3 Alternative production technologies

In order to improve the conventional production pathways and to reduce costs, significant efforts have been made to develop alternative production pathways. A central focus has been put on the in-situ removal of water in DME-synthesis. In the indirect route, water removal has the potential to increase the methanol conversion to nearly full conversion. This in turn leads to a simplification of the downstream purification process. In the direct route, in-situ water removal is considered a necessity to commercialize a CO_2-based production, since this would displace the water gas shift equilibrium. The studied concepts hereby are reactive distillation, sorption-based water removal and membrane-based water removal, which are presented in the following sections.

Sorption based

The aforementioned thermodynamic limitation through water generation in the CO_2-based direct route has lead to research focusing on the in-situ removal of water. One solution may be the adsorption of water in the reactor. Iliuta et al. [112] proposed a fixed bed reactor that was packed with a homogeneous mixture of bifunctional catalyst for DME production and zeolite particles for water adsorption. The simulation results indicated that the CO_2-conversion is strongly increased in the sorption-enhanced reactor compared to a conventional fixed-bed reactor. This is due to the shift of the water gas shift equilibrium. Furthermore, the amount of unreacted methanol is decreased, as the thermodynamic limitation of the methanol dehydration reaction is reduced by the water removal. The enhancement of CO_2-conversion and DME selectivity increases with increasing CO_2-level in the feed.

It is important to note that the adsorption process results in dynamic operation of the reactor/adsorber, leading to the practical challenge of realizing an overall continuous production process. Hamidi et al. [113] established a simulation model of a fixed bed reactor for methanol dehydration with continuous adsorbent regeneration. Hereby zeolite adsorbent is continuously fed to the top of the reactor and withdrawn from the lower end. In a separate regenerator, the water is removed from the adsorbent and fresh adsorbent can be recycled into the reactor. An alternative approach is the cyclic regeneration of the adsorbent as soon as the capacity limit is reached [112]. The adsorbent regeneration is typically conducted by pressure swing, temperature swing, concentration swing and combinations thereof. Since the regeneration process consists of several steps and usually takes longer than the reaction step, van Kampen et al. [114] simulated a sorption-enhanced DME synthesis process based on three reactors. Each reactor is operated independently and in periodic order. This way, a continuous process can be established based on three discontinuously operated reactors. One

reactor is in the reaction step, while the other two reactors are in the regeneration phase consisting of a blowdown step for pressure reduction, purging, heating and repressurization. A reaction time of 112.5 min and a total regeneration time of 225 min were assumed for the simulation.

The sorption-enhanced DME synthesis was demonstrated experimentally and proofed to allow a DME yield of more than 80%, even when utilising pure CO_2 as carbon source [115]. The major drawback however is the cyclic discontinuous operation of the reactors and the high technical effort required to achieve a continuous synthesis. Furthermore, the purge gas used in the purge step is still present in the reactor at the beginning of the reaction step. When using an external purge gas, this adds an additional component to the process, thus complicating the purification process. Using syngas for purging in contrast would unfavourably impact the material balance of the process. Another issue that needs to be addressed is the blowdown gas, emerging in the pressure reduction step. This gas consists mainly of syngas and water at low pressure. Thus, a separate drying and repressurization step would be required in order not to send this stream to waste.

Membrane based

An alternative principle for the in-situ removal of water is the membrane separation. This approach is based on a semipermeable membrane, selectively allowing water to be transported out of the reactor while retaining all other components. To increase the trans-membrane driving force, the membrane is swept at low pressure.

Iliuta et al. [116] examined the effect of in-situ water removal in a membrane reactor on the direct DME synthesis theoretically in a simulation model. It was confirmed, that DME yield and selectivity increase with an increasing membrane permeance. This effect was more distinct for higher COR. The authors pointed out that the implementation of such membrane reactors requires membranes with good thermal and mechanical stability, high membrane permeances and permselectivity towards water [116].

Lee et al. [117] prepared alumina-silica composite membranes and tested the membranes in a reactor for DME synthesis from methanol. The membranes proved to be stable at 250 °C and successfully enhanced the conversion of methanol.

Diban et al. [118] studied the influence of membrane properties on the reactor performance in the direct DME synthesis from CO_2-containing syngas. Real properties of zeolite membranes found in literature were used in order to provide realistic simulation results. It was found that the use of zeolite membranes indeed enhances CO_2 conversion due to the in-situ removal of

water from the equilibrium. However, DME yields are reduced in the membrane reactor compared to a conventional packed bed reactor. This was attributed to the low water permselectivity of the studied zeolite membranes leading to a considerable mass transfer of methanol from the reactor side to the sweep gas side. Although this in-situ methanol removal enhanced methanol yields, the removal of methanol prevented the further dehydration to DME, thus reducing the DME yield. The highest CO_2 conversions were achieved for a membrane with high water permselectivity and low permeance [118].

Ateka et al. [109] simulated direct DME synthesis in a membrane reactor and reported a 25% increase in DME yield for the hydrogenation of CO_2 compared to a conventional packed bed reactor. Different sweeping modes and agents were furthermore examined. Nonetheless, it was concluded that the influence is minor. Despite the promising results, the authors pointed out that obtaining membranes that are stable at the conditions of direct DME synthesis presents a tremendous challenge.

Membrane reactors are an interesting emerging pathway in order to realize the direct DME synthesis in the prospect of a CO_2 based production as was demonstrated in the mentioned simulation studies. However, for a practical implementation the high demands on the membranes need to be fulfilled. Direct DME synthesis presents a challenging environment for the implementation of membranes due to high temperatures and pressures and the presence of water inducing the requirement of hydrothermal stability. Zeolite membranes seem to be the most adequate material for these demands. Yet the reproducible fabrication presents the limiting challenge for a successful commercialization [119].

1.3.4 Reactive distillation

Reactive distillation is often seen as the front-runner in process intensification and is based on the synergistic combination of reaction and separation in a single unit operation [120,121]. As the product of the reaction is continuously removed from the reaction equilibrium, a full conversion of otherwise equilibrium-limited reactions can be achieved. In addition to the simultaneous removal and purification of the product, this averts the requirement of a separate reagent recovery and reagent recycle step.

Figure 1-5 shows the process design for DME production based on methanol, when using reactive distillation compared to the conventional indirect route with reactor-separator-recycle sequence. As can be seen, the application of reactive distillation (RD) can replace one reactor and two distillation columns. Apart from simplifying the process, the concept has the potential

of reducing the heat demand compared to the conventional process due to numerous aspects [122]:

1. The reaction occurs in the liquid phase. Thus, no energy intensive evaporation of the MeOH feed is required.
2. The distillation column reboiler duty is reduced by integrating the exothermic MeOH dehydration heat into the column.
3. Since water is produced and separated in the RD column, water containing crude MeOH may directly be used as feedstock, thus neglecting the crude MeOH distillation step necessary in the conventional indirect production route.

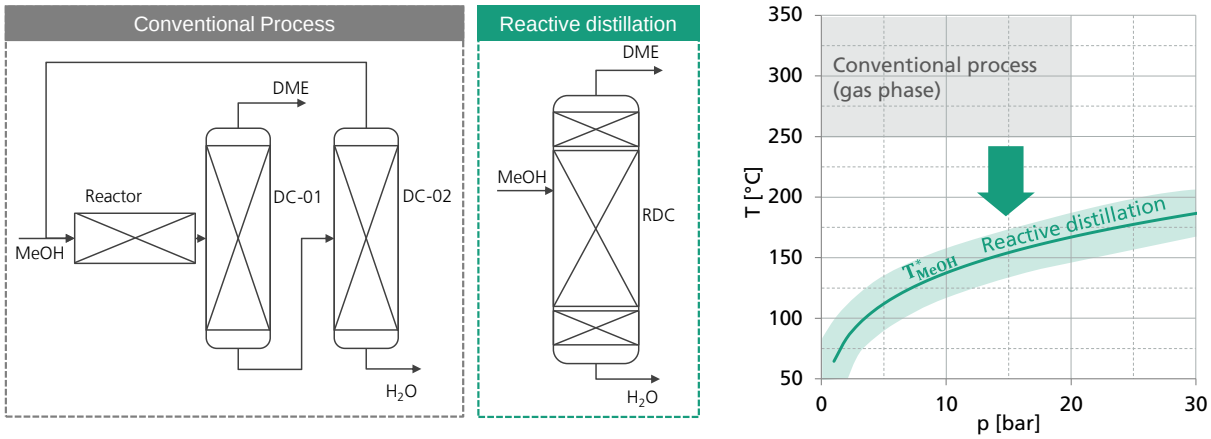

Figure 1-5: Simplified process flow diagram of the conventional indirect process and the reactive distillation process (left). Operating window of both processes (right).

In the ternary system DME-MeOH-H_2O, DME is the light boiler and H_2O is the heavy boiler. According to the boiling temperatures of the components, DME is removed from the top of the column as distillate and H_2O is the bottoms product. The reaction educt MeOH is the middle boiler and thus held in the reactive section in the middle of the column. Accordingly, in the top of the column, DME needs to be separated from MeOH and in the bottom section of the column, H_2O is separated from MeOH. Considering the relative volatilities, the thermal fractionation of the H_2O-MeOH system presents the more challenging separation task compared to the DME-MeOH system. Since MeOH enriches in the reactive section in the middle of the column the temperature in the reactive section is in proximity to the MeOH boiling point at the respective column pressure. This system-immanent phase equilibrium implies a coupling of the reaction temperature with the column pressure. Consequently, the high

temperatures of the conventional synthesis could only be achieved at excessive pressures. In turn, at moderate column pressures, significantly lower reaction temperatures are demanded compared to the conventional gas phase reaction as illustrated in Figure 1-5. At these conditions, conventional catalysts such as γ-Al_2O_3 show very limited activity and consequently, alternative catalysts such as ion exchange resins need to be used for the successful application of RD.

1.4 Research gap and problem definition

Despite the advantages of reactive distillation and the first operating commercial reactive distillation plant with a production capacity of ca. 10 kt_{DME} a^{-1} [123], research regarding the reaction kinetics of MeOH dehydration in the liquid phase is still limited to the use of the ion exchange resin (IER) Amberlyst® 35 with the reported kinetic models varying significantly among different scientific publications. Table 1-3 summarizes the current public literature on the reaction kinetics of DME synthesis in liquid phase.

Table 1-3: Experimental parameter ranges and kinetic models of liquid phase MeOH dehydration to DME found in literature [71–73].

	An et al. [71]	**Lei et al. [72]**	**Hosseininejad et al. [73]**
Catalyst	Amberlyst 35	Unspecified IER	Amberlyst 35
Reactor type	Batch	Fixed-bed	Batch
Phase	Liquid-vapor	Liquid	Liquid-vapor
Temperature [°C]	70 – 130	118 – 150	110 – 135
$y_{H2O,\ Feed}$ [mol mol^{-1}]	0 – 0.13	0 – 0.2	0 – 0.13
Pressure [bar]	8.2	20	9
Kinetic model	ER	ER + Power law	LH

Besides the limited temperature range examined, the water content in the feed is limited to a molar fraction of 0.13 and 0.2, respectively. This, however, is insufficient for the description of reaction kinetics in the reactive distillation process, where water molar fractions up to $y_{H2O} = 0.4$ are present in the reactive section of the column [124]. Additionally, most of the kinetic investigations in literature were carried out in batch reactors at vapor-liquid equilibrium, thus distorting the kinetic measurements due to the partial evaporation of the highly volatile DME from the liquid reaction phase.

For a profound evaluation of the RD process, a kinetic model covering the entire temperature and composition range is needed. Furthermore, the potential of alternative catalysts besides Amberlyst® 35 should be explored.

On the process level, a few publications exist on the simulation-based investigations of the DME reactive distillation concept. Thereby, the authors used the RADFRAC model of Aspen Plus [71,124–127]. Along with stationary simulations, dynamic process intensification has also been investigated [126,128]. Besides process simulations, the concept of DME RD has also been demonstrated experimentally. Di Stanislao et al. [129] conducted experiments at an operating pressure of 8 bar in a DN 50 pressure distillation column using KATAPAK catalytic packing equipped with Amberlyst 35. However, only a MeOH conversion of 71 % and a DME purity of 90 mol.-% could be achieved. Su et al. [130] also used Amberlyst 35 in a pressure distillation column operated at 6.4 bar. However, the authors were not able to achieve a full conversion of the MeOH feed and the DME product purity did not exceeded. 58 wt.-%.

Within all these investigations of the DME RD process, the full conversion of MeOH to produce pure DME in a single unit operation – the main objective of applying RD – has never been demonstrated experimentally. In the simulation studies, different kinetic models were applied for process simulation and the reported energy demands of the processes vary significantly among each other. Furthermore, none of the kinetic models available in literature was validated in a RD column.

Besides the examination of a single RD column achieving a full MeOH conversion in a single unit operation, process concepts extending the RD column by additional unit operations such as a gas-phase fixed bed reactor or an additional distillation column were evaluated [72,124,131]. A simulation of a reactive dividing wall column was performed by Kiss et al. [131] and Gor et al. [125].

Beyond these concepts, numerous promising process alternatives are conceivable, such as the combination of a RD column with a liquid phase pre-reactor or side-reactor, or the conventional reaction-separation-recycle sequence with a liquid phase reactor instead of the conventional gas-phase reactor. All those concepts should be evaluated and compared to fully understand and exploit the potential of the liquid phase MeOH dehydration.

1.5 Objective and outline of the thesis

The central objective of this dissertation is the scientific investigation and development of an integrated process concept for the energy-efficient production of DME from CO_2 and H_2. The focus lies on the process intensification of the MeOH dehydration step by applying the concept of reactive distillation. In the scope of the thesis, the potential of reactive distillation will be systematically explored by following the entire chain of process development from catalyst

screening to techno-economic evaluation of potential process concepts. The objective of the thesis is divided into three sections:

1. Catalyst screening and kinetic model development

The first objective is the exploration of potential catalysts for the liquid phase MeOH dehydration in the operating range of reactive distillation processes, which is characterized by significantly lower reaction temperatures. Building on a catalyst screening, extended kinetic experiments of promising catalysts shall be conducted with the target of developing a formal kinetic model. The investigations shall address the following research questions:

- Which catalysts are stable and active in the liquid phase MeOH dehydration at temperatures suitable for reactive distillation, i.e. <200 °C?
- Are conventional kinetic approaches sufficient for describing the reaction rate over the whole operating range present in reactive distillation processes?

2. Process characterization and experimental validation

The second objective is the characterization and of the reactive distillation process under industrially relevant conditions employing the catalyst identified in the catalyst screening. Furthermore, the developed formal kinetic model and thermodynamic model shall be validated experimentally under process conditions. Specific research questions to be answered are the following:

- Is the process capable of completely converting a crude MeOH feed to pure DME and water?
- Is the developed formal kinetic model obtained from liquid phase measurements valid under the process conditions in the vapor-liquid equilibrium?
- Which process parameters define an appropriate and efficient process operation?

3. Process optimization and techno-economic assessment

The last objective is the design and comparison of extended process concepts based on the liquid phase DME synthesis. Each process shall be optimally designed with respect to minimizing the net production cost and compared with the conventional. The following research questions shall be answered:

- How expensive is the DME production from MeOH based on a reactive distillation process?
- Can the process be optimized by complementing the reactive distillation with additional unit operations?

The outline of the PhD thesis and the used experimental and simulative methods are summarized in Figure 1-6. Experiments were conducted on three levels, with batch screening experiments (chapter 2.1.1), kinetic measurements (chapter 2.1.1) and reactive distillation experiments (chapter 3.2) being performed in three different test stands. Simulations were performed on two levels: the reactor level simulated by a self-developed Matlab® reactor model (chapter 2.1.2 to 2.1.4) and the process level, implemented in the Aspen Plus flowsheet simulator (chapter 3.3).

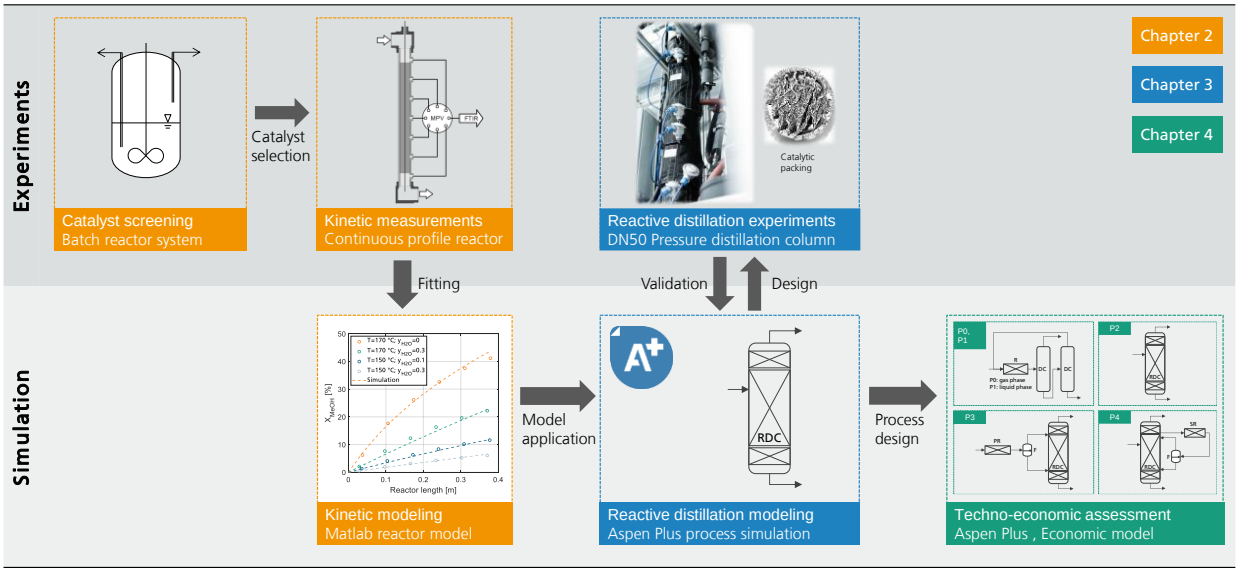

Figure 1-6: Outline of the PhD thesis and used experimental and simulative methods divided by three chapters.

2 Catalyst screening and reaction kinetics of liquid phase DME synthesis under reactive distillation conditions

Declaration of contributions:

Malte Gierse conceptualized the work, designed, and constructed the test stands, performed the experiments, processed and organized the data, developed and validated the kinetic model and reactor model, developed the kinetic fitting methodology, analysed the results, and wrote the manuscript.

Leon Steiner supported in constructing the batch test stand and conducting the batch experiments, supported in the development of the reactor model, and contributed to the discussion.

Max Bontrup supported in conducting the profile reactor experiments, supported in the execution of the kinetic fitting, and contributed to the discussion.

Jörg Sauer supervised the work, contributed to the discussion, and reviewed the manuscript.

Ouda Salem conceptualized and supervised the work, contributed to the discussion, and reviewed the manuscript.

Chapter redrafted after the following main publication:

Semmel, M.; Steiner, L.; Bontrup, M.; Sauer, J.; Salem, O. (2022): Catalyst screening and reaction kinetics of liquid phase DME synthesis under reactive distillation conditions. In *Chem. Eng. J.*, p. 140525. DOI: 10.1016/j.cej.2022.140525.

Abstract

While conventional DME synthesis is exclusively operated in a gas phase heterogenous reaction system, reactive distillation unveils the potential for a process intensified, compact and efficient DME production. In a catalyst screening, various solid acid catalysts were examined in the liquid phase dehydration of methanol to DME. Ion exchange resins proofed to be more active than zeolites and more stable than perfluorsulfonic acids. Reaction kinetics on the two most promising commercial ion exchange resins, the oversulfonated resin Amberlyst® 36 and the chlorinated resin Treverlyst CAT400 were studied in a profile reactor setup over the full range of water fractions relevant for DME reactive distillation processes. CAT400 was found to show a lower activity than Amberlyst® 36 at identical temperatures. However, due to the higher thermal stability, significantly higher conversions could be achieved. In the kinetic fitting, it was found that the conventional ER and LH mechanisms are not capable to describe the experimental data over the wide range of water fractions due to the highly non-linear inhibition by water resulting from the distinct swelling properties of ion exchange resins. To account for this behaviour, a new kind of kinetic model with dedicated water inhibition term is introduced and discussed. This model allows the precise description of reaction kinetics over the whole studied operating range for both investigated catalysts and reflects the temperature-dependent inhibition by water. The new kinetic model is an essential building block for the design of industrial scale DME reactive distillation processes.

2.1 Material and Methods

In this chapter the experimental methods including the chemicals as well as catalysts used in this study are presented. As two different test stands were utilized for catalyst screening and kinetic measurements, they are described in separate sections. Finally, the simulation model as well as the parameter fitting methodology for the kinetic approaches will be introduced.

Chemicals

The chemicals used as feedstock and for the gas chromatograph (GC) calibration were synthesis grade MeOH (99.9 vol.-%, Chemsolute®), dimethyl ether 3.0 (99.9%, Linde plc) and deionized water obtained from the in-house system. Nitrogen of grade 5.0 was used for dilution purposes.

Ion exchange resins

Two types of cationic IER were used: Macroporous oversulfonated IER and macroporous chlorinated IER with significantly higher temperature stability, but lower acid capacity (see Table 2-1). Amberlyst® 36 (A36) was obtained from Merck KGaA, Treverlyst IER were supplied by CHEMRA GmbH and the Purolite IER were supplied by Purolite GmbH. Each IER was dried in a vacuum oven (50 mbar, 100 °C, 24 h) and weighed in dry state as distinct reference. After drying, the resin was submerged in MeOH for at least 2 h to achieve the fully swollen state.

Table 2-1: IER used in this study with their corresponding technical data.

IER	Acid capacity q [meq g^{-1}]	Max. temperature [°C]	Resin type
Amberlyst 36	5.4	150	Oversulfonated
Treverlyst CAT 360	5.4	150	Oversulfonated
Treverlyst CAT400	2.7	190	Sulfonated and chlorinated
Purolite CT 275	5.2	130	Oversulfonated
Purolite CT 169	4.7	130	Oversulfonated
Purolite CT 482	2.7	190	Sulfonated and chlorinated

Zeolites

The four zeolites used within this study exhibit different Si/Al-ratios and frameworks and were supplied by Clariant AG. Zeolites provided in powder form were pelletized first, to obtain a starting material comparable to the zeolites provided in extruded form. Finally, all zeolites were crushed and sieved to a particle size between 300 µm and 700 µm.

Table 2-2: Zeolites used in this study with their corresponding technical data.

Zeolite	Si/Al	Zeolite framework	Original form
H-CZB 30	30	BEA	Powder
H-CZB 150	150	BEA	Extruded
H-CZP 90	90	MFI	Extruded
H-CZM 40	40	MOR	Extruded

Perfluorsulfonic acids

Two variants of solid perfluorsulfonic acids, namely Nafion® NR 40 (DuPont de Nemours) and Aquivion PW79S (Solvay GmbH) were used. This catalyst class is characterized by a lower acid capacity but a higher acid strength and higher temperature stability compared to IER [132].

Table 2-3: Perfluorsulfonic acids used in this study with their corresponding technical data.

IER	Acid capacity q [meq g^{-1}]	Max. temperature [°C]	Chlorinated?
Nafion NR40	1.0	200	No
Aquivion PW79S	1.23 – 1.3	240	No

2.1.1 Experimental setup and procedure

Catalyst screening

The catalyst screening was conducted in a parallelized batch autoclave system manufactured by H.E.L. Group, consisting of 8 parallel stirred batch autoclaves with a reactor volume of 60 ml each. These autoclaves were filled with 35 ml of MeOH and 1 g of each respective catalyst. The reactors were pressurized with nitrogen to 30 bar to prevent the MeOH feed from evaporating. Mixing throughout the experiments was ensured by a mechanical stirrer with a variable rotational speed up to 1000 rpm. During the heating period kept below 10 min for all experiments as well as the screening experiments, the stirrer was operated at a constant speed of 500 rpm. It was validated that the stirrer speed has no influence on the conversion pursuing a mass transfer limitation test at different stirring speeds. Each autoclave could be heated individually by a thermal oil basin and an electric copper heating jacket. Reaction temperature was monitored and controlled by a thermocouple placed in direct contact with the reaction mixture. All catalysts were screened at a temperature of 150 °C, those with higher temperature stability were also tested at 170 °C. After a reaction time of 2 h the reaction was quenched, and a sample was withdrawn via an immersion pipe equipped with a sinter filter (10 µm pore

diameter) to prevent unintended catalyst withdrawal. Analysis of the sample composition was done with an Agilent 6890 GC equipped with HP-Plot Q column (30 m column length, 0.53 mm internal diameter, 40 µm film thickness) and a thermal conductivity detector. The oven temperature was 100 °C, the detector temperature was 220 °C. Due to the high vapor pressure of the liquid mixture, a liquid injection into the GC was not feasible, and the sample needed to be completely evaporated prior to analysis in the GC. For this purpose, samples were withdrawn in a pressurized sample apparatus and subsequently injected into an evaporation system consisting of a heated pressure vessel before being injected to the GC. Each sample was analysed three times to minimize measurement errors. Figure 2-1 shows a simplified illustration of the complete screening setup.

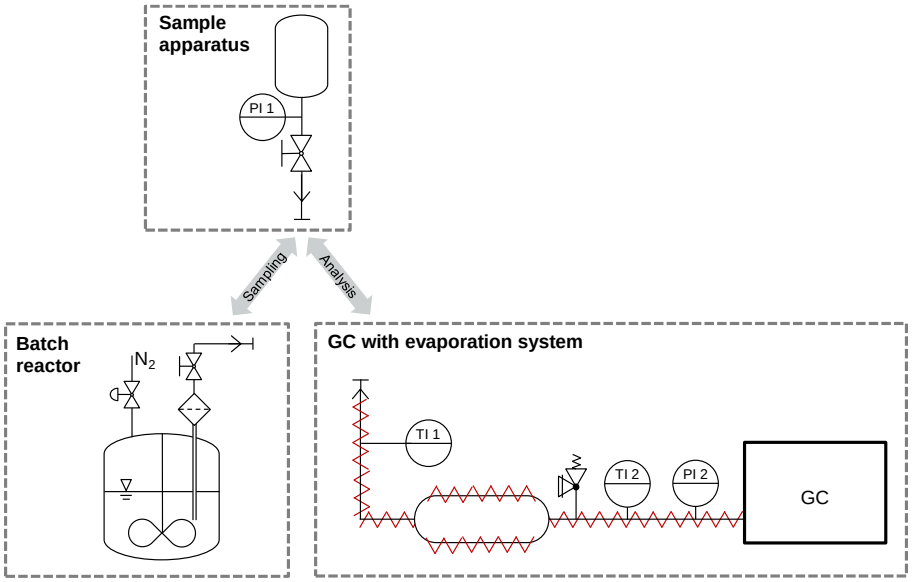

Figure 2-1: Process setup for the catalyst screening consisting of the batch reactor system, the sample apparatus and the evaporation system coupled with the GC.

Kinetic measurements

A schematic flow diagram of the used Kinetic Investigations and Screening Setup developed at Fraunhofer ISE [133] is illustrated in Figure 2-2. Mixtures of MeOH and H_2O were added in a feed tank with a volume of 2.5 l and dosed to the reactor by coupling an HPLC-pump and a Coriolis mass flow controller. The reaction was performed in a profile reactor consisting of a stainless-steel tube with a length of 450 mm and 8 mm internal diameter equipped with fibre optical temperature measurement system. The reactor was jacketed in a solid aluminium shell equipped with four heating cartridges to allow uniform heating and dissipation of exothermic

reaction heat. All experiments showed a nearly ideally isothermal temperature profile with less than 0.5 K deviation from the mean temperature throughout the reactor.

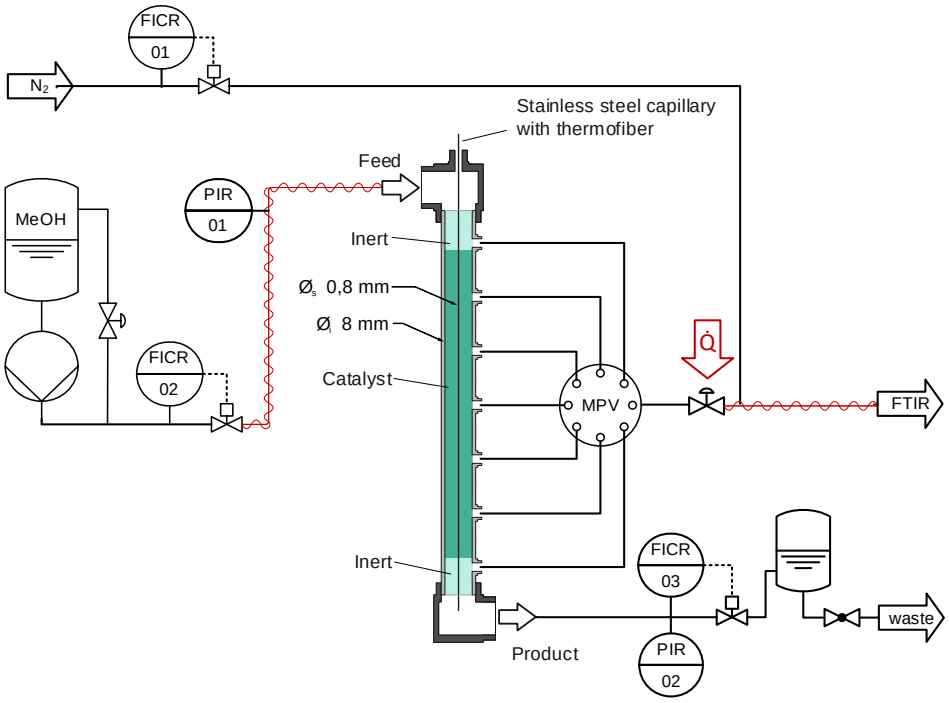

Figure 2-2: Process flow diagram of the kinetic test stand with liquid feed dosing, profile reactor and the corresponding FT-IR analytics.

The reactor was filled with a catalyst bed of commercial IER, held in place by two inert beds of SiO_2 (600 - 710 µm, Sigmund Lindner GmbH). To achieve a homogenous catalyst bed without cavities, the reactor was filled with the fully swollen resin while rinsing with MeOH. Centred inside the reactor tube is a stainless-steel capillary of 0.8 mm external diameter equipped with a glass fibre for fibre optic measurement of the axial temperature profile. Due to axial variation of the refractive index, waveguide geometry distortions or local defects light guided through this glass fibre is backscattered. Applying discrete Fourier transformation the resulting signal can be translated to a high-resolution temperature profile [134,135]. A spatial resolution of 2.6 mm and a temporal resolution of 5 s was selected for the measurement campaign in this study. The fibre optic measurement system was calibrated by heating the reactor isothermally to a reference temperature measured with a Pt-100 temperature sensor. The resulting calibration curve was then fitted with a third order polynomial (see supplementary material SI1.1).

For the measurement of the composition profile in the reactor, sampling ports are axially distributed with a spacing of 68 mm and connected to a multiposition valve (MPV), transferring

the selected stream to a back-pressure regulator heated by an electric heating band. Here, the liquid stream was completely evaporated and consequently forwarded to an MKS Multigas™ 2030 on-line (FT-IR) spectrometer with an optical path length of 35 cm for analysis. The reactants MeOH, DME, H_2O and potential side products such as CH_4 and Formaldehyde were calibrated. The calibration method was provided by ASG Analytik-Service AG. The reaction product was diluted with nitrogen to avoid condensation of the evaporated sample and to improve spectral quality by avoiding excessive absorption of the infrared beam. The reactor outlet mass flow was controlled by a second Coriolis mass flow controller, thus allowing a precise adjustment of the distribution between reactor outlet stream and sampling port stream.

The experimental conditions of the measured data points are summarized in Table 2-4 and were chosen to allow a precise modelling of the apparent kinetics of commercial sized IER particles over the relevant operating range. Each combination of the listed parameters was performed experimentally. A36 experiments were not performed at the combination of $y_{H2O,\,Feed} = 0.5$ at T_R=110 °C and T_R=120 °C as well as the combination of T_R=110 °C at $y_{H2O,\,Feed} = 0.3$, due to the negligibly low MeOH conversion at those conditions. The kinetic measurements for A36 were performed at a pressure of 40 bar, while for Treverlyst CAT400 (CAT400), the higher operating temperature necessitated a higher operating pressure of 70 bar to guarantee a liquid phase reaction without partial evaporation of the mixture. Pressure variation was verified to have no influence on the conversion of the reaction. Mole fractions of MeOH and H_2O in the feed were varied to examine the water-influence on reaction kinetics independent of the DME content. High water contents up to $y_{H2O} = 0.5$ were examined for two reasons:

1. In the composition profile of DME reactive distillation processes, water fractions up to $y_{H2O} = 0.4$ are present [124].
2. The crude MeOH in CO_2-based MeOH synthesis contains a water content up to $y_{H2O} = 0.5$ [102].

Due to the profile reactor concept, every reactor profile comprises 6 measurement points of different weight hourly space velocity (WHSV). The $WHSV_{Reactor}$ of the reactor was defined as the mass flow of the feed (including water) divided by the mass of catalyst in the reactor:

$$WHSV_{Reactor} = \frac{\dot{m}_{\mathrm{Feed}}}{m_{\mathrm{cat,Reactor}}} \tag{8}$$

To ensure the absence of external mass transfer limitations at all studied operation points, the reactor was operated at different sampling ports and different feed flows to achieve a constant $WHSV_{Reactor}$ under varying flow velocities.

At the maximum operating temperature and no water in the feed it was verified that the flow velocity had no influence on MeOH conversion and thus external mass transfer limitations are negligible in the investigated range (see supplementary material SI1.3). Furthermore, the influence of internal mass transfer was estimated using the Weisz-Prater parameter and it was found that internal mass transfer limitations can be neglected (see supplementary material SI1.3). Consequently, the measured kinetics is intrinsic. Since the reaction rate decreases with lower temperature and higher water content in the feed, it is guaranteed that reaction kinetics is the limiting step at all operating points considered. The filled catalyst bed height was 410 mm for both IER. Due to differences in bed density between the two IER, the total catalyst mass varied slightly. For the measurement of a concentration profile, the sampling ports were selected against the flow direction. Due to the on-line analytics, a steady state operation could be observed in the software of the FT-IR. Once steady state was achieved, the reactor was operated constantly for another minute in which FT-IR measurements were averaged. Considering the measurement frequency of 1 Hz, this corresponds to a 60-fold replicated measurement.

Table 2-4: Experimental operating parameters applied during the kinetic measurements

Variable	Unit	A36	CAT400
$WHSV_{Reactor}$	h^{-1}	16 - 270	16 - 220
Temperature	°C	110; 120; 130; 140; 150	140; 150; 160; 170; 180
Pressure	bar	40	70
$y_{H2O, Feed}$	mol mol^{-1}	0; 0.02; 0.1; 0.3; 0.5	0; 0.02; 0.1; 0.3; 0.5
Catalyst mass	g	7.38	7.48

Acid capacity determination

Determination of the IER's acid capacity was performed by titration. For this purpose, dried catalyst was put in an excess of a standard NaOH solution ($c_{NaOH,0}$=0.1 mol L^{-1}) overnight to neutralise all acid groups. Subsequently, the supernatant NaOH solution was titrated with sulfuric acid (c_{H2SO4}=0.1 mol L^{-1}) to determine the base concentration of the NaOH solution in equilibrium $c_{NaOH,eq}$. By comparing the base concentration with the original standard NaOH solution concentration, the acid capacity q_{IER} of the catalyst can be calculated according to equation (9):

$$q_{IER} = \frac{n_{H^+}}{m_{IER}} = \frac{V_{sample} \cdot \left(c_{NaOH,0} - c_{NaOH,eq} \right)}{m_{IER}} \quad (9)$$

2.1.2 Reactor modelling

The reactor model was based on a one-dimensional steady state reactor model assuming ideal plug flow behaviour. At the studied conditions, the dimensionless Bodenstein number at the experimental conditions applied in the kinetic study was calculated to be Bo=476 based on the dimensionless Péclet number, Schmidt number and Reynolds number as described in Kraume et al. [136]. Consequently the neglection of axial dispersion is justified [136]. The basis of the model is the material balance over the length of the reactor L, as described in equation (10).

$$\frac{d\dot{n}_i}{dL} = r_i \cdot \rho_{cat,bulk} \cdot \mathrm{A} \quad (10)$$

Due to the effective dissipation of exothermic heat, the profile reactor was nearly ideally isothermal. To account for the minor temperature changes along the reactor bed, the fibre optic measured temperature profile of each experimental run was implemented in the simulation model to simulate every increment of the reactor with the precise measured temperature. Consequently, no energy balance was required in the reactor simulation. An impulse balance was omitted since the pressure drop in all the experiments was measured below 100 mbar. The thermochemical properties and transport properties of the liquid mixture required for the reactor modelling and the calculation of the Bodenstein number, were calculated based on the correlations summarized in the supplementary material SI1.6.

2.1.3 Kinetic modelling

The examined kinetic models were derived from the Hougen-Watson approach. Hereby a distinction was made between the LH and the ER mechanism: While the LH mechanism assumes that two MeOH molecules adsorb on two adjacent active sites Z of the catalyst, the Eley-Rideal mechanism assumes the adsorption of only one MeOH molecule on an active site, which then reacts with another MeOH molecule from the bulk phase. After the surface reaction, the reaction products DME and water desorb into the liquid bulk phase.

	LH	ER
Adsorption:	$MeOH + Z \rightleftarrows MeOH^*Z$	$MeOH + Z \rightleftarrows MeOH^*Z$
Surface reaction:	$2\,MeOH^*Z \rightleftarrows DME^*Z + H_2O^*Z$	$MeOH + MeOH^*Z \rightleftarrows DME^*Z + H_2O^*Z$
Desorption:	$DME^*Z \rightleftarrows DME + Z$ $H_2O^*Z \rightleftarrows H_2O + Z$	$DME^*Z \rightleftarrows DME + Z$ $H_2O^* \rightleftarrows H_2O + Z$

Depending on the rate-determining step (RDS) being either the MeOH adsorption, the surface reaction, or the product desorption, three kinetic expressions can be derived for each mechanism, respectively. All the kinetic expressions can be described by the general mathematical Hougen-Watson expression, as described by equation (11) [137].

$$r_{DME} = \frac{\text{kinetic term} \cdot \text{driving force}}{(\text{adsorption term})^n} \tag{11}$$

IER exhibit a significant swelling behaviour, leading to a significant increase in volume when subjected to a polar medium. Since more polar components have a higher affinity towards the electronegative sulfonic groups in the resin, swelling is a highly selective process, leading to a preferred adsorption of the more polar components over the less polar components. [138–140] Due to the low polarity of DME compared to the strong polarity of MeOH and water, DME has a significantly lower affinity towards the electronegative sulfonic groups in the resin and consequently, the adsorption term of DME was neglected in the reaction network. Furthermore, the term $\frac{1}{K_{MeOH}}$ was neglected because it was supposed to be very small compared to the other components of the denominator and consequently the adsorption term in the kinetic expression can be simplified, as shown in the rate equations summarized in Table 2-5. A detailed exemplary derivation of the presented rate equations is shown in the supplementary material SI1.7.

Table 2-5: Basic rate equations for LH and ER mechanism depending on the RDS

RDS	LH		ER	
Adsorption of MeOH	$r_{\mathrm{DME}} = \frac{k\cdot\left(y_{\mathrm{MeOH}} - \left(\frac{y_{\mathrm{DME}}\cdot y_{\mathrm{H_2O}}}{K_{\mathrm{eq}}}\right)^{0.5}\right)}{\left(\frac{y_{\mathrm{DME}}\cdot y_{\mathrm{H_2O}}}{K_{\mathrm{eq}}}\right)^{0.5} + K_{\mathrm{ads}}\cdot y_{\mathrm{H_2O}}}$	(12)	$r_{\mathrm{DME}} = \frac{k\cdot\left(y_{\mathrm{MeOH}} - \frac{y_{\mathrm{DME}}\cdot y_{\mathrm{H_2O}}}{K_{\mathrm{eq}}\cdot y_{\mathrm{MeOH}}}\right)}{\left(\frac{y_{\mathrm{DME}}\cdot y_{\mathrm{H_2O}}}{K_{\mathrm{eq}}\cdot y_{\mathrm{MeOH}}}\right) + K_{\mathrm{ads}}\cdot y_{\mathrm{H_2O}}}$	(13)
Surface-reaction	$r_{\mathrm{DME}} = \frac{k\cdot\left(y_{\mathrm{MeOH}}^2 - \frac{y_{\mathrm{DME}}\cdot y_{\mathrm{H_2O}}}{K_{\mathrm{eq}}}\right)}{(y_{\mathrm{MeOH}} + K_{\mathrm{ads}}\cdot y_{\mathrm{H2O}})^2}$	(14)	$r_{\mathrm{DME}} = \frac{k\cdot\left(y_{\mathrm{MeOH}}^2 - \frac{y_{\mathrm{DME}}\cdot y_{\mathrm{H_2O}}}{K_{\mathrm{eq}}}\right)}{y_{\mathrm{MeOH}} + K_{\mathrm{ads}}\cdot y_{\mathrm{H2O}}}$	(15)
Desorption of H_2O	$r_{\mathrm{DME}} = \frac{k\cdot\left(K_{\mathrm{eq}}\frac{y_{\mathrm{MeOH}}^2}{y_{\mathrm{DME}}} - y_{H_2O}\right)}{K_{\mathrm{ads}}\cdot y_{\mathrm{MeOH}} + K_{eq}\frac{y_{\mathrm{MeOH}}^2}{y_{\mathrm{DME}}}}$	(16)	$r_{\mathrm{DME}} = \frac{\frac{k_{\mathrm{H_2O}}}{K_{\mathrm{H_2O}}}\left(K_{\mathrm{eq}}\frac{y_{\mathrm{MeOH}}^2}{y_{\mathrm{DME}}} - y_{\mathrm{H_2O}}\right)}{K_{\mathrm{ads}}\cdot y_{\mathrm{MeOH}} + K_{\mathrm{eq}}\frac{y_{\mathrm{MeOH}}^2}{y_{\mathrm{DME}}}}$	(17)

With

$$K_{eq} = \exp\left(1.743 + \frac{887.9}{T}\right) \tag{18}$$

Own correlation based on the Gibbs free energy of reaction according to Aspen Plus.

$$K_{Ads} = \frac{K_{H_2O}}{K_{MeOH}} = \exp\left(K_{Ads,1} - \frac{K_{Ads,2}}{T}\right) \tag{19}$$

$$k = k_0 \cdot \exp\left(\frac{-E_A}{R\,T}\right) \tag{20}$$

To account for the strong inhibitory effect of water, a dedicated inhibition term was introduced. This term incorporates the fact, that water has a very high affinity towards the active sites, thus blocking some of the acid sites which consequently cannot participate in the reaction. The fraction of acid sites blocked by water θ_{H2O} can be expressed either by the Langmuir or the Freundlich adsorption isotherm as shown in

Table 2-6 [141]. Consequently, the inhibition term is defined as $\eta_w = 1 - \theta_{H2O}$. By adding the water inhibition term, the kinetic rate equation was extended by the sorption coefficient K_W expressed by the two additional fitting parameters K_{W1} and K_{W2} and in case of the Freundlich-based approach by the Freundlich exponent α expressed by the additional fitting parameter K_α.

$$K_W = \exp\left(K_{W1} - \frac{K_{W2}}{T}\right) \tag{21}$$

$$\alpha = \frac{K_\alpha}{T} \tag{22}$$

Table 2-6: Fraction of acid sites blocked by water θ_{H2O} and resulting water inhibition term η_w according to Langmuir [141] and Freundlich isotherm [142].

Adsorption isotherm	$\boldsymbol{\theta_{H2O}}$		**Water inhibition term: $\mathbf{1-\theta_{H2O}}$**	
Langmuir, one water molecule blocks one active site	$\theta_{H2O} = \frac{K_W \cdot y_{H2O}}{1+K_W \cdot y_{H2O}}$	(23)	$\eta_w = \frac{1}{1+K_W \cdot y_{H2O}}$	(24)
Langmuir, one water molecule blocks two active sites	$\theta_{H2O} = \frac{K_W \cdot \sqrt{y_{H2O}}}{1+K_W \cdot \sqrt{y_{H2O}}}$	(25)	$\eta_w = \frac{1}{1+K_W \cdot \sqrt{y_{H2O}}}$	(26)
Freundlich	$\theta_{H2O} = K_W \cdot y_{H2O}^{\frac{1}{\alpha}}$	(27)	$\eta_w = 1 - K_W \cdot y_{H2O}^{\frac{1}{\alpha}}$	(28)

The resulting overall reaction rate expression is obtained by multiplying the conventional ER and LH rate expressions with the water inhibition term. Hereby the amount of acid sites involved in the reaction mechanism (ER: 1, LH: 2) needs to be considered and consequently the water inhibition term is squared for the LH-models [143]. The resulting rate expressions of the extended kinetic models are summarized in Table 2-7.

Table 2-7: Extended rate equations for LH and ER mechanism with added water inhibition term. RDS: surface reaction.

Water correction term	**LH**		**ER**	
Langmuir, one water molecule blocks one active site	$r_{\mathrm{DME}} = \frac{k \cdot \left(y_{\mathrm{MeOH}}^2 - \frac{y_{\mathrm{DME}} \cdot y_{\mathrm{H_2O}}}{K_{\mathrm{eq}}}\right)}{(y_{\mathrm{MeOH}} + K_{\mathrm{ads}} \cdot y_{\mathrm{H2O}})^2} \cdot \frac{1}{(1+K_{\mathrm{W}}\, y_{\mathrm{H2O}})^2}$	(29)	$r_{\mathrm{DME}} = \frac{k \cdot \left(y_{\mathrm{MeOH}}^2 - \frac{y_{\mathrm{DME}} \cdot y_{\mathrm{H_2O}}}{K_{\mathrm{eq}}}\right)}{y_{\mathrm{MeOH}} + K_{\mathrm{ads}} \cdot y_{\mathrm{H2O}}} \cdot \frac{1}{1+K_{\mathrm{W}}\, y_{\mathrm{H2O}}}$	(30)
Langmuir, one water molecule blocks two active sites	$r_{\mathrm{DME}} = \frac{k \cdot \left(y_{\mathrm{MeOH}}^2 - \frac{y_{\mathrm{DME}} \cdot y_{\mathrm{H_2O}}}{K_{\mathrm{eq}}}\right)}{(y_{\mathrm{MeOH}} + K_{\mathrm{ads}} \cdot y_{\mathrm{H2O}})^2} \cdot \frac{1}{\left(1+K_{\mathrm{W}} \sqrt{y_{\mathrm{H2O}}}\right)^2}$	(31)	$r_{\mathrm{DME}} = \frac{k \cdot \left(y_{\mathrm{MeOH}}^2 - \frac{y_{\mathrm{DME}} \cdot y_{\mathrm{H_2O}}}{K_{\mathrm{eq}}}\right)}{y_{\mathrm{MeOH}} + K_{\mathrm{ads}} \cdot y_{\mathrm{H2O}}} \cdot \frac{1}{1+K_{\mathrm{W}} \sqrt{y_{\mathrm{H2O}}}}$	(32)
Freundlich	$r_{\mathrm{DME}} = \frac{k \cdot \left(y_{\mathrm{MeOH}}^2 - \frac{y_{\mathrm{DME}} \cdot y_{\mathrm{H_2O}}}{K_{\mathrm{eq}}}\right)}{(y_{\mathrm{MeOH}} + K_{\mathrm{ads}} \cdot y_{\mathrm{H2O}})^2} \cdot (1 - K_{\mathrm{W}}\, y_{\mathrm{H2O}}^{\frac{1}{\alpha}})$	(33)	$r_{DME} = \frac{k \cdot \left(y_{\mathrm{MeOH}}^2 - \frac{y_{\mathrm{DME}} \cdot y_{\mathrm{H_2O}}}{K_{\mathrm{eq}}}\right)}{y_{\mathrm{MeOH}} + K_{\mathrm{ads}} \cdot y_{\mathrm{H2O}}} \cdot (1 - K_{\mathrm{W}}\, y_{\mathrm{H2O}}^{\frac{1}{\alpha}})$	(34)

In total, 12 different rate equations were derived, 6 basic ER and LH rate equations (Eq.(12)-(17)), and 6 extended ER and LH rate equations (Eq. (29)-(34)).

2.1.4 Kinetic fitting and validation

The reactor model (section 2.1.2) was implemented in MATLAB® (version R2020a) and used to simulate all measured data points. Besides feed mass flow and composition, the measured temperature profiles obtained during the experiments were considered in the reactor simulation. An overview of the methodology is illustrated in Figure 2-3.

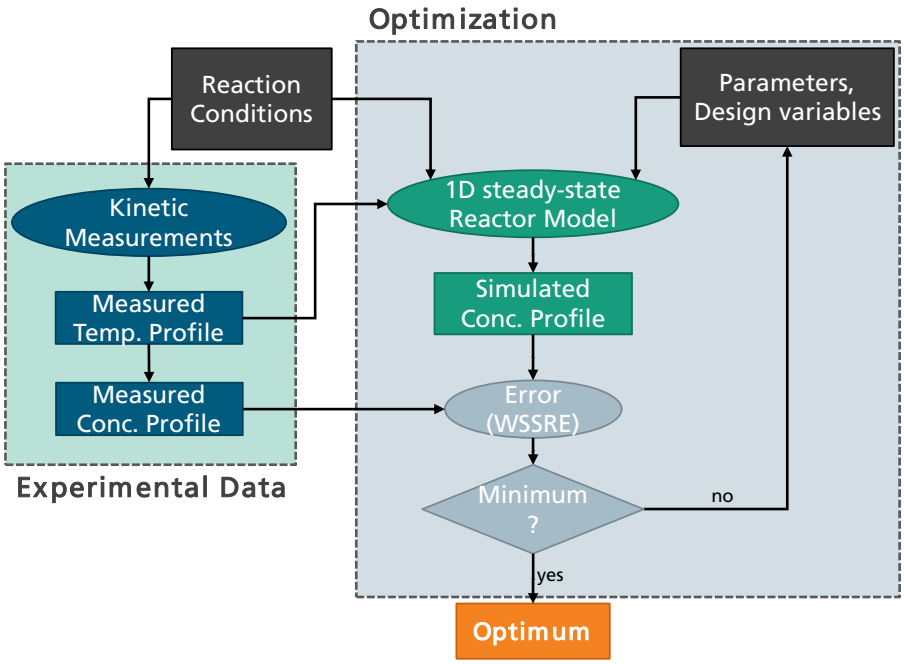

Figure 2-3: Kinetic fitting methodology applied in this study.

The deviation between simulated and experimental reaction conversion was minimized in an optimization by varying the fitting parameters of the respective kinetic model. The objective function for the fitting was defined as the weighted sum of squared relative errors (WSSRE) of MeOH conversion X. Due to the equimolar reaction equation, the MeOH conversion can be calculated based on the molar fractions.

$$WSSRE = \sum_{j=1}^{J} \left(\frac{X_{\mathrm{MeOH,Exp,i}} - X_{\mathrm{MeOH,Sim,i}}}{X_{\mathrm{MeOH,Exp,i}}} \cdot 100 \cdot w_{\mathrm{j}} \right)^2 \tag{35}$$

$$X_{\mathrm{MeOH}} = \frac{\dot{n}_{\mathrm{MeOH,0}} - \dot{n}_{\mathrm{MeOH}}}{\dot{n}_{\mathrm{MeOH,0}}} = \frac{y_{\mathrm{MeOH,0}} - y_{\mathrm{MeOH}}}{y_{\mathrm{MeOH,0}}} \tag{36}$$

$$w_{\mathrm{j}} = \frac{P_{\mathrm{j}}}{\bar{P}} \tag{37}$$

The relative error was preferred to the absolute error to avoid a disproportionate weighting of operating points with high conversion. Due to a large variation in feed compositions and reaction temperatures, the conversion in the experiments varied significantly. Using the absolute error of the MeOH conversion would consequently lead to an underweighting of operating points with low temperature and/or low MeOH feed concentration. To account for the higher precision of measurements with increasing bed height (see supplementary material SI1.2) a weighting factor w_j was additionally considered, defined as the sampling port number P_j divided by the mean sampling port number $\bar{P}$. Experimental data obtained in the examination of external mass transport limitations was not used for the kinetic fitting to avoid an overweight of experimental data with a feed of pure MeOH.

The minimization of the WSSRE was performed with a Nelder-Mead simplex algorithm [144] implemented by the *fminsearch* function in MATLAB®. To avoid local minima, the algorithm was started from 6 randomly distributed starting parameters and respectively called repeatedly until the result of two consecutive optimization runs was identical.

The function's residuals and Jacobian matrix at the optimization solution were calculated using the Matlab® function *lsqnonlin*. Confidence intervals were obtained based on the Jacobian matrix and residuals with the MATLAB® function *nlparci*.

2.2 Results and Discussion

2.2.1 Catalyst screening in batch reactor

Figure 2-4 illustrates the MeOH conversion for all catalysts tested in the screening experiments. Both perfluorsulfonic acids Nafion and Aquivion proved to be unstable and are thus not included in the diagram. No side-products were detected for any examined catalyst. Macroporous oversulfonated IER (green) exhibit the highest catalytic activity at 150 °C, with conversions between 30% and 40%. A36, CAT 360 and CT275 DR show a comparable conversion of more than 37%, while only 30.1% were obtained with CT169 DR. This trend can partly be related to the acid capacity of the IER, which is slightly lower for CT169 DR compared to the other oversulfonated resins (compare Table 2-1). The chlorinated IER (blue) generally show lower MeOH conversions at 150 °C than the oversulfonated resins with the exception of CT169 DR which shows a similar conversion. Due to the higher temperature stability of the chlorinated resins however, higher conversions than with the oversulfonated resins can be achieved when the reaction temperature is increased to 170 °C. This result emphasizes the

potential of high-temperature stable resins in the liquid phase MeOH dehydration and evokes the need for kinetic models of DME-synthesis using chlorinated IER to fully explore their potential.

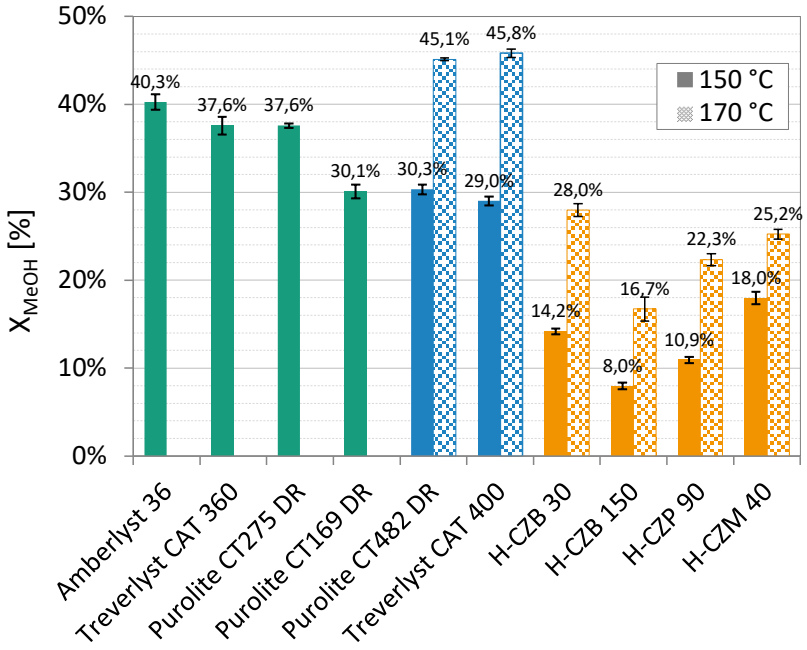

Figure 2-4: MeOH conversion to DME in batch autoclaves using various catalysts at 150 °C (solid bar) and 170 °C (checkered bar) respectively. Reaction parameters: 35 ml MeOH sample volume, 1 g catalyst, 30 bar initial reaction pressure, 2 h reaction time, 500 rpm stirrer speed. All tests were carried out using pure MeOH feed.

Regarding the performance of zeolites, a correlation between the Si/Al-ratio and the catalytic activity can be drawn at 170 °C. At 150 °C the correlation can be drawn with the exception of H-CZB 30, which shows a lower conversion than expected. Lower Si/Al-ratios increase the acidity of the zeolite and consequently its activity. In the gas-phase DME synthesis, an optimal Si/Al ratio needs to be found in order to find a compromise between activity and selectivity [62]. In contrast, the liquid phase DME synthesis at mild conditions allows lower Si/Al ratios without compromising selectivity. However, regarding the absolute activity at the studied conditions, all the tested zeolites were outperformed by oversulfonated resins and chlorinated resins. Even the most active zeolite was found less active at 170 ° than the least active IER at 150 °C. Since no absolute maximum is indicated for the operating temperature of zeolites, conversions exceeding 45 % might be possible at temperatures above 170 °C. However, higher temperatures would require increased operational pressures in a reactive distillation process. Furthermore, at such conditions, the deactivation by Si dissolution from the zeolite needs to be critically evaluated as shown by Sun et al. [145].

Both perfluorsulfonic acids investigated in this study proved to be unstable under the reaction conditions applied. While the exposure of Nafion NR40 to MeOH at room temperature led to a strong swelling, the catalyst was completely dissolved under the reaction conditions. Aquivion PW79S showed a strong structural change from its crystalline state to a highly swollen state in MeOH at room temperature and a gel-type state after the reaction. The evaporation of the reaction product led to significant residues, indicating a partial dissolution of the Aquivion. The different behaviour of both perfluorsulfonic acids can be explained by the shorter side chain of Aquivion compared to Nafion, leading to a stronger electrostatic attraction of the side chain and the polymer backbone. In summary, the perfluorsulfonic acids considered here were found inappropriate for the liquid phase DME synthesis and are thus not further considered.

2.2.2 Kinetic measurements in profile reactor

Overall, A36 as the most active oversulfonated resin and CAT400 as the most active chlorinated resin were determined as the most promising catalysts among all considered catalysts and were thus selected for detailed kinetic measurements. In the profile reactor measurements, a significant shrinkage of the catalyst bed after the filling process could be detected by investigation of the axial temperature profile along the reactor. Due to the vertical alignment of the reactor, this shrinkage led to a reduced catalyst mass in the reactor part upstream of the first sampling port. The exact extend of the bed shrinkage could be quantified by the temperature jump based on the exothermic heat released in the section of the catalyst bed but not in the inert bed. Further information regarding these findings is provided in the supplementary material SI1.2. At all examined reaction conditions, no side-products could be detected confirming the analysis in the batch campaign.

Figure 2-5 compares the MeOH conversion of both catalysts for all reaction temperatures and feed water fractions. For simplification, only the conversion at the last sampling port is shown, corresponding to $WHSV_{Reactor}$ = 16.2 h^{-1}.

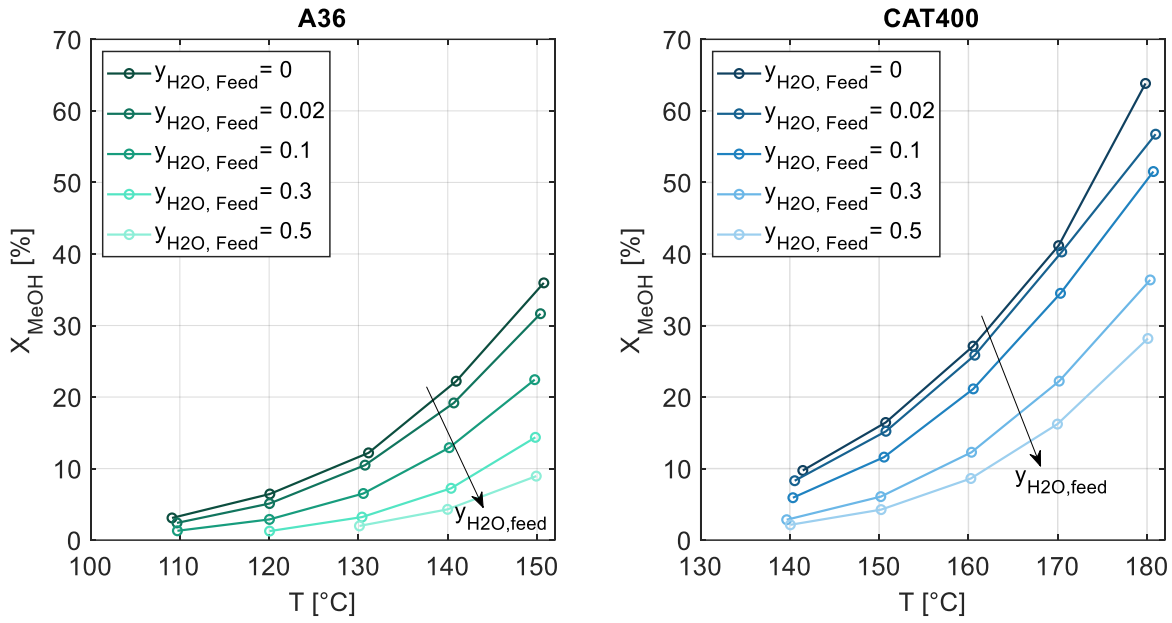

Figure 2-5: MeOH conversion over reaction temperature obtained with A36 and CAT400 for various water fractions in the feed. Display of the last sampling port at $WHSV_{Reactor}$ = 16.2 h^{-1} only.

Each curve shows a characteristic exponential behaviour as expected by the Arrhenius equation. Furthermore, the inhibiting effect of water is apparent when comparing the curves of different feed water fractions. Hereby it becomes obvious, that the water inhibition is nonlinear, with a feed water fraction of 10 % leading to a conversion reduction of 38 % for A36 (at 150 °C). When comparing both catalysts at the same operating temperature and water feed fraction, it can be noticed that the conversion of CAT400 is lower by a factor of approximately two. This lower activity can quantitatively be explained by the ratio of acid capacity q_{A36}/q_{CAT400} = 5.4/2.7 = 2. However, the lower activity of CAT400 is overcompensated by the higher maximum operating temperature. Only a temperature increase of 10-15 °C – depending on the feed water fraction – is required to achieve the same MeOH conversion. When comparing both catalysts at the maximum operating temperature, the MeOH conversion with CAT400 is higher by a factor of 3 and 1.8 at feed water fractions of 0.5 and 0, respectively. These measurements clearly show that despite their lower acid capacity, chlorinated IER show great potential for the liquid phase MeOH dehydration.

During the measurement campaign, explicit benchmark conditions were applied immediately after the filling of the catalyst and repeatedly afterwards at different times during the measurement campaign. This way, the conversion at a specific time could be related to the initial conversion with fresh catalyst to examine a potential decrease in catalyst activity during

the measurement campaign. Furthermore, the acid capacity of the fresh and used catalysts were determined experimentally. Hereby, a noticeable decrease in conversion and acid capacity was observed for both catalysts. Details regarding this can be found in the supplementary material SI1.4. However, due to the limited number of data points and the limited operating time, it remains unclear whether the activity loss is just an initial behaviour, or a continuous trend. Consequently, no definite statement can be made regarding the long-term stability of the catalysts examined in the kinetic study. Future work should focus on long-term experiments, examining the IER stability under various operating conditions.

2.2.3 Kinetic modelling

While all published literature on DME synthesis on IER assume a very fast educt adsorption and product desorption compared to the surface reaction, kinetic models with adsorption or desorption as RDS have not been examined yet. Figure 2-6 shows the WSSRE of both fitted basic ER and LH models with the RDS being either the adsorption of MeOH (Ads), the surface reaction (SR) or the desorption of water (Des) for both catalysts examined in the kinetic study. Every model was fitted based on all measured datapoints listed in the supplementary material SI1.8. The graph clearly indicates that for both ER and LH, the model with the surface reaction as RDS represents the best fit regardless of the used catalyst. This result indicates that adsorption and desorption are in fact faster than the surface reaction. For this reason, in the following sections only the two models ER_{SR} and LH_{SR} are investigated further.

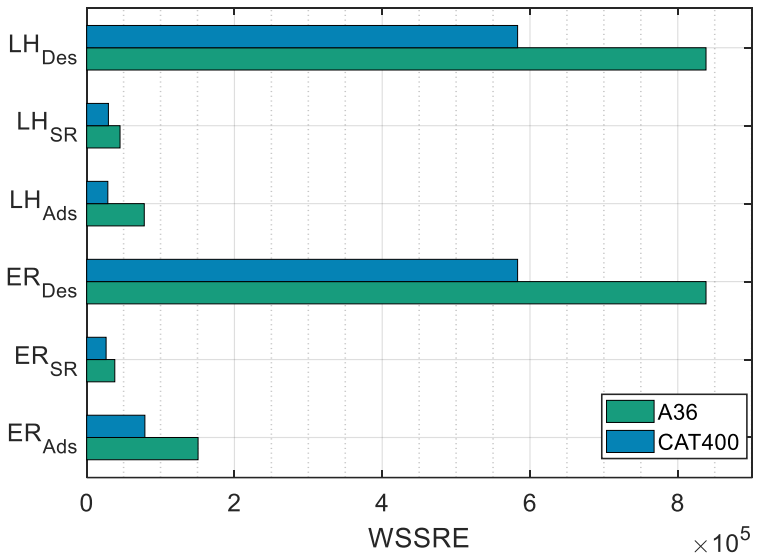

Figure 2-6: WSSRE of fitted basic ER and LH models with the RDS being either adsorption, surface reaction or desorption for both catalysts examined in the kinetic study.

To compare ER_{SR} and LH_{SR} model in more detail, Figure 2-7 shows the relative error of experimental data and simulation data depending on reaction temperature and water fraction of feed for A36 and CAT400. A positive relative error indicates a higher simulated than measured conversion.

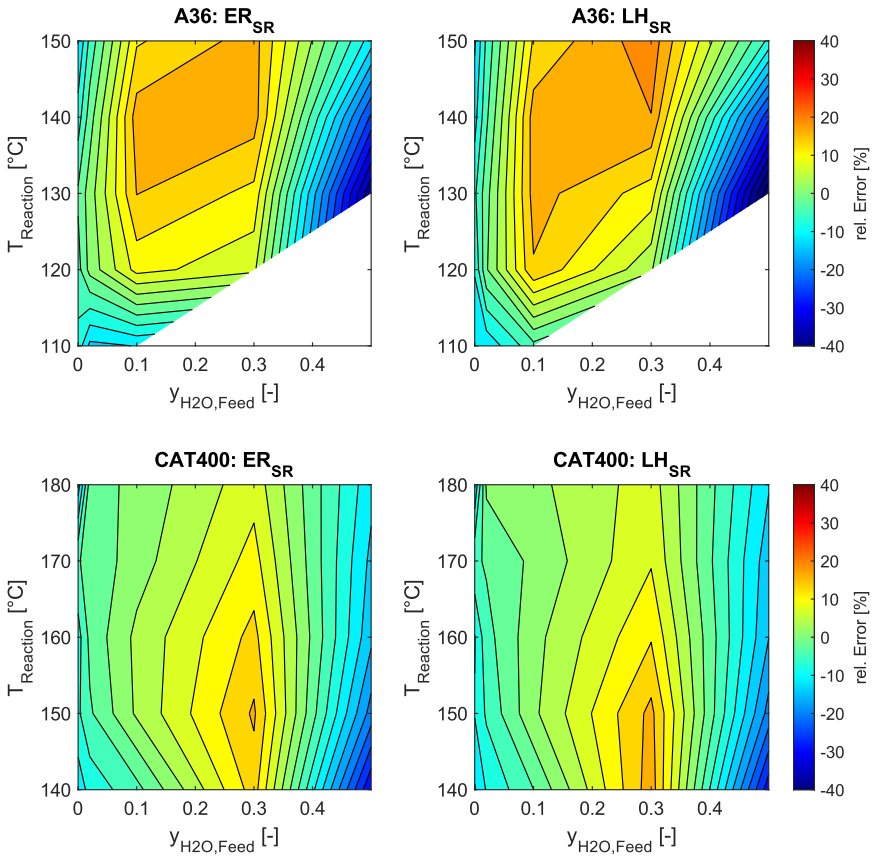

Figure 2-7: Relative error of experimental data and simulation data depending on reaction temperature and water fraction of feed. ER_{SR} and LH_{SR} model for A36 (top) and CAT400 (bottom).

The distribution of the relative error is comparable for both kinetic models, consequently both models are equally capable to describe the measured data. However, it becomes obvious that the error of both models depends significantly on the water fraction. While both models deliver a high precision at low water fractions, water fractions between 0.2-0.35 lead to a significant overestimation of the catalyst's activity. Furthermore, water fractions > 0.4 lead to a strong underestimation of the reaction rate. This model inaccuracy is more pronounced for A36 compared to CAT400. The severe influence of water can be attributed to the selective swelling of ion exchange resins, leading to a highly nonlinear relation between the composition in the bulk phase and the composition at the active sites. In the kinetic studies of Hosseininejad et al. [73], An et al. [71] and Lei et al. [72] kinetic measurements were performed only up to water

fractions of 0.2. Consequently, the ER or the LH model were found to be appropriately precise by these authors. Extension of the water fractions in the reactor feed considered in this work marks a deficit of both ER and LH to describe the non-linear inhibition effect caused by water. Consequently, a new type of kinetic model is required to allow for a precise kinetic modelling in the whole reactive section of a reactive distillation process, where water mole fractions up to 0.4 are present.

To account for the strong nonlinear inhibitory effect of water both ER_{SR} and LH_{SR} models were extended by the water inhibition term η_w, thereby introducing six new kinetic models, each of which exhibiting two (Langmuir based inhibition terms) or three (Freundlich-based inhibition term) additional fitting parameters, respectively. In principle, the water inhibition term could also be combined with the models with adsorption or desorption as RDS. However, due to the significantly larger error of these models as shown in Figure 2-6 and to prevent and exuberant amount of models, these combinations were not furtherly investigated. Figure 2-8 shows the resulting WSSRE of the fitted basic and extended models for both catalysts. It can clearly be seen that the extension of the models by a water inhibition term leads to a significant improvement for the LH and ER model in the case of both catalysts. Thereby, the LH model with inhibition term outperforms the ER model with inhibition term for both catalysts.

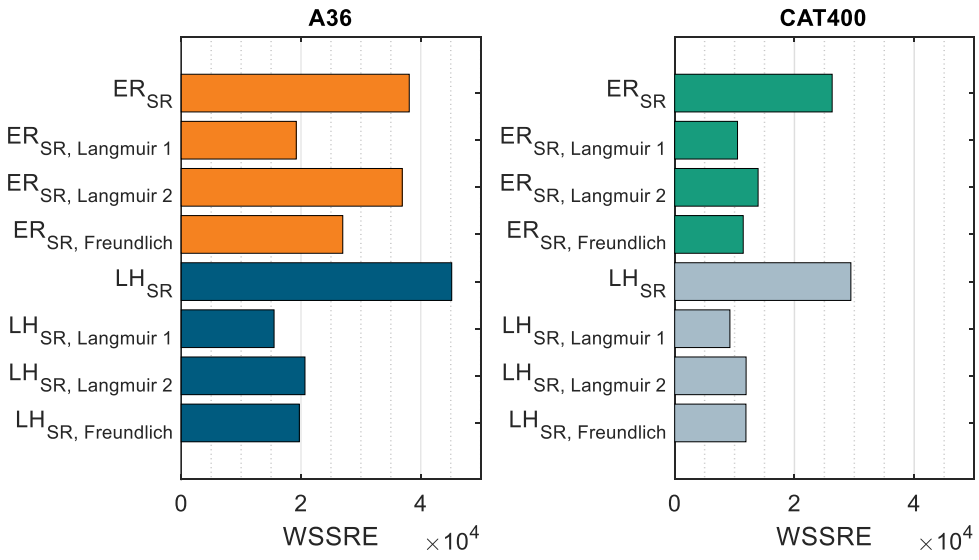

Figure 2-8: WSSRE of conventional LH_{SR} and ER_{SR} model and extended models with water inhibition term.

The $LH_{SR,\ Langmuir\ 1}$ model, representing one active site being blocked by one water molecule represents the best model performing better than all other extended models. Therefore, the $LH_{SR,\ Langmuir\ 1}$ model will be used throughout the following discussion. During the fitting

procedure of this model, it was found that the ratio of adsorption constants K_{ads} approached a value of zero. Consequently, K_{ads} can be omitted, leading to a simplified rate expression and a reduced number of fitting parameters without compromising the model quality. The corresponding kinetic parameters of the model including 95 % confidence intervals (CI) are shown in Table 2-8. The model parameters of all other models shown in Figure 2-8 are listed in the supplementary material SI1.5 of this publication. The apparent activation energies are comparable for A36 and CAT400 and were found to be similar to the values discussed in literature [73,146]. The confidence intervals of all four parameters are small, indicating a strong statistic significance of each parameter.

Table 2-8: Parameters for the proposed kinetic model $LH_{SR,\ Langmuir\ 1}$ for A36 and CAT400.

Parameter	Unit	Proposed kinetic parameter	95% CI±
A36			
k_0	mol kg_{Cat}^{-1} s^{-1}	8.089e9	2.284e6
E_A	kJ mol^{-1}	91.56	0.0200
K_{W1}	-	-4.2255	9.733e-4
K_{W2}	K	-2360.9	0.635
CAT400			
k_0	mol kg_{Cat}^{-1} s^{-1}	5.973e10	1.135e7
E_A	kJ mol^{-1}	101.98	0.0168
K_{W1}	-	0.4118	1.999e-4
K_{W2}	K	-345.2587	0.756

To compare the performance of the extended kinetic model $LH_{SR,\ Langmuir\ 1}$ with the basic model LH_{SR} ones in more detail, Figure 2-9 provides the relative error of the experimental and simulation data depending on reaction temperature and water fraction for both catalysts.

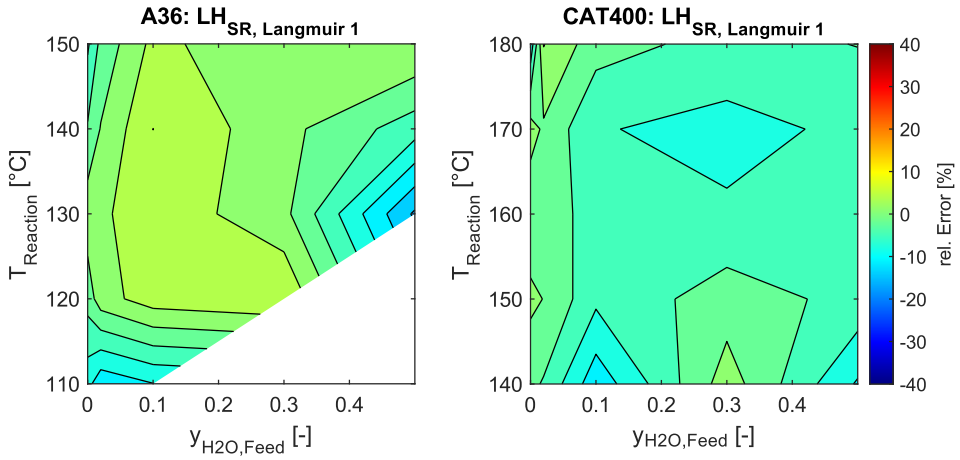

Figure 2-9: Relative error of experimental data and simulation data depending on reaction temperature and water fraction of feed. Results for the extended $LH_{SR,\ Langmuir\ 1}$ model with water inhibition factor for both catalysts.

The contour plots indicate a significant improvement of the model precision over the whole examined operating range. Especially in the region of high water fractions, a great improvement could be obtained with the extended model $LH_{SR,\ Langmuir\ 1}$. The maximum relative error obtained accounts to 15 % (LH_{SR}: 44 %) and 10 % (LH_{SR}: 28 %) for A36 and CAT400, respectively. The slightly higher relative errors for A36 could be attributed to the low absolute conversions at low temperatures, as even small absolute differences then lead to a high relative error.

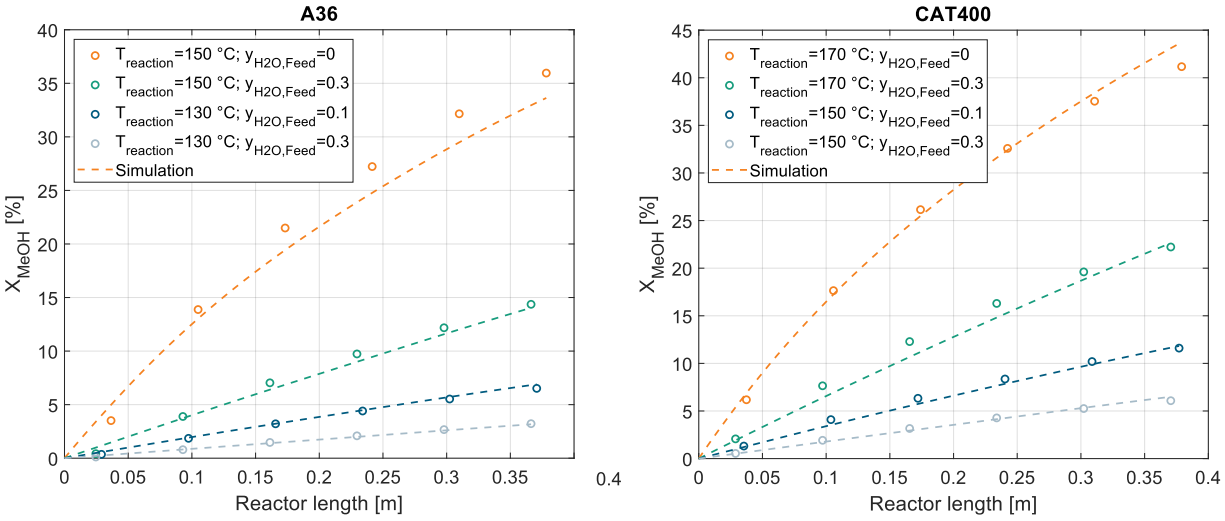

Figure 2-10: Measured conversion profiles for exemplary reaction temperatures and feed water fractions for both catalysts. Corresponding simulated conversion profile based on the $LH_{SR,\ Langmuir\ 1}$ model.

Figure 2-10 compares the measured and simulated conversion profiles for some exemplary operating points for both catalysts investigated in the kinetic study. As expected by the low relative error throughout the operating window, measured and simulated conversion profiles fit very well, regardless of reaction temperature, water fraction or overall conversion.

To illustrate the non-linear inhibition effect of water, Figure 2-11 shows the relative reaction rate $\frac{r_{DME}}{r_{DME}(y_{H2O}=0)}$ at various MeOH-H_2O mixtures calculated based on the extended kinetic model for A36 and CAT400, respectively. Since the initial reaction rate, thus without the presence of formed DME is shown in the graph, the rate equation can be simplified, and the relative reaction rate is equivalent to the water inhibition factor η_W.

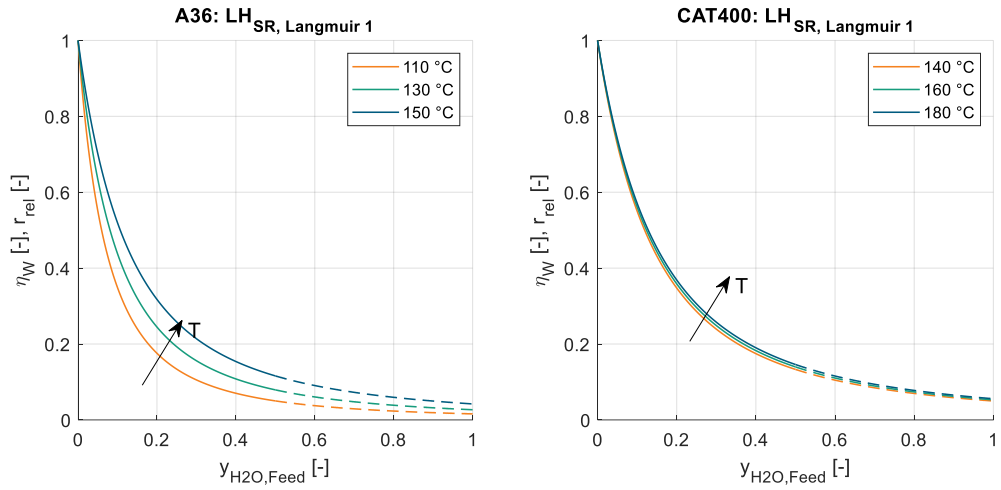

Figure 2-11: Inhibition effect of water η_W and relative reaction rate r_{rel} depending on water content and temperature. Relative reaction rate defined as reaction rate at specific water content compared to reaction rate at pure MeOH feed.

For both catalysts, the water inhibition factor decreases sharply at low water fractions and more moderately with increasing water fractions, meaning that small amounts of water inhibit the reaction disproportionately strong. This result is in accordance with the findings of other authors who studied the influence of water on IER catalysed reactions [143,147,148]. Furthermore, a significant temperature dependence of the water inhibition can be observed, with increasing temperature leading to a less pronounces water inhibition. Consequently, the high-temperature stable CAT400 shows a lower degree of water inhibition in the examined operation range. Regarding an industrial application, this indicates a major advantage in a reactive distillation column, where water is present throughout the reactive zone. Especially in a reactive distillation column using crude MeOH as feedstock this advantage is even more prominent as the average water fraction in the column is in this case even higher.

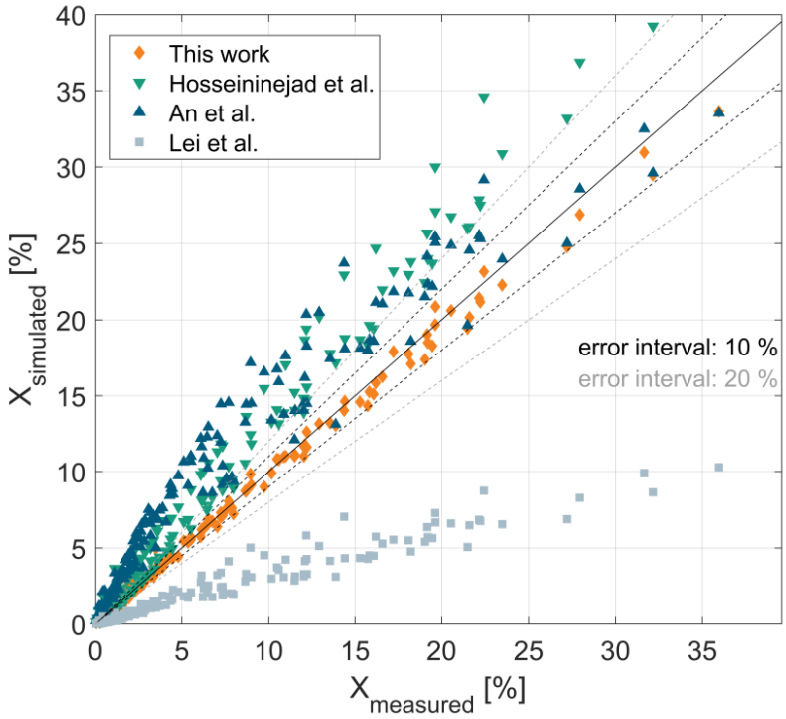

Figure 2-12: Parity plot for the MeOH conversion. Experiments were carried out at the profile reactor with A36. Simulations were carried out using kinetic models from literature as published and the $LH_{SR,\ Langmuir\ 1}$ model from this work.

Figure 2-12 compares the proposed extended kinetic model $LH_{SR,\ Langmuir\ 1}$ with the existing kinetic models from literature. The parity plot hereby compares the measured conversion from the kinetic study of this work using A36 with the simulated conversion using the respective kinetic model from literature. Hereby it has to be emphasized, that different catalysts are being compared. Amberlyst 35 was used in the work of Hosseininejad et al. [73] and An et al. [71] and an unspecified IER was used in Lei et al. [72]. However, due to the similarity in acid capacity of Amberlyst 35 and A36, the authors found a comparison between these different catalysts studies to be useful. The three models from literature show a strong deviation among each other and deviate considerably from the experimental data of this work. The model of Lei et al. reflects much lower conversions throughout the operating window. This result indicates that unspecified IER used in this study exhibited a significantly lower acid capacity than A36. The model proposed by An et al. shows significantly higher conversions at most datapoints, nevertheless, at high conversions, the model is in accordance with the measurements in this work. The best overall agreement from the literature models is achieved with the model of Hosseininejad, however, significant deviations still exist. It has to be mentioned that the kinetic models of An and Hosseininejad were developed based on experiments with Amberlyst 35 and is hereby compared to experimental data using A36. Yet, considering the small difference

in acid capacity between those two catalysts (5.2 and 5.4 meq g^{-1}) the large deviations are surprising. This underlines the significance of the water inhibition term for a kinetic model with wide operating range regarding the water content.

2.3 Conclusion and Outlook

DME is a promising energy carrier in the PtX context with various promising applications. Shifting the reaction from the gas to the liquid phase enables new process concepts in DME production such as reactive distillation with a decreased energy demand and reduced process equipment. However, under the moderate reaction temperatures in liquid phase, conventional catalysts show insufficient activity. Consequently, new catalysts are required to enable these intensified process concepts on an industrial scale. In a catalyst screening campaign, two classes of cationic IER, different types of zeolites and perfluorsulfonic acids were tested at 150 °C and – if possible, regarding the respective catalyst's thermal stability – at 170 °C. During these experiments, the oversulfonated IER A36 and the chlorinated IER CAT400 were identified as the most promising catalysts regarding MeOH conversion and mechanical stability.

Using a profile reactor acquiring both axial temperature and concentration profiles along the reactor, detailed kinetic measurements were conducted for these two catalysts at feed water molar fractions of 0 - 0.5 and reaction temperatures of 110-150 °C (A36) and 140-180 °C (CAT400), respectively. Hereby, a significant shrinkage of the catalyst bed due to the distinct swelling behaviour of IER could be quantified based on the exothermic heat visible in the fibre optical based high-resolution temperature profile. In the kinetic measurements, the reaction rate has proven to be highly sensitive to the reaction temperature and the water fraction. While at identical temperature CAT400 showed less activity than A36, the higher temperature stability of CAT400 allowed to overcompensate the lower acid capacity, resulting in significantly higher conversions than with A36. Both catalysts showed a reduction of activity over the course of the measurement campaign, indicating that for an industrial long-term application reduced operating temperatures might be required. However, further studies are required to examine the long-term stability under various operating conditions.

The kinetic fitting shows, that both the classical ER and LH type kinetic models were unable to describe the strongly non-linear influence of water on the reaction rate sufficiently. For this reason, three different water inhibition terms were introduced to account for the blockage of active sites by water molecules. The water inhibition term based on a Langmuir adsorption isotherm with the assumption that one water molecule blocks two active sites provided the best

fitting results. When coupled with the LH mechanism, the resulting kinetic model allowed for precise modelling of the reaction rate over the entire measured range for both catalysts investigated in the kinetic study. Furthermore, it was found that the water inhibition is significantly affected by temperature, leading to a lower water inhibition at higher reaction temperatures. For this reason, the chlorinated IER, which was operated at a higher temperature, showed a less pronounced water inhibition compared to the oversulfonated resin.

To the best of our knowledge, the proposed kinetic models offer the highest range of validity of all available kinetic models for the liquid phase MeOH dehydration. Both catalysts considered for the kinetic study in this work were found to be promising candidates for the application in the liquid phase DME synthesis. Due to their different temperature operating windows, the process design of a reactive distillation column is significantly influenced by the catalyst selection. The use of CAT400 enables higher reaction rates and consequently a more compact column design, however the investment cost for a higher column pressure and a heat supply at an increased temperature level should be considered and optimized. The two presented models allow for precise modelling of the reaction kinetics in the operating range of reactive distillation and consequently laying the foundation for a realistic design of DME reactive distillation processes and a profound scientific comparison of both catalysts at process level.

3 Demonstration and experimental model validation of the DME synthesis by reactive distillation in a pilot-scale pressure column

Declaration of contributions:

Malte Gierse conceptualized the work, selected the column internal layout, performed the experiments, processed, and organized the data, performed all process simulations, analysed the results, and wrote the manuscript.

Innokentij Bogatykh conceptualized the work, designed the sampling system of the column, performed the experiments, contributed to the discussion, and reviewed the manuscript.

Benedikt Steinbach supported in conducting the experiments, contributed to the discussion, and reviewed the manuscript.

Jörg Sauer supervised the work, contributed to the discussion, and reviewed the manuscript.

Jens-Uwe Repke reviewed the manuscript.

Ouda Salem conceptualized and supervised the work, contributed to the discussion, and reviewed the manuscript.

Chapter redrafted after the following main publication:

Semmel, M.; Bogatykh, I.; Steinbach, B.; Sauer, J.; Repke, J.; Salem, O. (2023): Demonstration and experimental model validation of the DME synthesis by reactive distillation in a pilot-scale pressure column. In *React. Chem. Eng.* (8), pp. 2309–2322. DOI: 10.1039/D3RE00200D.

Abstract

The dehydration of methanol to produce the hydrogen carrier and alternative fuel dimethyl ether (DME) is an equilibrium limited reaction, resulting in a relatively complex and expensive production process. A promising method for process intensification is reactive distillation (RD), as this allows the synthesis and purification of DME in a single unit operation. However, existing kinetic models for liquid phase DME synthesis have never been validated in an industrially relevant reactive distillation environment, preventing a detailed model-based design of industrial-scale applications.

In this work, a pilot-scale pressure distillation column was used to successfully demonstrate the feasibility of the process involving pure and crude MeOH feed using the catalyst A36. Based on the measured composition and temperature profiles, a kinetic model could successfully be validated for the RD system. A process simulation model was developed in Aspen Plus to analyse an industrial-scale process and validated on the pilot scale. Hereby the influences of column size, methanol feed purity and catalyst selection were examined in detail.

3.1 Physicochemical characteristics of the RD system

The chemical system studied in this publication is the DME synthesis by dehydration of MeOH according to the following equation:

$$2\,CH_3OH \rightleftharpoons CH_3OCH_3 + H_2O \qquad \Delta H_R^0 = -23.5\,kJ \cdot mol^{-1} \tag{38}$$

The reaction is conventionally conducted in a gas-phase reaction at 220-360 °C at a pressure of 1-20 bar and catalysed by γ-Al_2O_3. The reaction is exothermic and thermodynamically limited. In the industrial realization, conversions around 80% are typically achieved. Lower temperatures could enhance thermodynamic equilibrium. However, as the activity of γ-Al_2O_3 is insufficient at lower temperatures, the reaction conditions are set at these conditions since decades [31]. The reaction product containing water, DME and non-converted MeOH needs to be thermally fractionated in two steps in order to recycle the MeOH to the reactor and increase the C-efficiency. Reactive distillation is a way to simplify the production process by overcoming the chemical equilibrium through in-situ removal of the reaction products H_2O and DME. Hereby, the reaction needs to be shifted to the liquid phase and to a lower temperature, considering the operating range of liquid phase reaction catalysts and the operational pressure of RD.

In the ternary system DME-MeOH-H_2O, DME is the light boiler and H_2O is the heavy boiler. According to the boiling temperatures of the components, DME is removed from the top of the column as distillate and H_2O is the bottoms product, i.e., the liquid removed from the reboiler. The reaction educt MeOH is the middle boiler and thus held in the reactive section in the middle of the column. Accordingly, in the top of the column, DME needs to be separated from MeOH and in the bottom section, H_2O is separated from MeOH. Considering the relative volatilities, the thermal fractionation of the H_2O-MeOH system presents the more challenging separation task compared to the DME-MeOH system. Since MeOH enriches the reactive section in the middle of the column, the temperature in the reactive section is in proximity to the MeOH boiling point at the respective column pressure. This system-immanent phase equilibrium implies a coupling of the reaction temperature with the column pressure. Consequently, the high temperatures of the conventional synthesis could only be achieved at excessive pressures. In turn, at moderate column pressures, significantly lower reaction temperatures are demanded compared to the conventional gas phase reaction as illustrated in Figure 3-1.

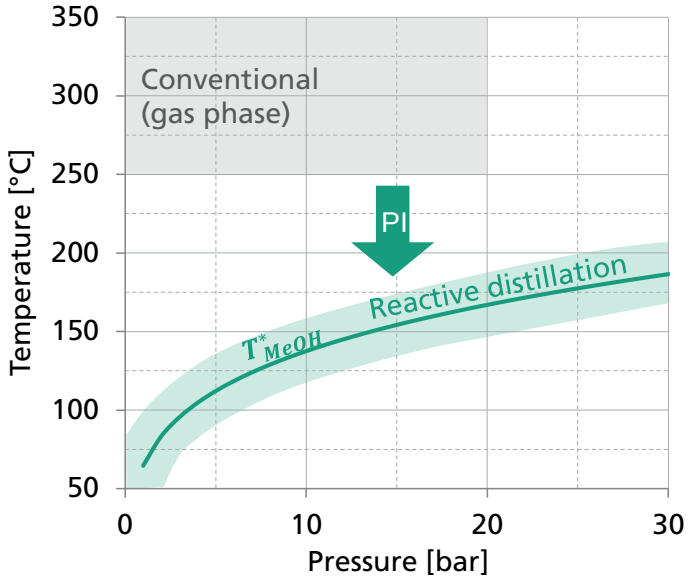

Figure 3-1: Boiling point curve of MeOH and resulting operating window of a process-intensified (PI) reactive distillation process for DME synthesis compared to the operating conditions of the conventional gas phase reaction. Illustration from Semmel et al. [149].

The ternary system exhibits a miscibility gap between DME and H_2O at low MeOH fractions. However, since MeOH is the middle boiler, mixtures with high H_2O and DME content do not occur in the reactive distillation column and the process is not affected by the miscibility gap.

3.2 Material and Methods

3.2.1 Materials

Synthesis grade MeOH (99.9 %, Bestchem GmbH) was obtained in industrial barrels. Besides using pure MeOH, a 1:1 molar mixture of MeOH and deionized H_2O obtained in the in-house laboratory was used as a feedstock. A36 was purchased from Sigma Aldrich in its wet form. To avoid the loss of catalyst through the mesh of the KATAMAX® catalytic packing, the catalyst was sieved to remove the fine fraction. The coarse fraction was filled into the pockets of the packing in a partially dried, pourable state. The catalytic packing was only filled partially, leaving room for the volume expansion due to catalyst swelling. Subsequently, the filled catalytic packing was exposed to H_2O in a horizontal position, to reduce mechanical stress on the catalyst during the swelling process. The overall catalyst mass in the RD column was 0.213 kg (referring to its dry state, reference drying conditions: 50 mbar, 100 °C for 24 hours).

3.2.2 Pilot scale pressure distillation column

The reactive distillation process was realized in a pilot-scale pressure distillation column from ILUDEST Destillationsanlagen GmbH shown Figure 3-2. The stainless steel DN50 column has a total height of 4.4 m, a packing height of 2.45 m and can be operated up to a pressure of 16 bara.

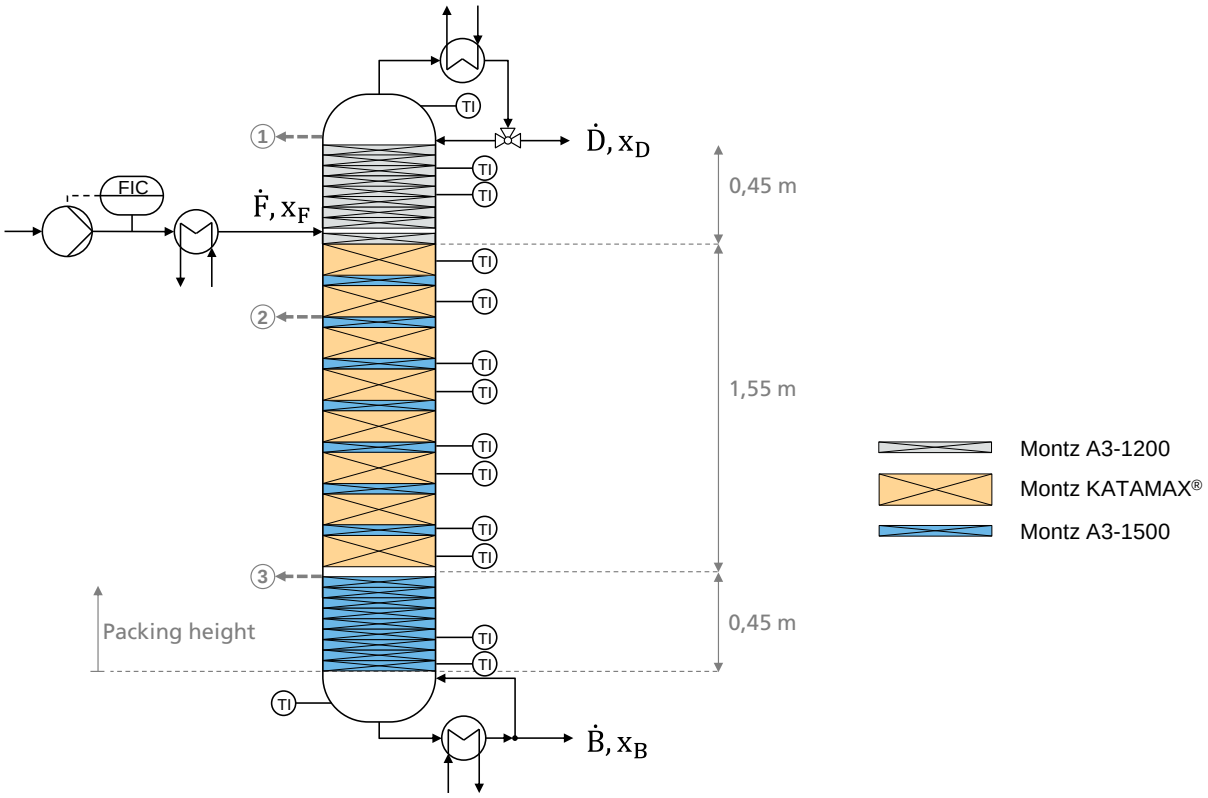

Figure 3-2: Simplified process flow diagram of the pilot reactive distillation setup including positions of sample positions, thermocouples, and packed height of the three sections.

The top of the column is equipped with a coiled tube condenser tempered by a cryostat (Huber AG). The condenser was operated at 0 °C, implying a subcooling of the distillate. The subcooling was necessary to achieve high DME purity in the distillate. Downstream the condenser, the distillate was split by a time-controlled, pneumatic three-way valve. The reflux ratio was set by the respective reflux and withdrawal time and was controlled by a PID controller to achieve a desired target temperature in the top stage of the column. The distillate was continuously transferred to the distillate storage vessel. The natural circulation evaporator of the column was heated electrically to allow a direct measurement of the heat demand. The heat input was controlled by a PID controller to achieve a desired temperature at the bottom of the reactive zone. The bottoms product was continuously transferred to the bottoms product

storage vessel to achieve a constant reboiler filling level. Both the distillate and the bottoms product storage vessel were equipped with a hydrostatic level indicator, allowing the derivation of the respective incoming volume flows. To allow an adiabatic operation, the column was jacketed by isolated mantle heaters, operated at the current column temperature. The temperature profile along the column was measured by 12 axially distributed Pt-100 elements with direct contact to the medium. Along the column, sampling ports for the withdrawal of gaseous samples were constructed on three different positions.

The column can be classified by three zones with individual packing configurations to account for the local hydraulic conditions as determined beforehand based on process simulations:

1. Upper rectifying section for the separation of DME and MeOH, equipped with 9 Montz A3-1200 structured packings (grey) with a height of 50 mm per element.
2. The reactive section for the incorporation of the catalyst, equipped with 8 Montz KATAMAX® catalytic packing with a height of 150 mm per element (orange). One layer of Montz A3-1500 (blue) was added between two corresponding elements of catalytic packing to account for the low separating efficiency of the catalytic packings on this scale and to increase the number of theoretical stages in the reactive zone.
3. The lower rectifying section for the separation of H_2O and MeOH was equipped with 9 Montz A3-1500 (blue) structured packings with a height of 50 mm per element.

The feedstock was stored under pressure in a vessel and dosed by a gear pump controlled by a Coriolis mass flow meter (Krohne). The feed stream was preheated to a temperature of 50 °C in a heat exchanger and subsequently introduced to the column above the reactive zone. Small amounts of N_2 (grade 5.0) were used for the level indicators of the column reboiler, feed and product vessels as well as for the pressure control of the distillation column.

The operating temperature of A36 is limited to 150 °C for thermal stability reasons of the sulphonated groups and to avoid leaching according to the manufacturer's datasheet[150]. Due to the vapor-liquid equilibrium (VLE) inside the column, the column pressure was adapted to prevent a temperature rise above this threshold in the reactive zone of the column. In the measurement campaign, column pressure, feed composition and feed mass flow were varied during the experiments. The experimental conditions of all measured operating points are presented in the results section.

For RD column start-up, the column reboiler was filled with H_2O and heated with total reflux mode. As soon as the temperature rise approached the reactive section, MeOH was fed to the column to keep the temperature throughout the reactive section below 150 °C. After a significant amount of DME was produced and the temperature in the upper rectifying section approached the dew point of DME, the desired reflux ratio was set. Since the start-up procedure was very time-consuming (>3 h), the column was operated continuously without shut down for several days and nights. The time required until a new steady state was reached after changing the operating point was at least 1 h (changing the RR) or more than 3 h (changing the feed flow). Every operating point was held at constant conditions for at least 30 minutes to ensure steady state was achieved.

3.2.3 Analytical methods

The three sampling ports were connected to a multi-position valve via heated capillaries to withdraw samples from the gas phase at the selected stages. The gas stream of the selected sampling port was diluted with N_2 and transferred to an MKS Multigas™ 2030 on-line FT-IR spectrometer with an optical path length of 5.11 m, while the other two sampling capillaries were dead ended. After switching the sample port on the MPV, typically 30 s of retention time were required until the new concentration was achieved in the FT-IR. Consequently, the position was varied in an interval of 1 minute. Within the time frame of steady state operation, every sampling point was analysed multiple times to ensure a reproducible measurement of the gas phase composition. Details of this column analysis system developed by ASG Analytik Service AG can be found in Bogatykh et al. [151]. In addition to the FT-IR measurements, an online GC (Agilent 8860, thermal conductivity detector) was used to analyse the composition of the distillate product and to validate the FT-IR measurements.

3.3 Simulation

A profound and validated simulation model of a reactive distillation process is required to allow the design of the process, optimize process parameters, and evaluate the key performance indicators (KPI) of the reactive distillation process and thus to lay the foundation for a techno-economic analysis of the process concept. The RD process implemented in Aspen Plus is shown in Figure 3-3. Since the RD already integrates synthesis and product purification, the process flowsheet is relatively simple. Compared to the experiments, only a product-to-feed heat exchanger to recover the heat of the water by-product stream was added to the flowsheet for heat integration.

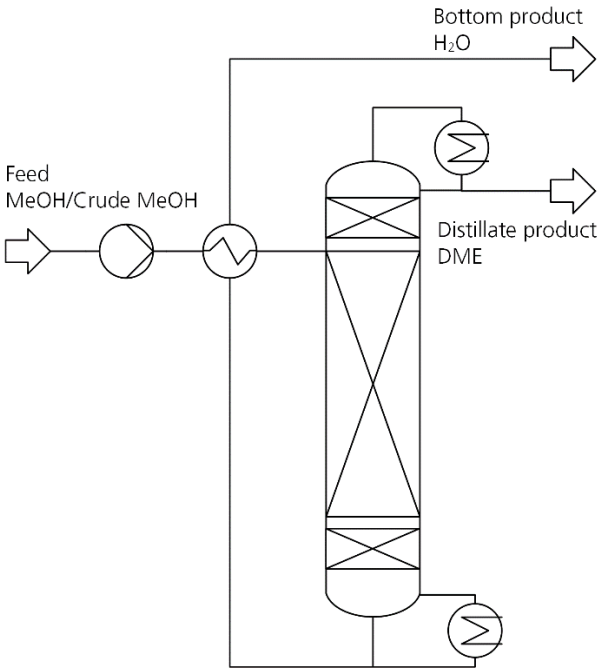

Figure 3-3: Process flowsheet used for the process simulation.

The column pressure was adjusted by a design specification so that a certain maximum temperature is reached on the lowest stage of the reactive section. Since this stage is the one with the highest stage temperature, this maximum temperature is not exceeded in any other catalyst containing stage. To achieve the desired DME purity, the reflux ratio was adjusted by another design specification so that a distillate purity of >99.9 mol.-% DME was reached. The distillate to feed ratio of the column is set to 0.5 mol mol^{-1} in the simulation program, corresponding to a full conversion of MeOH. The water purity does not need to be specified, since the satisfaction of the constraints for DME purity and distillate to feed ratio only allow operating points with pure water in the bottoms product. The influence of the design parameters (number of stages of each section, feed stage, total catalyst mass) on the process are evaluated in the results section. In any configuration, the total catalyst mass in the RD column was distributed equally over all stages of the reactive section. The pressure drop over the column was neglected, since the comparatively high operating pressure leads to low gas velocities and thus low pressure losses.

3.3.1 Simulation approach

Modelling distillation columns, two approaches can be distinguished. The equilibrium stage model assumes the vapor and liquid streams leaving the stage to be in phase equilibrium with

each other. In contrast, the non-equilibrium model or so-called rate-based model aims to consider the actual transport rates based on mass and heat transfer between vapor and liquid phase. Hereby, a diffusion model such as the Maxwell-Stefan approach is required [152]. Opposed to conventional distillation columns, the reaction needs to be modelled on each reactive stage in RD columns. Hereby an equilibrium-based reaction model can be applied, assuming an instantaneously reached chemical equilibrium. Alternatively, a kinetic approach can be applied, considering the reaction rate based on a kinetic model.

DME reactive distillation is characterized by a slow reaction, according to the definition of Schoenmakers and Bessling [153], since the reaction needs significantly more time than the typical residence time on each stage to reach the chemical equilibrium. The high relative volatility of the components leads to a rather low number of required separation stages. Consequently, an RD process in DME production is limited by the reaction rather than the separation.

Thus, the equilibrium stage model was used in combination with a kinetic approach for modelling the reaction in the scope of this work. The RD was simulated with the RADFRAC model of the simulation environment Aspen Plus® incorporating the reaction kinetics on each reactive stage. By default, RADFRAC only allows for the implementation of power-law type kinetic rate equations. To allow the modelling of other extended mathematical expressions, the respective rate equation was implemented by a Fortran subroutine. In the simulation, the reaction was assumed to proceed in the liquid phase only [154]. Consequently, on each reactive stage, the reaction rate was calculated based on the respective stage temperature, liquid molar fraction of the components and catalyst mass per stage.

3.3.2 Reaction kinetics and equilibrium

The experimental part of this work is conducted using the IER A36. IER are known to exhibit a distinct swelling behaviour, leading to a significant increase in volume and mass when exposed to a liquid solvent such as methanol or H_2O. Due to the permanent liquid flow and the surface tension of the medium the IER particles are expected to be permanently contacted to the liquid phase. Consequently, in an RD process the IER will always be in the swollen state defined by the liquid composition of the respective stage. Thus, to correctly model the reaction in the RD column, the liquid composition of the respective stage needs to be coupled with a kinetic model measured under liquid conditions.

In an earlier publication of our group [149], A36 and CAT400 were identified as the two most promising catalysts for RD by screening various catalysts. Furthermore, a novel kinetic model

accounting for the RD operating conditions was proposed based on experimental kinetic measurements in a fixed-bed profile reactor. During these kinetic experiments, the reaction pressure was significantly higher than in the VLE of the RD process to guarantee pure liquid operating conditions. However, it was experimentally proven that the pressure has no influence on the reaction rate, since the reaction takes place in the incompressible liquid phase. [149]

Due to the higher operating temperature of CAT400 and the corresponding higher pressure rating requirements of the distillation column, A36 was chosen for the experimental part of this work. The intrinsic kinetic rate equation introduced by Semmel et al. [149] is based on a LH approach extended by a water inhibition term given by equation (39) and the corresponding parameters given in Table 3-1. The catalyst mass m_{cat} is referring to the water-free dry state of the catalyst.

$$r_{\mathrm{DME}} = \frac{k \cdot \left(x_{\mathrm{MeOH}}^2 - \frac{x_{\mathrm{DME}} \cdot x_{\mathrm{H_2O}}}{K_{\mathrm{eq}}} \right)}{x_{\mathrm{MeOH}}{}^2} \cdot \frac{1}{(1 + K_{\mathrm{W}} \cdot x_{\mathrm{H2O}})^2} \tag{39}$$

With

$$k = \mathrm{k}_0 \cdot \exp\left(\frac{-\mathrm{E_A}}{R\,T}\right) \tag{40}$$

$$K_W = exp\,(K_{W1} - \frac{K_{W2}}{T}) \tag{41}$$

$$K_{eq} = exp\,(1.743 + \frac{887.9}{T}) \tag{42}$$

Table 3-1: Kinetic parameters for the two catalysts A36 and CAT400 [149].

Parameter	Unit	A36	CAT400
k_0	mol kg_{Cat}^{-1} s^{-1}	8.089e9	5.973e10
E_A	kJ mol^{-1}	91.56	101.98
K_{W1}	-	−4.2255	0.4118
K_{W2}	K	−2360.9	−345.2587

During the kinetic experiments carried out in our previous work, the influence of external mass transport was found to be negligible within the entire range of applied liquid loads of 0.5-5 m^3 h^{-1} m^{-2} (reference: cross sectional area of empty pipe) [149]. Liquid loads in RD processes strongly depend on the column design and the process characteristics, however, typically exceed 1 m^3 h^{-1} m^{-2} [155–157]. Consequently, no external mass transfer limitation is to be expected in the RD column.

Internal mass transfer limitations were identified to be negligible in the kinetic study, even at the highest reaction rate, i.e., conditions of maximum educt concentration and temperature. Under the reactive distillation conditions applied in this work, the reaction rate was always lower than the maximum rate within the kinetic study. Since the diffusion coefficient in liquid phase is independent of the pressure, the internal diffusion in the catalyst particle is not affected by the reactive distillation conditions. Thus, in reactive distillation no internal mass transport limitation is to be expected either. Consequently, the kinetic equation was found fully applicable to the reactive distillation conditions applied in this work without the consideration of internal or external mass transport.

In the scope of the RD investigations, the $WHSV_{RD}$ is defined as the ratio of feed mass flow of MeOH and the catalyst mass in the RD column. It should be noted that this definition is different from the $WHSV_{Reactor}$ of the reactor in chapter 2, where water was included in the feed mass flow. Thus, $WHSV_{RD}$ indicates the amount of MeOH that needs to be converted per catalyst mass in the RD column.

$$WHSV_{RD} = \frac{\dot{m}_{\mathrm{Feed,MeOH}}}{m_{\mathrm{cat,RD}}} \tag{43}$$

3.3.3 Thermodynamic and physical properties

The used thermodynamic model was regressed based on binary and ternary experimental VLE data of the DME-MeOH-H_2O system and is described in detail by Ye et al. [158]. It incorporates the Peng-Robinson equation of state (EOS) with Wong-Sandler mixing rules and the UNIFAC-PSRK model for the calculation of the activity coefficients. The small amounts of N_2 used for the level indicators of the column were not considered in the simulation model. A detailed list of all models used for the calculation of thermodynamic and physical properties in Aspen Plus® is shown in the supplementary material SI2.4.

3.3.4 Data analysis and generation of continuous profile

The experimental column profile data of each steady-state operating point consists of the gas phase analysis on three positions and the temperature measurement on 14 positions. However, a continuous temperature and liquid composition profile is required to allow the evaluation of literature kinetic models and calculate the DME production rate according to the kinetic model. A continuous temperature profile was achieved by spline interpolation of the discrete experimental temperature data. Due to the low axial resolution of the gas phase

analysis, a simple interpolation was considered inappropriate. Instead, the gas and liquid phase composition exhibiting a bubble or dew point equivalent to the measured temperature were calculated by modelling of the component system's VLE.

Considering the degrees of freedom, this procedure is only possible for binary systems, or ternary systems where the fraction of one component is known. As experimentally confirmed by the gas phase measurement at the sampling port below the reactive zone, no DME was present in the lower rectifying section. This can be explained by to the absence of catalyst in this section of the column and the low boiling temperature of DME. Consequently, the composition in this section could directly be calculated based on the measured temperature and the thermodynamic modelling of the binary MeOH-H_2O system. In the reactive zone, however, all three components are present. Consequently, one component must be estimated to determine the composition. Hereby, the water fraction was interpolated linearly between the sampling ports #2 and #3. This assumption is going to be validated below in the results section. The residual fraction of DME and MeOH was then calculated based on the measured temperature and the thermodynamic modelling of the ternary system. Following this methodology, continuous temperature and liquid composition profiles were calculated based on the discrete experimental data. Vice versa, the dew temperature of the measured gas phase was calculated on each sampling position to allow a comparison with the measured temperature and consequently evaluate the consistency of the measured data. Hereby it was found that the temperature measurement and dew temperature of the analysed gas phase are consistent, providing confidence in the measured data. More details about this methodology are available in the supplementary material SI2.1.

3.4 Results and Discussion

3.4.1 Experimental results

In total, 19 experiments were carried out over a total time on stream (TOS) of 150 h. Table 3-2 summarizes the key operating parameters of all the performed experiments in the pilot-scale RD column. A detailed table with all experimental data, including the temperature profile and all gas phase compositions, is included in the supplementary material 0. The temperatures, column pressure, gas compositions, feed mass flow and reboiler duty were explicitly measured.

The reflux ratio is defined by the reflux mass flow divided by the withdrawal mass flow and can be estimated by dividing the reflux time interval by the withdrawal time interval of the three-way valve:

$$RR = \frac{\dot{n}_{\text{reflux}}}{\dot{n}_{\text{distillate}}} \approx \frac{\Delta t_{\text{reflux}}}{\Delta t_{\text{distillate}}} \tag{44}$$

However, in the experiments it was found that this estimation is not precise at high reflux ratios. Consequently, in this work the reflux ratio was calculated by combining the explicitly measured data with the mass and energy balance of the column, as shown in the supplementary material SI2.3. Thereby, the MeOH conversion and the condenser duty are also calculated.

Table 3-2: Key operating parameters of all experiments carried out in the pilot-scale column.

# Exp.	p_{column}	$\dot{m}_{Feed}$	$x_{MeOH,Feed}$	RR_{calc}	$x_{DME,distillate}$	$x_{H2O,bottoms}$	X_{MeOH}	$Q_{reboiler}$	$Q_{condenser}$
	bara	kg h^{-1}	mol mol^{-1}	[-]	[mol mol^{-1}]	[mol mol^{-1}]	[-]	[W]	[W]
1	12.0	0.30	1	12.8	98.0%	98.0%	98.1%	433.6	408.9
2	12.0	0.40	1	14.0	98.7%	96.8%	97.8%	613.4	581.2
3	12.0	0.20	1	9.1	92.9%	98.5%	95.6%	231.2	215.3
4	12.0	0.20	1	11.0	96.9%	99.2%	98.1%	257.4	241.2
5	12.0	0.20	1	10.7	96.7%	99.3%	98.0%	251.7	235.8
6	12.0	0.30	1	10.4	96.9%	99.0%	98.0%	370.1	345.5
7	12.0	0.30	1	5.8	86.5%	98.9%	92.3%	259.6	236.9
8	12.0	0.30	1	5.2	80.2%	98.9%	88.6%	257.0	235.0
9	12.0	0.30	1	4.3	77.4%	99.0%	86.9%	230.4	208.9
10	12.5	0.30	1	10.3	96.4%	98.0%	97.3%	367.3	343.5
11	12.5	0.40	1	12.6	96.7%	98.4%	97.6%	584.0	552.2
12	12.5	0.40	1	8.9	88.8%	98.3%	93.3%	477.7	448.0
13	12.5	0.40	1	8.6	89.5%	98.4%	93.8%	462.5	432.6
14	12.5	0.50	1	7.2	80.9%	98.1%	88.8%	554.0	517.8
15	12.5	0.50	1	11.0	92.6%	97.9%	95.2%	683.9	644.1
16	12.5	0.40	1	13.9	98.3%	98.7%	98.5%	619.8	587.3
17	12.5	0.40	1	20.7	99.9%	95.8%	97.8%	856.2	824.1
18	12.5	0.50	0.5	17.5	97.2%	98.4%	96.3%	642.9	584.7

The distillate was analysed with respect to potential side products. For all experiments, no side product formation was detected, confirming the results of the kinetic measurements previously executed in a fixed-bed reactor [149]. In the distillate and the bottoms product, the only identified impurity was unseparated MeOH. Due to the limited column height, the number of packings in the upper rectifying section had to be reduced to a minimum to leave room for the reactive section. Consequently, the DME distillate purity in most experiments is below

99 mol.-%. Yet, to demonstrate the production of norm compliant DME, experiment E17 was conducted with a particularly high RR.

For clarity, a few general remarks applying to all measured operating points will be made based on the experimental data of the exemplary experiment E1 as shown in Figure 3-4. Furthermore, the continuous profile calculated by the methodology described in the simulation chapter is presented.

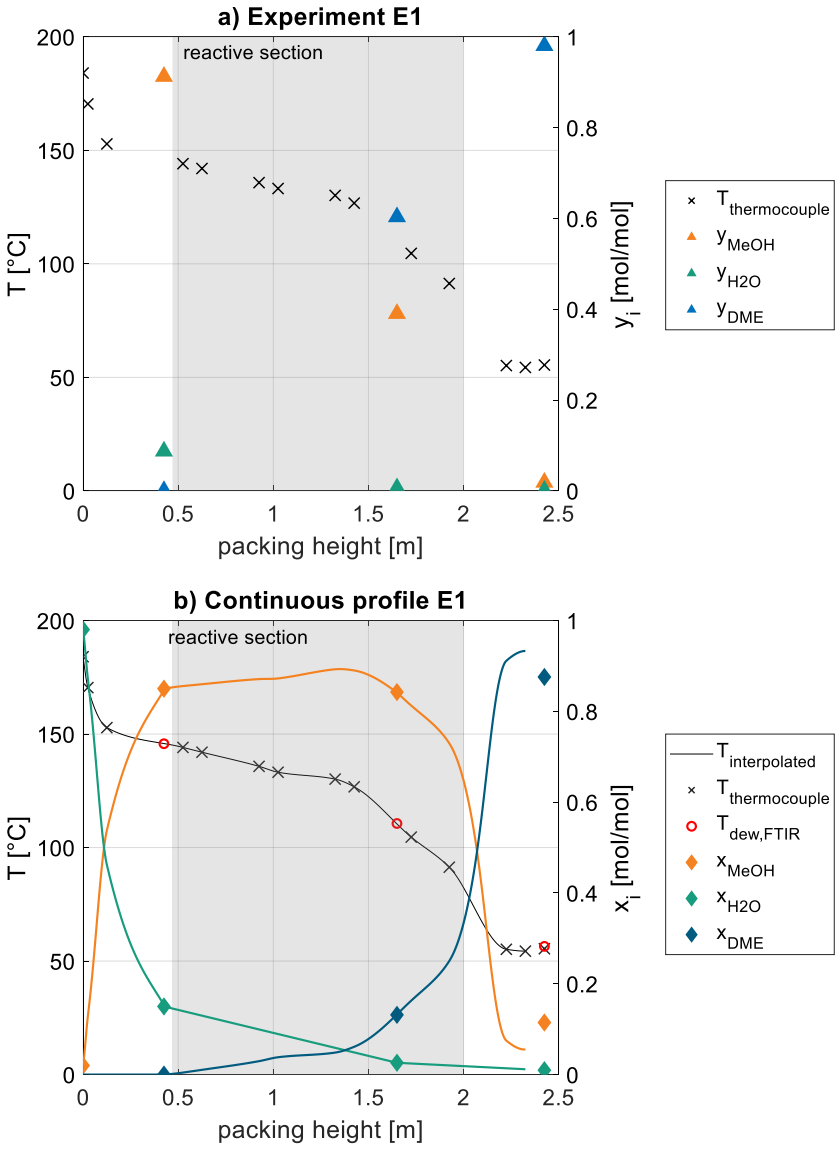

Figure 3-4: a) discrete measured temperature and gas phase composition along the packing height of the column; b) calculated continuous temperature obtained by interpolation and liquid phase composition profile obtained from measured gas phase composition according to the methodology described in the simulation chapter; Exemplary representation for experiment #1; Operating pressure 12.0 bar, feed mass flow 0.3 kg h^{-1} pure MeOH.

At this exemplary operating point, the reboiler of the column operates at a temperature of 184 °C, corresponding to a water purity of 98 mol.-% at the operating column pressure of 12 bar. Above the reboiler a sharp temperature drop over a short column height is visible, representing an effective separation of water and MeOH, as can also be seen at the gas phase analysis (a) at 0.425 m, where only 9 mol.-% water are present. In the interpolated continuous profile (b), this corresponds to an equilibrium liquid concentration of 15 mol.-% water. The dew temperature of the measured gas phase composition at this position (red circle) agrees very well with the measured temperature (blue line), indicating a strong consistency of the measurements.

At the lower end of the reactive section at 0.47 m, the composition is rich in MeOH and low in water which is beneficial from a kinetic perspective, since water has a strong inhibition effect on the reaction rate [149]. The lower and middle part of the reactive section (0.5-1.5 m) are characterized by a linear temperature decrease with increasing column height. In the upper third of the reactive section, above 1.5 m, the slope of the temperature profile is decreasing significantly which can be explained by an increasing concentration of the low-boiler DME. This observation is reinforced considering the high DME fraction of 60 mol.-% in the gas phase (a) at 1.65 m. In the calculated continuous column profile (b), this corresponds to an equilibrium liquid concentration of only 13 mol.-%. Between the measured composition at 0.425 m and 1.65 m, the linear interpolation of the water fraction is visible. In contrast, the DME and MeOH fraction are calculated based on the measured temperature. At the sampling position at 1.625 m, a high consistency between the measured temperature and the dew point of the gas phase analysis is clear. Overall, the whole reactive section is characterized by a high liquid MeOH mole fraction of >73 mol.-%. While this is beneficial from a kinetic perspective, the steep temperature decrease in the upper third of the reactive section significantly lowers the reaction rate in this region of the column. In an industrial process realization, this behaviour should be avoided by improving the separation in the upper rectifying section, e.g., increasing the number of theoretical separation stages. As a result, less DME would be present in the reactive section, thus decreasing the temperature gradient within the reactive packing and thereby increasing the reaction rate. Due to the limited column height, this was not possible as it would not leave enough space for the reactive section.

In the upper rectifying section, the temperature is decreasing further to 54 °C due to the purification of DME by rectification. The gas phase analysis shows a high distillate purity of 98 mol.-% DME. A slightly higher temperature of the top thermocouple compared to the second uppermost thermocouple can be observed. This is most likely due to an unreached

thermodynamic equilibrium in the upper rectifying section, resulting from a short liquid-gas contact time. For this reason, the match between calculated composition profile and measured composition is not ideal in this section of the column.

Figure 3-5 shows the temperature profiles of the experiments E1, E2 and E4. These experiments are characterized by different feed mass flows, resulting in different $WHSV_{RD}$. At the same time, a comparable distillate and bottoms purity, thus MeOH conversion is maintained by varying RR.

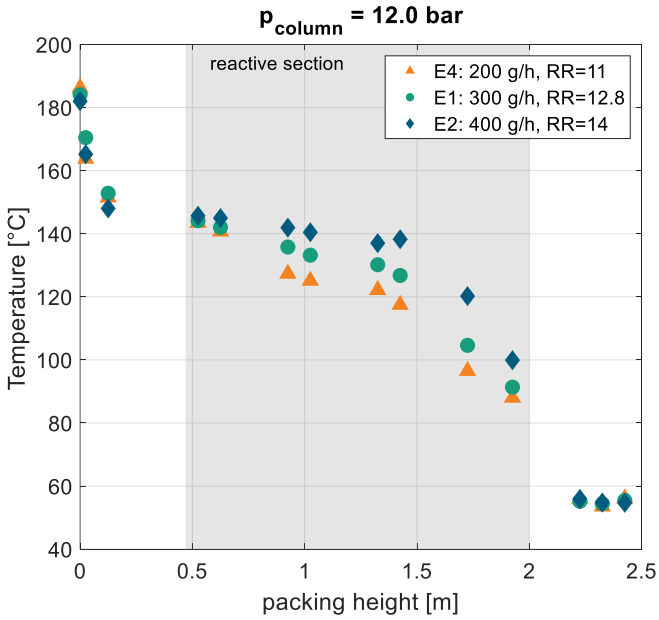

Figure 3-5: Measured temperature profiles of the experiments E1, E2 and E4 along the packing height of the column. The feed mass flow is varied and the reflux ratio is adapted in order to achieve a comparable distillate purity.

The three temperature profiles have comparable bottoms and distillate temperatures, however the temperatures in the reactive section differ significantly. While the profiles show a linear temperature decrease between 0.5-1.5 m and an identical temperature at 0.5 m, the slope of the temperature profiles decreases with increasing feed mass flow. This leads to a flatter temperature profile and consequently a higher average temperature in the reactive section enabling higher reaction rates required for the conversion of the higher feed mass flow. Furthermore, an increasing RR with increasing $WHSV_{RD}$ is evident. This shows that the conversion of more feedstock by a higher average reaction temperature is only enabled by an increase of the RR. Vice versa, by reducing the $WHSV_{RD}$ through a lower feed mass flow, the RR can be reduced. From an industrial perspective, this implies a conflict of objectives when designing the RD: Increasing the column size results in higher investment cost, however, at a

constant feed mass flow the RR decreases, thus leading to a lower energy demand in the column reboiler and consequently reduced operating costs. To solve this conflict of objectives, rigorous process optimization is required to identify an appropriate column design. The same trend can be observed when comparing the reboiler duties of E10 with E11 or E13 with E15.

Figure 3-6 compares the experiments E10 and E18 to examine the influence of water in the feed. The crude MeOH feed mass flow in E18 is 0.5 kg h^{-1}, corresponding to 0.32 kg h^{-1} of MeOH considering the MeOH concentration of 50 mol.-%. Thus, the amount of MeOH is comparable to experiment E10 with 0.3 kg h^{-1} of pure MeOH feed.

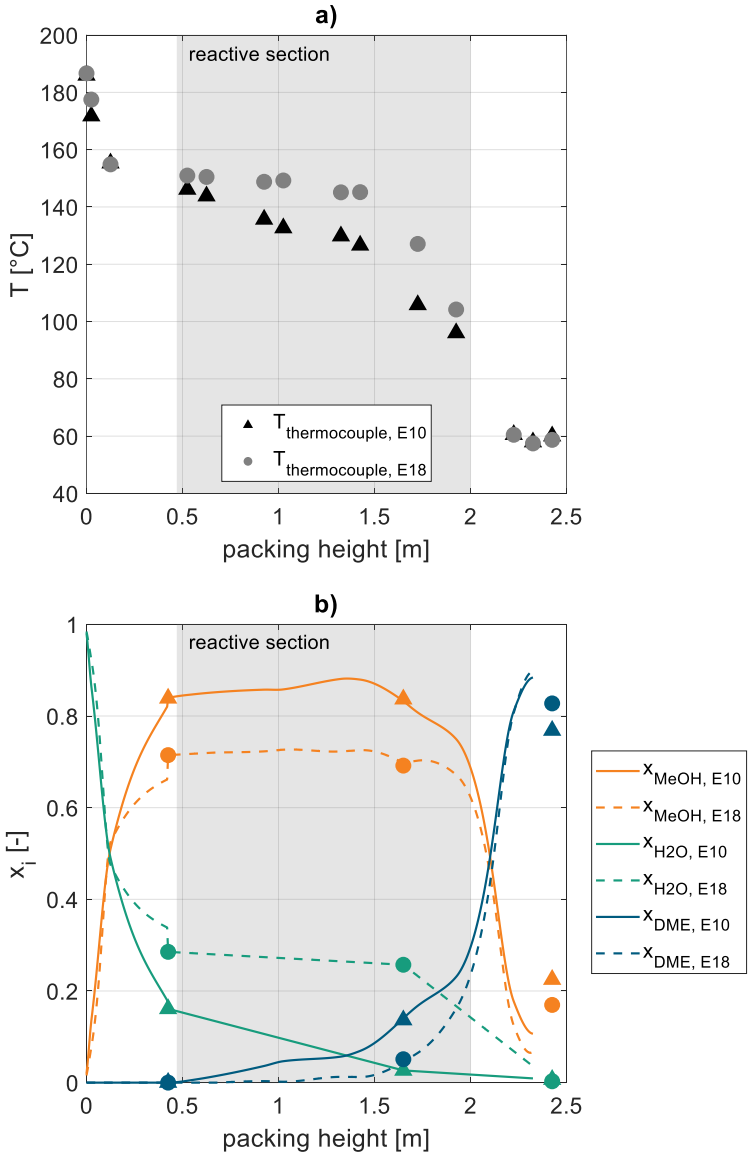

Figure 3-6: Comparison of the experiments E10 (pure MeOH feed) and E18 (crude MeOH feed). Measured temperature profile (a) and calculated liquid composition profile (b) of both experiments along the packing height of the column.

The crude MeOH experiment E18 shows a significantly higher temperature in the reactive section than E10, due to a flatter temperature profile. As discussed before, this is the consequence of the higher RR of E18 compared to E10 (17.5 vs. 10.3). The higher average temperature in the reactive section is required to maintain a high reaction rate despite the higher water content due to the crude MeOH feed. As shown in Figure 3-6 b) the liquid profile of E18 generally shows a higher water concentration throughout the reactive section. Particularly in the upper part of the reactive section, the water concentration is considerably higher since the water in the crude MeOH is fed directly on top of the reactive section. To reduce the water concentration in the reactive section, a lower feed position could be beneficial. At the lower end of the reactive section, E18 shows a higher water mole fraction than E10, while the bottoms product purity of E18 and E10 is nearly identical. Consequently, the MeOH-H_2O separation in the lower rectifying zone is more effective in E18, which can also be explained by the higher RR. The reboiler duty of E18 is significantly higher than E10 (642.9 W vs. 367.3 W), due to the higher required RR.

This measurement proves the feasibility of a one-step process to produce purified DME from crude MeOH under industrially relevant conditions. This presents a major process simplification, allowing to omit the crude MeOH distillation step and reduce the investment cost of the process within the system boundary of syngas to DME. From an industrial perspective, it is important to note the energy demand of the RD increases when using crude MeOH. However, this implementation can lead to a total process efficiency increase compared to a DME synthesis based on pure MeOH feed, as no energy demand is required for the omitted crude MeOH distillation column. Process simulations including economic aspects are therefore required.

3.4.2 Model validation

A key challenge in modelling RD is the precise description of the reaction kinetics. Particularly the transfer of the kinetic model from laboratory kinetic reactors to the actual RD column often yields unsatisfying results [156,159]. In the following, the calculated continuous column profiles were used to evaluate various literature kinetic models in terms of their suitability to describe the actual kinetic behaviour in the RD column. Hereby, the temperature and liquid composition on each column height increment are used to calculate the reaction rate profile and evaluate the overall DME production rate by integrating over the whole reactive section. By comparing the simulated DME production rate to the actual withdrawn mole flow of DME in the distillate

product, the suitability of the examined literature kinetic models for their application in RD can be compared.

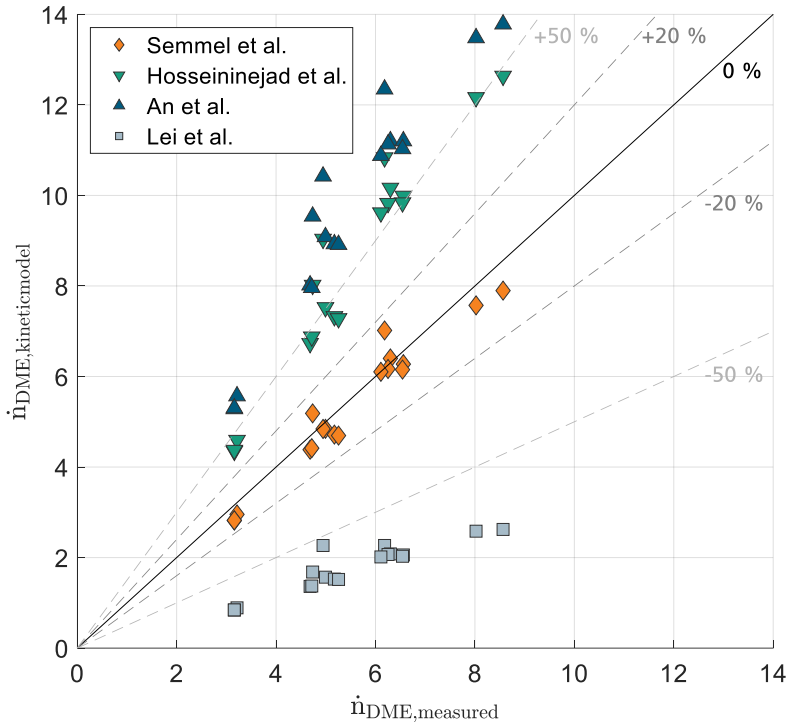

Figure 3-7: Measured distillate flow rate $\dot{n}_{DME,measured}$ over simulated overall reaction rate $\dot{n}_{DME,kinetic\ model}$ evaluated based on calculated continuous column profiles and different kinetic models [71–73,149]. Parity plot for all measured experimental datapoints E1-E18.

Figure 3-7 compares the measured DME distillate flow with the simulated overall DME production rate predicted by the respective literature kinetic model in a parity plot. The model of Lei et al. [72] shows an extreme underestimation of the amount of produced DME, predicting less than half of the actually measured DME distillate for all conducted experiments. In contrast, the kinetic models proposed by An et al. [71] and Hosseininejad et al. [73], respectively overestimate the reaction rate significantly. Hereby it needs to be considered, that An and Hosseininejad use Amberlyst 35 instead of A36 as catalyst, which might lead to slight deviations in the kinetic behaviour. However, both catalysts show a very similar acid capacity and were reported to show nearly identical MeOH conversion in a catalyst screening [73]. More likely, the small water concentration range considered in the kinetic studies of An et al. and Hosseininejad et al. (0-13 mol.-% and 0-20 mol.-%, respectively) leads to a deviation in reaction rate due to the required extrapolation of their kinetic model. Summarizing all

experiments, a temperature range of 78-151 °C and a water concentration range of 0.18-28.5 mol.-% was examined in the reactive section.

Compared to the other literature models, the model proposed by Semmel et al. [149] predicts the measured distillate stream very well and thus presents a suitable model for describing the kinetics of DME reaction over the large temperature and concentration range appearing in RD columns. Experiment E18 with crude MeOH feed and a significantly higher water concentration in the reactive section is also described well by the kinetic model. While a slight scattering of the measurements can be observed, TOS of the catalysts at the respective experiment has no influence on whether the distillate flow is higher or lower than predicted by the kinetic model. In the case of a catalyst deactivation, experiments at a later point in the measurement campaign would tend to show lower distillate flows than predicted by the model. As this was not observed, no significant catalyst deactivation was observed over the total TOS of 150 h. This verdict should be confirmed by performing longer TOS operation.

Importantly, the great agreement of the kinetic model – despite the significantly different operating conditions in RD and kinetic reactor – cannot be taken for granted. The kinetic model for A36 was derived in a fixed-bed profile reactor operated under a pressure of 40 bar to guarantee a reaction solely in the liquid phase at unambiguous conditions. In contrast, the significantly lower pressure in the RD leads to the reaction occurring under conditions where the gas and liquid phase coexist. The light-boiler DME, formed at the active site inside the catalyst pores, could potentially lead to a partial evaporation inside the catalyst pores which in turn would hamper the internal mass transport inside the catalyst, as reported by Datsevich et al. [160]. Furthermore, fluid dynamic non-idealities in the catalytic packing of the RD, such as liquid bypassing of the catalyst or insufficient catalyst usage by non-wetted or stagnant zones of the catalyst could lead to significantly reduced reaction rates under RD conditions [156]. The observations based on the experiments presented in this work are free of such influences, and the kinetic model by Semmel et al. [149] could be successfully validated for the application in RD. At industrial scale, fluid dynamic non-idealities are less likely to occur compared to the comparatively small column diameter used in this work. Therefore, the application of the kinetic model for an industrial design of RD columns was found feasible.

To further validate the whole process simulation model applying the kinetic model of Semmel et al. in the reactive section, the continuous column profiles of experiment E1 with the column profiles acquired by the Aspen Plus process simulation are compared in Figure 3-8. Hereby, the parameters applied in the experiment (catalyst mass, feed stage, feed flow, feed composition and temperature, and RR) were applied in the process model. The number of

stages of each zone in the simulation was set to $N_{rect,\ upper}$=4, $N_{rect,\ lower}$=3, and $N_{reactive}$=7 to match the experimental data. The number of theoretical stages in each experiment could only be estimated, as the separation efficiency of the packing could not be stated by the manufacturer at the conditions applied in this study. Furthermore, the separation efficiency depends on the hydraulic conditions at the specific location of the packing and at each experiment.

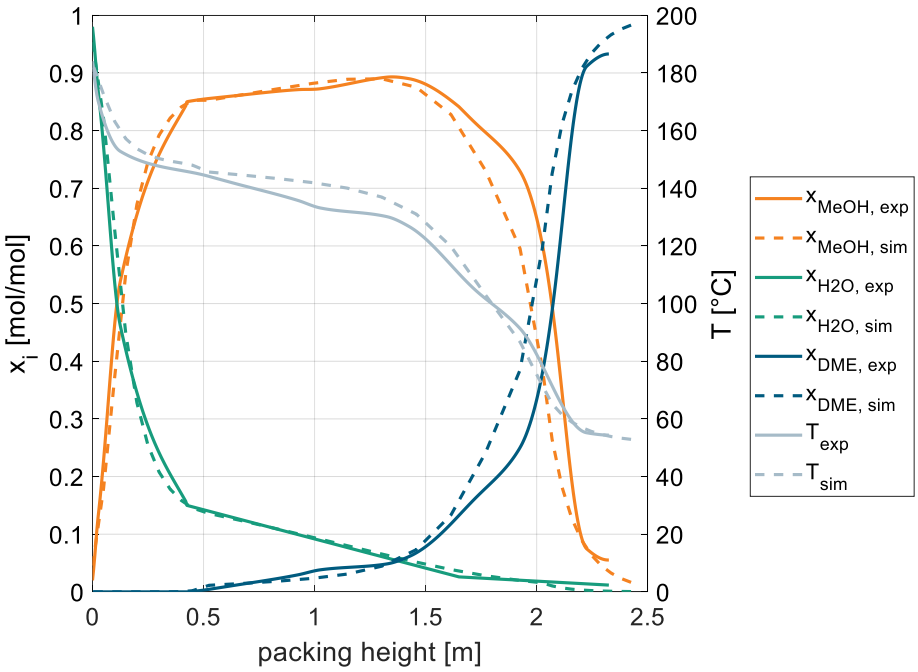

Figure 3-8: Comparison between experiment and process simulation; Experimentally determined continuous temperature and liquid composition profile of experiment E1 (solid lines) and simulated temperature and liquid composition profile (dashed lines) at the conditions applied in the experiment; For the simulation, the stage numbers of the RD column were set to $N_{rect,\ upper}$=4, $N_{rect,\ lower}$=3, $N_{reactive}$=7.

A very good fit for each component liquid composition profile as well as the temperature profile can be observed along the whole packing height of the column. Particularly, the water composition profile in the reactive section is indeed almost ideally linear, as assumed in the methodology for calculating the continuous profiles.

Yet, it needs to be emphasized, that the operating conditions in the pilot-scale reactive distillation column differ from the conditions in an industrial scale RD plant: Due to the limited size of the pilot-scale distillation column used in this work and the height required for the two rectifying sections, only a relatively low catalyst mass could be introduced in the reactive section. At the same time, the feed mass flow could not be reduced indefinitely to ensure appropriate F-factors and avoid a dewetting of the packings [161]. Consequently, the operating

points examined in this work are characterized by a rather high $WHSV_{RD}$, requiring a high RR. As mentioned above, this operating point is likely to be non-optimal for the plant economics due to a high energy demand of the process. For this reason, the following chapter examines the RD process based on the validated process simulation at a wider range of operating conditions, including the economically more favourable operating range with lower RR.

3.4.3 Process analysis

the following, a large-scale RD process to produce DME with a production capacity of 100,000 t a^{-1} is simulated using the design parameters given below. The RADFRAC column was simulated according to the flowsheet in Figure 3-3. A sensitivity study of the process was conducted to define the main influencing parameters on the reboiler duty of the RD column, as shown in Figure 3-9. These can be distinguished by parameters related to the reaction kinetics and parameters related to the distillation. The base case configuration of the sensitivity study is shown in brackets:

1. Kinetic parameters
    a. Catalyst mass (19.2 t)
    b. Max. operating temperature of the catalyst (150 °C)
2. Distillation parameters
    a. Number of stages in upper rectifying section (10)
    b. Number of stages in lower rectifying section (14)
    c. Number of stages in reactive section (25)

The modification of the operating temperature of the catalyst was achieved by variation of the column pressure.

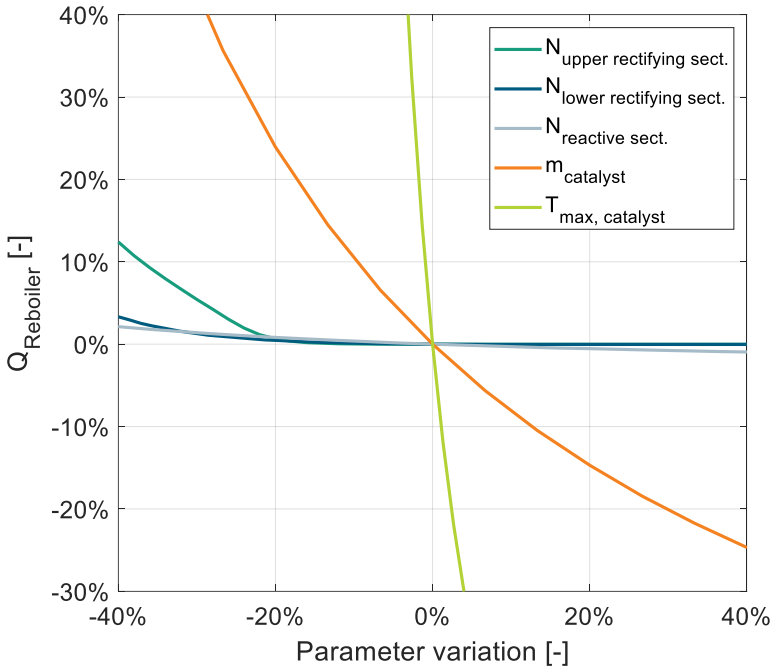

Figure 3-9: Sensitivity study of kinetic parameters and distillation parameters on the reboiler duty of the RD column.

The sensitivity study shows that the parameters influencing the reaction kinetics, i.e., temperature and catalyst mass, are the main limiting factors for the design of the reactive distillation process. The number of stages in the two rectifying sections must not fall below the required stage number, otherwise the reflux ratio needs to be increased to achieve the desired purity and consequently the reboiler duty is increased. In this case, the RR is dominated by the distillation. A further increase in the number of rectifying stages beyond the minimum does not reduce the reboiler duty. In this case, the RR is dominated by the reaction. The number of stages in the reactive section (while keeping the same catalyst mass in the RD column) shows a very small sensitivity over the whole parameter range examined.

In contrast, the kinetic parameters show a significantly higher sensitivity than the distillation parameters. An increase of the catalyst mass leads to a reduced reboiler duty of the column. This can be explained in accordance with the experiments: An increase of the catalyst mass leads to a reduced $WHSV_{RD}$ and consequently a lower reaction temperature and a less flat temperature profile is required which can be achieved by a lower RR. The curve of the variation of the catalyst mass per stage represents a proportional manipulation of the reaction rate and is synonymous for a kinetic model with respectively higher or lower pre-exponential factor. The maximum operating temperature of the catalyst shows a drastically higher sensitivity since the

reaction temperature affects the reaction rate exponentially. However, this parameter represents a theoretical reflection as no catalyst with higher operating temperature and identical kinetic behaviour exists. Nonetheless, it shows that the use of catalysts with higher operating temperature presents a strong lever for improving the process efficiency.

Overall, it can be derived, that reaction kinetics is the key to optimizing the energy efficiency of the DME RD process. If the number of stages in both rectifying sections is large enough, which is already achieved at comparably low stage numbers, the required RR is dominated by the reaction and the reboiler duty can only be reduced by increasing the reaction rate.

Figure 3-10 shows the specific reboiler duty per ton of produced DME in dependence of the feed stage N_{Feed} for different water mole fractions $x_{H2O,Feed}$ of the feed. The absolute methanol flow of the feed was kept constant at 17.5 t h^{-1}, while an additional water mass flow was added to achieve the respective molar fraction. The catalyst mass in the RD column was 64 t, resulting in a $WHSV_{RD}$ of 0.27 h^{-1}. The used catalyst for the simulation was A36 and the maximum operating temperature in the reactive section was set to 130 °C by varying the column pressure as described in the simulation chapter. The resulting operating pressure of all operating points considered in Figure 3-10 was between 6.4-7.2 bar depending on the feed stage and the feed composition.

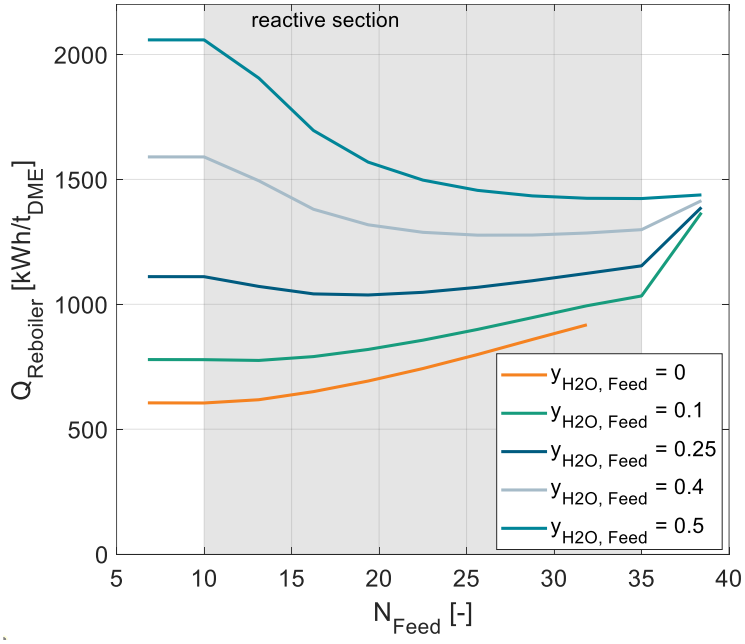

Figure 3-10: Specific reboiler duty per ton of produced DME in dependence of the feed stage N_{Feed} for various molar water fractions in the feed. $WHSV_{RD}$ =0.27 h^{-1}. $N_{rect, upper}$ = 10, $N_{rect, lower}$ = 14, $N_{reactive}$ = 25. Use of A36 in the reactive section with T_{max} = 130 °C.

The simulations show a clear increase of the specific reboiler duty with increasing water mole fraction of the feed. This trend agrees well with the experimental measurements, where the specific reboiler duty increases roughly by a factor of two when comparing a crude MeOH feed (50 mol.-% H_2O) with a pure MeOH feed. Furthermore, it can be seen, that the optimal feed stage varies with the feed composition, resulting in a lower optimal feed position with increasing water fraction of the feed. For a pure MeOH feed, the top reactive stage (10) is the optimal feed stage. In contrast, a feed stage of 35 is optimal for a feed with 50 % H_2O. With this feed composition, feeding at stage 10 would lead to a 45 % higher energy demand. This behaviour underlines the importance of a proper simulation-based design of the RD column.

As mentioned in the simulation chapter the kinetic parameters for the two catalysts A36 and CAT400 are available. While CAT400 exhibits a lower acid capacity and consequently is less active than A36 at identical conditions, it offers a higher thermal stability leaving potential for an increase in reaction rate. In the following, the influence of the catalyst choice on the RD process performance is examined. The maximum operating temperature was set to 130 °C for A36 and to 160 °C for CAT400, representing a lower temperature than the respective manufacturers specification to allow a long-term stability of the catalysts.

Figure 3-11 compares A36 and CAT400 with respect to the specific energy demand per ton of DME as a function of the $WHSV_{RD}$ of the RD column. For both pure MeOH (a) and crude MeOH feed (b), the specific reboiler duty increases with increasing $WHSV_{RD}$, as already discussed in the sensitivity study and confirmed by the experiments. Consequently, the energy demand of the RD process strongly dependents on the dimensioning of the RD column. Moreover, all operating points with complete MeOH conversion can be found along the operating lines in the graphs. This behaviour leads to a conflict of objectives between operating costs and investment costs that can only be solved by rigorous techno-economic evaluation. The optimal feed stage for CAT400 for pure and crude MeOH was determined analogously to Figure 3-10, details are shown in the supplementary material SI2.5.

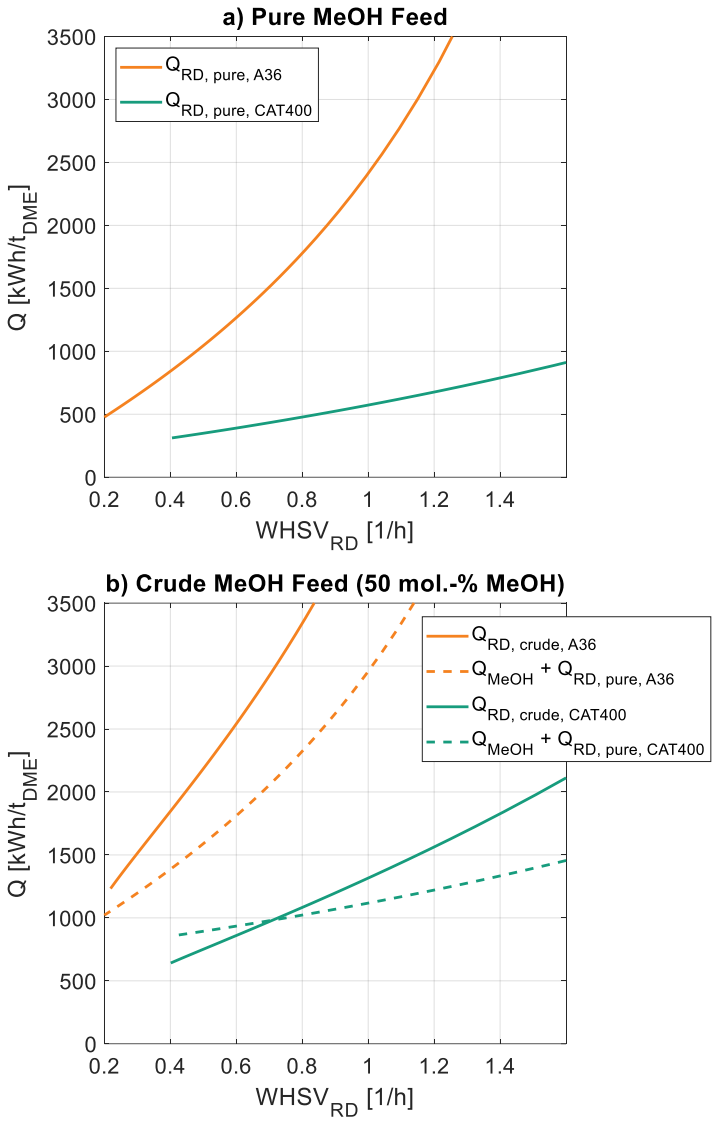

Figure 3-11: Specific reboiler duty per ton of produced DME as a function of the $WHSV_{RD}$ of the RD column. Comparison between A36 (orange) and CAT400 (green). Results for pure MeOH feed (top) and crude MeOH feed (bottom) with 50 mol.-% H_2O and 50 mol.-% MeOH. $N_{rect,\ upper}$ = 10, $N_{rect,\ lower}$ = 14, $N_{reactive}$ = 25. N_{Feed} = 10 in case of pure MeOH feed for both A36 and CAT400. In case of crude MeOH feed N_{Feed} = 35 (A36) or N_{Feed} = 25 (CAT400).

Comparing the two catalysts for pure MeOH feed, a clearly lower reboiler duty using CAT400 can be identified throughout the $WHSV_{RD}$ range. At $WHSV_{RD}$=0.4 and $WHSV_{RD}$=1.4 the reboiler duty is reduced by 63 % and 81 %, respectively when using CAT400 instead of A36. This strong reduction is possible through the significantly higher reaction rate achievable due to the 30 °C higher operating temperature of CAT400 and the strong sensitivity of the reboiler duty to the operating temperature as discussed in the sensitivity study. Similarly, for a specific reboiler duty of 750 kWh t_{DME}^{-1}, 74 % less catalyst mass and consequently a 74 % smaller

reactive section is required for the full conversion of the same amount of MeOH. The column pressure is in the range of 13.4-15 bar for CAT400 and 6.6-8.0 for A36, depending on the $WHSV_{RD}$. This presents a disadvantage of CAT400 and implies another conflict of objectives that can only be answered in a techno-economic evaluation: While the increased temperature stability of CAT400 allows a higher reaction rate and thus a smaller column, the wall thickness of the column would need to be increased to account for the higher operating pressure.

Regarding a crude MeOH feed, analogous conclusions can be drawn with CAT400 allowing a reduction of the reboiler duty by 68 % and 66 % at a $WHSV_{RD}$ of 0.8 and 0.4, respectively. Compared to pure MeOH feed, the reboiler duty is roughly twice as high when using a crude MeOH feed for both catalysts. While this presents a significant increase in energy demand, it needs to be evaluated in view of the energy demand saved by omitting the crude MeOH distillation. For the purification of a CO_2-based crude MeOH, a specific energy demand of Q_{MeOH}=391.4 kWh t_{MeOH}^{-1} has been reported by Nyari et al. [162] corresponding to 544.6 kWh t_{DME}^{-1} considering the stoichiometry of the DME synthesis. The dashed line in

Figure 3-11 b) shows the resulting energy demand when adding the energy demand for the crude MeOH distillation column to the reboiler duty of the RD column operated with pure MeOH feed. The curves of the energy demand show that for CAT400 below a $WHSV_{RD}$ of 0.7 h^{-1} feeding the crude MeOH directly to the RD column requires less energy than purifying the crude MeOH in a dedicated distillation column and then feeding the pure MeOH to the RD column. Above $WHSV_{RD}$=0.7 h^{-1}, using crude MeOH for the RD feed is less energy efficient. For A36, using a dedicated crude MeOH distillation column presents the more efficient process configuration throughout the entire examined $WHSV_{RD}$ range. However, it needs to be emphasized that regardless of the energy demand, feeding crude MeOH to the RD also has the benefit of reducing the investment cost of the plant, since a whole distillation column can be omitted. In order to entirely evaluate these two process options, further investigations by rigorous process simulation including techno-economic considerations are required.

3.5 Conclusion and Outlook

DME is witnessing an increasing interest as a PtX product due to its outstanding characteristics as LPG alternative and as an environmentally benign global hydrogen carrier. For DME production, reactive distillation presents a promising process intensification technique, which reduces both the energy demand and the investment cost of the process. In the present work, a pilot-scale pressure distillation column was equipped with A36 to demonstrate the technical feasibility of the reactive distillation process under industrially relevant conditions. A total of 18

experiments were conducted in which the pressure, reflux ratio and feed mass flow were varied. It was observed that various feed flows can be converted with the identical distillate purity by adjusting the reflux ratio. However, this leads to an increased specific energy demand of the column reboiler, since the reflux ratio needs to be increased to flatten the temperature profile in the reactive section. Furthermore, the effect of using crude MeOH feed instead of pure MeOH was examined experimentally. Hereby, a significant increase in the reboiler duty was observed for crude methanol operation. This was due to the fact that the reflux ratio needs to be increased considerably to maintain a high reaction rate, despite the high concentration of the inhibiting water in the reactive section. Based on continuous column profiles obtained by coupling the experimental data with VLE modelling, the different kinetic models could be applied at the reactive distillation process conditions. Hereby it was validated that the model proposed by Semmel et al. [149] was the only model, among those presently discussed in the literature for this system, that is capable of predicting the measured amount of DME in the distillate stream. A simulation of the complete DME RD process was done by implementing this kinetic model in combination with an experimentally validated thermodynamic phase equilibrium model into Aspen Plus.

Using this validated process model, the design parameters were evaluated with respect to their influence on the reboiler duty. It was found that the kinetic parameters are the key influencing factors for reducing the energy demand of the process. This can be achieved either by increasing the amount of catalyst, using more active catalyst, or by raising the operating temperature. Furthermore, it was concluded that the reboiler duty is not sensitive to the number of stages. The influence of feeding crude MeOH to the RD was rigorously examined by process simulation complementary to the experimental validation. It was shown that with increasing feed water fraction, the reboiler duty increases and the optimal feed stage shifts towards lower reactive stages. The experimental trend of a reduced energy demand with decreasing $WHSV_{RD}$ could be verified by the simulations for the examined catalysts A36 and CAT400 as well as with pure and crude MeOH. CAT400, which was evaluated by simulation only, shows a significantly higher performance, in general, which leads to a potential reduction in energy demand by up to 81 % compared to using the same mass of A36 catalyst. This effect is primarily attributed to the higher thermal stability of CAT400, which allows for higher temperature operation and consequently higher reaction rates in the reactive section. This should be further investigated in experiments and validated. When using crude MeOH (50 mol.-% H_2O) instead of pure MeOH, the DME purity can be maintained, but the energy demand of the RD process roughly doubles. This could be relevant in integrated PtX plants where MeOH and DME production from renewable feedstock are coupled. Also, the direct use

of crude MeOH in the RD column, instead of using a dedicated MeOH column, saves energy. Thus, the overall energy demand of DME production, starting from crude MeOH, can be lowered. The amount of energy savings depends on the process design and is a matter of current evaluation using a complete process flow sheet-based, techno-economic analysis which considers an expanded system boundary. Only then can a quantitative comparison between A36 and CAT400 be drawn, and a profound statement on whether the omission of the dedicated crude MeOH distillation column is beneficial can be made. Moreover, the process concept of RD can be developed further, e.g., by interconnection with a separate fixed-bed reactor in order to reduce the column size and thus the overall plant cost. The optimization, evaluation and comparison of these process concepts using state-of-the-art techno-economic evaluations are a matter of current research in our group. The findings there will be addressed in future publications. With the experimentally validated process model developed in this work, a scientifically profound foundation has been developed for the industrial design and engineering of RD processes for large scale DME production.

4 Optimized design and techno-economic analysis of novel DME production processes

Declaration of contributions:

Malte Gierse conceptualized the work, developed the process simulation, developed the process concepts, developed the optimization methodology, performed parts of the simulations, processed, and organized the data, analysed the results, and wrote the manuscript.

Maximilian Kerschbaum supported in performing the simulations and developing the optimization methodology, contributed to the discussion, and reviewed the manuscript.

Benedikt Steinbach supported in developing the process simulation, supported in developing the process concepts, contributed to the discussion, and reviewed the manuscript.

Jörg Sauer supervised the work, contributed to the discussion, and reviewed the manuscript.

Ouda Salem conceptualized and supervised the work, contributed to the discussion, and reviewed the manuscript.

Chapter redrafted after the following main publication:

Semmel, M.; Kerschbaum, M.; Steinbach, B.; Sauer, J.; Salem, O. (2023): Optimized design and techno-economic analysis of novel DME production processes. In *Reaction Chemistry & Engineering*. DOI: 10.1039/D3RE00333G.

Abstract

The shift from gas to liquid phase DME synthesis enables intensified process concept towards efficient large scale DME production. In this work, four process concepts based on the liquid phase DME synthesis were proposed and optimized. A comprehensive economic model was applied with the objective of minimizing the total production cost. All concepts were evaluated applying our previously validated reaction kinetics for commercial ion exchange resin selected catalysts. Furthermore, every process concept was studied with pure MeOH feed and water-rich (crude) MeOH feedstock. The conventional gas-phase DME production process was simulated and evaluated using the same technical and economic parameters to serve as a benchmark. Using chlorinated high temperature stable IER catalyst led to significant cost reduction in all the considered concepts. This was due to the higher reaction rate enabled by the higher operating temperature of this catalyst. In integrated process concept with H_2 and CO_2 as sustainable feedstock, it was shown that the reactive distillation process shows 27 % lower production cost, when the crude methanol is directly fed to the DME process instead of being purified in a dedicated crude methanol distillation column. A further techno-economic optimization can be achieved when complementing the reactive distillation column with an additional reactor. Overall, the process concept of a reactive distillation column with side reactor presents the most promising process concept, enabling 39 % lower production cost than the conventional gas-phase process. By heat integration with a CO_2-based MeOH plant, a DME production technology with no external heat demand and net conversion cost of 54.4 € t_{DME}^{-1} is possible.

4.1 Process overview and system boundaries

In total, 5 process concepts were evaluated in this work as summarized in Figure 4-1. Process P0 presents the conventional gas-phase DME process, consisting of a feed evaporator, a gas phase reactor converting MeOH via dehydration to DME and H_2O, and two distillation columns with MeOH recycle. In comparison, process P1 also consists of a reactor-separation-recycle configuration. However, the reactor is operated in liquid phase and consequently no evaporation step is required. Process P2 is the intensified process alternative based on a stand-alone reactive distillation column (RDC).

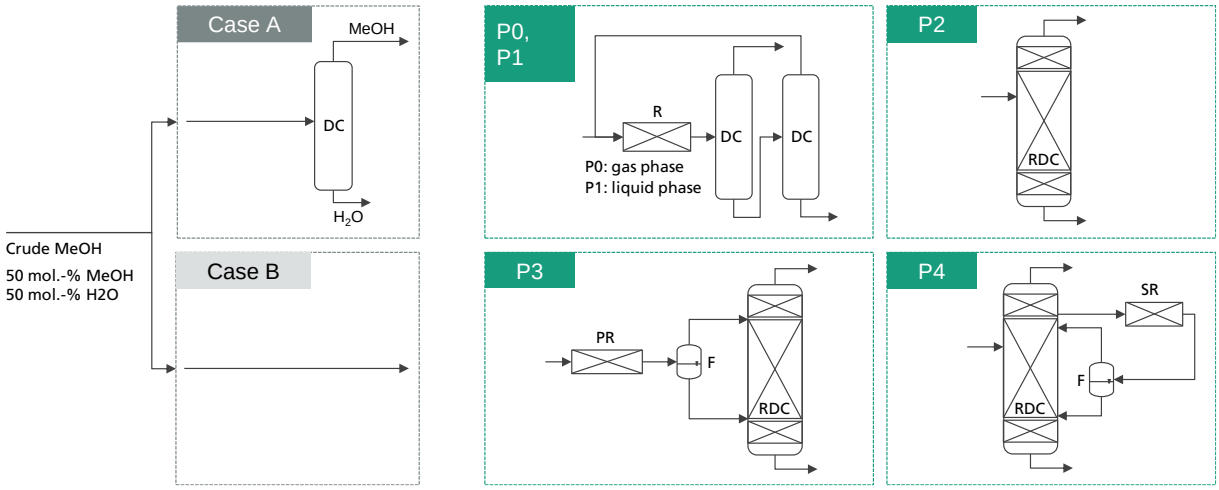

Figure 4-1: Simplified process flowsheets of the examined process concepts. P1-P4 are studied for the case of integrating a dedicated crude MeOH distillation column (case A) and for the case of feeding crude MeOH directly into the respective DME process (case B). The conventional process P0 is only analysed including the crude MeOH distillation column.

While the advantages of this process were already discussed, the RDC entails particularly two challenges: On the one hand, the RDC exhibits a system inherent temperature profile across the reactive section. This prevents conducting the reaction at the optimal temperature level in the entire reactive section, thus demanding a large amount of catalyst in the RDC. On the other hand, the insertion of catalyst into a distillation column requires relatively expensive column internals such as catalytic packings. These two challenges can potentially be overcome by the integration of a fixed-bed reactor into the process, in which a partial reaction conversion can be achieved. While this additional reactor is limited by the thermodynamic equilibrium, it allows the reaction to be carried out isothermally at the optimal reaction temperature and without the need for expensive internals. Two possible allocations of this strategy are process P3, complementing the RDC with a pre-reactor (PR) and process P4 adding a side-reactor (SR)

to the RDC. In both processes, the reactor product is forwarded to a flash in order to obtain a DME-rich phase and a water-rich phase. Both streams are fed to the RDC on separate stages.

The reference feedstock for the process is pure methanol. For comparison, crude MeOH feed is considered, consisting of 50 mol.-% water and 50 mol.-% MeOH at a temperature of 25 °C. The composition was chosen following Nyari et al. [162] and presents a typical composition for a CO_2-based MeOH synthesis process. For all novel process concepts, two cases are distinguished: In the first case, water is removed from the crude MeOH by a dedicated crude MeOH distillation (CMD) step and pure MeOH is fed to the DME process. In the second case, the water containing crude MeOH is fed directly to the respective DME process, thus saving the cost for the dedicated CMD column. For the conventional process, the crude MeOH is always purified. Moreover, all process concepts are examined for two IER catalysts:

1. The oversulfonated IER A36. Max. operating temperature: 130 °C.
2. The chlorinated IER CAT400. Max. operating temperature: 160 °C.

The maximum operating temperatures of the catalysts considered in this work is below the manufacturer's specification to avoid catalyst deactivation and increase the lifetime of the catalyst.

In the processes containing a liquid phase reactor (P1, P3, P4) the reactor is operated at a reaction pressure of 47 bar (A36) and 76 bar (CAT400).

4.2 Methods

Process design together with energy- and mass balances were performed by process simulation using Aspen Plus V12.1. Using all relevant technical and sizing data from the process simulation, an economic evaluation of the process was conducted using a literature based factorial economic model based on the model by Albrecht et al. [163] which was implemented in Microsoft Excel and is described later. The converged material and energy balances were extracted in the Excel sheet to derive capital expenditures (CAPEX), operational expenditures (OPEX) and total production cost.

4.2.1 Process optimization

The reactive distillation process for DME synthesis exhibits an inherent target conflict between reboiler duty and column size. Consequently, an economically reasonable process design is only possible by a techno-economic analysis of the process. In this work, each process concept is optimized by minimizing the resulting net conversion cost (NCC). While the process concepts

P0 and P2 have been investigated in literature, P1, P3 and P4 are novel. Consequently, no empirical values regarding the process design variables are available. For this reason, in this work an iterative two-step process design is conducted as illustrated in Figure 4-2.

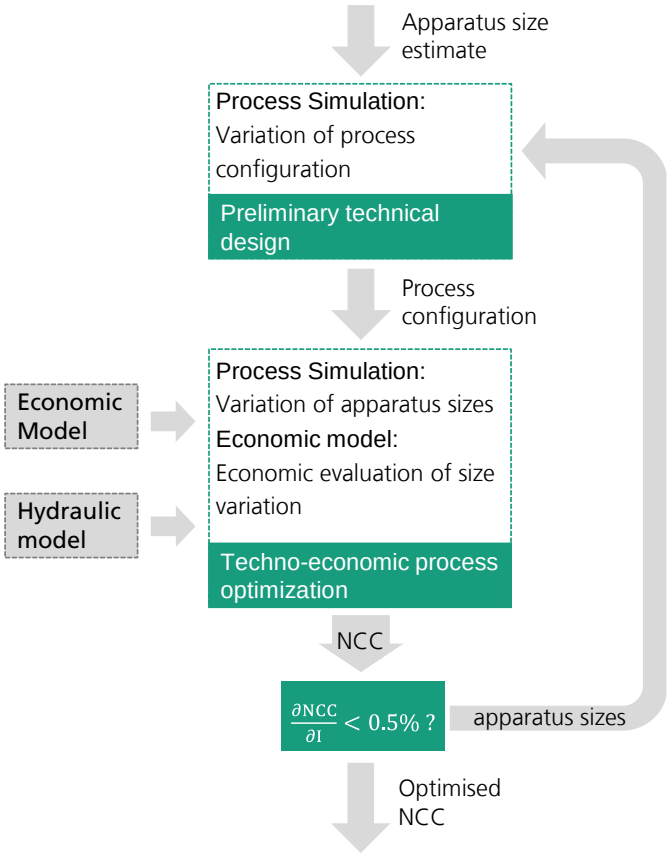

Figure 4-2: Methodology of total cost optimized process design of each process.

In a first step, a preliminary technical design study of the process is conducted. Hereby, an initial estimate must be provided for the apparatus sizes (catalyst mass in the RDC and/or reactor size) and the main technical design parameters (e.g., feed stages, withdrawal stage) excluding sizing parameters are then varied by means of a sensitivity study. The varied parameters in each process are shown in Table 4-1. The case with the minimum energy demand of the process is then selected as pre-optimized process configuration. For the processes P0 and P1, the feed stages to the distillation columns were adopted from Bildea et al. [124] and consequently no preliminary technical design study was required.

The second step is the techno-economic process optimization where the optimal apparatus sizes for the current process configuration are identified. A sensitivity study is conducted, varying the size of the RDC and/or reactor. In case of P4, also the mole flow of the side stream

is varied as it has a significant influence on the sizing of the SR. Table 4-1 summarizes the sizing parameters varied in the techno-economic process optimization. For every simulated case, the NCC are calculated based on the presented economic model. The case resulting in the minimal NCC presents the optimized process sizing for the current process configuration.

Since the sizing of the apparatuses influences the process design, the optimal process configuration obtained in the preliminary technical design may change under different apparatus sizes. Consequently, an iterative methodology was applied and a minimum of two iterations was conducted for each process. When the NCC between two iterations reduced by less than 0.5 %, the procedure was finished.

The size variation of the PR/SR was performed by varying only the length of the reactor. The reactor diameter was kept constant to allow an effective heat transfer and maintain isothermal conditions. The size of the RDC was varied in the simulation by modifying the amount of catalyst on each stage. For every case, the column diameter is calculated based on a beforehand derived hydraulic regression function. In practice, a reduced amount of catalyst would also lead to a reduced height of the reactive section and thus a reduced number of theoretical stages. However, as shown in a previous publication, this effect can be neglected, since the number of theoretical stages in the reactive section has no significant influence on the reboiler duty of the RDC.

Table 4-1: Overview over all parameters varied in the preliminary design and the techno economic optimization in each process.

Process	Preliminary technical design	Techno economic optimization
P0	-	$m_{Cat,Reactor}$
P1	-	$m_{Cat,Reactor}$
P2	N_{Feed}	$m_{Cat,RDC}$
P3	$N_{Feed,DME\text{-}rich}$ $N_{Feed,H2O\text{-}rich}$	$m_{Cat,RDC}$ $m_{Cat,PR}$
P4	N_{Feed} N_{WD} $\dot{n}_{Side}$ $N_{RCY,DME\text{-}rich}$ $N_{RCY,H2O\text{-}rich}$	$m_{Cat,RDC}$ $m_{Cat,SR}$ $\dot{n}_{Side}$

4.2.2 Process flowsheet simulation

Steady-state process simulations are performed using the equation-oriented solution algorithm in Aspen Plus, since the sequential-modular approach was not able to converge the complex flowsheets with numerous design specifications. The thermodynamic data in the simulation platform are implemented using the Peng-Robinson EOS with Wong-Sandler mixing rules and

the activity coefficient according to the UNIFAC-PSRK model, using the parameters by Ye et al. [158]. The pressure drop in all unit operations was neglected.

Heat exchangers

All heat exchangers are designed as counterflow shell and tube heat exchangers with a minimum temperature difference of 10 K [164]. Cooling water was assumed to be available at 15 °C and a maximum temperature increase of the cooling water by 5 K was considered [163]. The heat transition coefficient used in the heat exchangers can be found in the supplementary material SI3.5.

Pumps

All pumps are designed as centrifugal pumps with an assumed isentropic efficiency of 80 % [165].

Liquid phase reactor

The liquid phase reactors in the processes P1, P2 and P4 are designed as isothermal fixed bed reactors. While this design is more expensive than an adiabatic design, it allows an operation at the highest possible reaction rate while not exceeding the maximum operating temperature of the catalyst. Consequently, the reactor is designed as a shell and tube heat exchanger and the catalyst is assumed to be employed inside the tubes with a tube diameter of 0.08 m. The length and number of tubes were varied according to the identified catalyst mass needed for the desired conversion. For process simulation, the plug flow reactor (PFR) model of Aspen Plus is used. The liquid phase reaction kinetics for the two IER catalysts A36 and CAT400 proposed by Semmel et al. [149] were implemented by a Fortran subroutine. The rate equation and the corresponding parameters used for both catalysts are shown in the supplementary material SI3.3. The bulk density of the MeOH-swollen IER catalyst of 363 kg m^{-3} was experimentally determined.

Gas phase reactor

The gas phase reactor of the conventional process P0 is designed as an adiabatic fixed-bed reactor with an inner diameter of 0.5 m. It is modelled as PFR using the kinetics by Bercic et al. [166]. This kinetic expression was fitted for industrial-sized 3 mm particles of γ-Al_2O_3. The catalyst bulk density is 882 kg m^{-3} [166]. It should be noted that there was a correction of the

rate equation of the apparent kinetics in the original source very recently [167]. The rate equation and the corresponding parameters are shown in the supplementary material SI3.4. Older publications using the uncorrected version of the kinetic model consequently obtained significant deviations in reaction rate.

Reactive distillation column

The RDC is simulated using an equilibrium-based separation approach based on the RADFRAC model. On the catalyst containing reactive stages in the middle of the column, the reaction is modelled using the kinetics by Semmel et al. [149] implemented by a Fortran subroutine. The top and bottom section of the column do not contain catalyst and are modelled as rectifying stages only. The upper rectifying section includes 10 theoretical stages, the lower rectifying section includes 15 theoretical stages. The reactive section was implemented with 40 theoretical stages.

The operating pressure of the RDC is varied by a design specification so that the maximum temperature in the reactive section is equal to the maximum operating temperature of the used catalyst. A second design specification modifies the RR so that the DME purity equals 99.9 mol.-% under full MeOH conversion. Details regarding the RDC modelling and the thermodynamic properties calculation can be found in Semmel et al. [168]

The $WHSV_{RD}$ of the RDC is defined as follows:

$$WHSV_{RD} = \frac{\dot{m}_{Feed,MeOH}}{m_{catalyst,RDC}} \tag{45}$$

The catalyst is assumed to be introduced into the column using catalytic packing internals such as KATAPAK®. Catalytic packing internals are available with different distribution between catalyst bags and corrugated wire gauze sheets. In a previous study, it was shown that DME RD is a kinetically limited process and consequently, at a constant catalyst mass, the number of stages in the reactive section has a negligible influence on the process [168]. As a result, a catalytic packing design with maximum catalyst capacity should be employed for DME synthesis. The catalyst volume fraction of this packing type χ_{cp} (volume of catalyst bulk divided by packing volume) at industrial scale is typically 0.55 according to Hoffmann et al. [169]. Consequently, the volume of the reactive section can be calculated from the required catalyst mass according to the following equation:

$$V_{reactive\ section} = \frac{m_{cat}}{\rho_{cat,bulk} \cdot \chi_{cp}} \tag{46}$$

The rectifying sections are equipped with conventional structured packing (Mellapak) with a HETP of 0.5 [170].

Distillation columns

The distillation columns in all processes are modelled using the RADFRAC standard equilibrium-based model in Aspen Plus. Structured packings (Mellapak) with a HETP of 0.5 [170] were selected as column internals. The column diameter was calculated with the Aspen internal hydraulics tool.

4.2.3 Economic model

Economic evaluation of each process was done based on the factorial method approach. A detailed description of the methodology is described by Albrecht et al. [163]. According to AACE (Association for the Advancement of Cost Engineering) class three and four, an accuracy of ±30 % can be expected based on this methodology [171]. The year 2020 was chosen as base year. The used economic assumptions are summarized in Table 4-2.

Table 4-2: Economic parameters and assumptions.

Parameter	Unit	Value
Plant capacity	t_{DME} y^{-1}	100,600
Plant availability	h y^{-1}	8,000
Location	-	Germany
Base year	-	2020
Project lifetime t_{op}	y	20
Interest rate I	%	5 [164]
Working capital share W	-	0.1 [163]
Exchange rate	$€_{2020}$ $\$_{2020}^{-1}$	0.876 [172]
Labour cost	€ h^{-1}	41.0 [173]

The overall production costs are composed of the CAPEX and OPEX of the plant.

CAPEX

CAPEX is calculated as fixed capital investment (FCI) based on the equipment cost EC_i of the main process equipment and Lang factors F_j. Annualized capital cost (ACC) is then derived from FCI using the interest rate I, working capital share W and the plant operation time t_{op} according to equation (47) and (48). The Lang factors are summarized in the supplementary material SI3.5.

$$FCI = (1 + F_{Contractor} + F_{Contingency}) \cdot \left(1 + \sum_{j} F_{dir,j} + \sum_{k} F_{ind,k}\right) \cdot \sum_{i} EC_i \quad (47)$$

$$ACC = FCI \cdot \left(\frac{\mathrm{I} \cdot (1+\mathrm{I})^n}{(1+\mathrm{I})^n - 1} + \frac{W}{1-\mathrm{W}} \cdot \mathrm{I} \cdot \mathrm{t_{op}}\right) \quad (48)$$

The equipment cost are calculated by regressed cost functions based on the published cost data by Peters et al. [174]. Each cost function is scaled with all relevant sizing parameters of the respective apparatus to account for the economy of scale. Additional costs due to pressure stability are accounted for by a dedicated pressure correction function. All cost functions and corresponding pressure correction functions including their range of validity can be found in the supplementary material 0. To account for temporal cost variation, the Chemical Engineering Plant Cost Index CEPCI is used for scaling the cost data from the reference year to the desired year.

OPEX

OPEX is divided into direct OPEX ($OPEX_{dir}$) and indirect OPEX ($OPEX_{ind}$). $OPEX_{dir}$ consists of the cost for steam, cooling water and electricity according to equation (49). Furthermore, the catalyst cost is considered as $OPEX_{dir}$ due to the regular replacement catalysts. In this study the lifetime of IER was assumed as 1 year and that of γ-Al_2O_3 as 3 years [175].

$$OPEX_{dir} = \sum_{\mathrm{j}=1} E_{power,\mathrm{j}} \cdot c_{power,\mathrm{j}} + \sum_{j=\mathrm{k}} \dot{m}_{steam,\mathrm{k}} \cdot c_{steam,\mathrm{k}} + \dot{m}_{cool} \cdot c_{cool} + \frac{m_{cat} \cdot c_{cat}}{l_{cat}} \quad (49)$$

In the scope of this work, OPEX were calculated irrespective of the feedstock cost. Since no purges are present in all DME processes, the feedstock demand is identical for every process and consequently, the addition of a constant feedstock cost to all processes would only “dilute” the influence of the DME process. When calculating the net production cost (NPC), feedstock cost can be included afterwards, as shown later. The required amount of steam is calculated based on the heat demand according to the process simulation. Steam costs are distinguished between low and medium pressure steam. Details and cost of all used utilities are presented in Table 4-3.

Table 4-3: Parameters and cost of the used operating supplies.

Operating supplies	Cost
Low pressure steam, 4 bar	22.8 € t^{-1}
Medium pressure steam, 20 bar	23.1 € t^{-1}
Cooling water, 15 °C	0.0035 € m^{-3}
Electricity	55.72 € MWh^{-1}
A36 catalyst[+]	7.5 € kg^{-1}
CAT400 catalyst[*]	18 € kg^{-1}

[+]Cost assumed to be identical to comparable oversulfonated IER Amberlyst 35[26]

*Cost assumed to be identical to comparable the chlorinated IER Amberlyst 45[26]

$OPEX_{ind}$ contains all other additional expenses for plant operation excluding operating labour and is calculated using the Lang factors shown in the supplementary material SI3.5. Consequently, $OPEX_{ind}$ scale partially with the FCI.

Operating labour

Operating labour was estimated using the correlation for fluid processes by Peters et al. [174] shown in the supplementary material SI3.5.

NCC

NCC, representing the total cost for producing DME from crude MeOH are calculated from the ACC, total OPEX and the annual cost for operating labour according to:

$$NCC = \frac{ACC + OPEX_{ind} + OPEX_{dir} + h_{labour} \cdot C_{labour}}{\dot{m}_{DME}} \quad (50)$$

Operating labour is calculated based on the specific labour cost C_{labour} and the man-hours h_{labour} estimated by the correlation from Peters et al. [174], taking the number of processing steps into account.

Note that this is the same equation as typically used for the calculation of NPC. However, since crude MeOH feedstock cost are not accounted for in the $OPEX_{dir}$, the resulting cost are conversion cost, comprising the cost for upgrading crude MeOH to DME, rather than NPC including the feedstock cost. However, the NCC can be directly correlated to give the total NPC based on the specific crude MeOH feedstock cost $C_{Crude\ MeOH}$ and the mass ratio between feedstock and product according to the stoichiometry:

$$NPC = NCC_{DME} + \frac{\dot{m}_{\mathrm{Crude\ MeOH}}}{\dot{m}_{\mathrm{DME}}} \cdot C_{\mathrm{Crude\ MeOH}} \quad (51)$$

If crude MeOH costs are not available, the NPC can also be calculated based on the CO_2 and H_2 feedstock cost, when additionally considering the NCC of the MeOH (NCC_{MeOH}) plant:

$$NPC = NCC_{DME} + \frac{\dot{m}_{\mathrm{CO_2}}}{\dot{m}_{\mathrm{DME}}} \cdot C_{\mathrm{CO_2}} + \frac{\dot{m}_{\mathrm{H_2}}}{\dot{m}_{\mathrm{DME}}} \cdot C_{\mathrm{H_2}} + NCC_{MeOH} \quad (52)$$

Whereas the NCC_{MeOH} are defined analogous to equation (50).

4.3 Results and Discussion

In the following section, first, the final configuration and KPI of the optimized processes P0-P4 are presented and discussed. Then, the processes are compared at their respective optimal configuration and a systematic comparison between the two feed cases is done for every concept, meaning that the cost for the CMD is added to the DME processes if operated with pure MeOH feed. After the DME process with the lowest NCC is determined, a sensitivity study for this process is shown and the process is heat-integrated with a CO_2-based MeOH plant. Furthermore, NPC are given in dependence of crude MeOH feedstock price.

4.3.1 Optimization of each process

4.3.1.1 P0: Conventional process

The conventional gas-phase process P0 was optimized with regard to the ideal catalyst mass. Figure 4-3 illustrates NCC of converting pure MeOH feedstock into purified DME. The costs are shown in dependence of the catalyst mass in the gas-phase reactor and are broken down into ACC, $OPEX_{ind}$, and $OPEX_{dir}$.

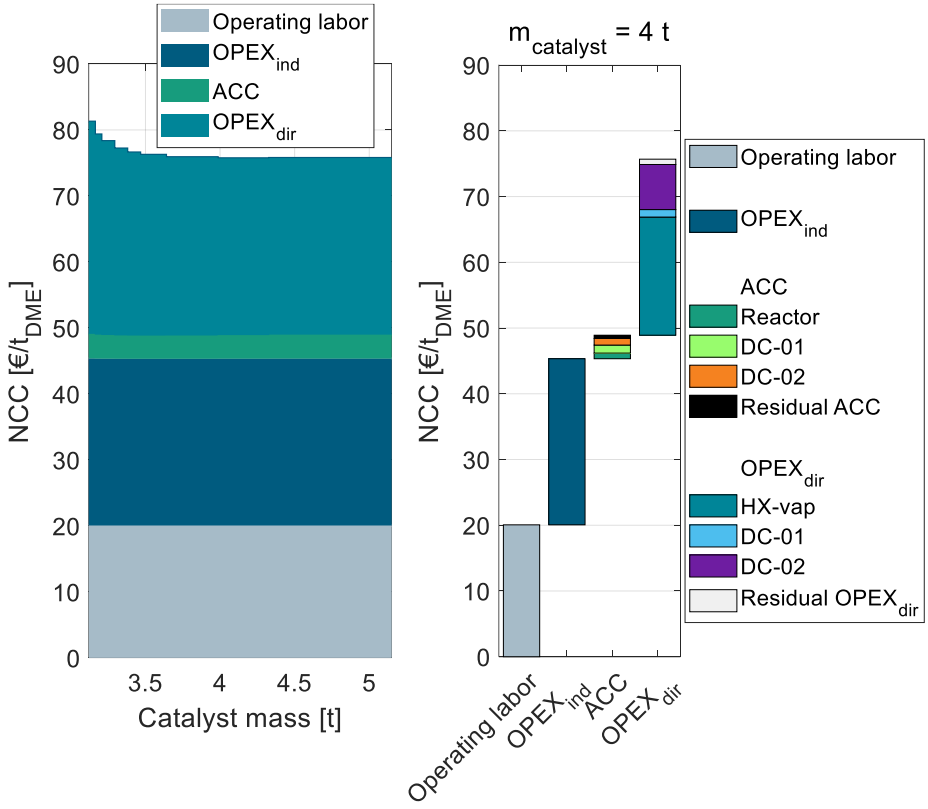

Figure 4-3: NCC of the conventional process P0 in dependence of the catalyst mass in the conventional gas-phase reactor broken down into ACC, OPEXind, and OPEXdir.

The process P0 is dominated by indirect and direct OPEX, ACC only contribute a minor share to the NCC. For a small catalyst mass <4 t, $OPEX_{dir}$ decrease with increasing catalyst mass. This can be explained by the increasing MeOH conversion in the reactor and a smaller amount of unreacted MeOH that needs to be recycled and purified in DC-02. At a catalyst mass of 4 t the reactor approaches equilibrium and consequently the additional increase in catalyst mass has no beneficial influence on the $OPEX_{dir}$ but only lead to increased ACC. Correspondingly, the NCC reaches a minimum at 4 t. This value is significantly smaller than the catalyst mass reported by Bildea et al. [124] or Michailos et al. [175] since these publications are still based on the erroneous kinetic data from the original publication. The authors of the original publication recently published a correction [167] of the kinetic model, which was adopted in this work leading to significantly smaller reactor sizes than reported so far. Regarding the feed MeOH mass flow of 17.5 t h^{-1} for the DME production capacity of 100 kt a^{-1}, this corresponds to $WHSV_{RD}$=4.4 h^{-1}. A detailed cost breakdown at the optimal catalyst mass is given on the right side of Figure 4-3. ACC consist almost equally of the reactor, the two distillation columns and the residual apparatuses (pump and heat exchangers). $OPEX_{dir}$ is dominated by the steam

demand for the evaporator HX-vap and the reboiler of DC-02. Catalyst cost is included in the residual $OPEX_{dir}$ and is negligible.

The overall heat demand of the process is 761.8 kWh t_{DME}^{-1}, which is in accordance with the results of Michailos et al. [175] (904 kWh t_{DME}^{-1}) and Bildea et al. [124] (714 kWh t_{DME}^{-1}). The resulting NCC are 75.7 € t_{DME}^{-1}. Table 4-4 sums up the KPI of the process P0 with the optimized reactor size.

Table 4-4: KPI at optimized process configuration of the conventional process P0 for pure MeOH feed.

		Pure MeOH
Parameter	**Unit**	**γ-Al_2O_3**
$m_{Cat, Reactor}$	t	4.0
$X_{MeOH, Reactor}$	-	0.8
RR_{DC-01}	-	3.8
RR_{DC-02}	-	1.5
Q_{Heat}	kWh t_{DME}^{-1}	761.8
NCC	€ t_{DME}^{-1}	75.7

4.3.1.2 P1: Liquid-phase reactor

Table 4-5 shows the KPI of process P1 with the optimized reactor size for both catalysts and feedstock scenarios.

Table 4-5: KPI at optimized process configuration of process P1 for pure and crude MeOH feed and both catalysts.

		Pure MeOH		Crude MeOH	
Parameter	**Unit**	**A36**	**CAT400**	**A36**	**CAT400**
$m_{Cat, Reactor}$	t	18.0	8.8	24.1	16.2
$X_{MeOH, Reactor}$	-	0.45	0.88	0.16	0.56
RR_{DC-01}	-	2.0	0.5	10.1	1.7
RR_{DC-02}	-	1.1	1.7	1.1	1.3
Q_{Heat}	kWh t_{DME}^{-1}	1,393.4	257.9	5,913.8	1,005.0
NCC	€ t_{DME}^{-1}	135.0	66.9	346.9	116.7

For pure MeOH feed and A36, the cost-optimal configuration is a reactor with 18 t of catalyst, corresponding to a single-pass MeOH conversion of 45 %. Using CAT400 instead, a smaller reactor with 8.8 t allows a conversion of 88 % due to the significantly higher reaction rate enabled by the higher temperature stability of CAT400. Compared to the conventional gas-phase reaction, the liquid phase dehydration entails the advantage of a higher equilibrium conversion due to the lower temperatures ($X_{MeOH,Equil.}$=93 % @160 °C [149]). However, the slower reaction kinetics demands a higher catalyst mass (8.8 t CAT400 vs. 4 t γ-Al_2O_3).

The RR of DC-01 is significantly lower, as the higher conversion leads to a lower MeOH fraction and higher DME fraction, simplifying the separation. Due to the higher conversion with CAT400, less MeOH needs to be recycled, which reduces the mass flow in both columns. For this reason, the overall heat demand of the process Q_{Heat} with CAT400 is 81 % lower than with A36. NCC are 50 % lower.

For a crude MeOH feed, the same trend can be observed with CAT400 leading to less catalyst mass, yet a higher MeOH conversion and consequently a lower heat demand and NCC. Compared to using pure MeOH however, the cost-optimal reactor size is bigger and exhibits a smaller MeOH conversion since the reaction is inhibited by the high water concentration.

4.3.1.3 P2: Stand-alone RDC

The RDC without additional reactor (P2) was optimized regarding the ideal RDC size and the optimal feed stage. Table 4-6 shows the KPI of the final optimized configuration.

Table 4-6: KPI at optimized process configuration of process P2 for pure and crude MeOH feed and both catalysts.

		Pure MeOH		Crude MeOH	
Parameter	**Unit**	**A36**	**CAT400**	**A36**	**CAT400**
N_{Feed}	-	9	9	50	30
$m_{Cat, RDC}$	t	40.4	17.2	56.8	26.4
RR	-	7.6	5.2	12.8	8.3
Q_{Heat}	kWh t_{DME}^{-1}	897.4	569.1	1,515.3	913.6
NCC	€ t_{DME}^{-1}	95.2	69.8	134.3	91.0

To analyse this process in more detail, Figure 4-4 shows exemplarily for CAT400 and pure MeOH feed the NCC of the process P2 broken down into ACC, $OPEX_{ind}$ and $OPEX_{dir}$ and operating labour on the left side.

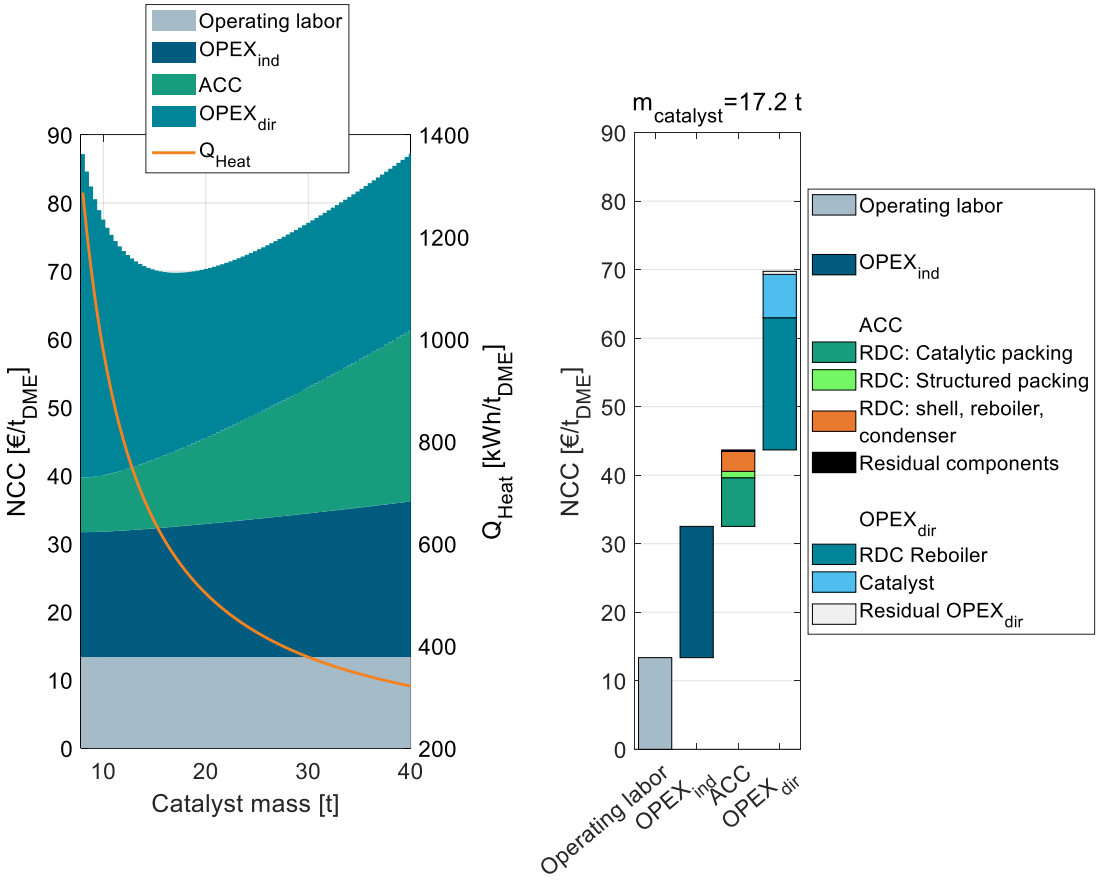

Figure 4-4: Heat demand and NCC of the RD process P2 with CAT400 and pure MeOH feed in dependence of the catalyst mass in the RDC broken down into ACC, $OPEX_{ind}$, and $OPEX_{dir}$ (left) as well as detailed cost breakdown at the cost optimum (right).

The figure illustrates the RDC-inherent target conflict between capital expenses and operating expenses: While a small RDC with little catalyst mass leads to low ACC, a high RR and consequently a high energy demand is required to achieve the desired full MeOH conversion in the RDC. Increasing the catalyst mass of the RDC increases the ACC, since the column size and the amount of catalytic packing increases but reduces the RR and $OPEX_{dir}$ so that an optimum catalyst mass of 17.2 t can be identified. The corresponding $WHSV_{RD}$ is 1.02 h^{-1}. The exact position of the minimum depends on all assumptions influencing the ACC or OPEX. While only one cost optimal RDC size exists, this optimum is rather “flat”. Consequently, the RDC size and the resulting energy demand of the process can be designed in a wide range without the NCC deviating significantly from the optimal configuration. Also, in case of temporally reduced feed availability, the plant can be operated at lower $WHSV_{RD}$ which will reduce the specific energy demand of the plant.

Compared to the conventional process P0, the RD process is characterized by higher ACC which can majorly be attributed to the higher required catalyst mass due to the significantly lower reaction temperature. $OPEX_{dir}$ are comparable for both processes: While the RD process P2 has lower steam cost due to a lower energy demand (569 kWh t_{DME}^{-1} vs. 762 kWh t_{DME}^{-1}), this benefit is compensated by the significantly higher catalyst cost to the higher catalyst mass and the lower assumed catalyst lifetime of IER compared to γ-Al_2O_3. The right side of Figure 4-4 shows the detailed cost breakdown at the optimum catalyst mass. The ACC are dominated by the RDC, particularly the cost of the catalytic packing internals and the cost for the RDC shell, reboiler and condenser. In contrast, the cost for the other process components (pump, heat exchangers) and the structured packing in the RDC are almost negligible. $OPEX_{dir}$ are dominated by the heat demand of the RDC reboiler, but the influence of catalyst cost is also significant.

In comparison with CAT400, the process P2 with A36 shows its optimum at a significantly higher catalyst mass of 40.8 t. Nevertheless, the required RR is higher than for CAT400, again underlying the great benefit of the higher reaction rate through higher temperature stability. As a consequence, CAT400 is able to reduce both the RDC size and the energy demand compared to A36.

For crude MeOH, the optimal feed stage moves down to the bottom of the reactive section, where the water-containing crude MeOH better fits the column profile. As another consequence of crude MeOH feed, the energy demand and the required catalyst mass is higher as the reaction kinetic is hampered by the higher water content of the feed and more water needs to be evaporated in the reboiler in total. Also, for crude MeOH CAT400 shows significant improvements compared to A36 regarding energy demand and NCC. Interestingly, even CAT400 with crude MeOH feed leads to lower NCC than A36 with pure MeOH feed.

4.3.1.4 P3: RDC with pre-reactor

Process P3 adds significant complexity compared to P2, as the reactor product from the PR performs flash separation and consequently 2 feed stages need to be optimized. Table 4-7 shows the optimized parameters and KPI. For both feeds and catalysts, the configuration is very similar with the feed stage of the DME-rich phase being in the upper rectifying section and that of the H_2O-rich phase in the lower rectifying section or the last stage of the reactive section (A36 with pure MeOH feed).

Table 4-7: KPI at optimized process configuration of process P3 for pure and crude MeOH feed and both catalysts.

		Pure MeOH		Crude MeOH	
Parameter	**Unit**	**A36**	**CAT400**	**A36**	**CAT400**
$N_{Feed,\ DME\text{-}rich}$	-	7	9	9	7
$N_{Feed,\ H2O\text{-}rich}$	-	50	56	56	54
$m_{Cat,\ PR}$	t	10.8	8.4	8.2	11.1
$X_{MeOH,\ PR}$	-	0.52	0.91	0.09	0.52
$m_{Cat,RDC}$	t	23.0	1.6	40.0	9.2
RR	-	5.7	0.8	13.1	6.2
Q_{Heat}	kWh t_{DME}^{-1}	755.5	238.0	1,529.5	783.2
NCC	€ t_{DME}^{-1}	88.9	52.4	129.5	85.5

Besides the two feed stages, the optimal size needs to be determined for PR and RDC. While a larger PR leads to increased cost for the reactor, the increased MeOH conversion allows the RDC to be smaller or operate at lower RR. Consequently, a target conflict between PR size and RDC size is present in the system.

Figure 4-5 illustrates this interplay between PR and RDC size. For each RDC size an optimal PR size can be identified. With increasing RDC size, the optimal PR size decreases, the best configuration globally is a PR with 10.8 t and an RDC with 23 t of catalyst of catalyst.

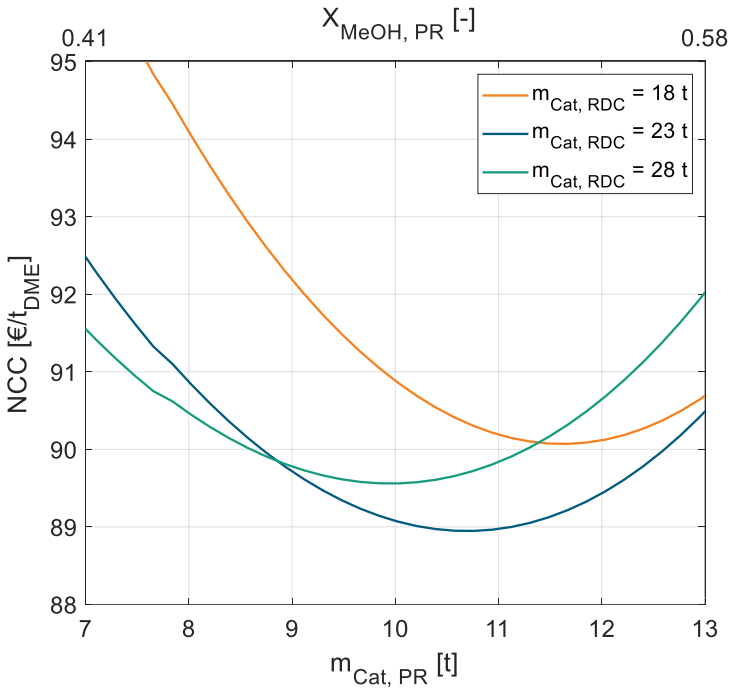

Figure 4-5: NCC of the process P3 in dependence of the catalyst mass in the liquid-phase PR for different RDC sizes. Exemplary for Pure MeOH Feed and A36.

Comparing the influence of catalyst and feed, similar trends can be observed as in the previous processes: The use of CAT400 leads to lower required catalyst mass in the RDC and PR, lower RR in the RDC and lower NCC of the process. Also, crude MeOH feed results in higher catalyst masses, higher RR and higher NCC.

Comparing the process P3 to P2 based on the KPI presented in Table 4-6 and Table 4-7, the benefit of the PR can be quantified: For pure MeOH feed, the NCC are reduced by 7 % (A36) and 25 % (CAT400), respectively. The heat demand is reduced even further by 16 % (A36) or 58 % (CAT400). Interestingly, despite adding a unit operation compared to the stand-alone RDC, the total catalyst mass in the optimal configuration is reduced, in case of CAT400 with pure MeOH feed even by 52 %. This can be explained by a more effective utilisation of the catalyst in the PR, since an isothermal operation is possible as opposed to the immanent RDC temperature profile. PR and RDC complement each other: At conversion significantly below the chemical equilibrium, the PR is beneficial as it delivers the ideal reaction temperature and is not significantly equilibrium inhibited. The cumbersome conversion of the residual MeOH in contrast is more effectively performed in the RDC, where the in-situ product removal from the chemical equilibrium allows a full conversion.

For crude MeOH feed, the benefit of the PR is significantly less pronounced with NCC only decreasing by 4 % (A36) and 6 % (CAT400). This shows a clear disadvantage of the PR concept with crude MeOH: the crude MeOH feed directly enters the PR, where the reaction is heavily inhibited by water and consequently the MeOH conversion is significantly lower compared to a pure MeOH feed.

4.3.1.5 P4: RDC with side-reactor

Table 4-8 shows the optimized process configurations of the process P4. Due to the large number of 7 optimization variables in this process, a graphical representation of the optimum is neglected.

Table 4-8: KPI at optimized process configuration of process P4 for pure and crude MeOH feed and both catalysts.

		Pure MeOH		Crude MeOH	
Parameter	**Unit**	**A36**	**CAT400**	**A36**	**CAT400**
N_{Feed}	-	7	11	56	15
N_{WD}	-	7	13	7	9
$N_{RCY,\ DME\text{-}rich}$		9	11	7	7
$N_{RCY,\ H2O\text{-}rich}$		58	56	56	56
$\dot{n}_{Side}$	kmol h^{-1}	375	675	250	525
$m_{Cat,\ SR}$	t	10.5	7.3	10.0	8.7
$X_{MeOH,\ SR}$	-	0.66	0.86	0.76	0.85
$m_{Cat,RDC}$	t	23.2	1.0	28.4	10.4
RR	-	5.5	1.5	12.9	5.5
Q_{Heat}	kWh t_{DME}^{-1}	726.5	317.2	1,555.4	715.6
NCC	€ t_{DME}^{-1}	87.7	54.2	123.5	79.8

For pure MeOH and both catalysts and crude MeOH with A36, the feed stage N_{Feed} is similar the stand-alone RD process P2. For crude MeOH and CAT400 however, a feed stage at the top of the reactive section proved to be more efficient than in the lower rectifying section. For both catalysts and feeds, the configuration of the withdrawal and recycle stages is almost identical. The withdrawal stage N_{WD} is located at the top or right above the reactive section where the MeOH concentration in the column is the highest. An exemplary column profile is given in the supplementary material SI3.9. The position of the recycle stages $N_{RCY,\ DME\text{-}rich}$ and $N_{RCY,\ H2O\text{-}rich}$ is almost identical to the feed stages $N_{Feed,\ DME\text{-}rich}$ and $N_{Feed,H2O\text{-}rich}$ in P3. For pure MeOH feed and both catalysts, also the sizes of SR and RDC are very similar to the sizes of RDC and PR obtained in P3. Consequently, also the RR, heat demand and the resulting NCC are comparable. The similarity between both processes can be explained, since in both processes (nearly) pure MeOH is fed to the reactor. While in P3, the pure MeOH is fed directly to the reactor, in P4 it enters the RDC first, and a MeOH-rich stream is withdrawn from the top of the reactive section. Thus, the PR in P3 and the SR in P4 operate under nearly identical conditions and therefore, the similar process configuration and performance of P3 and P4 can be explained.

For crude MeOH feed in contrast, the process configuration and performance of P3 and P4 differ from each other: For A36 a MeOH conversion of 76 % is achieved in the SR, while in the PR only 9 % conversion are reached in the optimal configuration. For CAT400, 85 % of the fed MeOH is converted in the SR and only 52 % in the PR. As mentioned before, the process performance of P3 suffers significantly from a crude MeOH feed, since the reaction in the PR is strongly inhibited by the water content of the feed. Contrarily, in process P4, the crude MeOH is first fed to the RDC, and a MeOH-enriched side stream is fed to the SR. This way, the water

inhibition in the SR is significantly reduced compared to the PR and consequently the process P4 performs better with a crude MeOH feed than P3. Precisely, in case of CAT400, P4 leads to 3 % higher NCC than P3 for pure MeOH feed, but to 7 % lower NCC than P3 for crude MeOH feed.

4.3.2 Process Comparison

In all process concepts P1-P4, the NCC are significantly higher when using crude MeOH (case B) instead of pure MeOH (case A) feedstock. However, to allow a fair comparison, the cost for the dedicated CMD must be accounted for in case pure MeOH is fed to the DME process. For this reason, the NCC_{CMD} of converting crude MeOH to pure MeOH with the CMD column were calculated using the same economic model as for the DME processes. The resulting NCC_{CMD} of 55.8 € t_{DME}^{-1} were added to all processes P1-P4 fed with pure MeOH. A detailed table with the KPI of the CMD is given in the supplementary material SI3.2. Figure 4-6 shows the results of all processes for both catalysts and both feed cases. The cost for the CMD is illustrated as grey bar. The DME processes operated with A36 are illustrated as light green (pure MeOH feed, case A) or dark green (crude MeOH feed, case B) bar and the processes operated with CAT400 are illustrated as light blue (pure MeOH feed, case A) or dark blue (crude MeOH feed, case B) bar. The cost of the conventional process P0 including the cost for the CMD is shown as dashed line.

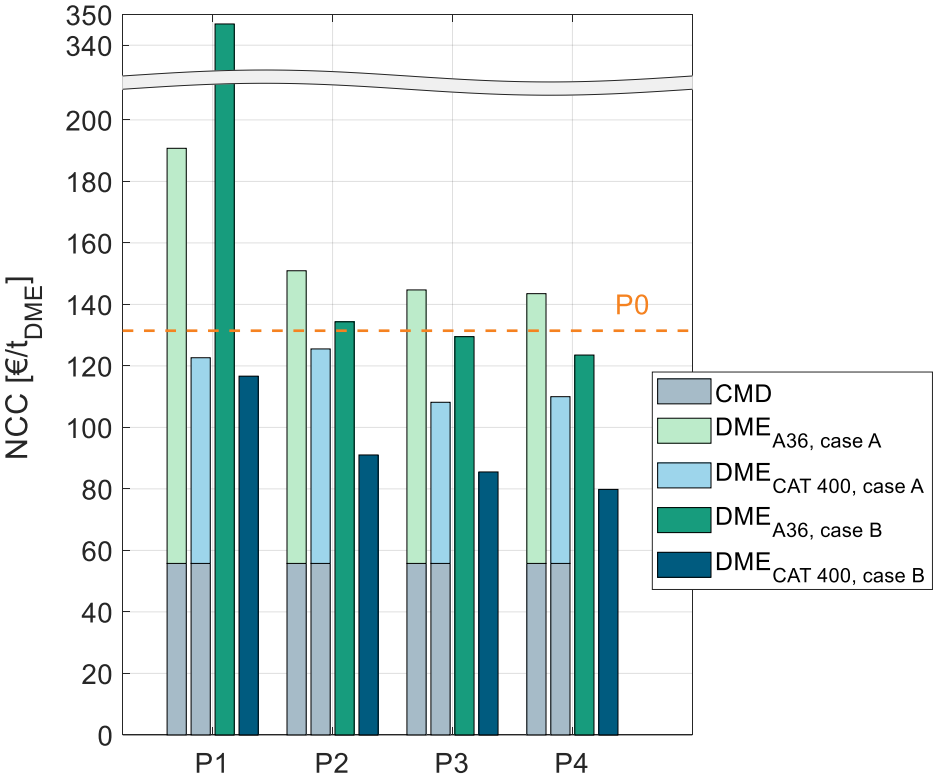

Figure 4-6: Overview of total NCC for all 4 DME processes with both catalysts for pure MeOH feed (case A) and crude MeOH feed (case B) including the cost for the CMD in case A. Comparison with the conventional process P0.

For all process concepts the use of CAT400 leads to significant cost reduction compared to A36. Consequently, the higher catalyst cost of CAT400 and the higher pressure demands on the process due to the higher operating temperature of CAT400 are clearly overcompensated by the increased reaction rate, resulting in lower apparatus sizes and – indirectly – lower energy demand.

The liquid phase reaction process P1 exhibits very high NCC when using A36, especially in case B the NCC are nearly 3 times higher than for the conventional process P0. Using the more active CAT400 instead, the process performs significantly better, outperforming the conventional process slightly. Remarkably, with CAT400 the process concept P1 performs also well with crude MeOH feed (case B) yielding slightly lower cost than in case A although the water containing crude MeOH is directly fed to the reactor without prior water removal.

The RD process P2 generally shows lower NCC than P1. For both catalysts, directly feeding crude MeOH is preferable to using a dedicated CMD column. For CAT400, this leads to a NCC reduction of 27 %. Compared to the conventional process, P2 with CAT400 and crude MeOH feed exhibits 31 % lower conversion costs.

Complementing the RDC with a PR or SR allows even lower conversion costs. The best process overall is the RDC with SR and direct crude MeOH feed to the RDC. In this case, the NCC can be reduced by 39 % compared to the conventional process. When pure MeOH feed is already available, process P3 with CAT400 presents the best process with a 31 % NCC reduction compared to the conventional process.

4.3.3 Sensitivity study

A techno-economic analysis is always based on a manifold of economic parameters and assumptions. To estimate the influence of some economic parameters on the overall NCC, a sensitivity study was conducted. This was done exemplarily for the best process P4 with CAT400 and crude MeOH feed. Hereby the optimal SR and RDC size were re-evaluated for every parameter variation instead of maintaining the original configuration that might be non-optimal for the varied parameters. E.g., in case of increased steam cost, the configuration would shift towards bigger SR and RDC to reduce the energy demand at the expense of higher CAPEX. The results of the sensitivity study are shown in Figure 4-7.

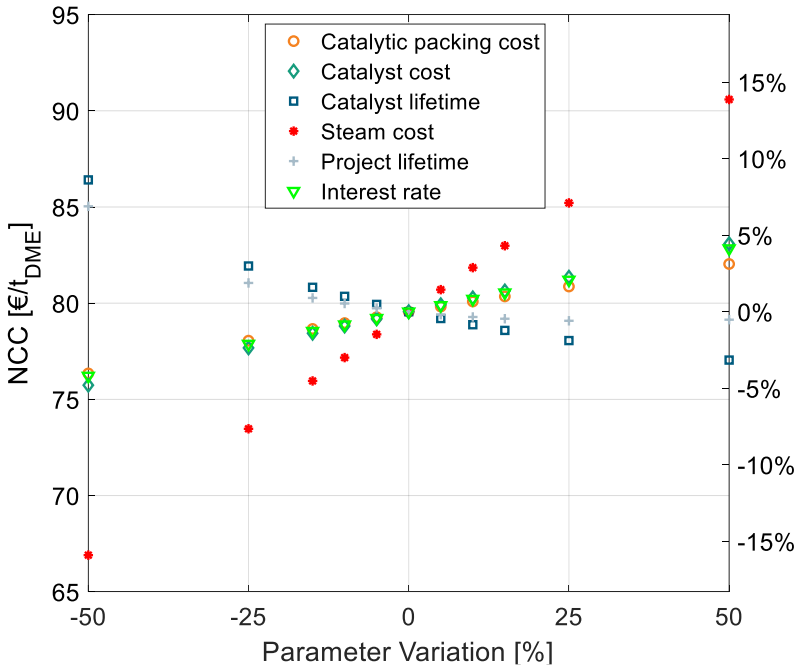

Figure 4-7: Sensitivity analysis of economic parameters on the NCC of the process P4 with CAT400 and crude MeOH feed (case B).

The cost of the catalytic packing, catalyst cost and catalyst lifetime have a significant, but comparatively small influence on the NCC. Same applies to the economic parameters, namely interest rate and project lifetime. Steam cost present the most sensitive parameter, since it

dominates the OPEX of the process, which present a high share of the NCC. Yet, a 50 % increase of steam cost increases the NCC by less than 15 %, thus underlying the significance of the values obtained in this work.

4.3.4 Process Integration

The comparison and optimization of the processes was conducted with crude MeOH at 25 °C as system input. No heat integration was performed to allow a systematic comparison independent of system specific boundary conditions. In practice however, a heat integration of the DME synthesis with the MeOH synthesis is a logical step since the exothermic heat of the MeOH reactor can be integrated into the DME process. Especially when crude MeOH is used as the feedstock for DME synthesis and the dedicated CMD column is omitted, significant amounts of heat are available from the MeOH synthesis. To examine the influence of heat integration, the best DME process presented in the previous chapter (P4, CAT400, case B) was heat integrated with MeOH synthesis. The process configuration and apparatus sizes of the DME process are the same as presented in Table 4-8. The MeOH plant was simulated in Aspen Plus according to Mantei et al. [164]. Key technical parameters of the MeOH process are shown in the supplementary material 0. The flowsheet of the integrated process is shown in Figure 4-8.

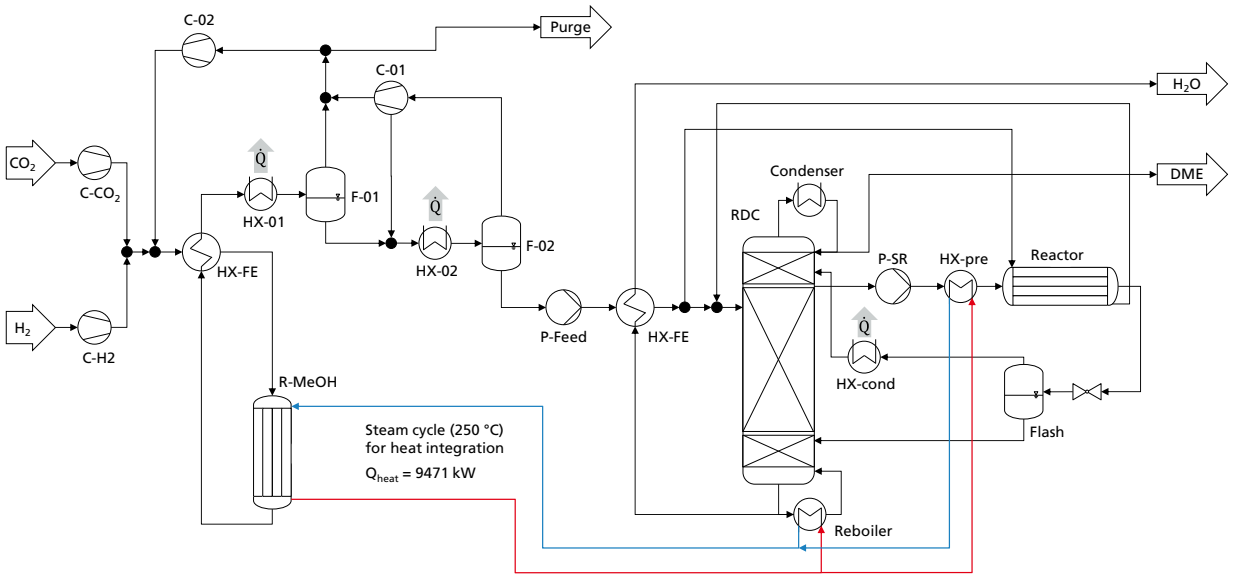

Figure 4-8: Flowsheet of the heat integrated MeOH and DME synthesis plant producing DME from CO_2 and H_2.

The simulated MeOH synthesis plant has an annual production capacity of 218,640 t crude MeOH, corresponding to 140,000 t of pure MeOH. The isotherm MeOH reactor operates at

250 °C and releases an exothermic heat of 9.47 MW, corresponding to 754 kWh t_{DME}^{-1}. The RDC reboiler operates at 190 °C, allowing the full integration of the MeOH exothermic heat into the DME process. As the MeOH reactor is a steam cooled tube and shell type reactor, the generated steam can directly be heat integrated with the reboiler of the RDC without the necessity of additional process equipment. The medium temperature heat released in the condensation of the MeOH synthesis reactor product (HX-01) does not need to be heat integrated and is consequently still available e.g., for a direct air capture process.

Figure 4-9 breaks down the heat demand of the DME process P4 considering this heat integration on the left side. The EC breakdown on the right part of Figure 4-9 shows that RDC and side reactor contribute almost equally to the overall EC. The residual components – namely heat-exchangers, pumps, and the flash separator – are almost negligible. The cost of the RDC is dominated by the catalytic packing rather than the cost for the column shell itself. This detail shows again the benefit of using high-temperature stable IER since the higher activity allows a smaller reactive section, which leads to proportionally decreasing cost for the catalytic packing. In contrast, the additional cost for the pressure stability of the column plays a less important role. Moreover, the large cost share of the catalytic packing shifts the focus to potential alternative methods of employing the catalyst in the RDC, such as catalyst bales or the placement on trays [152,176].

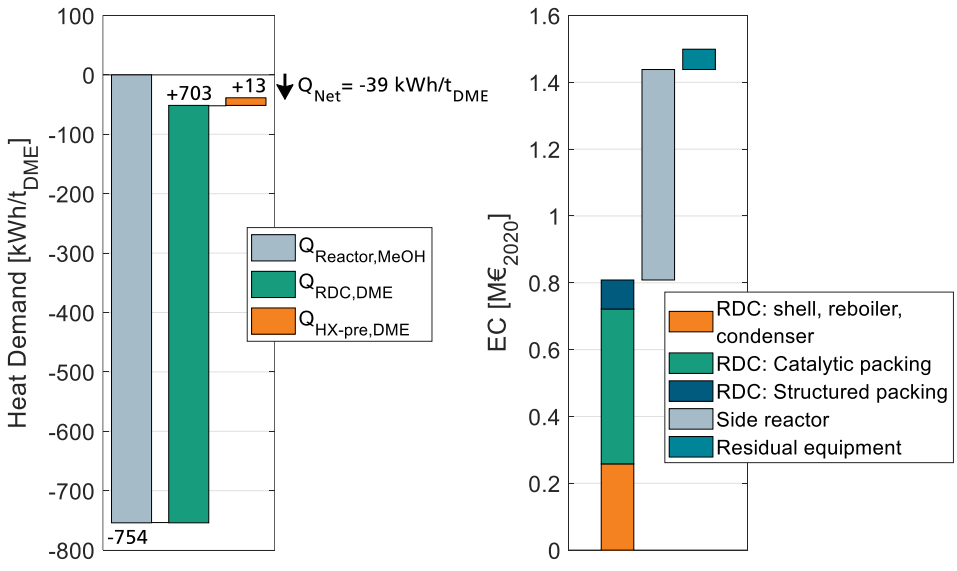

Figure 4-9: Heat demand of process P4 when heat integrated with the reactor of a MeOH synthesis plant (left) and equipment cost breakdown of DME process (right).

On the left side of the diagram, the exothermic heat of the MeOH reactor is displayed as negative energy demand. Consequently, it is offset against the two energy demanding apparatuses of the DME process, namely the RDC and the side reactor feed heat exchanger HX-pre. From the illustration a net heat demand of Q_{Net} = -39 kWh t_{DME}^{-1} at MeOH reaction temperature can be identified, implying the integrated process releases more heat than it consumes. The only energy demand of the DME process is the electric energy required for the pumps P-Feed and P-SR which is 11.4 kWh_{el} t_{DME}^{-1}. The MeOH synthesis plant has no external heat demand either, as a feed to product heat exchanger is sufficient to heat up the feed gas. Overall, the process P4 allows a DME production process from CO_2 and H_2 feedstock with no external heat demand. Instead, the process entails the possibility to export 39 kWh of MP steam per ton of DME produced. This is a decisive advantage in the PtX context, where plants are more likely to be constructed in remote areas without the infrastructure commonly found in chemistry parks. Integrating the “free” heat from the MeOH synthesis reduces the NCC of the process from 79.6 € t_{DME}^{-1} (no heat integration, Table 4-8) to 55.6 € t_{DME}^{-1} as the steam costs can be omitted. As the amount of exothermic heat is even higher than the heat demand, in this process configuration, the residual excess heat of 39 kWh t_{DME}^{-1} would be dissipated. Consequently, by reoptimizing the process under the boundary condition of using the entire available exothermic heat, a new optimal configuration can be found, that is characterized by a higher reboiler duty of the RDC but lower CAPEX. Table 4-9 sums up the KPI at this process design configuration.

Table 4-9: KPI of process P4 for crude MeOH feed and CAT400 at optimized process configuration when heat integrated with MeOH plant.

		Crude MeOH
Parameter	**Unit**	**CAT400**
N_{Feed}	-	15
N_{WD}	-	9
$N_{RCY,\ DME\text{-}rich}$		7
$N_{RCY,\ H2O\text{-}rich}$		56
$\dot{n}_{Side}$	kmol h^{-1}	525
$m_{Cat,\ SR}$	t	8.9
$X_{MeOH,\ SR}$	-	0.87
$m_{Cat,RDC}$	t	8.8
RR	-	5.9
Q_{Heat}	kWh t_{DME}^{-1}	0
NCC	€ t_{DME}^{-1}	54.4

4.3.5 Calculation of NPC

All results presented to this point reflect the NCC, considering all cost related to the DME synthesis itself, but disregarding the cost for the MeOH feedstock. Since the crude MeOH cost is dependent on many factors, Figure 4-10 shows the NPC of DME produced via P4 with CAT400 and crude MeOH feed as a function of the crude MeOH cost. The process design configuration of P4 was chosen as shown in Table 4-9. For comparison, the theoretical minimum NPC is shown. In this case, the OPEX and CAPEX for the DME process are neglected and only feedstock cost is considered.

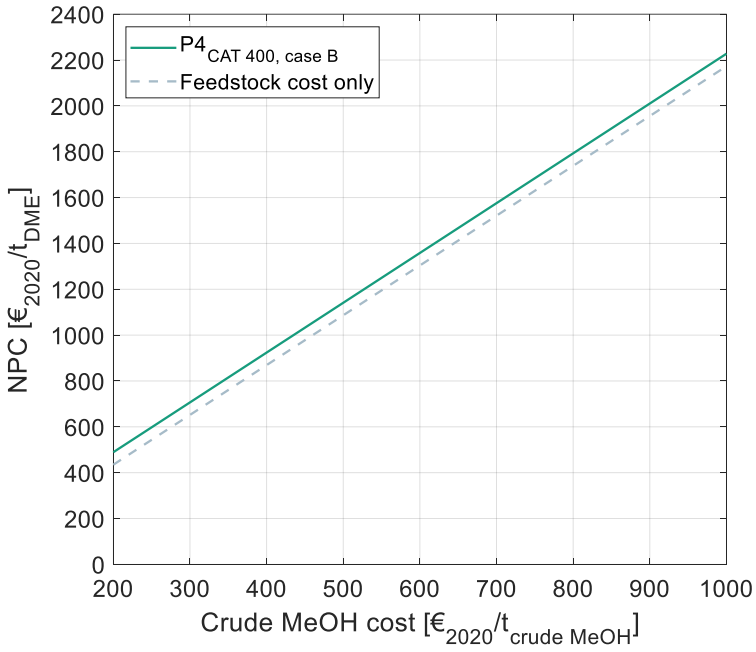

Figure 4-10: NPC of DME in dependence of the crude MeOH feedstock cost, as calculated by eq. (51). Cost for optimal process presented in this work and comparison with theoretical minimal cost, when neglecting all cost for the DME process.

The NPC increase linear with the crude MeOH cost, thereby reflecting the linear character of equation (51). The NCC of the DME process are visible as the vertical distance between the two lines in the diagram.

4.4 Conclusions and Outlook

DME shows very promising properties for a global transport of green hydrogen. Shifting the reaction phase of DME synthesis from gas to liquid opens up new possibilities towards the design of novel efficient process concepts. In the scope of this work, four process concepts were proposed and rigorously optimized with respect to the ideal process configuration and

the ideal size of the RDC and/or reactor. The used process simulation platform was validated in previous works based on kinetic measurements and under industrially relevant conditions in a pressure reactive distillation column. Based on the respective optimal design, all processes were systematically compared regarding technical and economic parameters. Hereby, every process concept was evaluated comparing two employed IER catalysts and comparing pure and crude MeOH feed, respectively. Furthermore, the conventional gas-phase process was simulated and evaluated as a reference case.

Throughout all proposed processes, the use of the high-temperature stable IER CAT400 proofed to be significantly beneficial in terms of energy demand and production cost. Consequently, the higher operating pressure with this catalyst can be overcompensated by the higher activity. Employing CAT400, all proposed processes show lower production cost than the conventional process. This can be attributed to the lower energy demand of the liquid phase processes. Interestingly, the reduced energy demand overcompensates the higher CAPEX, that can be traced back to the more expensive isothermal reactor required in liquid phase DME synthesis and/or the high cost for the catalytic packings in the RDC.

All processes with RDC (P2-P4) benefit from directly feeding crude MeOH to the DME process as opposed to a prior purification in a CMD column. While the stand-alone RD process P2 enables 31 % lower production cost than the conventional gas phase process, the RD process can be optimized even further, when complementing the RDC with a pre-reactor (P3) or side-reactor (P4). Despite the additional unit operation, these two process concepts allow a more efficient process and a reduced catalyst mass. The process P3 presents the lowest production cost for a pure MeOH feed, allowing a 31 % reduction of NCC compared to the conventional process. When feeding crude MeOH however, process P4 is superior, as the crude MeOH is purified in the RDC prior to entering the reactor. Overall, the process P4 with crude MeOH feed and employing CAT400 presents the best process, leading to a 39 % NCC reduction compared to the conventional gas-phase process. By heat integration of this process with a CO_2-based MeOH synthesis, NCC of 54.4 € t_{DME}^{-1} were achieved and it was demonstrated, that a plant without external heat demand can be realized, presenting a particularly beneficial process concept in the PtX context. This novel process configuration allows economically competitive DME production at large scale relying on state-of-the-art process components.

5 Summary, Conclusions and Outlook

5.1 Summary and Conclusions

The superordinate objective of this thesis was the scientific investigation and development of an integrated process concept to produce DME from MeOH based on RD. In pursuing this objective, the first step was the identification of suitable catalysts based on a catalyst screening in a high throughput batch reactor system. Thereby, sulfonated IER catalysts showed the highest activity, particularly the oversulfonated IER A36 and the chlorinated IER CAT400 emerged as the most promising catalysts opposed to the significantly less active zeolites and unstable PFSA catalysts. In kinetic investigations of both catalysts in a continuous profile reactor setup operated in liquid phase, CAT400 prove to be less active than A36 when compared at the same temperature. However, the higher temperature stability of CAT400 overcompensated this, leading to significantly higher reaction rates reported with CAT400. In modelling the reaction kinetics, both the ER and the LH approach were found to be unable to describe the reaction rate over the large operating range examined experimentally. Three different water inhibition terms were introduced to the model to account for the non-linear water inhibition induced by the selective swelling of the IER catalysts. The model $LH_{SR,\ Langmuir\ 1}$, assuming the surface reaction being the rate determining step and a water inhibition based on the Langmuir adsorption isotherm prove to be the most suitable approach. This way, a formal kinetic model was obtained that precisely describes the reaction kinetics throughout the entire measured operating range.

In order to validate the obtained model under RD process conditions, experiments using a DN50 pressure distillation column were performed. Using A36 introduced to the column in catalytic packings, 18 steady state experiments were carried out, therein varying the feed mass flow, feed composition, column pressure, reboiler duty and reflux ratio. The full conversion of the fed MeOH to pure DME with purities up to 99.9 mol.-% could be demonstrated successfully for pure MeOH feed and crude MeOH feed, a mixture of water and MeOH. As key characteristic of the process it was found that various feed amounts can be completely converted preserving the DME product purity by increasing the reflux ratio. This entails a system-inherent CAPEX/OPEX target conflict when designing the RD column, as a higher reflux ratio allows a smaller and cheaper column but increases the reboiler duty. Similarly, the feed of crude MeOH leads to a higher required reflux ratio to compensate the inhibitory effect of the increased water concentration in the reactive section. The discrete temperature and gas phase composition

measurements were coupled with VLE-modelling, which allowed to prove the consistency of the measurements. Furthermore, continuous liquid phase composition and temperature profiles were obtained for every experiment. By applying the kinetic model to these continuous profiles, the DME generation rate in the reactive section could be simulated and compared to the experimentally obtained amount of DME. Doing so, the proposed kinetic model obtained from liquid phase flow reactor measurements could be validated successfully under RD process conditions. The kinetic model together with a thermodynamic model was integrated into the equilibrium based RADFRAC distillation model in Aspen Plus. The resulting reactive distillation process simulation model was then validated with the experimental column profiles. A model-based sensitivity study of the RD column was performed based on the process model. Therein it was found that the kinetic parameters, i.e., the catalyst mass and the operating temperature determine the reboiler duty of the process. In contrast, the number of stages in the reactive section and the two rectifying sections has a negligible influence on the process. The number of stages in the upper and lower rectifying section need to exceed a minimum stage number, while additional stages have no beneficial effect on the reboiler duty.

The final objective of this thesis was the development and evaluation of promising process concepts. Besides the conventional process with adiabatic gas phase reactor, four different concepts based on the liquid phase DME synthesis were investigated:

1. A conventional reactor-separation-recycle sequence with a liquid phase isothermal reactor,
2. a stand-alone RD column,
3. a RD column complemented with pre-reactor,
4. a RD column complemented with side-reactor.

All process concepts were evaluated for the two catalysts A36 and CAT400 and with crude MeOH feed as the system boundary. Two cases were distinguished: Firstly, purifying the MeOH in a dedicated crude MeOH distillation column and feeding pure MeOH to the DME process, and secondly, directly feeding the crude MeOH to the DME process. Each process was optimized with respect to the optimal configuration and apparatus dimensions by minimizing the conversion cost of converting crude MeOH to DME. A factorial economic model was used in conjunction with the validated Aspen Plus process simulation to evaluate all processes.

All liquid-phase processes exhibited lower CAPEX and OPEX when using CAT400 instead of A36. This is due to the higher activity enabled by the higher operating temperature of this catalyst and overcompensates the higher operating pressure required at higher operating

temperature. Compared to the conventional process, all liquid phase processes require higher CAPEX due to the more expensive isothermal reactor and the high cost for the catalytic packing in the RD column. However, due to the significantly lower energy demand, this drawback is overcompensated, resulting in lower conversion cost of the liquid phase processes with CAT400 compared to the conventional process. The stand-alone RD process benefits significantly from feeding the crude MeOH directly to the RD column instead of priorly purifying it in a dedicated crude MeOH distillation column. Compared to the conventional process, the RD process with CAT400 and crude MeOH feed allows a reduction in conversion cost of 31 %. A further optimization is achieved when complementing the RD column with a side reactor. This way conversion costs can even be reduced by 39 % compared to the conventional process. It was shown that heat integration of this process with the MeOH synthesis allows a DME process from CO_2 and H_2 without external heat demand as the reboiler duty of the RD column can be entirely covered by the exothermic heat available from the MeOH plant. In this case, the NCC amount to 54.0 € t_{DME}^{-1}. This is particularly beneficial for PtX plants in remote areas without the availability of a heat network.

The concept of RD in DME synthesis has been thoroughly investigated by experiments and simulations and optimization potential has been pointed out on both catalyst and process level. The methods and models developed in this work present an off-the-shelf solution for the validated design and economic evaluation of RD processes.

5.2 Outlook

In this thesis, the RD concept has been demonstrated under industrially relevant conditions using a commercial catalyst and standardized components. Nevertheless, a scale-up of the integrated RD with side-reactor process is required to demonstrate the feasibility on an industrial scale. In the scope of this work only the stand-alone RD process with A36 as catalyst could be demonstrated due to the pressure limitations of the available distillation column. Future investigations should extend these investigations by demonstrating the RD process with a side-reactor and CAT400 catalyst, as this was identified as the most promising process concept in this work. Furthermore, real crude MeOH of a CO_2-based MeOH synthesis should be used as feedstock to investigate the influence of potential side-products of MeOH synthesis on the DME RD process. This entails potential challenges such as side-products compromising the catalyst stability, hampering the distillate purity, or enriching in the RD column.

For an industrial application of the RD process, the choice of catalytic internals presents a significant optimization potential, as the catalytic packing internals considered in the techno-

economic analysis of this thesis present a significant cost driver of the process. Since in the substance system of this work the number of theoretical stages in the reactive section plays a subordinate role compared to the amount of catalyst, alternative catalytic internals with increased catalyst volume fraction at the cost of a lower separation efficiency appear promising.

On the catalyst level, the long-term stability of the IER catalysts should be explored in detail. Thereby, the effect of using real process streams has to be considered, especially when using crude MeOH as a feedstock. Also, the influence of the operating temperature needs to be measured, to allow the development of a degradation model that allows a precise definition of an industrially realistic operating strategy.

Last but not least, the reactive distillation process with side reactor could be compared to the direct route of DME production. Hereby, a rigorous process comparison in dependence of the syngas carbon oxide ratio should be performed to evaluate the effect of CO_2, that is expected to particularly influence the direct route.

6 References

[1] S. Drünert, U. Neuling, T. Zitscher, M. Kaltschmitt, Power-to-Liquid fuels for aviation – Processes, resources and supply potential under German conditions, Applied Energy 277 (2020) 115578. https://doi.org/10.1016/j.apenergy.2020.115578.

[2] M. Prussi, L. Laveneziana, L. Testa, D. Chiaramonti, Comparing e-Fuels and Electrification for Decarbonization of Heavy-Duty Transports, Energies 15 (2022) 8075. https://doi.org/10.3390/en15218075.

[3] P. Schühle, R. Stöber, M. Semmel, A. Schaadt, R. Szolak, S. Thill, M. Alders, C. Hebling, P. Wasserscheid, O. Salem, Dimethyl ether/CO2 - a hitherto underestimated H2 storage cycle, Energy & Environmental Science 16 (2023) 3002–3013. https://doi.org/10.1039/D3EE00228D.

[4] M. Wietschel, L. Zheng, M. Arens, C. Hebling, O. Ranzmeyer, A. Schaadt, C. Hank, A. Sternberg, Herkel, Metastudie Wasserstoff: Auswertung von Energiesystemstudien, 2021.

[5] B. Gil, A. Fievez, B. Zajaczkowski, Pool boiling heat transfer coefficient of dimethyl ether and its azeotropic ternary mixtures, International Journal of Heat and Mass Transfer 171 (2021) 121063. https://doi.org/10.1016/j.ijheatmasstransfer.2021.121063.

[6] W. Maus (Ed.), Zukünftige Kraftstoffe, Springer Berlin Heidelberg, Berlin, Heidelberg, 2019.

[7] T.A. Semelsberger, R.L. Borup, H.L. Greene, Dimethyl ether (DME) as an alternative fuel, Journal of Power Sources 156 (2006) 497–511. https://doi.org/10.1016/j.jpowsour.2005.05.082.

[8] BioAge Group LLC, Volvo Trucks to begin limited production of DME heavy-duty trucks in NA in 2015; customer trials; Oberon partnership - Green Car Congress, 2013. https://www.greencarcongress.com/2013/06/dme-20130607.html (accessed 11 July 2023).

[9] AB Volvo, Mack Trucks tests alternative fuel DME | Volvo Group, 2017. https://www.volvogroup.com/en-en/news/2017/jan/mack-trucks-tests-alternative-fuel-dme.html (accessed 11 July 2023).

[10] Ford-werke GmbH, Ford leitet Forschungsprojekt an Diesel-Motoren, die mit Kraftstoffen aus CO2 nahezu rußfrei betrieben, 2015. https://www.presseportal.de/pm/6955/3120034 (accessed 11 July 2023).

[11] M. Matzen, Y. Demirel, Methanol and dimethyl ether from renewable hydrogen and carbon dioxide: Alternative fuels production and life-cycle assessment, Journal of Cleaner Production 139 (2016) 1068–1077. https://doi.org/10.1016/j.jclepro.2016.08.163.

[12] C. Arcoumanis, C. Bae, R. Crookes, E. Kinoshita, The potential of di-methyl ether (DME) as an alternative fuel for compression-ignition engines: A review, Fuel 87 (2008) 1014–1030. https://doi.org/10.1016/j.fuel.2007.06.007.

[13] S. Schemme, R.C. Samsun, R. Peters, D. Stolten, Power-to-fuel as a key to sustainable transport systems – An analysis of diesel fuels produced from CO_2 and renewable electricity, Fuel 205 (2017) 198–221. https://doi.org/10.1016/j.fuel.2017.05.061.

[14] W. Willems, M. Pannwitz, M. Zubel, J. Weber, Sauerstoffhaltige Kraftstoffe im selbstzündenden Verbrennungsmotor, MTZ Motortech Z 81 (2020) 28–37. https://doi.org/10.1007/s35146-019-0186-z.

[15] S.H. Park, C.S. Lee, Combustion performance and emission reduction characteristics of automotive DME engine system, Progress in Energy and Combustion Science 39 (2013) 147–168. https://doi.org/10.1016/j.pecs.2012.10.002.

[16] N. Wu, W. Zhang, Z. Huang, Impact of dimethyl ether on engine seal materials, Front. Energy Power Eng. China 2 (2008) 279–284. https://doi.org/10.1007/s11708-008-0042-1.

[17] S.C. Sorenson, Dimethyl Ether in Diesel Engines: Progress and Perspectives, Journal of Engineering for Gas Turbines and Power 123 (2001) 652–658. https://doi.org/10.1115/1.1370373.

[18] Z. Azizi, M. Rezaeimanesh, T. Tohidian, M.R. Rahimpour, Dimethyl ether: A review of technologies and production challenges, Chemical Engineering and Processing: Process Intensification 82 (2014) 150–172. https://doi.org/10.1016/j.cep.2014.06.007.

[19] S. Schemme, J.L. Breuer, M. Köller, S. Meschede, F. Walman, R.C. Samsun, R. Peters, D. Stolten, H2-based synthetic fuels: A techno-economic comparison of alcohol, ether and hydrocarbon production, International Journal of Hydrogen Energy 45 (2020) 5395–5414. https://doi.org/10.1016/j.ijhydene.2019.05.028.

[20] T.H. Fleisch, A. Basu, R.A. Sills, Introduction and advancement of a new clean global fuel: The status of DME developments in China and beyond, Journal of Natural Gas Science and Engineering 9 (2012) 94–107. https://doi.org/10.1016/j.jngse.2012.05.012.

[21] Dr. V.K. Saraswat, Ripunjaya Bansal, India's Leapfrog to Methanol Economy, 2017.

[22] Bioenergy International, Oberon Fuels Partners with SHV Energy to Accelerate Use of Renewable DME, 2020. https://bioenergyinternational.com/oberon-fuels-partners-with-shv-energy-to-accelerate-use-of-renewable-dme/to-accelerate-use-of-renewable-dme-rdme-to-decarbonize-transportation/ (accessed 11 July 2023).

[23] L. Du, S. Lou, G. Chen, G. Zhang, F. Kong, Z. Qian, C. Du, Y. Gao, S. Sun, G. Yin, Direct dimethyl ether fuel cells with low platinum-group-metal loading at anode: Investigations of operating temperatures and anode Pt/Ru ratios, Journal of Power Sources 433 (2019) 126690. https://doi.org/10.1016/j.jpowsour.2019.05.096.

[24] B.C. Ong, S.K. Kamarudin, S. Basri, Direct liquid fuel cells: A review, International Journal of Hydrogen Energy 42 (2017) 10142–10157. https://doi.org/10.1016/j.ijhydene.2017.01.117.

[25] D. Kashyap, H. Teller, A. Schechter, Dimethyl Ether Oxidation on an Active SnO 2 /Pt/C Catalyst for High-Power Fuel Cells, ChemElectroChem 6 (2019) 2407–2414. https://doi.org/10.1002/celc.201900216.

[26] Q. Li, G. Wu, C.M. Johnston, P. Zelenay, Direct Dimethyl Ether Fuel Cell with Much Improved Performance, Electrocatalysis 5 (2014) 310–317. https://doi.org/10.1007/s12678-014-0196-z.

[27] Q. Zhang, Z. Li, S. Wang, W. Xing, R. Yu, X. Yu, The electro-oxidation of dimethyl ether on platinum-based catalyst, Electrochimica Acta 53 (2008) 8298–8304. https://doi.org/10.1016/j.electacta.2008.05.044.

[28] B. Gavriel, R. Sharabi, L. Elbaz, Direct Electro-oxidation of Dimethyl Ether on Pt-Cu Nanochains, ChemSusChem 10 (2017) 3069–3074. https://doi.org/10.1002/cssc.201700702.

[29] C. Ledesma, E. López, T. Trifonov, Á. Rodríguez, J. Llorca, Catalytic reforming of dimethyl ether in microchannels, Catal. Today 323 (2019) 209–215. https://doi.org/10.1016/j.cattod.2018.03.011.

[30] T. Zhang, K. Ou, S. Jung, B. Choi, Y.-B. Kim, Dynamic analysis of a PEM fuel cell hybrid system with an on-board dimethyl ether (DME) steam reformer (SR), International

Journal of Hydrogen Energy 43 (2018) 13521–13531. https://doi.org/10.1016/j.ijhydene.2018.05.098.

[31] M. Müller, U. Hübsch, Dimethyl Ether, in: Ullmann's Encyclopedia of Industrial Chemistry, Wiley-VCH Verlag GmbH & Co. KGaA, Weinheim, Germany, 2012, p. 39.

[32] S.Y. Park, C.-H. Shin, J.W. Bae, Selective carbonylation of dimethyl ether to methyl acetate on Ferrierite, Catalysis Communications 75 (2016) 28–31. https://doi.org/10.1016/j.catcom.2015.12.006.

[33] Q. Qian, M. Cui, J. Zhang, J. Xiang, J. Song, G. Yang, B. Han, Synthesis of ethanol via a reaction of dimethyl ether with CO 2 and H 2, Green Chem 20 (2018) 206–213. https://doi.org/10.1039/C7GC02807E.

[34] Y. Liu, K. Murata, M. Inaba, I. Takahara, Synthesis of ethanol from methanol and syngas through an indirect route containing methanol dehydrogenation, DME carbonylation, and methyl acetate hydrogenolysis, Fuel Process. Technol. 110 (2013) 206–213. https://doi.org/10.1016/j.fuproc.2012.12.016.

[35] F.J. Keil, Methanol-to-hydrocarbons: process technology, Microporous and Mesoporous Materials 29 (1999) 49–66. https://doi.org/10.1016/S1387-1811(98)00320-5.

[36] S. Lee, M. Gogate, C.J. Kulik, Methanol-to-gasoline vs. DME-to-gasoline II. Process comparison and analysis, Fuel Science and Technology International 13 (1995) 1039–1057. https://doi.org/10.1080/08843759508947721.

[37] P. Pérez-Uriarte, A. Ateka, A.T. Aguayo, A.G. Gayubo, J. Bilbao, Kinetic model for the reaction of DME to olefins over a HZSM-5 zeolite catalyst, Chem. Eng. J. 302 (2016) 801–810. https://doi.org/10.1016/j.cej.2016.05.096.

[38] P. Pérez-Uriarte, M. Gamero, A. Ateka, M. Díaz, A.T. Aguayo, J. Bilbao, Effect of the Acidity of HZSM-5 Zeolite and the Binder in the DME Transformation to Olefins, Ind. Eng. Chem. Res. 55 (2016) 1513–1521. https://doi.org/10.1021/acs.iecr.5b04477.

[39] S.A. Tabak, S. Yurchak, Conversion of methanol over ZSM-5 to fuels and chemicals, Catal. Today 6 (1990) 307–327. https://doi.org/10.1016/0920-5861(90)85007-B.

[40] K.D. Vertin, J.M. Ohi, D.W. Naegeli, K.H. Childress, G.P. Hagen, C.I. McCarthy, A.S. Cheng, R.W. Dibble, Methylal and Methylal-Diesel Blended Fuels for Use in Compression-Ignition Engines, 1999.

[41] D. Oestreich, L. Lautenschütz, U. Arnold, J. Sauer, Production of oxymethylene dimethyl ether (OME)-hydrocarbon fuel blends in a one-step synthesis/extraction procedure, Fuel 214 (2018) 39–44. https://doi.org/10.1016/j.fuel.2017.10.116.

[42] Q. Zhang, W. Wang, Z. Zhang, Y. Han, Y. Tan, Low-Temperature Oxidation of Dimethyl Ether to Polyoxymethylene Dimethyl Ethers over CNT-Supported Rhenium Catalyst, Catalysts 6 (2016) 43. https://doi.org/10.3390/catal6030043.

[43] W. Wang, X. Gao, Q. Yang, X. Wang, F. Song, Q. Zhang, Y. Han, Y. Tan, Vanadium oxide modified H-beta zeolite for the synthesis of polyoxymethylene dimethyl ethers from dimethyl ether direct oxidation, Fuel 238 (2019) 289–297. https://doi.org/10.1016/j.fuel.2018.10.098.

[44] X.-J. Gao, W.-F. Wang, Y.-Y. Gu, Z. Zhang, J.-F. Zhang, Q. Zhang, N. Tsubaki, Y.-Z. Han, Y.-S. Tan, Synthesis of Polyoxymethylene Dimethyl Ethers from Dimethyl Ether Direct Oxidation over Carbon-Based Catalysts, ChemCatChem 10 (2018) 273–279. https://doi.org/10.1002/cctc.201701213.

[45] Q. Zhang, Y. Tan, C. Yang, Y. Han, MnCl2 modified H4SiW12O40/SiO2 catalysts for catalytic oxidation of dimethy ether to dimethoxymethane, Journal of Molecular Catalysis A: Chemical 263 (2007) 149–155. https://doi.org/10.1016/j.molcata.2006.08.044.

[46] Q. Zhang, Y. Tan, G. Liu, C. Yang, Y. Han, Promotional effects of Sm2O3 on Mn-H4SiW12O40/SiO2 catalyst for dimethyl ether direct-oxidation to dimethoxymethane, Journal of Industrial and Engineering Chemistry 20 (2014) 1869–1874. https://doi.org/10.1016/j.jiec.2013.09.004.

[47] W. W, Z. Q, VOx Modified H-Beta Zeolite for Dimethyl Ether Direct Oxidation to Polyoxymethylene Dimethyl Ethers, Chem Sci J 7 (2016). https://doi.org/10.4172/2150-3494.1000124.

[48] Arnold et al., Die Rolle von Dimethylether (DME) als Schlüsselbaustein synthetischer Kraftstoffe aus erneuerbaren Rohstoffen, in: W. Maus (Ed.), Zukünftige Kraftstoffe, Springer Berlin Heidelberg, Berlin, Heidelberg, 2019, pp. 532–561.

[49] E. Ströfer, H. Schelling, H. Hasse, S. Blagov WO2006134081A1, 2006.

[50] P. Haltenort, K. Hackbarth, D. Oestreich, L. Lautenschütz, U. Arnold, J. Sauer, Heterogeneously catalyzed synthesis of oxymethylene dimethyl ethers (OME) from dimethyl ether and trioxane, Catalysis Communications 109 (2018) 80–84. https://doi.org/10.1016/j.catcom.2018.02.013.

[51] C.F. Breitkreuz, N. Schmitz, E. Ströfer, J. Burger, H. Hasse, Design of a Production Process for Poly(oxymethylene) Dimethyl Ethers from Dimethyl Ether and Trioxane, Chemie Ingenieur Technik 90 (2018) 1489–1496. https://doi.org/10.1002/cite.201800038.

[52] M.C. Bauer, A. Kruse, The use of dimethyl ether as an organic extraction solvent for biomass applications in future biorefineries: A user-oriented review, Fuel 254 (2019) 115703. https://doi.org/10.1016/j.fuel.2019.115703.

[53] P. Boonnoun, A. Shotipruk, H. Kanda, M. Goto, Optimization of rubber seed oil extraction using liquefied dimethyl ether, Chemical Engineering Communications 206 (2019) 746–753. https://doi.org/10.1080/00986445.2018.1522502.

[54] J. Cho, T.H. Kim, K.S. Lee, Compositional modeling and simulation of dimethyl ether (DME)-enhanced waterflood to investigate oil mobility improvement, Pet. Sci. 15 (2018) 297–304. https://doi.org/10.1007/s12182-017-0212-z.

[55] Y. Onaka, A. Miyara, K. Tsubaki, Experimental study on evaporation heat transfer of CO2/DME mixture refrigerant in a horizontal smooth tube, International Journal of Refrigeration 33 (2010) 1277–1291. https://doi.org/10.1016/j.ijrefrig.2010.06.014.

[56] N.-H. Kim, Application of the Natural Refrigerant Mixture R-290/DME to a Soft Ice Cream Refrigerator, Int. J. Air-Cond. Ref. 24 (2016) 1650027. https://doi.org/10.1142/S2010132516500279.

[57] M. Bertau, H. Offermanns, L. Plass, F. Schmidt, H.-J. Wernicke, Methanol: The Basic Chemical and Energy Feedstock of the Future: Asinger's Vision Today, Springer-Verlag, Heidelberg, 2014.

[58] A. Bakhtyari, M.R. Rahimpour, Methanol to Dimethyl Ether, in: Methanol, Elsevier, 2018, pp. 281–311.

[59] F. Pontzen, W. Liebner, V. Gronemann, M. Rothaemel, B. Ahlers, CO_2-based methanol and DME – Efficient technologies for industrial scale production, Catalysis Today 171 (2011) 242–250. https://doi.org/10.1016/j.cattod.2011.04.049.

[60] Bernd Ahlers, Gerhard Birke, Harald Koempel (Air Liquide Global E&C Solutions Germany GmbH) US 8,884,074 B2, 2014.

[61] Kazuo Shoji, Satoshi Terai US2004/0034255A1, 2004.

[62] E. Catizzone, G. Bonura, M. Migliori, F. Frusteri, G. Giordano, CO_2 Recycling to Dimethyl Ether: State-of-the-Art and Perspectives, Molecules 23 (2017). https://doi.org/10.3390/molecules23010031.

[63] F. Yaripour, Z. Shariatinia, S. Sahebdelfar, A. Irandoukht, The effects of synthesis operation conditions on the properties of modified γ-alumina nanocatalysts in methanol dehydration to dimethyl ether using factorial experimental design, Fuel 139 (2015) 40–50. https://doi.org/10.1016/j.fuel.2014.08.029.

[64] F. Yaripour, F. Baghaei, I. Schmidt, J. Perregaard, Synthesis of dimethyl ether from methanol over aluminium phosphate and silica–titania catalysts, Catalysis Communications 6 (2005) 542–549. https://doi.org/10.1016/j.catcom.2005.05.003.

[65] L. Liu, W. Huang, Z. Gao, L. Yin, The Dehydration of Methanol to Dimethyl Ether over a Novel Slurry Catalyst, Energy Sources, Part A: Recovery, Utilization, and Environmental Effects 32 (2010) 1379–1387. https://doi.org/10.1080/15567030903030724.

[66] Q. Zhu, J.N. Kondo, R. Ohnuma, Y. Kubota, M. Yamaguchi, T. Tatsumi, The study of methanol-to-olefin over proton type aluminosilicate CHA zeolites, Microporous and Mesoporous Materials 112 (2008) 153–161. https://doi.org/10.1016/j.micromeso.2007.09.026.

[67] N. Khandan, M. Kazemeini, M. Aghaziarati, Determining an optimum catalyst for liquid-phase dehydration of methanol to dimethyl ether, Applied Catalysis A: General 349 (2008) 6–12. https://doi.org/10.1016/j.apcata.2008.07.029.

[68] J. Sun, G. Yang, Y. Yoneyama, N. Tsubaki, Catalysis Chemistry of Dimethyl Ether Synthesis, ACS Catal. 4 (2014) 3346–3356. https://doi.org/10.1021/cs500967j.

[69] F.S. Ramos, A.D. de Farias, L. Borges, J.L. Monteiro, M.A. Fraga, E.F. Sousa-Aguiar, L.G. Appel, Role of dehydration catalyst acid properties on one-step DME synthesis over physical mixtures, Catal. Today 101 (2005) 39–44. https://doi.org/10.1016/j.cattod.2004.12.007.

[70] M. Xu, J.H. Lunsford, D. Goodman, A. Bhattacharyya, Synthesis of dimethyl ether (DME) from methanol over solid-acid catalysts, Applied Catalysis A: General 149 (1997) 289–301. https://doi.org/10.1016/S0926-860X(96)00275-X.

[71] W. An, K.T. Chuang, A.R. Sanger, Dehydration of Methanol to Dimethyl Ether by Catalytic Distillation, Department of Chemical and Materials Engineering,University of Alberta, Edmonton, (2004).

[72] Z. Lei, Z. Zou, C. Dai, Q. Li, B. Chen, Synthesis of dimethyl ether (DME) by catalytic distillation, Chemical Engineering Science 66 (2011) 3195–3203. https://doi.org/10.1016/j.ces.2011.02.034.

[73] S. Hosseininejad, A. Afacan, R.E. Hayes, Catalytic and kinetic study of methanol dehydration to dimethyl ether, Chemical Engineering Research and Design 90 (2012) 825–833. https://doi.org/10.1016/j.cherd.2011.10.007.

[74] J. Bandiera, C. Naccache, Kinetics of methanol dehydration on dealuminated H-mordenite: Model with acid and basic active centres, Applied Catalysis 69 (1991) 139–148. https://doi.org/10.1016/S0166-9834(00)83297-2.

[75] H. Bateni, C. Able, Development of Heterogeneous Catalysts for Dehydration of Methanol to Dimethyl Ether: A Review, Catal. Ind. 11 (2019) 7–33. https://doi.org/10.1134/S2070050419010045.

[76] A.R. Keshavarz, M. Rezaei, F. Yaripour, Nanocrystalline gamma-alumina: A highly active catalyst for dimethyl ether synthesis, Powder Technology 199 (2010) 176–179. https://doi.org/10.1016/j.powtec.2010.01.003.

[77] E. Catizzone, M. Migliori, A. Purita, G. Giordano, Ferrierite vs. γ-Al2O3: The superiority of zeolites in terms of water-resistance in vapour-phase dehydration of methanol to dimethyl ether, Journal of Energy Chemistry 30 (2019) 162–169. https://doi.org/10.1016/j.jechem.2018.05.004.

[78] J. Boon, J. van Kampen, R. Hoogendoorn, S. Tanase, F.P. van Berkel, M. van Sint Annaland, Reversible deactivation of γ-alumina by steam in the gas-phase dehydration of methanol to dimethyl ether, Catalysis Communications 119 (2019) 22–27. https://doi.org/10.1016/j.catcom.2018.10.008.

[79] V. Barbarossa, R. Viscardi, A. Di Nardo, A. Santagata, Kinetic Parameter Estimation for Methanol Dehydration to Dimethyl Ether Over Sulfonic and Polymeric Acid Catalysts, J Chem Technol Biotechnol (2020). https://doi.org/10.1002/jctb.6372.

[80] S. Hosseini, M. Taghizadeh, A. Eliassi, Optimization of hydrothermal synthesis of H-ZSM-5 zeolite for dehydration of methanol to dimethyl ether using full factorial design, Journal of Natural Gas Chemistry 21 (2012) 344–351. https://doi.org/10.1016/S1003-9953(11)60375-7.

[81] C. Ortega, M. Rezaei, V. Hessel, G. Kolb, Methanol to dimethyl ether conversion over a ZSM-5 catalyst: Intrinsic kinetic study on an external recycle reactor, Chem. Eng. J. 347 (2018) 741–753. https://doi.org/10.1016/j.cej.2018.04.160.

[82] K.-S. Ha, Y.-J. Lee, J.W. Bae, Y.W. Kim, M.H. Woo, H.-S. Kim, M.-J. Park, K.-W. Jun, New reaction pathways and kinetic parameter estimation for methanol dehydration over modified ZSM-5 catalysts, Applied Catalysis A: General 395 (2011) 95–106. https://doi.org/10.1016/j.apcata.2011.01.025.

[83] E. Catizzone, A. Aloise, M. Migliori, G. Giordano, The effect of FER zeolite acid sites in methanol-to-dimethyl-ether catalytic dehydration, Journal of Energy Chemistry 26 (2017) 406–415. https://doi.org/10.1016/j.jechem.2016.12.005.

[84] E. Catizzone, S. van Daele, M. Bianco, A. Di Michele, A. Aloise, M. Migliori, V. Valtchev, G. Giordano, Catalytic application of ferrierite nanocrystals in vapour-phase dehydration of methanol to dimethyl ether, Applied Catalysis B: Environmental 243 (2019) 273–282. https://doi.org/10.1016/j.apcatb.2018.10.060.

[85] G.R. Moradi, F. Yaripour, P. Vale-Sheyda, Catalytic dehydration of methanol to dimethyl ether over mordenite catalysts, Fuel Process. Technol. 91 (2010) 461–468. https://doi.org/10.1016/j.fuproc.2009.12.005.

[86] B. Sabour, M.H. Peyrovi, T. Hamoule, M. Rashidzadeh, Catalytic dehydration of methanol to dimethyl ether (DME) over Al-HMS catalysts, Journal of Industrial and Engineering Chemistry 20 (2014) 222–227. https://doi.org/10.1016/j.jiec.2013.03.044.

[87] A. Aloise, A. Marino, F. Dalena, G. Giorgianni, M. Migliori, L. Frusteri, C. Cannilla, G. Bonura, F. Frusteri, G. Giordano, Desilicated ZSM-5 zeolite: Catalytic performances assessment in methanol to DME dehydration, Microporous and Mesoporous Materials (2020) 110198. https://doi.org/10.1016/j.micromeso.2020.110198.

[88] M. Migliori, A. Aloise, E. Catizzone, G. Giordano, Kinetic Analysis of Methanol to Dimethyl Ether Reaction over H-MFI Catalyst, Ind. Eng. Chem. Res. 53 (2014) 14885–14891. https://doi.org/10.1021/ie502775u.

[89] M. Migliori, A. Aloise, G. Giordano, Methanol to dimethylether on H-MFI catalyst: The influence of the Si/Al ratio on kinetic parameters, Catal. Today 227 (2014) 138–143. https://doi.org/10.1016/j.cattod.2013.09.033.

[90] D. Masih, S. Rohani, J.N. Kondo, T. Tatsumi, Low-temperature methanol dehydration to dimethyl ether over various small-pore zeolites, Applied Catalysis B: Environmental 217 (2017) 247–255. https://doi.org/10.1016/j.apcatb.2017.05.089.

[91] D. Varışlı, T. Dogu, Production of clean transportation fuel dimethylether by dehydration of methanol over Nafion catalyst, Gazi Univ. J. Sci. 21 (2008) 37–41.

[92] A. Ciftci, N.A. Sezgi, T. Dogu, Nafion-Incorporated Silicate Structured Nanocomposite Mesoporous Catalysts for Dimethyl Ether Synthesis, Ind. Eng. Chem. Res. 49 (2010) 6753–6762. https://doi.org/10.1021/ie9015667.

[93] N.V.Kolesnichenko, A.B.Kulikov, A.L.Maximov, A.I.Nehaev, R.V.Kulumbekov V.G.Barabanov*, V.V.Kornilov*, Dehydration of Methanol on the Catalyst based on perfluorinated Copolymer F-4SF, Fluorine Notes (2011).

[94] W. Alharbi, E.F. Kozhevnikova, I.V. Kozhevnikov, Dehydration of Methanol to Dimethyl Ether over Heteropoly Acid Catalysts: The Relationship between Reaction Rate and Catalyst Acid Strength, ACS Catal. 5 (2015) 7186–7193. https://doi.org/10.1021/acscatal.5b01911.

[95] C.P. Dalia Liuzzi, Heteropolyacid based catalysts for the production of dimethyl ether from Heteropolyacid based catalysts for the production of dimethyl ether from methanol. Effects of reaction pressure and nature of the support, 2019.

[96] M.J. Valero-Romero, E.M. Calvo-Muñoz, R. Ruiz-Rosas, J. Rodríguez-Mirasol, T. Cordero, Phosphorus-Containing Mesoporous Carbon Acid Catalyst for Methanol Dehydration to Dimethyl Ether, Ind. Eng. Chem. Res. 58 (2019) 4042–4053. https://doi.org/10.1021/acs.iecr.8b05897.

[97] C. Moreno-Castilla, F. Carrasco-Marín, C. Parejo-Pérez, M. López Ramón, Dehydration of methanol to dimethyl ether catalyzed by oxidized activated carbons with varying surface acidic character, Carbon 39 (2001) 869–875. https://doi.org/10.1016/S0008-6223(00)00192-5.

[98] J. Jasińska, B. Krzyżyńska, M. Kozłowski, Influence of activated carbon modifications on their catalytic activity in methanol and ethanol conversion reactions, Open Chemistry 9 (2011). https://doi.org/10.2478/s11532-011-0078-7.

[99] M. Stiefel, R. Ahmad, U. Arnold, M. Döring, Direct synthesis of dimethyl ether from carbon-monoxide-rich synthesis gas: Influence of dehydration catalysts and operating conditions, Fuel Process. Technol. 92 (2011) 1466–1474. https://doi.org/10.1016/j.fuproc.2011.03.007.

[100] D.S. Marlin, E. Sarron, Ó. Sigurbjörnsson, Process Advantages of Direct CO2 to Methanol Synthesis, Front. Chem. 6 (2018) 446. https://doi.org/10.3389/fchem.2018.00446.

[101] H. Goehna, P. Koenig, Producing methanol from CO2: The keys are a catalyst that can tolerate a high CO2 concentration and an unusual process configuration. The keys

are a catalyst that can tolerate a high CO2 concentration and an unusual process configuration, Chem. Tech. (1994) 36–39.

[102] F. Nestler, M. Krüger, J. Full, M.J. Hadrich, R.J. White, A. Schaadt, Methanol Synthesis - Industrial Challenges within a Changing Raw Material Landscape, Chemie Ingenieur Technik 90 (2018) 1409–1418. https://doi.org/10.1002/cite.201800026.

[103] M.R. Gogate, The direct dimethyl ether (DME) synthesis process from syngas I. Process feasibility and chemical synergy in one-step LPDME tm process, Petroleum Science and Technology 36 (2018) 547–554. https://doi.org/10.1080/10916466.2018.1428628.

[104] X.D. Peng, B.A. Toseland, A.W. Wang, G.E. Parris, Progress in development of LPMDE process: kinetics and catalysts, in: Coal Liquefaction and Solid Fuels Contractors Review Conference, 1997.

[105] U. Mondal, G.D. Yadav, Perspective of dimethyl ether as fuel: Part I. Catalysis, Journal of CO2 Utilization 32 (2019) 299–320. https://doi.org/10.1016/j.jcou.2019.02.003.

[106] Xiang-Dong Peng, Barry W. Diamond, Tsun-Chiu Robert Tsao, Bharat Lajjaram Bhatt US6458856B1, 2002.

[107] A. Ateka, P. Pérez-Uriarte, M. Gamero, J. Ereña, A.T. Aguayo, J. Bilbao, A comparative thermodynamic study on the CO2 conversion in the synthesis of methanol and of DME, Energy 120 (2017) 796–804. https://doi.org/10.1016/j.energy.2016.11.129.

[108] J. Ereña, I. Sierra, A.T. Aguayo, A. Ateka, M. Olazar, J. Bilbao, Kinetic modelling of dimethyl ether synthesis from (H2+CO2) by considering catalyst deactivation, Chem. Eng. J. 174 (2011) 660–667. https://doi.org/10.1016/j.cej.2011.09.067.

[109] A. Ateka, J. Ereña, J. Bilbao, A.T. Aguayo, Strategies for the Intensification of CO 2 Valorization in the One-Step Dimethyl Ether Synthesis Process, Ind. Eng. Chem. Res. (2019). https://doi.org/10.1021/acs.iecr.9b05749.

[110] F. Frusteri, M. Migliori, C. Cannilla, L. Frusteri, E. Catizzone, A. Aloise, G. Giordano, G. Bonura, Direct CO 2 -to-DME hydrogenation reaction: New evidences of a superior behaviour of FER-based hybrid systems to obtain high DME yield, Journal of CO2 Utilization 18 (2017) 353–361. https://doi.org/10.1016/j.jcou.2017.01.030.

[111] M. de Falco, M. Capocelli, G. Centi, Dimethyl ether production from CO2 rich feedstocks in a one-step process: Thermodynamic evaluation and reactor simulation, Chem. Eng. J. 294 (2016) 400–409. https://doi.org/10.1016/j.cej.2016.03.009.

[112] I. Iliuta, M.C. Iliuta, F. Larachi, Sorption-enhanced dimethyl ether synthesis—Multiscale reactor modeling, Chem. Eng. Sci. 66 (2011) 2241–2251. https://doi.org/10.1016/j.ces.2011.02.047.

[113] M. Hamidi, F. Samimi, M.R. Rahimpour, Dimethyl ether synthesis in a gas–solid–solid trickle flow reactor with continuous adsorbent regeneration, Journal of the Taiwan Institute of Chemical Engineers 47 (2015) 105–112. https://doi.org/10.1016/j.jtice.2014.10.013.

[114] J. van Kampen, J. Boon, J. Vente, M. van Sint Annaland, Sorption enhanced dimethyl ether synthesis for high efficiency carbon conversion: Modelling and cycle design, Journal of CO2 Utilization 37 (2020) 295–308. https://doi.org/10.1016/j.jcou.2019.12.021.

[115] J. van Kampen, J. Boon, F. van Berkel, J. Vente, M. van Sint Annaland, Steam separation enhanced reactions: Review and outlook, Chemica Engineering Journal 374 (2019) 1286–1303. https://doi.org/10.1016/j.cej.2019.06.031.

[116] I. Iliuta, F. Larachi, P. Fongarland, Dimethyl Ether Synthesis with in situ H 2 O Removal in Fixed-Bed Membrane Reactor: Model and Simulations †, Ind. Eng. Chem. Res. 49 (2010) 6870–6877. https://doi.org/10.1021/ie901726u.

[117] K.-H. Lee, M.-Y. Youn, B. Sea, Preparation of hydrophilic ceramic membranes for a dehydration membrane reactor, Desalination 191 (2006) 296–302. https://doi.org/10.1016/j.desal.2005.07.026.

[118] N. Diban, A.M. Urtiaga, I. Ortiz, J. Ereña, J. Bilbao, A.T. Aguayo, Influence of the membrane properties on the catalytic production of dimethyl ether with in situ water removal for the successful capture of co2, Chemica Engineering Journal 234 (2013) 140–148. https://doi.org/10.1016/j.cej.2013.08.062.

[119] N. Diban, A.T. Aguayo, J. Bilbao, A. Urtiaga, I. Ortiz, Membrane Reactors for in Situ Water Removal: A Review of Applications, Industrial & Engineering Chemistry Research 52 (2013) 10342–10354. https://doi.org/10.1021/ie3029625.

[120] G.J. Harmsen, Reactive distillation: The front-runner of industrial process intensification, Chemical Engineering and Processing - Process Intensification 46 (2007) 774–780. https://doi.org/10.1016/j.cep.2007.06.005.

[121] A.A. Kiss, Novel Catalytic Reactive Distillation Processes for a Sustainable Chemical Industry, Top Catal 89 (2018) 479. https://doi.org/10.1007/s11244-018-1052-9.

[122] T. Cholewa, M. Semmel, F. Mantei, R. Güttel, O. Salem, Process Intensification Strategies for Power-to-X Technologies, ChemEngineering 6 (2022) 13. https://doi.org/10.3390/chemengineering6010013.

[123] A.C. Dimian, C.S. Bildea, A.A. Kiss (Eds.), Applications in design and simulation of sustainable chemical processes, 1st ed., Elsevier, Cambridge, 2019.

[124] C.S. Bîldea, R. Győrgy, C.C. Brunchi, A.A. Kiss, Optimal design of intensified processes for DME synthesis, Computers & Chemical Engineering 105 (2017) 142–151. https://doi.org/10.1016/j.compchemeng.2017.01.004.

[125] N.K. Gor, N.A. Mali, S.S. Joshi, Intensified reactive distillation configurations for production of dimethyl ether, Chemical Engineering and Processing - Process Intensification 149 (2020) 107824. https://doi.org/10.1016/j.cep.2020.107824.

[126] J. Liu, L. Gao, J. Ren, W. Liu, X. Liu, L. Sun, Dynamic Process Intensification of Dimethyl Ether Reactive Distillation Based on Output Multiplicity, Ind. Eng. Chem. Res. (2020). https://doi.org/10.1021/acs.iecr.0c03973.

[127] T.-W. Wu, I.-L. Chien, A Novel Energy-efficient Process of Converting CO2 to Dimethyl Ether with Techno-economic and Environmental Evaluation, Chemical Engineering Research and Design (2021). https://doi.org/10.1016/j.cherd.2021.10.013.

[128] I. Bogatykh, C. Hoffmann, V. Kozachynskyi, M. Illner, T. Osterland, T. Wilharm, J.-U. Repke, Insights into Dynamic Process Intensification for Reactive Distillation Columns, Chemical Engineering and Processing - Process Intensification 177 (2022) 108978. https://doi.org/10.1016/j.cep.2022.108978.

[129] M. Di Stanislao, A. Malandrino, R. Patrini, C. Pirovano, A. Viva, E. Brunazzi, DME synthesis via catalytic distillation: Experiments and simulation, Computer Aided Chemical Engineering (2007) 1077–1082. https://doi.org/10.1016/S1570-7946(07)80204-5.

[130] W.-B. Su, J.-H. Hwang, H.-Y. Huang, T.-K. Chang, Dehydration of methanol to dimethyl ether in a dual-catalyst system catalytic distillation tower, Journal of the Taiwan Institute of Chemical Engineers 59 (2016) 86–90. https://doi.org/10.1016/j.jtice.2015.07.037.

[131] A.A. Kiss, D.J.-P. Suszwalak, Innovative dimethyl ether synthesis in a reactive dividing-wall column, Computers & Chemical Engineering 38 (2012) 74–81. https://doi.org/10.1016/j.compchemeng.2011.11.012.

[132] M.A. Harmer, Q. Sun, Solid acid catalysis using ion-exchange resins, Applied Catalysis A: General 221 (2001) 45–62. https://doi.org/10.1016/S0926-860X(01)00794-3.

[133] Fraunhofer ISE, Fraunhofer ISE entwickelt mobilen Teststand für hochaufgelöste Power-to-X-Kinetikanalyse.

[134] J. Schwarz, D. Samiec (Eds.), B3.4 - Fiber-Optic Measurement of Temperature Profiles. AMA Service GmbH, Von-Münchhausen-Str. 49, 31515 Wunstorf, Germany, 2017.

[135] F. Nestler, V.P. Müller, M. Ouda, M.J. Hadrich, A. Schaadt, S. Bajohr, T. Kolb, A novel approach for kinetic measurements in exothermic fixed bed reactors: advancements in non-isothermal bed conditions demonstrated for methanol synthesis, React. Chem. Eng. 6 (2021) 1092–1107. https://doi.org/10.1039/D1RE00071C.

[136] M. Kraume, Transportvorgänge in der Verfahrenstechnik, Springer Berlin Heidelberg, Berlin, Heidelberg, 2012.

[137] G.F. Froment, K.B. Bischoff, J. de Wilde, Chemical Reactor Analysis and Design, thirdrd Edition, John Wiley & Sons, Inc, 2011.

[138] R. Soto, C. Fité, E. Ramírez, M. Iborra, J. Tejero, Catalytic activity dependence on morphological properties of acidic ion-exchange resins for the simultaneous ETBE and TAEE liquid-phase synthesis, React. Chem. Eng. 3 (2018) 195–205. https://doi.org/10.1039/c7re00177k.

[139] R. Tesser, M. Di Serio, L. Casale, L. Sannino, M. Ledda, E. Santacesaria, Acid exchange resins deactivation in the esterification of free fatty acids, Chem. Eng. J. 161 (2010) 212–222. https://doi.org/10.1016/j.cej.2010.04.026.

[140] E. van de Steene, J. de Clercq, J.W. Thybaut, Ion-exchange resin catalyzed transesterification of ethyl acetate with methanol: Gel versus macroporous resins, Chem. Eng. J. 242 (2014) 170–179. https://doi.org/10.1016/j.cej.2013.12.025.

[141] A. Jess, P. Wasserscheid, Chemical technology: An integral textbook, Wiley-VCH, Weinheim, 2013.

[142] Elizabeth Louisa du Toit, The rate inhibiting effect of water as a product on reactions catalysed by cation exchange resins: Formation of mesityl oxide from acetone as a case study. Dissertation, Pretoria, 2003.

[143] M.Á. Pérez-Maciá, R. Bringué, M. Iborra, J. Tejero, F. Cunill, Kinetic study of 1-butanol dehydration to di- n -butyl ether over Amberlyst 70, AIChE J 62 (2016) 180–194. https://doi.org/10.1002/aic.15020.

[144] J.C. Lagarias, J.A. Reeds, M.H. Wright, P.E. Wright, Convergence Properties of the Nelder--Mead Simplex Method in Low Dimensions, SIAM J. Optim. 9 (1998) 112–147. https://doi.org/10.1137/S1052623496303470.

[145] X. Sun, Y. Yang, Y. He, S. Zhu, Z. Liu, Stability of Zeolite HZSM-5 in Liquid Phase Dehydration of Methanol to Dimethyl Ether, Catal Lett (2020). https://doi.org/10.1007/s10562-020-03454-y.

[146] Pivi K. Kiviranta-Pääkkönen, Liisa K. Struckmann, Juha A. Linnekoski, and A. Outi I. Krause, Dehydration of the Alcohol in the Etherification of Isoamylenes with Methanol and Ethanol (1998).

[147] T. Baba, Y. Ono, Kinetic studies in liquid phase dehydration-cyclization of 1,4-butanediol to tetrahydrofuran with heteropoly acids, Journal of Molecular Catalysis 37 (1986) 317–326. https://doi.org/10.1016/0304-5102(86)85020-9.

[148] U. Limbeck, C. Altwicker, U. Kunz, U. Hoffmann, Rate expression for THF synthesis on acidic ion exchange resin, Chem. Eng. Sci. 56 (2001) 2171–2178. https://doi.org/10.1016/S0009-2509(00)00497-8.

[149] M. Semmel, L. Steiner, M. Bontrup, J. Sauer, O. Salem, Catalyst screening and reaction kinetics of liquid phase DME synthesis under reactive distillation conditions, Chem. Eng. J. (2022) 140525. https://doi.org/10.1016/j.cej.2022.140525.

[150] Lenntech, Product Data Sheet Amberlyst 36. https://www.lenntech.com/Data-sheets/Dow-Amberlyst-36-wet-L.pdf (accessed 11 July 2023).

[151] I. Bogatykh, M. Illner, F.-J. Nagler, H. Stein, T. Osterland, J.-U. Repke, Low-interference real-time at-line spectroscopic composition analysis for chemical plants, Meas. Sci. Technol. 34 (2023) 55902. https://doi.org/10.1088/1361-6501/acb78f.

[152] Taylor, Krishna, Modelling reactive distillation, Chem. Eng. Sci. 55 (2000) 5183–5229. https://doi.org/10.1016/S0009-2509(00)00120-2.

[153] H.G. Schoenmakers, B. Bessling, Reactive and catalytic distillation from an industrial perspective, Chemical Engineering and Processing - Process Intensification 42 (2003) 145–155. https://doi.org/10.1016/S0255-2701(02)00085-5.

[154] M. Sakuth, D. Reusch, R. Janowsky, Reactive Distillation, in: Ullmann's Encyclopedia of Industrial Chemistry, Wiley-VCH Verlag GmbH & Co. KGaA, Weinheim, Germany, 2012.

[155] M. Schmitt, H. Hasse, K. Althaus, H. Schoenmakers, L. Götze, P. Moritz, Synthesis of n-hexyl acetate by reactive distillation, Chemical Engineering and Processing - Process Intensification 43 (2004) 397–409. https://doi.org/10.1016/S0255-2701(03)00124-7.

[156] M. Schmitt, S. Blagov, H. Hasse, Mastering the Reaction Is the Key to Successful Design of Heterogeneously Catalyzed Reactive Distillation: A Comprehensive Case Study of Hexyl Acetate Synthesis, Ind. Eng. Chem. Res. 47 (2008) 6014–6024. https://doi.org/10.1021/ie0714504.

[157] P. Moritz, H. Hasse, Fluid dynamics in reactive distillation packing Katapak®-S, Chem. Eng. Sci. 54 (1999) 1367–1374. https://doi.org/10.1016/S0009-2509(99)00078-0.

[158] K. Ye, H. Freund, K. Sundmacher, Modelling (vapour+liquid) and (vapour+liquid+liquid) equilibria of {water (H2O)+methanol (MeOH)+dimethyl ether (DME)+carbon dioxide (CO2)} quaternary system using the Peng–Robinson EoS with Wong–Sandler mixing rule, The Journal of Chemical Thermodynamics 43 (2011) 2002–2014. https://doi.org/10.1016/j.jct.2011.07.016.

[159] E. von Harbou, A. Yazdani, M. Schmitt, C. Großmann, H. Hasse, Reaction Kinetics for Reactive Distillation Using Different Laboratory Reactors, Ind. Eng. Chem. Res. 52 (2013) 624–637. https://doi.org/10.1021/ie301428w.

[160] L.B. Datsevich, Alternating motion of liquid in catalyst pores in a liquid/liquid–gas reaction with heat or gas production, Catal. Today 79-80 (2003) 341–348. https://doi.org/10.1016/S0920-5861(03)00061-0.

[161] M.S. Ray, Distillation Design, by HZ. Kister, McGraw-Hill, New York, USA (1992). 710 pages. ISBN 0-07-034909-6, Dev. Chem. Eng. Mineral Process. 2 (1994) 255–256. https://doi.org/10.1002/apj.5500020411.

[162] J. Nyári, M. Magdeldin, M. Larmi, M. Järvinen, A. Santasalo-Aarnio, Techno-economic barriers of an industrial-scale methanol CCU-plant, Journal of CO2 Utilization 39 (2020) 101166. https://doi.org/10.1016/j.jcou.2020.101166.

[163] F.G. Albrecht, D.H. König, N. Baucks, R.-U. Dietrich, A standardized methodology for the techno-economic evaluation of alternative fuels – A case study, Fuel 194 (2017) 511–526. https://doi.org/10.1016/j.fuel.2016.12.003.

[164] F. Mantei, R.E. Ali, C. Baensch, S. Voelker, P. Haltenort, J. Burger, R.-U. Dietrich, N.v.d. Assen, A. Schaadt, J. Sauer, O. Salem, Techno-economic assessment and Carbon footprint of processes for the large-scale production of Oxymethylene Dimethyl Ethers from Carbon Dioxide and Hydrogen, Sustainable Energy Fuels (2021). https://doi.org/10.1039/D1SE01270C.

[165] D.W. Green, R.H. Perry, Perry's Chemical Engineers' Handbook, eighth ed., McGraw-Hill, New York, 2008.

[166] G. Bercic, J. Levec, Catalytic dehydration of methanol to dimethyl ether. Kinetic investigation and reactor simulation, Ind. Eng. Chem. Res. 32 (1993) 2478–2484. https://doi.org/10.1021/ie00023a006.

[167] G. Berčič, J. Levec, Correction to “Catalytic Dehydration of Methanol to Dimethyl Ether. Kinetic Investigation and Reactor Simulation”, Ind. Eng. Chem. Res. 62 (2023) 5449. https://doi.org/10.1021/acs.iecr.3c00674.

[168] M. Semmel, I. Bogatykh, B. Steinbach, J. Sauer, J.-U. Repke, O. Salem, Demonstration and experimental model validation of the DME synthesis by reactive distillation in a pilot-scale pressure column, React. Chem. Eng. (2023) 2309–2322. https://doi.org/10.1039/D3RE00200D.

[169] A. Hoffmann, C. Noeres, A. Górak, Scale-up of reactive distillation columns with catalytic packings, Chemical Engineering and Processing: Process Intensification 43 (2004) 383–395. https://doi.org/10.1016/S0255-2701(03)00121-1.

[170] Sulzer Ltd, Structured Packings: Energy-efficient, innovative & profitable, 2020.

[171] Association for the Advancement of Cost Engineering, 18R-97: Cost Estimate Classification System - As Applied in Engineering, Procurement, and Construction for the Process Industries: AACE International Recommended Practice No. 18R-97. https://web.aacei.org/docs/default-source/toc/toc_18r-97.pdf?sfvrsn=4 (accessed 11 July 2023).

[172] Europäische Zentralbank, Euro-Referenzkurse: US dollar (USD), 2023. https://www.ecb.europa.eu/stats/policy_and_exchange_rates/euro_reference_exchange_rates/html/eurofxref-graph-usd.de.html (accessed 17 March 2023).

[173] Eurostat-Pressestelle, Arbeitskosten in der EU, 2018.

[174] M.S. Peters, K.D. Timmerhaus, R.E. West, Plant design and economics for chemical engineers, fifthth ed., internat. ed., McGraw-Hill, Boston, 2003.

[175] S. Michailos, S. McCord, V. Sick, G. Stokes, P. Styring, Dimethyl ether synthesis via captured CO2 hydrogenation within the power to liquids concept: A techno-economic assessment, Energy Convers. Mgmt. 184 (2019) 262–276. https://doi.org/10.1016/j.enconman.2019.01.046.

[176] T. Keller, Reactive Distillation, in: Distillation, Elsevier, 2014, pp. 261–294.

[177] M. Baerns, A. Behr, A. Brehm, J. Gmehling, K.-O. Hinrichsen, H. Hofmann, R. Palkovits, U. Onken, A. Renken, Technische Chemie, second. Auflage, Wiley-VCH Verlag GmbH & Co. KGaA, Weinheim, 2013.

[178] J. Lilja, J. Aumo, T. Salmi, D. Murzin, P. Mäki-Arvela, M. Sundell, K. Ekman, R. Peltonen, H. Vainio, Kinetics of esterification of propanoic acid with methanol over a fibrous polymer-supported sulphonic acid catalyst, Applied Catalysis A: General 228 (2002) 253–267. https://doi.org/10.1016/S0926-860X(01)00981-4.

[179] J. Voggenreiter, A. Ferre, J. Burger, Scale-up of the Continuous Production of Poly(oxymethylene) Dimethyl Ethers from Methanol and Formaldehyde in Tubular Reactors, Ind. Eng. Chem. Res. 61 (2022) 10034–10046. https://doi.org/10.1021/acs.iecr.2c01468.

[180] DIPPR, Thermophysical Properties Laboratory Project 801, 2009. http://dippr.byu.edu/ (accessed 11 July 2023).

[181] VDI-Gesellschaft Verfahrenstechnik und Chemieingenieurwesen, VDI-Wärmeatlas, Springer Berlin Heidelberg, Berlin, Heidelberg, 2013.

[182] C.C. Li, Thermal conductivity of liquid mixtures, AIChE J 22 (1976) 927–930. https://doi.org/10.1002/aic.690220520.

[183] C.R. Wilke, P. Chang, Correlation of diffusion coefficients in dilute solutions, AIChE J 1 (1955) 264–270. https://doi.org/10.1002/aic.690010222.

[184] J.I. Kroschwitz, R.E. Kirk, D.F. Othmer, A. Seidel, Kirk-Othmer encyclopedia of chemical technology, [fifth. ed.], Wiley-Interscience, Hoboken, NJ, 2004.

[185] E. Brunazzi, R. Macías-Salinas, A. Viva, Calculation procedure for flooding in packed columns using a channel model, Chemical Engineering Communications 196 (2008) 330–341. https://doi.org/10.1080/00986440802359402.

Supplementary material

SI1. Supplementary material – chapter 2

SI1.1. Fibre calibration polynomial

Figure S 1 shows the calibration measurement temperatures and the corresponding calibration polynomial of the fibre optic measurement system. T_{Offset} represents the difference between reference temperature (Pt-100) and actual temperature signal on the uncalibrated fibre.

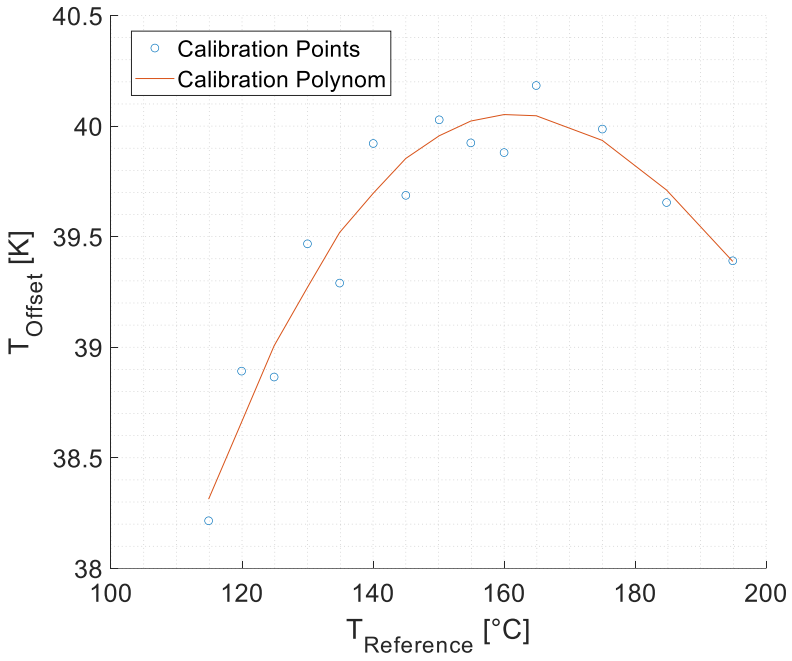

Figure S 1: Calibration points and corresponding calibration curve for the fibre optic temperature measurement system.

SI1.2. Catalyst bed shrinkage

The start of the catalyst bed in the reactor was be identified based on the high-resolution temperature profile. Due to the exothermic reaction the start of the reaction – and thus the start of the catalyst bed – could be quantified by a small, but measurable temperature increase. The shrinkage of the catalyst bed was then calculated for every measurement point. Due to the small degree of exothermic heat in the MeOH dehydration, especially at low reaction rates, the identified position of the catalyst bed varies slightly, resulting in a scatter of the identified points.

Based on a linear fit, an average catalyst bed shift was then calculated for each measurement day and taken into consideration in the reactor simulation when comparing experimental and simulated data. Figure S 2 shows the temporal evolvement of the catalyst bed shift over the time of the measurement campaign.

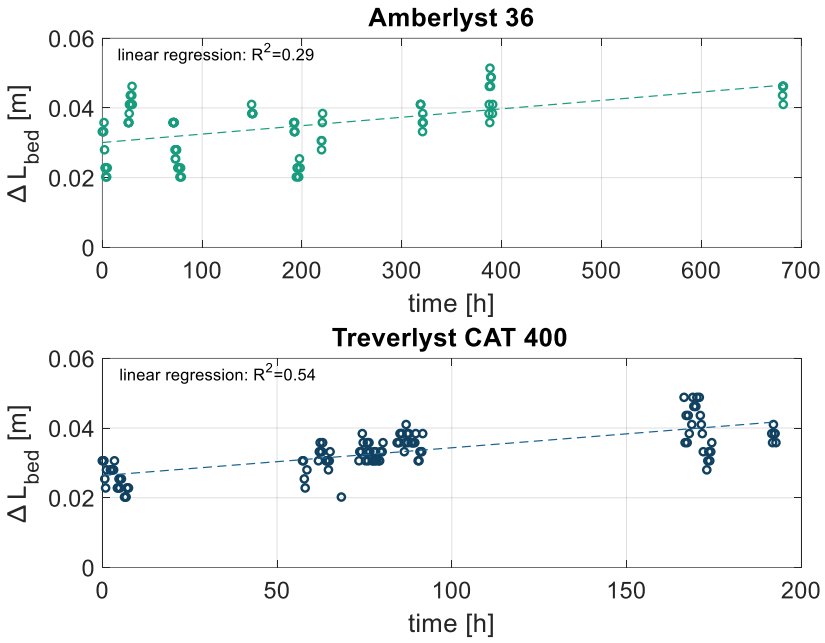

Figure S 2: Course of catalyst bed shift over TOS including linear regression.

As illustrated, just after the filling of the catalyst a significant shrinkage was detected. This is most likely a physical phenomenon resulting from the impulse of the liquid flow through the catalyst bed. However, after the initial shrinkage a further, dynamic shrinkage was detected. This was attributed to the loss of sulfonic groups in the IER, as shown in the measurement of the acid capacity. A lower acid capacity results in a reduced affinity of polar molecules towards the IER and consequently a less pronounced swelling behaviour.

SI1.3. Internal and external mass transfer significance

Internal mass transfer

The significance of internal mass transfer in the resin particle was estimated using the Weisz-Prater parameter ψ according to eq. (31).

$$\psi = L_{C,cat}^2 \cdot \frac{r_{obs} \cdot \rho_{cat}}{D_{eff} \cdot c_{MeOH}} \quad (1)$$

The characteristic length of the catalyst $L_{C,cat}$ is defined by the ratio of particle sphere volume divided by sphere surface area [177].

$$L_{C,cat} = \frac{d_{cat}}{6} \quad (2)$$

Since the influence of Knudsen diffusion can be neglected in the liquid phase, the effective diffusion coefficient D_{eff} is calculated based on the porosity and tortuosity of the catalyst

$$D_{eff} = \frac{\epsilon_{cat}}{\tau_{cat}} \cdot D_i \quad (3)$$

For ion exchange resins, $\frac{\epsilon_{cat}}{\tau_{cat}}$ is typically in the range of 0.25 - 0.5 [178]. For a conservative estimation, a value of 0.25 was used here.

The Weisz-Prater parameter was calculated at the operating point with the highest reaction rate throughout the measurement campaign, meaning the maximum operating temperature of the catalyst and a pure MeOH feed. The results are shown in Table S 1.

Table S 1: Weisz-Prater parameter at the operating point of highest reaction rate for both catalysts investigated in the kinetic study.

Catalyst	T [°C]	D_i [$m^2 s^{-1}$]	D_{eff} [$m^2 s^{-1}$]	Ψ [-]
A36	150	2.261 E-8	5.651 E-9	5.36 E-3
CAT400	180	2.906 E-8	7.264 E-9	1.91 E-2

The obtained values are much lower than 1 and consequently the influence of internal mass transfer is negligible in the reaction system.

External mass transfer

To examine potential external mass transfer limitations, multiple measurements were conducted at identical $WHSV_{Reactor}$ with the flow velocity varied by changing the sampling port and choosing the adequate feed mass flow. As seen in Figure S 3, the variation of the flow velocity has no significant effect on the MeOH conversion. Due to minor uncertainties in the quantification of the catalyst bed shift, that are more pronounced at low reactor lengths, a slight scattering of the measurement points is present for A36. However, it can be concluded, that no external mass transfer limitations were present under the studied conditions of the kinetic measurement campaign.

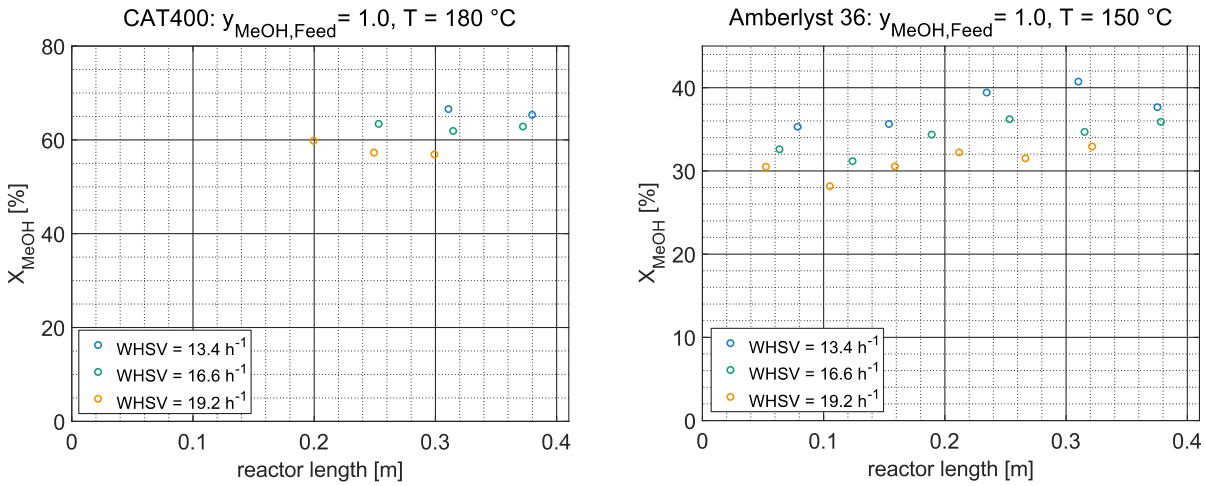

Figure S 3: Examination of the influence of external mass transfer limitations with the catalysts CAT400 (left) and A36 (right); Data points were measured at multiple bed positions with different flow velocities, but identical $WHSV_{Reactor}$.

SI1.4. Catalyst stability

Figure S 4 shows the conversion ratio at selected points in the measurement campaign. The conversion ratio is hereby defined as the MeOH conversion at benchmark conditions at the specified TOS divided by the MeOH conversion of the first benchmark. Both catalysts show a significant activity loss over the limited period of the measurement campaign. CAT400 thereby exhibits a higher activity loss than A36.

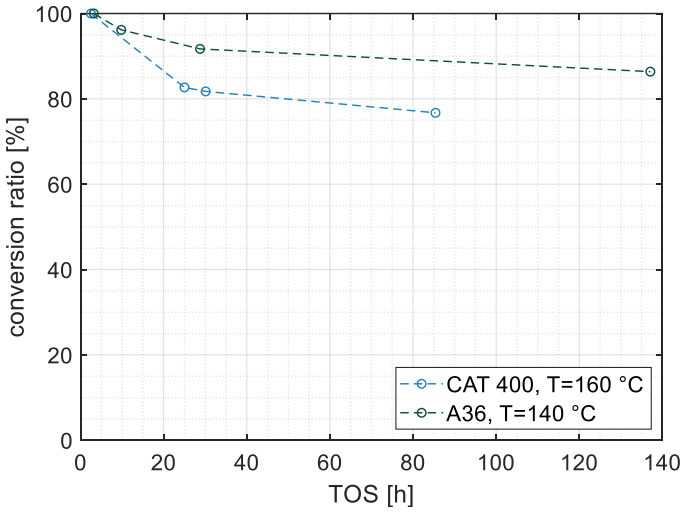

Figure S 4: Conversion ratio over TOS at distinct benchmark operating points. TOS defined as total operating time of the respective catalyst with $T_{Reactor}$ > 100 °C. $WHSV_{Reactor}$ = 16.2 h^{-1}, $y_{MeOH, Feed}$ = 1.0.

The main degradation mechanism known to occur in IER is the loss of sulfonic groups from the polymer matrix (leaching). To examine this phenomenon, the acid capacity of both catalysts was determined by titration before and after the measurement campaign (see Table S 2). The results show that the relative loss of acid capacity is similar for both catalysts and lower than the measured loss of conversion ratio in the benchmark measurements. This indicates the presence of another degradation mechanism, additional to leaching. A potential deactivation mechanism is chemical deactivation by the exchange of H^+-ions with cations. This deactivation is reversible and the IER can be regenerated with a strong acid [179]. Furthermore, this degradation mechanism seems to be more pronounced for CAT400 than for A36, leading to the assumption that this degradation mechanism is significantly influenced by temperature.

These measurements indicate a significant catalyst deactivation under the studied conditions. However, due to the limited operating time it remains unclear whether this is just an initial behaviour or a continuous trend. Furthermore, it should be tested if the degradation may be a result of the drying process in the vacuum dryer, in which the IER experience a significant pressure reduction and subsequent pressure increase. In the beginning of the campaign, the reactor product showed a light yellow colouring, which reduced with increasing measurement time and is most likely connected to the strong initial conversion loss after >50 h TOS, the reactor product showed no significant colouring, indicating that the washout of acid groups was significantly decreased. This observation goes with the reduced rate of conversion reduction at higher TOS. Nevertheless, the results suggest that the maximum operational temperature stated by the resin manufacturers might indeed be too high. This can first of all be attributed to the presence of water in the reaction, leading to an intensified degradation. In a potential industrial application, the operating temperature should thus probably be reduced in order to allow a longer catalyst lifetime. Determining an optimal operating temperature thus requires finding an ideal compromise between stability and activity of the catalyst and should be addressed in future research based on an extended campaign with significantly higher operational hours.

Table S 2: Acid capacity of the IER as stated by the manufacturer and as measured before and after the measurement campaign.

Catalyst	Acid capacity (manufacturer)	Measured acid capacity (new)	Measured acid capacity (used)	Measured relative loss of acid capacity
Unit	[meq g_{Cat}^{-1}]	[meq g_{Kat}^{-1}]	[meq g_{Cat}^{-1}]	[%]
A36	5,4	5,57	5,30	4,8
CAT400	2,7	3,03	2,90	4,3

SI1.5. Model parameters

The model parameters for all kinetic models presented are shown below for both catalysts examined in the kinetic study:

Table S 3: Parameters for all basic and extended ER and LH kinetic models with the surface reaction as RDS for both catalysts examined in the kinetic study.

Parameter	**Unit**	**ERSR**	**ERSR, Langmuir 1**	**ERSR, Langmuir 2**	**ERSR, Freundlich**
A36					
k_0	mol kg_{Cat}^{-1} s^{-1}	1.04E+09	6.46E+09	9.13E+11	7.59E+10
E_A	kJ mol^{-1}	84.92	90.56	100.03	86.52
$K_{Ads,1}$	-	3.21E-07	-5.113E+08	-3723.23	-7.624E+04
$K_{Ads,2}$	K	5.64E+04	-2.13E+09	-1.18E+07	-2.42E+08
K_{W1}	-	-	-7.53	2.207	-0.0521
K_{W2}	K	-	-4032.13	-787.30	-21.05
K_α	K	-	-	-	79232.01
CAT400					
k_0	mol kg_{Cat}^{-1} s^{-1}	3.211E+10	2.059E+11	3.003E+14	9.366E+11
E_A	kJ mol^{-1}	100.30	106.32	128.16	103.18
$K_{Ads,1}$	-	2.058E-03	-1.349E+04	-2.669E+24	-1.968E+04
$K_{Ads,2}$	K	2.494E+04	-4.629E+07	-8.599E+27	-6.751E+07
K_{W1}	-	-	0.210	8.390	-4.514E-02
K_{W2}	K	-	-625.46	2466.22	-14.18
K_α	K	-	-	-	21387.38

Parameter	Unit	LH_{SR}	$LH_{SR,\ Langmuir\ 1}$	$LH_{SR,\ Langmuir\ 2}$	$LH_{SR,\ Freundlich}$
A36					
k_0	mol kg_{Cat}^{-1} s^{-1}	7.69E+08	6.19E+09	1.04E+11	2.07E+10
E_A	kJ mol^{-1}	84.27	90.68	98.28	91.45
$K_{Ads,1}$	-	1.55E-05	147.65	-9.95	232.53
$K_{Ads,2}$	K	4.06E+04	5.31E+05	-3.12E+04	8.30E+05
K_{W1}	-	-	-5.000	0.136	-0.976
K_{W2}	K	-	-2669.65	-382.61	-371.67
K_α	K	-	-	-	2059.16
CAT400					
k_0	mol kg_{Cat}^{-1} s^{-1}	8.777E+09	7.612E+10	3.879E+11	9.016E+10
E_A	kJ mol^{-1}	95.97	102.84	106.92	101.41
$K_{Ads,1}$	-	0.0155	1818.11	-3.021	-1.622E+04
$K_{Ads,2}$	K	1.619E+04	6.873E+06	-6.92E+03	-5.565E+07
K_{W1}	-	-	0.070	1.413	-0.101
K_{W2}	K	-	-490.01	276.92	11.29
K_α	K	-	-	-	1469.31

SI1.6. Liquid properties used in the reactor model

Table S 4 summarizes all correlations used for the calculation of liquid properties required in the reactor model.

Table S 4: Correlations for the calculation of liquid properties required in the reactor model.

Property (liquid)	**Correlation pure substance**	**Correlation mixture**
Density	DIPPR equation 105 / 116 (water) [180] DIPPR 105: $P = a_{DIPPR} \cdot \left(b_{DIPPR}^{1+\left(1-\frac{T}{c_{DIPPR}}\right)^{d_{DIPPR}}} \right)^{-1}$ DIPPR 116: $P = a_{DIPPR} + b_{DIPPR} \cdot \tau_{red}^{0.35} + c_{DIPPR} \cdot \tau_{red}^{\frac{2}{3}} + d_{DIPPR} \cdot \tau_{red} + e_{DIPPR} \cdot \tau_{red}^{\frac{4}{3}}$ With $\tau_{red} = 1 - \frac{T}{T_c}$	VDI heat atlas [181] $\rho_{mix} = \left(\sum_i \frac{x_i}{\rho_i} \right)^{-1}$
Thermal conductivity	DIPPR equation 100 [180] $P = a_{DIPPR} + b_{DIPPR} \cdot T + c_{DIPPR} \cdot T^2 + d_{DIPPR} \cdot T^3 + e_{DIPPR} \cdot T^4$	Li et al. [182] $\lambda_{mix} = \sum_i \sum_j \frac{2 \cdot \phi_i \cdot \phi_j}{\lambda_i^{-1} + \lambda_j^{-1}}$ With $\phi_i = \frac{x_i \cdot v_i}{\sum_i x_i \cdot v_i}$
Dynamic viscosity	DIPPR equation 101 [180] $P = \exp\left(a_{DIPPR} + \frac{b_{DIPPR}}{T} + c_{DIPPR} \cdot \ln(T) \right) + d_{DIPPR} \cdot T^{e_{DIPPR}})$	VDI heat atlas [181] $\ln\left(\frac{\eta_{mix}}{\text{Pas}}\right) = \sum_i x_i \cdot \ln\left(\frac{\eta_i}{\text{Pas}}\right)$
Specific heat capacity	DIPPR equation 100 [180] $P = a_{DIPPR} + b_{DIPPR} \cdot T + c_{DIPPR} \cdot T^2 + d_{DIPPR} \cdot T^3 + e_{DIPPR} \cdot T^4$	Proportionate mean value of pure substance data [181] $c_{p,mix} = \sum_i x_i \cdot c_{p,i}$
Diffusion coefficient	-	Wilke-Chang equation [183] $\mathrm{D_i} = 1.17282 \cdot 10^{-16} \cdot \frac{(\varphi M)^{\frac{1}{2}} \cdot T}{\eta_{nondiff} \cdot (v_{bi})^{0.6}}$ With $\varphi M = \frac{\sum_{j \neq i} x_j \cdot \varphi_j \cdot M_j}{\sum_{j \neq i} x_j}$ v_{bi}: Liquid Molar Volume of pure component at boiling point φ_j: Association factor of solvent $\eta_{nondiff}$: liquid viscosity of all nondiffusing components

SI1.7. Detailed derivation of the kinetic expression

In the following a step-by-step derivation of the kinetic approach including all the simplifications described in section 2.2.3 is shown exemplarily for the case of a LH type kinetic with the surface reaction being the RDS.

General LH approach:

$$r_{DME} = \frac{\hat{k} \cdot K_{MeOH}^2 \cdot \left(y_{MeOH}^2 - \frac{y_{DME} \cdot y_{H_2O}}{K_{eq}}\right)}{\left(1 + K_{MeOH} \cdot y_{MeOH} + K_{DME} \cdot y_{DME} + K_{H_2O} \cdot y_{H_2O}\right)^2}$$

Neglection of DME-Adsorption term $K_{DME} \cdot y_{DME}$ due to low polarity of DME

$$r_{DME} = \frac{\hat{k} \cdot K_{MeOH}^2 \cdot \left(y_{MeOH}^2 - \frac{y_{DME} \cdot y_{H_2O}}{K_{eq}}\right)}{\left(1 + K_{MeOH} \cdot y_{MeOH} + K_{H_2O} \cdot y_{H_2O}\right)^2}$$

Mathematical rearrangement: $\cdot \frac{1}{\mathrm{K_{MeOH}}}$ in nominator and denominator

$$r_{DME} = \frac{\hat{k} \cdot K_{MeOH} \cdot \left(y_{MeOH}^2 - \frac{y_{DME} \cdot y_{H_2O}}{K_{eq}}\right)}{\left(\frac{1}{K_{MeOH}} + y_{MeOH} + \frac{K_{H_2O}}{K_{MeOH}} \cdot y_{H_2O}\right)^2}$$

Mathematical simplification: Combine K_{MeOH} and K_{H2O} to single fitting parameter $K_{Ads} = \frac{K_{H_2O}}{K_{MeOH}}$

$$r_{DME} = \frac{\hat{k} \cdot K_{MeOH} \cdot \left(y_{MeOH}^2 - \frac{y_{DME} \cdot y_{H_2O}}{K_{eq}}\right)}{\left(\frac{1}{K_{MeOH}} + y_{MeOH} + K_{Ads} \cdot y_{H_2O}\right)^2}$$

Neglection of $\frac{1}{K_{MeOH}} \rightarrow 0$ compared to significantly larger terms y_{MeOH} and $K_{Ads} \cdot y_{H_2O}$

$$r_{DME} = \frac{\hat{k} \cdot K_{MeOH} \cdot \left(y_{MeOH}^2 - \frac{y_{DME} \cdot y_{H_2O}}{K_{eq}}\right)}{\left(y_{MeOH} + K_{Ads} \cdot y_{H_2O}\right)^2}$$

Combine $\hat{k} \cdot K_{MeOH}$ to single fitting parameter k

$$r_{DME} = \frac{k \cdot \left(y_{MeOH}^2 - \frac{y_{DME} \cdot y_{H_2O}}{K_{eq}}\right)}{\left(y_{MeOH} + K_{Ads} \cdot y_{H_2O}\right)^2}$$

SI1.8. Experimental conditions of the kinetic measurements

Table S 5 and Table S 6 show the experimental conditions of every measured datapoint used for the kinetic fitting. The MPV position indicates the sample port analysed. The MPV position "2" corresponds to the first sampling port in the catalyst bed, MPV position "7" corresponds to the last sampling port downstream of the catalyst bed as shown in Figure 2-2. MPV position "1" was never selected as this position is only used for the measurement of the feed composition.

Table S 5: Experimental conditions applied throughout the kinetic measurements of A36.

Massflow feed [g h^{-1}]	$y_{MeOH, Feed}$ [mol mol^{-1}]	$T_{reaction, mean}$ [°C]	$p_{Reactor}$ [bar]	**MPV position** [-]	$WHSV_{Reactor}$ [h^{-1}]
119.5	1	140.0	40.2	7	16.2
119.7	1	140.2	40.0	6	19.8
119.7	1	140.1	40.1	5	25.3
119.6	1	140.2	40.1	4	35.2
119.7	1	140.3	40.0	3	57.8
119.4	1	140.0	40.2	2	160.7
119.5	1	140.9	40.3	7	16.2
119.5	1	141.0	40.2	6	19.8
119.4	1	141.0	40.2	5	25.3
119.5	1	141.0	40.2	4	35.2
119.4	1	141.0	40.2	3	57.9
119.4	1	140.6	40.2	2	163.1
119.7	1	150.8	40.2	7	16.2
119.9	1	150.9	40.0	6	19.8
120.0	1	151.0	40.0	5	25.5
119.8	1	151.0	40.0	4	35.5
119.7	1	151.0	40.1	3	58.5
119.7	1	151.0	40.1	2	167.9
119.6	1	109.1	40.3	7	16.2
119.7	1	109.2	40.1	6	19.8
119.7	1	109.2	40.1	5	25.5
119.9	1	109.2	40.2	4	35.7
119.6	1	109.3	40.2	3	59.2
119.7	1	109.3	40.2	2	175.7
119.1	1	120.1	40.3	7	16.1
119.6	1	120.1	40.2	6	19.8
119.4	1	120.1	40.2	5	25.4
119.3	1	120.1	40.2	4	35.5
119.5	1	120.1	40.1	3	59.2
119.2	1	120.2	40.1	2	175.1
119.2	1	141.2	40.2	7	16.2
119.3	1	141.2	40.1	6	19.8
119.5	1	141.2	40.1	5	25.4
119.2	1	141.2	40.2	4	35.5
119.2	1	141.2	40.1	3	59.0
119.2	1	141.2	40.2	2	175.1
119.3	1	131.1	60.2	7	16.2
119.0	1	131.1	60.1	6	19.7
119.6	1	131.1	60.1	5	25.5
119.0	1	131.1	60.1	4	35.5

119.0	1	131.1	60.1	3	59.3
119.6	1	131.1	60.1	2	180.9
120.2	1	140.5	40.1	7	16.3
119.8	1	140.6	40.0	6	19.9
119.5	1	140.7	40.0	5	25.5
119.4	1	140.7	40.0	4	35.7
119.3	1	140.7	40.0	3	59.8
119.0	1	140.5	40.0	2	183.3
119.9	0.98	109.7	40.2	7	16.3
120.0	0.98	109.7	40.1	6	19.9
120.2	0.98	109.8	40.1	5	25.7
120.1	0.98	109.7	40.1	4	36.2
119.8	0.98	109.7	40.1	3	61.1
119.9	0.98	109.8	40.1	2	197.2
120.3	0.98	120.0	40.1	7	16.3
120.2	0.98	120.0	40.0	6	20.0
119.3	0.98	120.1	40.0	5	25.5
119.9	0.98	120.1	40.1	4	36.2
119.8	0.98	120.1	40.1	3	61.1
119.8	0.98	120.1	40.1	2	197.1
119.9	0.98	130.7	40.1	7	16.2
120.1	0.98	130.8	40.0	6	19.9
119.5	0.98	130.8	40.0	5	25.6
119.7	0.98	130.8	40.0	4	36.1
119.7	0.98	130.8	40.0	3	61.0
119.8	0.98	130.9	40.0	2	197.0
119.8	0.98	140.7	40.1	7	16.2
119.2	0.98	140.6	40.0	6	19.8
120.0	0.98	140.6	40.0	5	25.7
119.3	0.98	140.6	40.0	4	36.0
120.8	0.98	140.5	40.0	3	61.6
120.6	0.98	140.5	40.0	2	198.4
120.0	0.98	150.4	40.1	7	16.3
120.1	0.98	150.4	40.0	6	19.9
119.6	0.98	150.4	40.0	5	25.6
119.9	0.98	150.4	40.0	4	36.2
119.9	0.98	150.3	40.0	3	61.1
120.3	0.98	150.3	40.0	2	197.9
120.1	0.90	109.7	40.3	7	16.3
120.0	0.90	109.8	40.1	6	19.9
120.0	0.90	109.8	40.1	5	25.8
120.0	0.90	109.8	40.1	4	36.4
120.0	0.90	109.9	40.1	3	61.9
120.0	0.90	109.9	40.1	2	207.7
120.0	0.90	120.0	40.3	7	16.3
120.0	0.90	120.0	40.1	6	19.9
120.1	0.90	120.0	40.1	5	25.8
119.8	0.90	120.1	40.1	4	36.3
120.0	0.90	120.1	40.1	3	61.9
119.9	0.90	120.1	40.1	2	207.5
119.7	0.90	130.5	40.2	7	16.2
119.9	0.90	130.6	40.1	6	19.9
120.0	0.90	130.6	40.1	5	25.8
120.0	0.90	130.6	40.1	4	36.4
120.1	0.90	130.7	40.1	3	61.9
119.6	0.90	130.7	40.1	2	206.9
120.1	0.90	140.2	40.2	7	16.3
120.1	0.90	140.1	40.1	6	19.9

120.3	0.90	140.2	40.1	5	25.8
120.1	0.90	140.2	40.1	4	36.4
119.5	0.90	140.1	40.0	3	61.7
120.0	0.90	140.2	40.1	2	207.7
121.5	0.90	149.7	40.2	7	16.5
119.8	0.90	149.8	40.1	6	19.9
119.7	0.90	149.8	40.1	5	25.7
120.3	0.90	149.8	40.1	4	36.5
120.0	0.90	149.8	40.1	3	61.9
120.0	0.90	149.8	40.1	2	207.7
120.0	0.47	130.1	40.3	7	16.3
120.0	0.47	130.1	40.1	6	20.0
120.0	0.47	130.2	40.1	5	25.9
119.9	0.47	130.2	40.1	4	36.9
120.0	0.47	130.2	40.1	3	64.0
120.0	0.47	130.4	40.1	2	240.0
119.9	0.47	140.0	40.5	7	16.3
119.9	0.47	140.0	40.1	6	20.0
119.9	0.47	140.1	40.1	5	25.9
120.0	0.47	140.1	40.1	4	36.9
120.0	0.47	140.2	40.1	3	64.0
120.0	0.47	140.2	40.1	2	240.0
119.6	0.71	120.0	40.3	7	16.2
119.5	0.71	120.0	40.1	6	19.9
119.6	0.71	120.0	40.1	5	25.9
119.5	0.71	120.0	40.1	4	36.8
119.7	0.71	120.0	40.1	3	63.9
119.5	0.71	120.1	40.2	2	241.2
119.7	0.71	130.4	40.3	7	16.2
119.6	0.71	130.4	40.2	6	19.9
119.5	0.71	130.4	40.2	5	25.8
119.6	0.71	130.5	40.2	4	36.8
119.6	0.71	130.5	40.2	3	63.9
119.6	0.71	130.5	40.2	2	241.4
119.7	0.71	140.4	40.3	7	16.2
119.6	0.71	140.4	40.1	6	19.9
119.6	0.71	140.4	40.2	5	25.8
119.7	0.71	140.5	40.1	4	36.8
119.7	0.71	140.5	40.2	3	64.0
119.6	0.71	140.5	40.2	2	241.4
119.6	0.71	149.8	40.3	7	16.2
119.5	0.71	149.8	40.1	6	19.9
119.6	0.71	149.8	40.1	5	25.9
119.7	0.71	149.9	40.2	4	36.8
119.6	0.71	149.9	40.1	3	63.9
119.6	0.71	149.9	40.1	2	241.4
119.9	0.49	149.9	40.4	7	16.3
120.0	0.49	150.0	40.1	6	20.0
119.9	0.49	150.1	40.2	5	26.0
119.9	0.49	150.2	40.2	4	37.2
120.0	0.49	150.3	40.1	3	65.5
120.0	0.49	150.4	40.2	2	268.7
120.0	1	140.7	40.3	7	16.3
120.0	1	140.8	40.2	6	20.0
120.0	1	140.8	40.3	5	26.1
120.0	1	140.9	40.3	4	37.3
120.0	1	140.9	40.3	3	65.6
120.0	1	140.9	40.2	2	271.1

Table S 6: Experimental conditions applied throughout the kinetic measurements of CAT400.

Massflow feed [g h^{-1}]	$y_{MeOH, Feed}$ [mol mol^{-1}]	$T_{reaction, mean}$ [°C]	$p_{Reactor}$ [bar]	**MPV position** [-]	$WHSV_{Reactor}$ [h^{-1}]
119.8	1	160.2	70.5	7	16.0
119.7	1	160.3	70.5	6	19.5
119.9	1	160.4	70.6	5	24.9
119.8	1	160.3	70.4	4	34.4
119.7	1	160.2	70.4	3	55.7
119.6	1	160.2	70.5	2	146.2
119.4	1	179.8	70.6	7	16.0
120.0	1	179.6	70.4	6	19.5
120.2	1	179.8	70.6	5	25.0
120.2	1	179.8	70.5	4	34.5
120.1	1	179.7	70.5	3	55.9
120.7	1	179.6	70.5	2	147.5
119.5	1	160.2	70.5	7	16.0
120.0	1	160.2	70.5	6	19.6
119.5	1	160.3	70.6	5	25.0
119.3	1	160.3	70.6	4	34.8
119.9	1	160.3	70.6	3	57.5
119.2	1	160.3	70.5	2	161.6
119.4	1	141.5	70.6	7	16.0
119.5	1	141.4	70.5	6	19.5
119.7	1	141.4	70.6	5	25.0
119.2	1	141.4	70.6	4	34.7
119.2	1	141.4	70.6	3	57.2
119.6	1	141.4	70.6	2	162.2
119.3	1	150.7	70.6	7	16.0
119.7	1	150.7	70.6	6	19.5
119.9	1	150.8	70.6	5	25.1
119.1	1	150.8	70.6	4	34.7
119.0	1	150.8	70.6	3	57.1
119.7	1	150.8	70.6	2	162.3
119.3	1	170.1	70.6	7	16.0
119.2	1	170.1	70.6	6	19.5
119.7	1	170.1	70.6	5	25.0
119.7	1	170.1	70.6	4	34.9
119.4	1	170.1	70.6	3	57.3
119.6	1	170.1	70.6	2	162.1
119.9	1	160.5	70.4	7	16.0
119.4	1	160.5	70.4	6	19.5
119.4	1	160.5	70.4	5	25.0
119.4	1	160.6	70.5	4	34.9
119.1	1	160.6	70.5	3	57.5
119.7	1	160.6	70.5	2	165.8
119.4	0.98	140.5	70.6	7	16.0
119.3	0.98	140.5	70.6	6	19.5
119.7	0.98	140.4	70.6	5	25.1
119.5	0.98	140.5	70.6	4	35.0
120.0	0.98	140.5	70.6	3	58.0
119.2	0.98	140.6	70.6	2	166.2
119.2	0.98	150.8	70.6	7	16.0
119.2	0.98	150.8	70.5	6	19.5
119.2	0.98	150.8	70.6	5	25.0
119.3	0.98	150.9	70.5	4	34.9
119.5	0.98	150.9	70.5	3	57.8
119.2	0.98	150.9	70.5	2	166.2

119.8	0.98	160.7	70.5	7	16.0
118.9	0.98	160.7	70.5	6	19.4
119.9	0.98	160.8	70.5	5	25.1
119.2	0.98	160.8	70.5	4	34.9
119.1	0.98	160.8	70.5	3	57.6
119.3	0.98	160.8	70.5	2	166.3
119.2	0.98	170.4	70.5	7	16.0
119.7	0.98	170.5	70.5	6	19.5
119.5	0.98	170.5	70.5	5	25.0
119.0	0.98	170.5	70.5	4	34.8
119.9	0.98	170.5	70.5	3	57.9
119.3	0.98	170.4	70.5	2	166.3
119.2	0.98	181.0	70.5	7	15.9
119.9	0.98	181.0	70.5	6	19.6
120.0	0.98	181.0	70.6	5	25.1
119.7	0.98	181.0	70.6	4	35.0
119.5	0.98	180.9	70.6	3	57.7
119.6	0.98	180.6	70.5	2	166.7
119.3	0.90	140.3	70.4	7	16.0
119.5	0.90	140.4	70.4	6	19.5
119.9	0.90	140.4	70.5	5	25.2
120.6	0.90	140.5	70.3	4	35.3
120.0	0.90	140.5	70.4	3	58.4
120.7	0.90	140.5	70.3	2	172.1
120.3	0.90	150.6	70.4	7	16.1
119.2	0.90	150.6	70.2	6	19.5
119.3	0.90	150.6	70.3	5	25.0
119.1	0.90	150.7	70.3	4	34.9
118.8	0.90	150.7	70.3	3	57.8
118.9	0.90	150.7	70.3	2	169.5
118.8	0.90	160.5	70.3	7	15.9
118.9	0.90	160.6	70.3	6	19.4
119.3	0.90	160.6	70.3	5	25.0
119.1	0.90	160.6	70.3	4	34.9
119.5	0.90	160.6	70.3	3	58.1
118.5	0.90	160.6	70.3	2	168.9
119.3	0.90	170.3	70.3	7	16.0
119.3	0.90	170.3	70.3	6	19.5
119.7	0.90	170.4	70.3	5	25.1
119.7	0.90	170.4	70.3	4	35.1
119.8	0.90	170.3	70.3	3	58.2
119.4	0.90	170.3	70.3	2	170.2
118.7	0.90	180.7	70.3	7	15.9
119.9	0.90	180.7	70.3	6	19.6
119.3	0.90	180.8	70.3	5	25.0
118.4	0.90	180.8	70.3	4	34.7
119.2	0.90	180.7	70.3	3	58.0
119.1	0.90	180.5	70.3	2	169.7
119.6	0.70	139.6	70.4	7	16.0
119.8	0.70	139.8	70.4	6	19.6
119.5	0.70	139.9	70.5	5	25.3
119.7	0.70	140.0	70.4	4	35.8
119.8	0.70	140.0	70.5	3	61.1
119.6	0.70	140.1	70.3	2	205.4
119.6	0.70	150.2	70.4	7	16.0
119.5	0.70	150.3	70.3	6	19.6
119.6	0.70	150.3	70.4	5	25.3
119.8	0.70	150.4	70.4	4	35.9

119.7	0.70	150.4	70.4	3	61.0
119.6	0.70	150.5	70.4	2	205.3
119.8	0.70	160.3	70.3	7	16.0
119.7	0.70	160.4	70.3	6	19.6
119.7	0.70	160.4	70.4	5	25.4
119.7	0.70	160.4	70.3	4	35.9
119.8	0.70	160.5	70.4	3	61.1
119.9	0.70	160.5	70.3	2	205.8
120.1	0.70	170.2	70.3	7	16.1
120.0	0.70	170.2	70.3	6	19.7
119.9	0.70	170.2	70.3	5	25.4
120.0	0.70	170.2	70.3	4	35.9
119.9	0.70	170.2	70.3	3	61.2
119.9	0.70	170.2	70.3	2	205.9
119.8	0.70	180.4	70.3	7	16.0
120.0	0.70	180.4	70.3	6	19.7
119.9	0.70	180.4	70.3	5	25.4
119.8	0.70	179.9	70.3	4	35.9
120.0	0.70	179.8	70.3	3	61.2
119.9	0.70	179.8	70.3	2	205.9
119.9	0.47	140.1	70.5	7	16.0
120.1	0.47	140.1	70.4	6	19.7
120.1	0.47	140.2	70.4	5	25.5
120.2	0.47	140.2	70.3	4	36.1
120.1	0.47	140.3	70.4	3	61.7
120.1	0.47	140.3	70.4	2	212.9
120.1	0.47	150.2	70.4	7	16.1
120.1	0.47	150.3	70.3	6	19.7
120.1	0.47	150.3	70.3	5	25.5
120.2	0.47	150.4	70.3	4	36.1
120.1	0.47	150.4	70.3	3	61.7
120.2	0.47	150.4	70.4	2	213.0
120.0	0.47	160.3	70.3	7	16.1
120.0	0.47	160.3	70.3	6	19.7
120.1	0.47	160.3	70.3	5	25.5
120.0	0.47	160.3	70.2	4	36.0
120.0	0.47	160.3	70.3	3	61.7
119.9	0.47	160.4	70.3	2	212.5
120.0	0.47	170.0	70.3	7	16.1
119.8	0.47	170.0	70.3	6	19.7
119.9	0.47	170.0	70.3	5	25.5
120.0	0.47	170.0	70.3	4	36.1
120.0	0.47	170.0	70.3	3	61.6
120.1	0.47	170.1	70.4	2	212.9
120.1	0.47	180.1	70.3	7	16.1
120.0	0.47	180.1	70.3	6	19.7
120.0	0.47	180.2	70.3	5	25.5
120.0	0.47	180.2	70.3	4	36.1
119.8	0.47	180.2	70.3	3	61.5
120.0	0.47	180.2	70.3	2	212.7
119.8	1	160.8	70.5	7	16.0
120.0	1	160.8	70.4	6	19.7
120.1	1	160.8	70.4	5	25.5
120.0	1	160.9	70.4	4	36.2
120.0	1	160.8	70.4	3	62.2
119.8	1	160.8	70.4	2	221.1

SI2. Supplementary material – chapter 3

SI2.1. Consistency of measured temperature and dew temperature of analysed gas phase composition

Figure S 5 shows the ratio of the dew temperature of the analysed gas phase composition and the measured temperature at the two sampling positions available in the reactive section (2 and 3). While a slight scattering of the temperature ratio can be observed the average temperature ratio is 0.9992 and 1.0000 for position 2 and 3, respectively. These results show that temperature measurement and gas phase analysis are in accordance with the VLE of the system, thus providing confidence in the measurements.

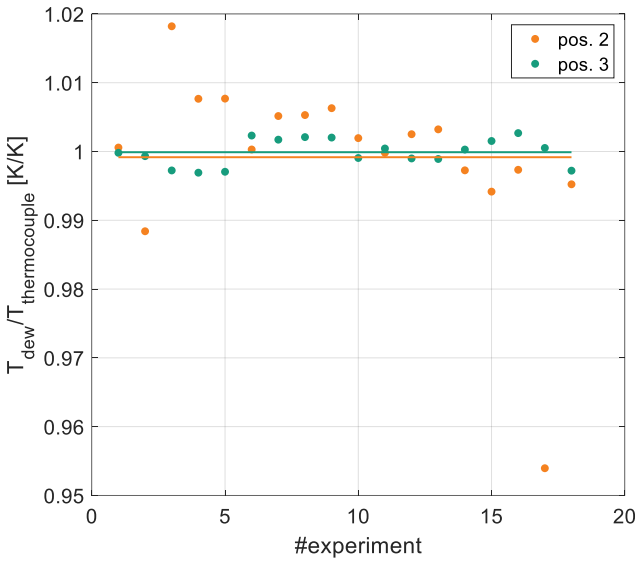

Figure S 5: Relative deviation between measured temperature and dew temperature of the measured gas phase composition.

SI2.2. Complete experimental dataset

Table S 7: Measured temperature data of all experiments performed in the pilot-scale column.

Exp.	TI14	TI13	TI12	TI11	TI10	TI9	TI8	TI7	TI6	TI5	TI4	TI3	TI2	TI1
-	°C	°C	°C	°C	°C	°C	°C	°C	°C	°C	°C	°C	°C	°C
1	184.1	170.5	152.8	144.1	142.0	135.8	133.2	130.2	126.8	104.6	91.4	55.2	54.4	55.4
2	182.0	165.2	148.0	145.7	145.0	141.9	140.5	137.0	138.3	120.2	99.9	55.9	54.8	54.7
3	185.0	162.7	151.5	143.4	141.3	128.2	126.0	123.2	121.2	100.9	90.1	63.0	57.3	63.9
4	186.2	163.8	151.5	143.5	140.7	127.3	125.1	122.2	117.5	96.5	88.0	56.0	53.5	56.1
5	186.5	172.0	151.5	143.6	140.7	127.6	125.5	122.6	117.8	96.8	88.3	56.0	53.8	56.4
6	185.8	174.7	151.4	144.2	143.1	140.3	139.8	129.8	131.0	103.6	94.7	55.9	54.7	56.5
7	185.7	175.2	151.5	144.2	142.0	139.6	138.9	128.9	131.0	109.9	104.3	72.7	66.3	78.3
8	185.8	168.3	151.5	144.1	141.7	138.8	138.0	129.5	131.3	113.0	108.2	84.1	78.9	87.8
9	185.9	166.8	151.5	144.1	141.5	138.7	137.8	129.5	131.4	114.1	109.7	88.5	85.4	91.0
10	186.0	171.7	155.3	146.1	143.8	135.7	132.7	129.8	126.6	105.8	96.0	60.5	57.9	60.0
11	186.5	173.1	152.3	146.8	146.4	143.3	139.0	136.1	135.3	112.2	101.0	61.2	58.2	60.5
12	186.4	167.9	154.4	147.1	145.9	143.5	139.3	136.0	134.2	116.9	109.6	71.1	65.7	76.0
13	186.5	168.1	154.2	147.1	145.8	143.6	140.0	135.1	134.1	116.2	109.1	70.7	65.8	75.3
14	186.0	171.6	152.4	147.2	146.8	144.5	144.6	139.9	139.5	126.3	116.6	80.8	73.7	88.6
15	185.7	176.7	151.4	147.7	147.2	144.8	145.2	140.4	140.4	124.1	110.1	66.9	61.0	67.3
16	187.1	172.2	154.0	146.9	146.6	144.0	139.1	136.4	136.2	111.3	97.9	57.7	56.1	57.1
17	182.2	175.7	149.8	147.5	146.8	144.0	139.5	130.5	134.2	113.6	78.0	53.9	53.9	54.9
18	186.7	177.5	154.9	151.0	150.5	148.8	149.2	145.1	145.2	127.1	104.2	60.5	57.4	58.7

Table S 8: Measured gas phase compositions on the three sampling positions of all experiments performed in the pilot-scale column.

	sampling position 1			sampling position 2			sampling position 3		
Exp.	y_{MeOH}	y_{H2O}	y_{DME}	y_{MeOH}	y_{H2O}	y_{DME}	y_{MeOH}	y_{H2O}	y_{DME}
-	mol.-%	mol.-%	mol.-%	mol.-%	mol.-%	mol.-%	mol.-%	mol.-%	mol.-%
1	1.9%	0.1%	98.0%	39.0%	0.6%	60.3%	91.3%	8.7%	0.0%
2	1.2%	0.1%	98.7%	54.7%	1.0%	44.4%	90.9%	9.1%	0.0%
3	7.0%	0.0%	92.9%	41.9%	0.8%	57.3%	85.8%	9.0%	5.2%
4	3.0%	0.1%	96.9%	31.5%	0.5%	68.1%	86.6%	8.8%	4.6%
5	3.2%	0.1%	96.7%	31.8%	0.5%	67.7%	86.6%	9.0%	4.4%
6	3.0%	0.1%	96.9%	39.5%	0.3%	60.2%	89.8%	10.1%	0.0%
7	13.5%	0.0%	86.5%	47.9%	0.6%	51.6%	89.3%	10.7%	0.0%
8	19.8%	0.0%	80.2%	51.4%	0.7%	47.9%	88.8%	11.1%	0.1%
9	22.6%	0.0%	77.4%	53.3%	0.8%	45.9%	88.6%	11.3%	0.1%
10	3.5%	0.1%	96.4%	38.5%	0.6%	60.8%	90.4%	9.4%	0.2%
11	3.1%	0.2%	96.7%	46.7%	1.1%	52.2%	90.7%	9.3%	0.0%
12	11.1%	0.1%	88.8%	52.5%	1.2%	46.2%	89.9%	10.0%	0.1%
13	10.4%	0.1%	89.5%	52.2%	1.3%	46.6%	89.7%	10.2%	0.2%
14	18.9%	0.3%	80.9%	63.5%	1.8%	34.6%	90.0%	10.0%	0.0%
15	7.4%	0.1%	92.6%	61.0%	1.1%	38.0%	87.2%	12.8%	0.0%
16	1.7%	0.0%	98.3%	46.4%	0.5%	53.1%	88.1%	11.8%	0.0%
17	0.1%	0.0%	99.9%	29.3%	0.3%	70.4%	89.0%	11.0%	0.0%
18	2.8%	0.0%	97.2%	52.8%	9.1%	38.1%	83.7%	16.3%	0.0%

SI2.3. Mass balance and energy balance of column

Since the MeOH dehydration is an equimolar reaction, the overall mass balance of the column is:

$$\dot{n}_{\mathrm{Feed}} = \dot{n}_{\mathrm{distillate}} + \dot{n}_{\mathrm{bottoms}} \tag{4}$$

In the component mole balance, the MeOH conversion X_M needs to be accounted for. Considering that no significant amounts of the light boiler DME will be in the bottoms product or the heavy boiler water in the distillate, the component mole balances are as follows:

MeOH balance
$$\dot{n}_{\mathrm{Feed}} \cdot x_{\mathrm{MeOH,Feed}} = \dot{n}_{\mathrm{Feed}} \cdot x_{\mathrm{MeOH,Feed}} \cdot X_M + \dot{n}_{\mathrm{distillate}} \cdot x_{\mathrm{MeOH,distillate}} + \dot{n}_{\mathrm{bottoms}} \cdot \mathrm{x}_{\mathrm{MeOH,bottoms}} \tag{5}$$

H_2O balance
$$\dot{n}_{\mathrm{Feed}} \cdot x_{\mathrm{H2O,Feed}} + \dot{n}_{\mathrm{Feed}} \cdot x_{\mathrm{MeOH,Feed}} \cdot \frac{X_M}{2} = \dot{n}_{\mathrm{bottoms}} \cdot \mathrm{x}_{\mathrm{H2O,bottoms}} \tag{6}$$

DME balance
$$\dot{n}_{\mathrm{Feed}} \cdot x_{\mathrm{MeOH,Feed}} \cdot \frac{X_M}{2} = \dot{n}_{\mathrm{distillate}} \cdot x_{\mathrm{DME,distillate}} \tag{7}$$

Rearranging the equations (4)-(7) an explicit formula for the calculation of the MeOH conversion can be found based on the measured composition of the bottoms product and the distillate.

$$X_M = \frac{x_{\mathrm{MeOH,Feed}} - x_{\mathrm{MeOH,bottoms}}}{\frac{x_{\mathrm{MeOH,Feed}}}{2 \cdot x_{\mathrm{DME,distillate}}} \cdot (x_{\mathrm{MeOH,distillate}} - x_{\mathrm{MeOH,bottoms}}) + x_{\mathrm{MeOH,Feed}}} \tag{8}$$

The energy balance of the column is given by the following equation:

$$\dot{n}_{\mathrm{Feed}} \cdot h_{\mathrm{Feed}} + Q_{\mathrm{reboiler}} = \dot{n}_{\mathrm{distillate}} \cdot h_{\mathrm{distillate}} + \dot{n}_{\mathrm{bottoms}} \cdot h_{\mathrm{bottoms}} + Q_{\mathrm{condenser}} \tag{9}$$

Rearranging the energy balance provides the condenser duty. Based on the condenser duty, the mole flow of the condensate can be obtained by an energy balance over the condenser:

$$\dot{n}_{\mathrm{condensate}} = \frac{Q_{\mathrm{condenser}}}{\Delta h_{\mathrm{condensate}}} \tag{10}$$

The enthalpy change of the condensate is calculated considering both the condensation enthalpy and enthalpy change due to subcooling based on the actual composition of the condensate according to the FT-IR analysis and the measured temperature T_{in} before the condenser and the subcooling temperature:

$$\Delta h_{\mathrm{condensate}} = \Delta h_{\mathrm{v,condensate}} + c_{p,\mathrm{condensate}} \cdot (T_{\mathrm{in}} - T_{\mathrm{subcool}}) \tag{11}$$

Knowing the mole flow of the condensate from eq. (10) and the measured distillate mole flow, the reflux ratio can be calculated:

$$RR = \frac{\dot{n}_{\text{reflux}}}{\dot{n}_{\text{distillate}}} = \frac{\dot{n}_{\text{condensate}} - \dot{n}_{\text{distillate}}}{\dot{n}_{\text{distillate}}} \tag{12}$$

SI2.4. Models for the Calculation of Thermodynamic and Physical Properties

Table S 9 summarizes the models used to calculate the thermodynamic and physical properties in Aspen Plus®. The interested reader is referred to the Aspen Plus® Help for further information on the models.

Table S 9: Models used for the calculation of thermodynamic and physical properties in Aspen Plus®.

Property	Route ID	Property	Route ID
PHIVMX	PHIVMX41	SL	SL22
PHILMX	PHILMX94	VV	VV01
HVMX	HVMX41	VL	VL01
HLMX	HLMX94	DL	DL01
GVMX	GVMX23	DV	DV02
GLMX	GLMX94	MUL	MUL01
SVMX	SVMX41	MUV	MUV01
SLMX	SLMX41	KV	KV04
VVMX	VVMX01	KL	KL04
VLMX	VLMX01	SIGL	SIGL01
MUVMX	MUVMX04	PHISMX	PHISMX00
MULMX	MULMX05	HSMX	HSMX02
KVMX	KVMX04	GSMX	GSMX02
KLMX	KLMX03	SSMX	SSMX01
DVMX	DVMX02	VSMX	VSMX02
DLMX	DLMX02	KSMX	KSMX01
SIGLMX	SIGLMX01	PHIS	PHIS00
PHIV	PHIV41	HS	HS02
PHIL	PHIL41	GS	GS02
HV	HV42	SS	SS02
HL	HL41	VS	VS01
GV	GV21	KS	KS01
GL	GL22	WSL	WATSOL00
SV	SV21	HCSL	HCSOL01

SI2.5. Influence of feed stage and feed composition for CAT400

Figure S 6 shows the specific reboiler duty per ton of produce DME in dependence of the feed stage and the water mole fraction of the feed. The absolute methanol flow of the feed was kept constant at 17.5 t/h, while an additional water mass flow was added to achieve the respective molar fraction. The catalyst mass in the RD column was 24 t, resulting in a $WHSV_{RD}$ of 0.73 h^{-1}. The used catalyst for the simulation was CAT400, the maximum operating temperature in the reactive section was set to 160 °C by varying the column pressure as described in chapter 4.4. The resulting operating pressure of all operating points shown was between 12.9-14.3 bar depending on the feed stage and the feed composition.

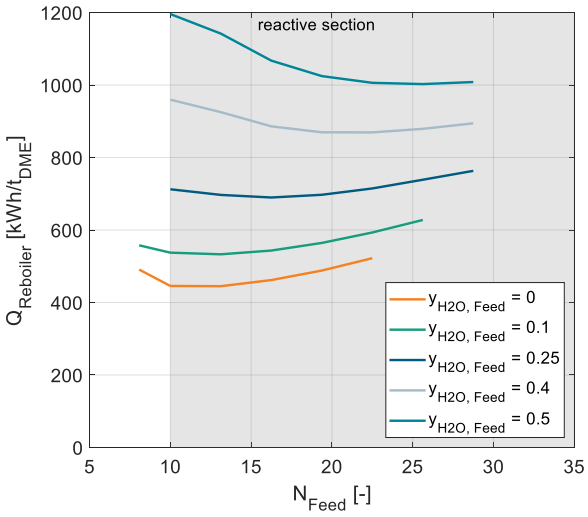

Figure S 6: Specific reboiler duty per ton of produced DME in dependence of the feed stage for various molar water fractions in the feed. $WHSV_{RD}$=0.73 h^{-1}. $N_{rect,\ upper}$=10, $N_{rect,\ lower}$=14, $N_{reactive}$=25. Use of CAT400 in the reactive section with T_{max}=160 °C.

SI3. Supplementary material – chapter 4

SI3.1. Detailed process description

In the following, the processes P0-P4 discussed in the main article are described in detail.

P0: Conventional Process

The conventional process is based on the gas-phase methanol dehydration over γ-Al_2O_3 in an adiabatic fixed-bed reactor as shown in Figure S 7. A detailed description is given by Bildea et al. [124].

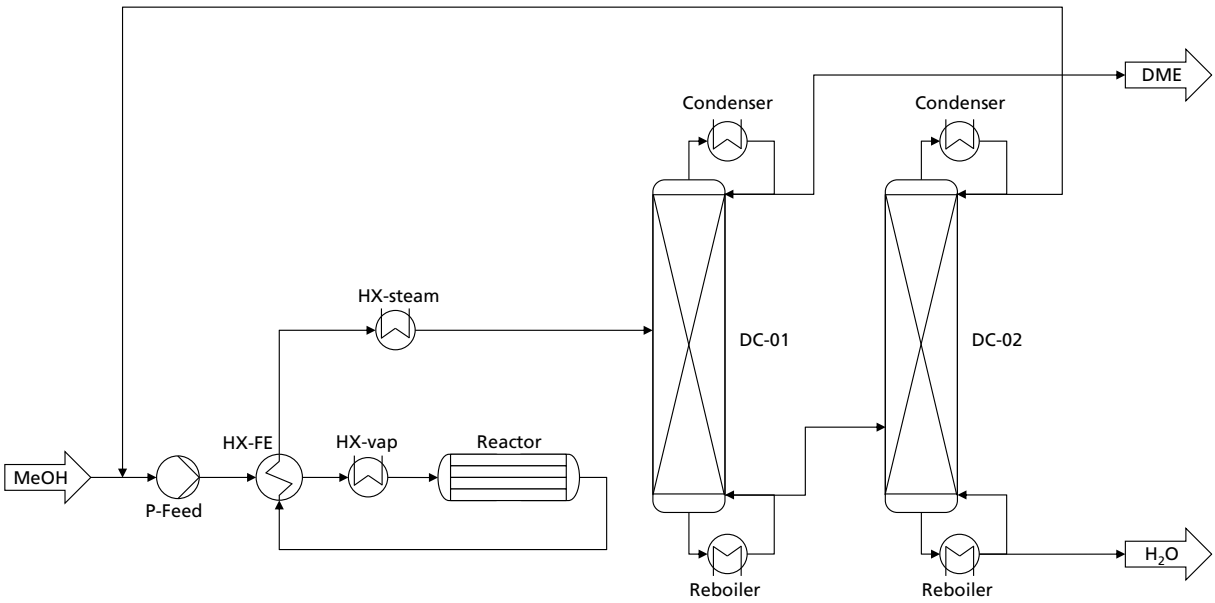

Figure S 7: Process flow diagram of process P0.

The crude MeOH is purified in a dedicated CMD column. The pure MeOH is mixed with recycled MeOH from the DME process and then pressurized to the reaction pressure of 12 bar, preheated by the feed-effluent heat exchanger HX-FE and evaporated in HX-vap prior to being fed to the adiabatic reactor, where the gaseous MeOH is dehydrated to DME and H_2O. The reactor effluent is cooled down in HX-FE, the remaining heat is used in the steam generator HX-steam. The cooled, but still gaseous reactor product is then fed to the DME column, where DME is withdrawn as distillate. The bottoms product consisting of MeOH and H_2O is forwarded to the second distillation column where the MeOH distillate is withdrawn and recycled and the water by-product is removed as bottom stream. The stage number and feed stage of both columns are taken from Bildea et al. [124], the column height and diameter were calculated based on the HETP of the packing and the Aspen internal hydraulics tool.

P1: Liquid phase reaction – separation – recycle

A significant energy demand in P0 is required for the evaporation of the MeOH feed. Consequently, in the process P1, the reaction was shifted to the liquid phase to explore the potential of increasing the energy efficiency of the process. Process P1 resembles P0, the major distinction however is the reaction phase being liquid rather than gaseous. This leads to a different reaction temperature and heat integration concept. Instead of an adiabatic reactor,

an isothermal reactor is implemented due to the temperature sensitivity of the IER catalysts. The flowsheet of this process is shown in Figure S 8.

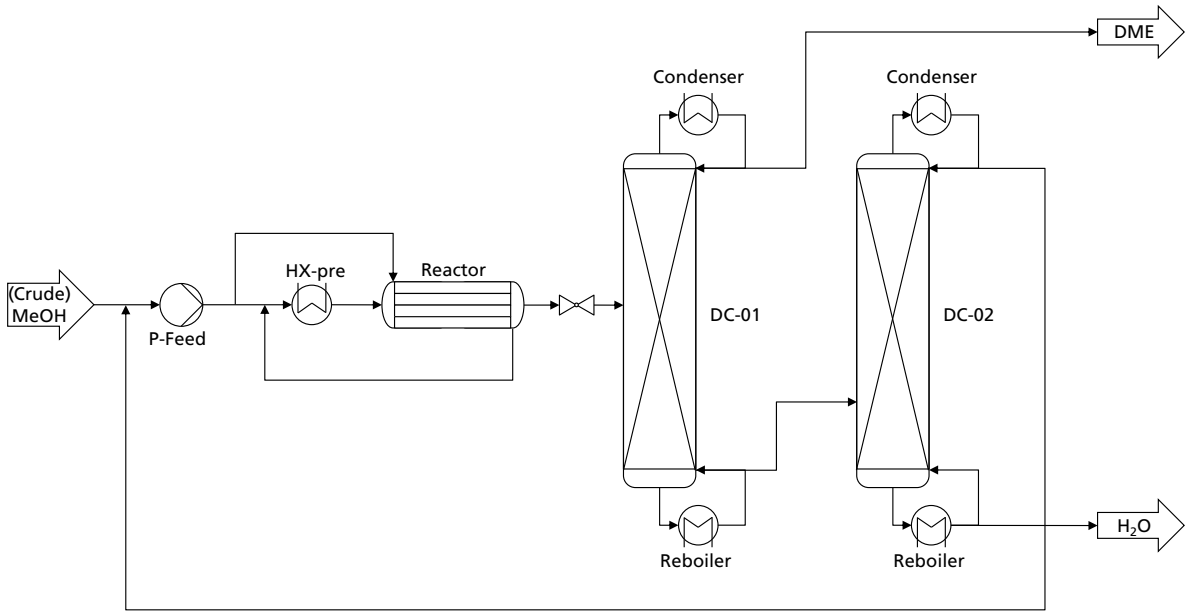

Figure S 8: Process flow diagram of process P1.

The cold feed is first mixed with recycled MeOH and then pumped to reaction pressure. The pressurized feed is then partially used as cooling medium for the isothermal liquid phase reactor. Thereby the feed is partially pre-heated. In an additional steam operated heat exchanger HX-pre, the feed is then conditioned to the final reaction temperature. In the liquid phase reactor, the MeOH is partially dehydrated to DME and H_2O. Subsequently the reactor product is throttled and fed to a series of two distillation columns. The pressure level and operating parameters of the distillation columns were adopted from P0.

P2: Stand-alone reactive distillation

P2 is a highly intensified process concept with the RDC being the central unit operation. Figure S 9 shows the corresponding process flow diagram.

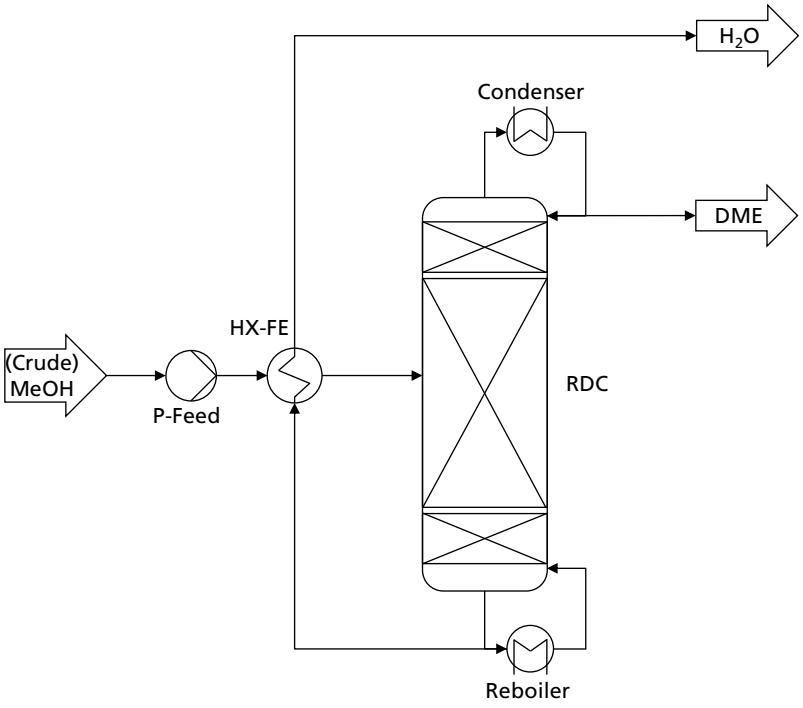

Figure S 9: Process flow diagram of process P2.

The feed is first pressurized, and heat integrated with the bottoms product of the RDC by HX-FE before entering the RDC in liquid state on the feed stage N_{Feed}. The size of the reactive section of the RDC is designed to allow a full conversion of the MeOH to DME and H_2O. Two rectifying sections above and below the reactive section are required to purify the products. The bottoms product is pure H_2O and is used to preheat the feed stream. The distillate product is pure DME.

P3: Reactive distillation column with pre-reactor

P3 presents an extension of P2 by adding a PR to the flowsheet. Figure S 10 shows the corresponding flowsheet. This additional reaction volume is expected to allow a smaller RDC which could lead to lower plant cost and energy demand.

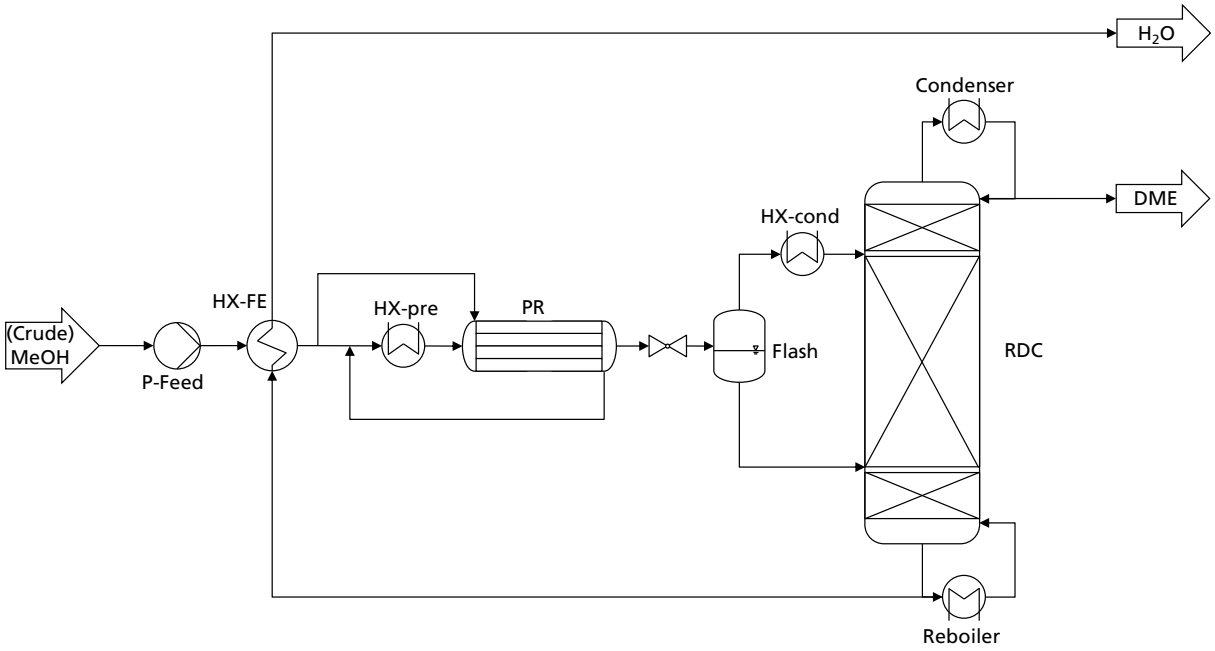

Figure S 10: Process flow diagram of process P3.

The fed MeOH is first pumped to the reactor operating pressure, which is significantly higher than the RDC pressure to attain a liquid phase reaction. For A36 and CAT400, a reactor pressure of 47 bar (T_{max}=130 °C) and 76 bar (T_{max}=160 °C) is required, respectively. The feed is heat integrated with the bottoms product of the RDC via HX-FE and with the PR to allow an isothermal reactor operation and to utilize the exothermic heat for further pre-heating of the feed. The steam operated HX-pre is then used for final feed conditioning. In the PR, MeOH is partially dehydrated, thus reducing the required amount of catalyst in the RDC. Due to the large difference in vapor pressure between DME and H_2O, feeding the reactor effluent to the RDC on a single stage is detrimental for the column profile. Feeding in the upper part of the column would mean introducing significant amounts of water to the reactive section, thus inhibiting the reaction. In contrast, feeding in the lower part of the column would lead to significant amounts of DME in the reactive section, reducing the boiling temperature of the mixture in the reactive section and thus reducing the reaction rate. For this reason, the reactor product is throttled to the column pressure and an adiabatic flash separation is performed between PR and RDC. The DME-rich gas phase is condensed in HX-cond and fed to the upper part of the RDC on stage $N_{Feed,DME\text{-}rich}$ while the H_2O-rich liquid phase is fed to the bottom part of the RDC on stage $N_{Feed,H2O\text{-}rich}$. In the RDC, the residual MeOH from the reactor product is fully converted and DME and H_2O are withdrawn as distillate and bottom stream, respectively.

P4: Reactive distillation column with side-reactor

Process P4 is characterized by a combination of RDC and SR. The underlying process flow diagram is shown in Figure S 11.

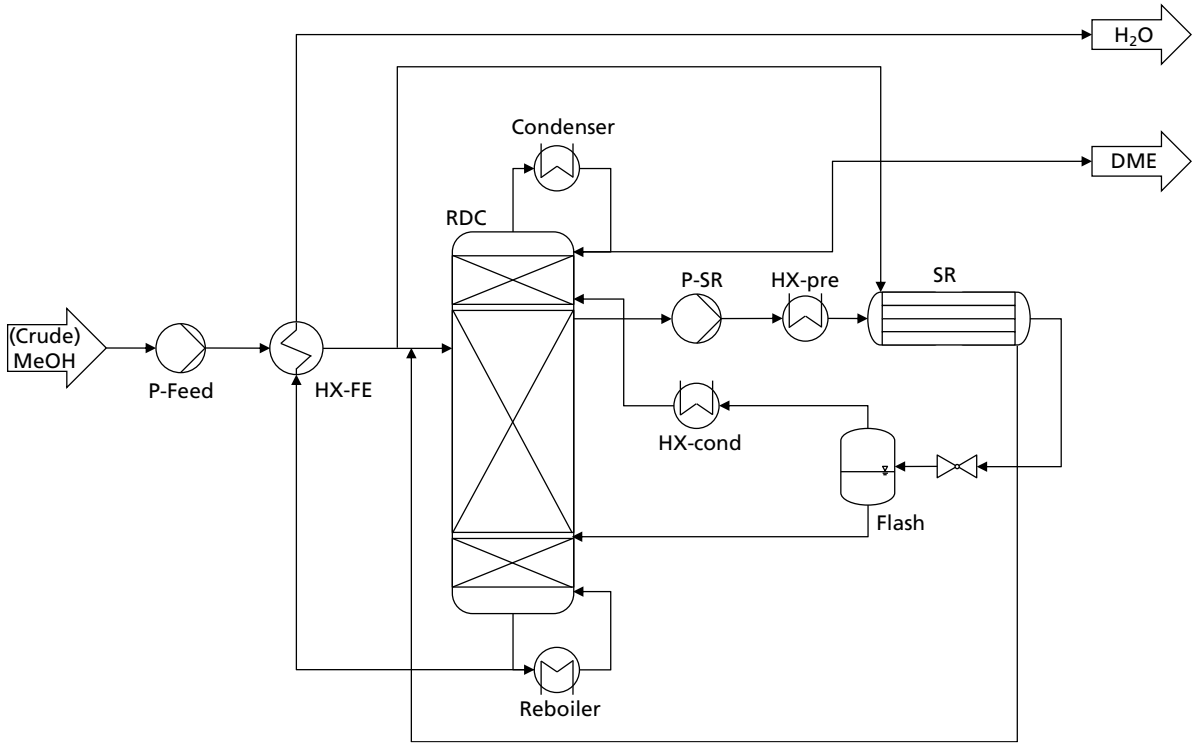

Figure S 11: Process flow diagram of process P4.

The feed stream is pumped to the operating pressure and fed to the RDC at N_{Feed}. Heat integration is then performed with the bottom product of the RDC via HX-FE and the preheated feed stream is partially used to cool the SR. The heat integration is analogous to P3. While the unit operations used are the same as in P3, the different arrangement of RDC and reactor gives more degrees of freedom: An additional withdrawal stage N_{WD} is implemented at the RDC, where the feed to the SR is withdrawn with a certain flow rate $\dot{N}_{Side}$, pumped to reaction pressure by P-SR and conditioned by HX-pre to reactor pressure and temperature of the SR. The same reaction conditions apply depending on the catalyst type as already explained for P3. The product mixture is throttled to the operating pressure of the RDC as in P3, and the resulting two-phase mixture is separated in an adiabatic flash separator. The DME-rich phase is condensed in HX-cond and recycled to the top of the RDC at $N_{RCY,\ DME\text{-}rich}$. The water-rich phase is directly recycled to the bottom RDC at $N_{RCY,\ H2O\text{-}rich}$. The RDC itself operates analogous to P2 and P3.

Crude MeOH distillation

In case of a pure MeOH feed to the DME process (case A), the water in the crude MeOH needs to be removed in a dedicated CMD column. Figure S 12 shows the corresponding flowsheet.

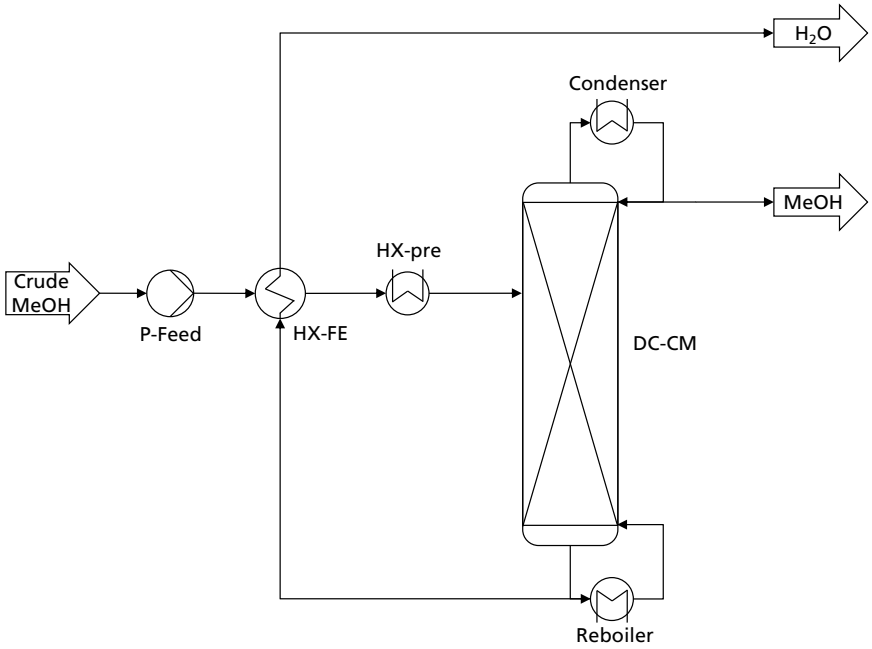

Figure S 12: Process flow diagram of the CMD process.

The crude MeOH is pre-heated in HX-FE, furtherly heated and partly evaporated HX-pre and then fed to the CMD column DC-CM operated at ambient pressure.

SI3.2. Detailed results of crude MeOH distillation step

Table S 10: KPI of crude MeOH distillation step

Unit Operation	Parameter	Unit	Value
HX-FE	Q	kW	846
HX-pre	Q	kW	8606
DC-CM	H_{column}	m	6
	d_{column}	m	2
	p	bar	1
	RR	-	1,5
	$Q_{Reboiler}$	kW	5500
	$Q_{Condenser}$	kW	-13315

SI3.3. Kinetic rate equation for the liquid phase MeOH dehydration

The kinetic rate equation for the liquid phase MeOH dehydration is presented according to Semmel et al. [149]. x_i denotes the liquid mole fraction of the component i.

$$r_{\mathrm{DME}} = \frac{k \cdot \left(x_{\mathrm{MeOH}}^2 - \frac{x_{\mathrm{DME}} \cdot x_{\mathrm{H_2O}}}{K_{\mathrm{eq}}}\right)}{x_{\mathrm{MeOH}}{}^2} \cdot \frac{1}{(1 + K_{\mathrm{W}} \cdot x_{\mathrm{H2O}})^2} \quad (13)$$

With

$$k = \mathrm{k}_0 \cdot \exp\left(\frac{-\mathrm{E_A}}{R\,T}\right) \quad (14)$$

$$K_W = exp\,(K_{W1} - \frac{K_{W2}}{T}) \quad (15)$$

$$K_{eq} = exp\,(1.743 + \frac{887.9}{T}) \quad (16)$$

Table S 11: Kinetic parameters for the liquid phase MeOH dehydration on the two catalysts A36 and CAT400 [149].

Parameter	Unit	A36	CAT400
k_0	mol $\mathrm{kg_{Cat}^{-1}}$ $\mathrm{s^{-1}}$	8.089e9	5.973e10
$\mathrm{E_A}$	kJ $\mathrm{mol^{-1}}$	91.56	101.98
$\mathrm{K_{W1}}$	-	−4.2255	0.4118
$\mathrm{K_{W2}}$	K	−2360.9	−345.2587

SI3.4. Kinetic rate equation for the gas phase MeOH dehydration

The kinetic rate equation for the conventional gas-phase DME synthesis from MeOH according to the corrected publication of Bercic et al. [167] X denotes the gaseous mole fraction of the component i in mole percent.

$$r_{\mathrm{DME}} = \frac{k_s \cdot K_{\mathrm{M}}^2 \left(X_{\mathrm{MeOH}}^2 - \frac{X_{\mathrm{DME}} \cdot X_{\mathrm{H_2O}}}{K}\right)}{\left(1 + 2 \cdot \sqrt{K_{\mathrm{M}} \cdot X_{\mathrm{MeOH}}} + K_{\mathrm{W}} \cdot X_{\mathrm{H_2O}}\right)^4} \quad (17)$$

Table S 12: Parameters for the apparent gas phase MeOH dehydration kinetics on industrial sized γ-Al_2O_3 catalyst [167].

Parameter	Unit	Value
$\mathrm{k_s}$	kmol $\mathrm{kg_{Cat}^{-1}}$ $\mathrm{h^{-1}}$	6.6E8 exp(-10800 $\mathrm{T^{-1}}$)
$\mathrm{K_M}$	$\%^{-1}$	7.2E-3 exp(830 $\mathrm{T^{-1}}$)
$\mathrm{K_W}$	$\%^{-1}$	4.5E-3 exp(1130 $\mathrm{T^{-1}}$)

SI3.5. Economic and technical assumptions for the TEA

Table S 13: Lang factors for the calculation of the fixed capital investment for fluid processing chemical plants based on equipment cost (EC) [174].

Cost component	Basis	Value
Direct plant cost (DPC)		
Equipment installation	EC	0.47
Instrumentation and control	EC	0.36
Piping (installed)	EC	0.68
Electrical (installed)	EC	0.11
Buildings including services	EC	0.18
Yard improvements	EC	0.1
Service facilities (installed)	EC	0.55
Indirect plant cost (IPC)		
Engineering and supervision	EC	0.33
Construction expenses	EC	0.41
Legal expenses	EC	0.04
Contingency and contractor's fee		
Contractor's fee	DPC + IPC	0.05
Contingency	DPC + IPC	0.1

Table S 14: Lang factors for the calculation of $OPEX_{ind}$ [174].

Cost component	Basis	Value
Operating Supervision (OS)	OL	0.15
Maintenance labour (ML)	FCI	0.01
Maintenance material (MM)	FCI	0.01
Operating supplies	ML+MM	0.15
Laboratory charges	OL	0.2
Insurance and taxes	FCI	0.02
Plant overhead costs (PO)	OL+OS+ML	0.6
Administrative costs	PO	0.25

Table S 15: Correlation for estimating the operating labour of large scale or fluid processes [174].

	Sizing parameter	Cost function
Operating labour (OL) in hours/day/processing step	Plant capacity C in kg day^{-1}	$\mathrm{OL} = 2.05 \cdot \mathrm{C}^{0.245}$

Table S 16: Heat transition coefficient used for the different heat exchangers in the studied processes [184].

Heat exchanger	Unit	Heat transition coefficient
Column reboiler	W m^{-2} K^{-1}	1750
Column condenser	W m^{-2} K^{-1}	700
HX-pre	W m^{-2} K^{-1}	1050
HX-cond	W m^{-2} K^{-1}	700
HX-FE (liquid-liquid, P1-P4)	W m^{-2} K^{-1}	700
HX-FE (gas-liquid, P0)	W m^{-2} K^{-1}	200
HX-vap (evaporation)	W m^{-2} K^{-1}	900
HX-vap (superheat)	W m^{-2} K^{-1}	300
HX-steam	W m^{-2} K^{-1}	200

SI3.6. Cost functions for equipment cost

Table S 17: Cost functions for calculation of the equipment cost in $\$_{2002}$ and $\$_{2012}$, respectively.

Apparatus	Sizing parameter	Cost function	Source
Pump	$\dot{V}$ in m^3 s^{-1}	$EC_{\$2002} = F_p \cdot (18963.48 \cdot \dot{V}^{0.4} + 222.35)$	Own regression based on Peters et al. [174]
Pump: pressure correction	p in kPa	$F_p = 0.000426 \cdot p + 0.59$	
Heat exchanger	A in m^2	$EC_{\$2002} = F_p \cdot (0.00004 \cdot A^3 - 0.08 \cdot A^2 + 93.38 \cdot A + 3506.2)$	Own regression based on Peters et al. [174]
Heat exchanger: pressure correction - tube	p in kPa	$F_p = 0.000020 \cdot p + 0.984$	
Heat exchanger: pressure correction – tube&shell	p in kPa	$F_p = 0.000070 \cdot p + 0.9349$	
Column shell	H in m, d in m	$EC_{\$2002} = F_p \cdot (4051.28 \cdot d^2 + 3538{,}89 \cdot d + 31.82 \cdot H^2 + 2041.8 \cdot H - 9891.17)$	Own regression based on Peters et al. [174]
Column shell: pressure correction	p in kPa	$F_p = 0.00037 \cdot p + 1.2265$	
Reactor (isotherm)	A in m^2	$EC_{\$2002} = F_p \cdot (0.00004 \cdot A^3 - 0.08 \cdot A^2 + 93.38 \cdot A + 3506.2)$	Own regression based on Peters et al. [174]
Reactor: pressure correction	p in kPa	$F_p = 0.000070 \cdot p + 0.9349$	
Reactor: tube diameter	d in m	$F_d = 710.93 \cdot d^2 - 16.56 \cdot d + 0.935$	
Reactor (adiabatic)	d in m, L in m	$EC_{\$2012} = \frac{1536.5}{280} \cdot 957.9 \cdot d^{1.066} \cdot L^{0.82} \cdot (2.18 + F_p)$	Bildea et al. [124]
Reactor (adiabatic): pressure correction	p in bar	$F_p = 1 + 0.0074 \cdot (p - 3.48) + 0.00023 \cdot (P - 3.48)^2$	
Flash[1]	H in m	$EC_{\$2002} = F_p \cdot (-2.29 \cdot H^2 + 387.6 \cdot H + 788.66)$	Own regression based on Peters et al. [174]
Flash: pressure correction	p in kPa	$F_p = 0.00040 \cdot p + 1.2265$	

[1] Correlation for flash diameter of 0.5 m.

SI3.7. Hydraulic regression function

The hydraulic design of the RDC was conducted according to Brunazzi et al. [185]. The basis of this design method is a quadratic equation (18) correlating the gas velocity with the total pressure drop of the wet packing $\frac{\Delta p_{wet}}{\Delta Z}$. The equation's solution is limited to the positive results.

$$\frac{\mathrm{a}\cdot\rho_{\mathrm{G}}\cdot P_D}{(\sin^2(\theta_{\mathrm{p}})\cdot\epsilon^3\cdot\mathrm{f_s}}\cdot\mathrm{u_{Gas}^2}+\frac{\mathrm{a}\cdot\eta_{\mathrm{G}}\cdot\mathrm{P_E}}{\sin(\theta_{\mathrm{p}})\cdot\epsilon^2\cdot\mathrm{d_{eq}}}\cdot\mathrm{u_{Gas}}-\frac{\Delta\mathrm{p_{wet}}}{\Delta\mathrm{Z}}\cdot\left(1-\mathrm{P_F}\cdot\mathrm{h_{L,Start}}\right)^5=0 \tag{18}$$

The quadratic equation is solved at the flooding point to yield the maximum gas velocity $\mathrm{u_{G,max}}$ before flooding. At the flooding point, the pressure drop is defined as follows:

$$\left(\frac{\Delta\mathrm{p_{wet}}}{\Delta\mathrm{z}}\right)_{\mathrm{f}}=\sqrt{\frac{1-\mathrm{P_F}\cdot\mathrm{h_{L,oc,0}}}{11\cdot\mathrm{P_F}\cdot\mathrm{P_C}\cdot\mathrm{h_{L,oc,0}}}}\cdot\rho_{\mathrm{L}}\cdot\mathrm{g} \tag{19}$$

The operating gas velocity $\mathrm{u_G}$ is selected to be 80 % of the maximum gas velocity:

$$\mathrm{u_{Gas}}=0.8\cdot\mathrm{u_{Gas,max}} \tag{20}$$

For the detailed entire calculation method the reader is referred to the original literature of Brunazzi et al. [185] and Hoffmann et al. [169].

Table S 18 shows the design parameters for the catalytic packing used in this work. They were adopted from the packing MULTIPAK®-II at large column diameters (>1 m) to account for the large production capacity of the plant considered in this work.

Table S 18: Used parameters for the catalytic packing.

Parameter	Unit	Value	Source
Specific surface area a	m^2/m^3	325	[169]
Void fraction packing ϵ	-	0.35	[169]
Catalyst volume fraction χ_{cp}		0.55	[169]
Inclination angel θ_p	°	45	[169]
Equivalent diameter d_{eq}	m	$\frac{4\cdot\epsilon}{\mathrm{a}}$	[169]
Wall factor f_s	-	1	Approximation for large column diameters
Void fraction catalyst bags ϵ_{CB}	-	0.3	[169]
Catalyst particle diameter d_{cat}	m	0.001	[150]
Packing parameter P_A	-	0.2	[169]
Packing parameter P_B	-	0.25	[169]
Packing parameter P_C	-	150	[169]
Packing parameter P_D	-	0.024	[169]
Packing parameter P_E	-	6.6	[169]
Packing parameter P_F	-	2	[169]

The hydraulic design is carried out for the reactive section only. The reactive stage with the highest gas load is the limiting stage and consequently used as design stage. The resulting column diameter for the reactive section is adopted for the entire column.

For every process and catalyst, varying the catalyst loading per stage different reflux ratios are generated. For each case the diameter of the column is determined according to the procedure just described. From all examined simulations, a regression function was obtained, which was then used to calculate the RDC diameter based on the RR of the respective case in the TEA.

All used hydraulic regression functions are summarized in Table S 19

Table S 19: Summary of the hydraulic regression functions for all RDC containing processes P2, P3 and P4 and for both studied catalysts.

Process	Catalyst	Regression function	Validity range
P2	A36	$d_{RDC} = -1.02E\text{-}8 \cdot RR^6 + 1.07E\text{-}6 \cdot RR^5 - 4.45E\text{-}5 \cdot RR^4 + 1.05E\text{-}3 \cdot RR^3 - 1.69E\text{-}2 \cdot RR^2 + 0.29 \cdot RR + 1.4$	RR = 8.5-25
	CAT400	$d_{RDC} = -1.07E\text{-}9 \cdot RR^6 + 1.64E\text{-}7 \cdot RR^5 - 1.04E\text{-}5 \cdot RR^4 + 3.64E\text{-}4 \cdot RR^3 - 8.35E\text{-}3 \cdot RR^2 + 2.03E\text{-}1 \cdot RR + 1.49$	RR = 2.2-30
P3	A36	$d_{RDC} = 1.74E\text{-}7 \cdot RR^6 - 1.23E\text{-}5 \cdot RR^5 - 3.45E\text{-}4 \cdot RR^4 - 4.86E\text{-}3 \cdot RR^3 + 3.26E\text{-}2 \cdot RR^2 + 7.54E\text{-}2 \cdot RR + 1.61$	RR = 1.7-21
	CAT400	$d_{RDC} = -3.1E\text{-}5 \cdot RR^6 + 1.31E\text{-}3 \cdot RR^5 - 2.23E\text{-}2 \cdot RR^4 + 0.20 \cdot RR^3 - 0.93 \cdot RR^2 + 2.41 \cdot RR - 0.77$	RR = 1.6-19
P4	A36	$d_{RDC} = -6.0E\text{-}9 \cdot RR^6 + 6.0E\text{-}7 \cdot RR^5 - 3.0E\text{-}5 \cdot RR^4 + 8.0E\text{-}4 \cdot RR^3 - 1.4E\text{-}2 \cdot RR^2 + 0.28 \cdot RR + 1.32$	RR = 5-25
	CAT400	$d_{RDC} = -3.0E\text{-}10 \cdot RR^6 + 8.0E\text{-}8 \cdot RR^5 - 7.0E\text{-}6 \cdot RR^4 + 3.0E\text{-}4 \cdot RR^3 - 7.8E\text{-}3 \cdot RR^2 + 0.21 \cdot RR + 1.24$	RR = 1.5-25

For the process P3 with CAT400 and pure MeOH feed, very low RR are achieved in the optimal configuration. Consequently, very small minimum hydraulic diameters are required which imply a very high column to achieve the desired total volume for the reactive section. To avoid unreasonably slim and high columns, a minimal RDC diameter of 1.5 m was defined for this process.

In all other processes, the RDC diameter according to the hydraulic regression functions were larger than 1.5 anyway.

SI3.8. Key technical parameters of the simulated MeOH plant

The MeOH plant is based on CO_2 and H_2 feedstock and produces enough MeOH required for a DME plant with the production capacity of 100 kt/a. The purge in the MeOH plant was set to a very small purge ratio of 0.01 %. The key technical parameters of the MeOH process are summarized in Table S 20.

Table S 20: Key technical parameters of the simulated MeOH process.

Parameter	Unit	Value
$\dot{n}_{Feed,H_2}$	kmol h^{-1}	1638.7
$\dot{n}_{Feed,CO_2}$	kmol h^{-1}	548
SN_{Loop}	-	4.88
Recycle Ratio	-	3.78
GHSV	h^{-1}	7569

The stoichiometric number SN is defined according to Nestler et al. [102] as follows:

$$SN = \frac{y_{H2} - y_{CO2}}{y_{CO2} + y_{CO}} \quad (21)$$

The Recycle Ratio is defined as the ratio between the mole flow of the loop stream and the mole flow of the MUG.

$$\text{Recycle Ratio} = \frac{\dot{n}_{\text{Loop}}}{\dot{n}_{\text{MUG}}} \quad (22)$$

Whereas the make-up gas (MUG) is the CO_2/H_2 mixture fed to the synthesis loop.

SI3.9. Column profiles of P4

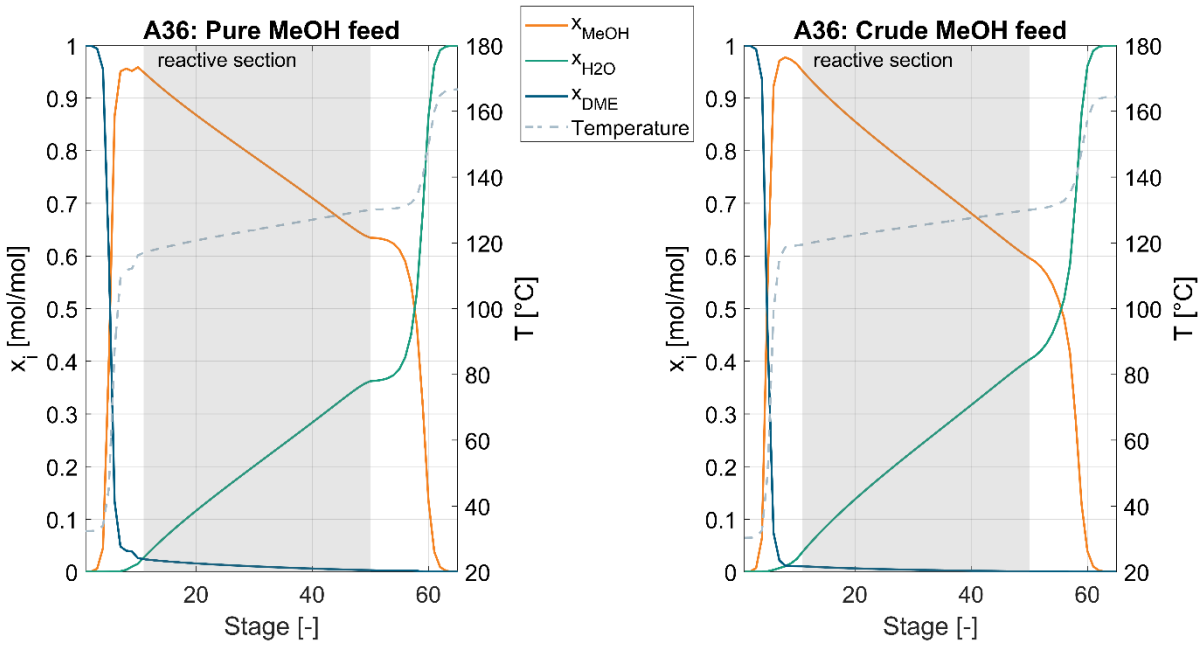

Figure S 13: Liquid composition profile and temperature profile of the RDC in process P4 with A36 as catalyst and pure MeOH feed (left) or crude MeOH feed (right).

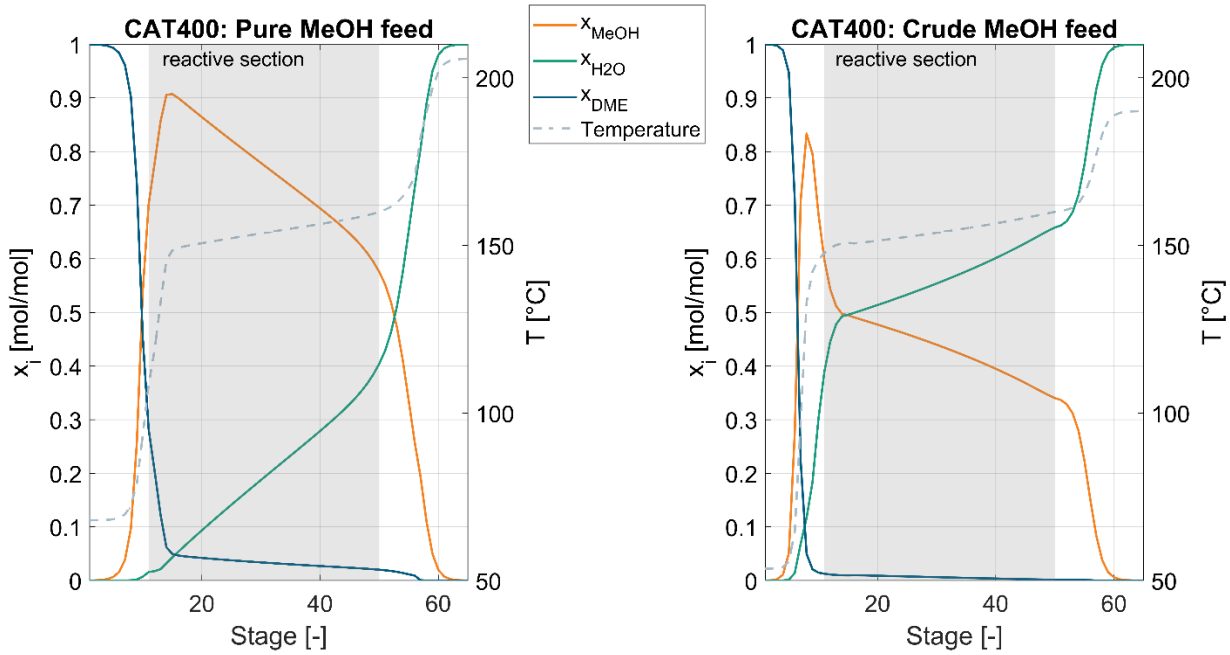

Figure S 14: Liquid composition profile and temperature profile of the RDC in process P4 with CAT400 as catalyst and pure MeOH feed (left) or crude MeOH feed (right).

Nomenclature

Abbreviations

Abbreviation	Designation
A36	Amberlyst® 36
ACC	Annualized capital cost
CAPEX	Capital expenditures
CAT400	Treverlyst CAT 400
CN	Cetane number
CI	Confidence interval
CMD	Crude methanol distillation
COR	Carbon oxide ratio
DME	Dimethyl ether
DPC	Direct plant cost
EC	Equipment cost
EOS	Equation of state
ER	Eley-Rideal
FCI	Fixed capital investment
FT	Fischer-Tropsch
FT-IR	Fourier-transform infrared spectroscopy
GC	Gas chromatograph
IER	Ion exchange resin
IPC	Indirect plant cost
LH	Langmuir-Hinshelwood
LPG	Liquefied petroleum gas
ML	Maintenance labour
MM	Maintenance material
MPV	Multiposition valve
MTG	methanol-to-gasoline
MTO	methanol-to-olefins
MTP	methanol-to-propylene
MUG	Make-up gas
OME	Polyoxymethylene dimethyl ethers
OS	Operating Supervision
OPEX	Operational expenditures
PFR	Plug flow reactor
PO	Plant overhead costs
PR	Pre-reactor
PtX	Power-to-X
RD	Reactive distillation
RDC	Reactive distillation column
RDS	Rate-determining step
RR	Reflux ratio

rWGS	Reverse water gas shift reaction
SR	Side-reactor
TOS	Time on stream
TI	Temperature indication
VLE	Vapour-liquid equilibrium
WGS	Water gas shift reaction
WHSV	weight hourly space velocity
WSSRE	Weighted sum of squared relative errors

Symbols (Latin)

Symbol	Designation	Unit
a	Specific surface area	$m^2\ m^{-3}$
A	Cross sectional area	m^2
c_i	Concentration of component i	$mol\ l^{-1}$
c_p	Specific heat capacity	$J\ kg^{-1}\ K^{-1}$
C	Specific cost	€ $(quantity\ unit)^{-1}$
d	Diameter	m
d_{eq}	Equivalent diameter	m
D	Diffusion coefficient	$m^2\ s^{-1}$
E_A	Activation energy	$J\ mol^{-1}$
f_s	Wall factor	-
F	Lang Factor	-
F_p	Pressure correction factor	-
F_d	Diameter correction factor	-
g	Gravity acceleration	$m\ s^{-2}$
h	Specific enthalpy	$J\ mol^{-1}$
h_L	Volumetric liquid holdup	m^3
h_{labour}	Person-hours	h
Δh_v	Enthalpy of vaporization	$J\ mol^{-1}$
H	Height	m
$\Delta H^0_{298\ K}$	Standard enthalpy of reaction	$J\ mol^{-1}$
I	Interest rate	-
J	Limit of counting index	-
k	Rate constant	$mol\ kg_{cat}^{-1}\ s^{-1}$
k_0	Pre-exponential factor	$mol\ kg_{cat}^{-1}\ s^{-1}$
K_{Ads}	Ratio of adsorption constants	-
K_α	Freundlich fitting parameter	K
K_{eq}	Equilibrium constant	-
K_i	Adsorption constant of component i	-
K_W	Sorption coefficient	-
l	Lifetime	years
L	Length	m
m	Mass	kg
$\dot{m}$	Mass flow	$kg\ s^{-1}$
n	Molar amount	mol

$\dot{n}$	Molar flow	mol s^{-1}
N	Stage number	-
NCC	Net conversion cost	€ t^{-1}
NPC	Net production cost	€ t^{-1}
p	Pressure	bar
P	Sampling port number	-
$P_A, P_B, P_C, P_D, P_E, P_F$	Packing parameter	-
q	Acid capacity	meq g^{-1}
Q	Heat flux	W
r	Reaction rate	mol s^{-1}
R	Universal gas constant	J mol^{-1} K^{-1}
SN	Stoichiometric number	-
t	Time	s
T	Temperature	K
T_i^*	Boiling temperature of component i	K
u	Velocity	m s^{-1}
v	Liquid molar volume	m^3 mol^{-1}
V	Volume	m^3
w	Weighting factor in kinetic fitting	-
W	Working capital share	-
x_i	Mole fraction of component i in liquid phase	mol mol^{-1}
X_i	Conversion of component i	-
y_i	Mole fraction of component i in gas phase	mol mol^{-1}
Δz	Length increment	m
Z	Active site	-

Symbols (Greek)

Symbol	Designation	Unit
α	Freundlich exponent	
ϵ	Porosity/void fraction	-
η	Dynamic viscosity	Pa s
η_w	Water inhibition term	-
θ_{H2O}	Fraction of acid sites blocked by water	-
θ_p	Inclination angle of packing with respect to the horizontal	°
λ	Thermal conductivity	W m^{-1} K^{-1}
ρ	Density	kg l^{-1}
τ	Tortuosity	-
τ_{red}	Reduced temperature	-
ϕ	Volume fraction	-
φ	Association factor of solvent	-
χ_{cp}	Catalyst volume fraction of catalytic packing	-
Ψ	Weisz-Prater parameter	-

Indices

Indice	Designation
0	Initial condition, before reaction, below gas loading point
Ads	Adsorption as rate-determining step
bi	pure component at boiling point
cat	Catalyst
cb	Catalyst bags
cool	Cooling medium
crude	Operated with crude methanol feedstock
equil	Chemical equilibrium
data	Data point
Des	Desorption as rate-determining step
dew	Related to dew point
dir	Direct
Freundlich	Water inhibition term based on Freundlich isotherm
gas	Refering to the gaseous phase
i	Component i
ind	Indirect
j	Counting index
K	Counting index
Langmuir 1	Water inhibition term based on Langmuir isotherm with one water molecule blocking one active site
Langmuir 2	Water inhibition term based on Langmuir isotherm with one water molecule blocking two active site
max	Maximum
mix	Mixture
oc	Open channels of catalytic packing
op	Plant operation
power	Electric power
pure	Operated with pure methanol feedstock
rel	Relative
reactive	Reactive stages
rect, lower	Lower rectifying stages
rect, upper	Upper rectifying stages
Side	Side stream
SR	Surface reaction as rate-determining step
wet	Referring to the wet packing
WD	Withdrawal stage

List of Figures

List of Tables

Publication list

Peer-reviewed journal publications

- Semmel, M.; Kerschbaum, M.; Steinbach, B.; Sauer, J.; Salem, O. (2023): Optimized design and techno-economic analysis of novel DME production processes. In *Reaction Chemistry & Engineering*. DOI: 10.1039/D3RE00333G.
- Schühle, P.; Stöber, R.; Semmel, M.; Schaadt, A.; Szolak, R.; Thill, S. et al. (2023): Dimethyl ether/CO2 - a hitherto underestimated H2 storage cycle. In Energy & Environmental Science 16 (7), pp. 3002–3013. DOI: 10.1039/D3EE00228D.
- Semmel, M.; Bogatykh, I.; Steinbach, B.; Sauer, J.; Repke, J.; Salem, O. (2023): Demonstration and experimental model validation of the DME synthesis by reactive distillation in a pilot-scale pressure column. In *React. Chem. Eng.* (8), pp. 2309–2322. DOI: 10.1039/D3RE00200D.
- Kubas, D.; Semmel, M.; Salem, O; Krossing, I. (2023): Is Direct DME Synthesis Superior to Methanol Production in Carbon Dioxide Valorization? From Thermodynamic Predictions to Experimental Confirmation. In *ACS Catal.*, pp. 3960–3970. DOI: 10.1021/acscatal.2c06207.
- Semmel, M.; Steiner, L.; Bontrup, M.; Sauer, J.; Salem, O. (2022): Catalyst screening and reaction kinetics of liquid phase DME synthesis under reactive distillation conditions. In *Chem. Eng. J.*, p. 140525. DOI: 10.1016/j.cej.2022.140525.
- Cholewa, T.; Semmel, M.; Mantei, F.; Güttel, R.; Salem, O. (2022): Process Intensification Strategies for Power-to-X Technologies. In *ChemEngineering* 6 (1), p. 13. DOI: 10.3390/chemengineering6010013.

Not peer-reviewed publications

- Semmel, M.; Salem, O. (2023): Entwicklung eines Reaktivdestillationsverfahrens zur Herstellung von Dimethylether. In *ENERGIEWIRTSCHAFTLICHE TAGESFRAGEN* (3), pp. 48–58. Available online at https://emagazin.et-magazin.de/
- Bürger, S.; Horch, F.; Geiling, J.; Öchsner, R.; Kolb, G.; Groos, U.; Semmel, M.; Schaadt, A. (2022): Einsatz von Wasserstofftechnologien in Mobilität und Transport. In Reimund Neugebauer (Ed.): Wasserstofftechnologien. Berlin, Heidelberg: Springer Berlin Heidelberg, pp. 123–153.

- Semmel, M.; Ali, R. E.; Ouda, M.; Schaadt, A.; Sauer, J.; Hebling, C. (2021): Power-to-DME: a cornerstone towards a sustainable energy system. In Giuseppe Spazzafumo (Ed.): Power to Fuel. How to Speed Up a Hydrogen Economy: Elsevier, pp. 123–151.

Invention disclosures

- Semmel, M.; Steinbach, B.; Salem, O. (2022): Verfahren zur Herstellung von Dimethylether: AZ: 10 2022 114 811.4. Submission date: 14.03.2023.

Conference contributions

- Semmel, M.; Salem, O.; Schaadt, A.; „Process Intensification Strategy Demonstrated by Innovative DME Synthesis“. C1 Building Blocks for Future Chemistry (2023), Oral presentation
- Semmel, M.; Salem, O.; Sauer, J. "DME Synthesis by Reactive Distillation: Modeling and Validation". 8th European Process Intensification Conference (2023), Oral presentation.
- Semmel, M.; Salem, O.; Sauer, J. "Dimethyl Ether (DME) Reactive Distillation: Reaction Kinetics and Validation". Annual Meeting on Reaction Engineering (2023), Poster contribution.
- Schaadt, A.; Semmel, M.; Salem, O.; Hebling, C. "DME as a global Point-to-Point H2 carrier: Process intensified DME Production - The INDIGO Technology". DGMK Conference: The Role of Catalysis for the Energy-Transition (2022), Poster contribution.
- Semmel, M.; Salem, O.; Sauer, J. "Kinetic investigations of DME synthesis at catalytic distillation conditions". Annual Meeting on Reaction Engineering (2022), Oral presentation.
- Semmel, M.; Salem, O.; Schaadt, A.; Sauer, J. "Kinetische Untersuchungen der DME-Synthese bei Reaktivdestillationsbedingungen”. Jahrestreffen der ProcessNet-Fachgruppen Abfallbehandlung und Wertstoffrückgewinnung, Energieverfahrenstechnik, Gasreinigung, Hochtemperaturtechnik, Rohstoffe (2022), Oral presentation.

- Semmel, M.; Salem, O.; Schaadt, A.; Sauer, J. "Entwicklung eines neuartigen Power-to-Liquid Verfahrens zur Herstellung von Dimethylether". Jahrestreffen der ProcessNet-Fachgruppe Energieverfahrenstechnik (2021), Oral presentation.